



HAL
open science

Cluster mass scaling relations through weak lensing measurements

Carolina Parroni

► **To cite this version:**

Carolina Parroni. Cluster mass scaling relations through weak lensing measurements. Instrumentation and Methods for Astrophysic [astro-ph.IM]. Université Sorbonne Paris Cité, 2017. English. NNT : 2017USPCC232 . tel-02141786

HAL Id: tel-02141786

<https://theses.hal.science/tel-02141786>

Submitted on 28 May 2019

HAL is a multi-disciplinary open access archive for the deposit and dissemination of scientific research documents, whether they are published or not. The documents may come from teaching and research institutions in France or abroad, or from public or private research centers.

L'archive ouverte pluridisciplinaire **HAL**, est destinée au dépôt et à la diffusion de documents scientifiques de niveau recherche, publiés ou non, émanant des établissements d'enseignement et de recherche français ou étrangers, des laboratoires publics ou privés.

UNIVERSITÉ DE PARIS 7 DENIS DIDEROT
Université Sorbonne Paris Cité (USPC)
UFR de PHYSIQUE
Ecole doctorale d'Astronomie et d'Astrophysique d'Île de France
Observatoire de Paris-Meudon
Laboratoire LERMA

THÈSE

Présentée en vue de l'obtention du titre de Docteur
Spécialité : ASTRONOMIE & ASTROPHYSIQUE

par:

Carolina PARRONI

Cluster mass scaling relations through weak lensing measurements

Thèse dirigée par Simona MEI

Soutenue le 11 Septembre 2017 devant le jury constitué de:

Yannick MELLIER	Président du jury
Geneviève SOUCAIL	Rapporteur
Matthias BARTELMANN	Rapporteur
Massimo MENEGHETTI	Examineur
Simona MEI	Directrice de thèse

Title: Cluster mass scaling relations through weak lensing measurements

Abstract: Galaxy clusters are essential cosmological and astrophysical tools, since they represent the largest and most massive gravitationally bound structures in the Universe. Through the study of their mass function, of their correlation function, and of the scaling relations between their mass and different observables, we can probe the predictions of cosmological models and structure formation scenarios. They are also interesting laboratories that allow us to study galaxy formation and evolution, and their interactions with the intra-cluster medium, in dense environments. For all of these goals, an accurate estimate of cluster masses is of fundamental importance. I studied the accuracy of the optical richness obtained by the RedGOLD cluster detection algorithm (Licitra et al. 2016) as a mass proxy, using weak lensing and X-ray mass measurements. I measured stacked weak lensing cluster masses for a sample of 1323 galaxy clusters in the CFHTLS W1 and in the NGVS at $0.2 < z < 0.5$, in the optical richness range 10-70. I tested different weak lensing mass models that account for miscentering, non-weak shear, the two-halo term, the contribution of the Brightest Cluster Galaxy, and the intrinsic scatter in the mass-richness relation. I found that the miscentering correction is necessary to avoid a bias in the measured halo masses, while the inclusion of the BCG mass does not affect the results. I calculated the coefficients of the mass-richness relation, and of the scaling relations between the lensing mass and X-ray mass proxies. My results are consistent with simulations and previous works in the literature.

Keywords: weak lensing, galaxy clusters, scaling relations

Titre: Relation d'échelle d'amas de galaxies à partir d'observations de lentilles gravitationnelles

Résumé : Les amas de galaxies sont des outils cosmologiques et astrophysiques essentiels, car ce sont les objets les plus grands et les plus massifs gravitationnellement liés dans l'Univers. L'étude de leur fonction de masse, de leur fonction de corrélation et des relations d'échelle entre leur masse et différentes observables nous permettent de tester les prévisions des modèles cosmologique et les scénarii de formation des structures. Ils sont aussi d'intéressants laboratoires pour l'étude de la formation et de l'évolution des galaxies, et de leur interactions avec le milieu qui les entourent, dans d'environnements denses. Pour y parvenir, estimer précisément leur masse revêt une importance fondamentale. J'ai étudié la précision de la richesse optique calculée par l'algorithme de détection d'amas RedGOLD (Licitra et al. 2016) en tant que mass proxy, en utilisant des mesures de lentilles gravitationnelles (weak lensing) et des observations en rayon X. J'ai mesuré les masses cumulées d'un échantillon de 1323 amas de galaxies dans le CFHTLS et NGVS à $0.2 < z < 0.5$, dans l'intervalle de richesse 10-70. J'ai testé différents modèles prenant en compte les erreurs sur la position du centre de l'amas, les effets de lentille non faible (non-weak shear), le "two-halo term", la contribution de la galaxie centrale brillante et la dispersion intrinsèque de la relation masse-richesse. J'ai montré que la correction de la position du centre est nécessaire pour éviter un biais dans la mesure de la masse, alors que l'ajout de la galaxie centrale n'affecte pas les résultats. J'ai calculé les coefficients de la relation masse-richesse et ceux de la relation d'échelle entre masses issues du weak lensing et celle estimées à partir d'observations dans les rayons X. Mes résultats sont en accord avec les simulations et les précédents travaux publiés.

Mots clefs: Lentilles gravitationnelles, amas de galaxies, relation d'échelle

CONTENTS

1	Galaxy Clusters	21
1.1	Theory	21
1.1.1	Cosmological model	21
1.1.2	Density perturbations and structure formation	26
1.1.3	Cluster formation	30
1.1.4	Mass profile	31
1.1.5	Mass function	32
1.1.6	Cluster mass and cosmology	33
1.2	Observations	38
1.2.1	Detection and catalog creation	38
1.2.2	Mass proxies	41
1.2.3	Scaling relations	43
2	Weak Lensing	45
2.1	Theory	46
2.1.1	Lens equation	46
2.1.2	Lensing potential	49
2.1.3	Shear and convergence	50
2.1.4	Ellipticity definition	53
2.1.5	Lens models	56
2.2	Applications	60
2.2.1	Galaxy-galaxy lensing	60
2.2.2	Galaxy cluster lensing	62
2.2.3	Peak statistics	67
2.2.4	LSS lensing	69
2.2.5	CMB lensing	70
2.3	Data and tools	73
2.4	Challenges for the future	75

3	Statistical Analysis	82
3.1	Bootstrap theory	82
3.2	MCMC theory	85
3.2.1	Metropolis-Hastings	87
3.2.2	Stretch Move	88
3.2.3	Autocorrelation time	90
3.3	Aperture mass statistics	91
4	The weak lensing analysis of CFHTLS and NGVS galaxy clusters	93
4.1	Aim of this work	93
4.2	Data	94
4.2.1	CFHTLenS and NGVSLenS	94
4.2.2	Photometric redshifts	96
4.3	Cluster catalogs	98
4.3.1	The RedGOLD Optical Cluster Catalogs	98
4.3.1.1	RedGOLD algorithm	98
4.3.1.2	Richness definition	99
4.3.1.3	CFHT-LS W1 and NGVS cluster catalogs	100
4.3.1.4	Weak lensing subsample selection	101
4.3.2	X-ray cluster catalog	102
4.4	Weak lensing analysis	106
4.4.1	Shear profile measurement	106
4.4.2	Shear profile model	108
4.4.2.1	$\Delta\Sigma_{\text{NFW}}$ profile	109
4.4.2.2	Miscentering Term	110
4.4.2.3	Non-weak Shear Term	112
4.4.2.4	Two-halo Term	113
4.4.2.5	Model extensions	113
4.4.3	Fit the model to the measured shear profile	114
4.5	Preliminary tests	118
4.5.1	Code validation	118
4.5.2	Background selection	121
4.5.2.1	Selection criteria	121
4.5.2.2	Magnitude limit	122
4.5.3	Cluster redshift cut	125
4.5.4	Richness binning	125
4.5.5	Stacking and shear components	129
4.5.6	Centering	130
4.5.6.1	Simulated shear maps	132
4.5.6.2	Simulated clusters	134

4.5.6.3	Weak lensing analysis of the observed Red-GOLD clusters	134
4.5.7	Joint fit	136
4.6	Results	141
4.6.1	Mass estimation	141
4.6.2	Mass-richness relation	147
4.6.3	Weak lensing mass vs X-ray mass proxies relations . .	150
5	Discussion	158
5.0.4	Comparison with previously derived mass-richness relations	158
5.0.5	Comparison with previously derived X-ray scaling relations	162
6	Conclusions and Perspectives	167
6.1	Summary and conclusions	167
6.2	Current projects	172
6.3	Future perspectives	176
A	Submitted paper	181

LIST OF FIGURES

1.1	The $\Lambda - CDM$ model	24
1.2	Dependance of the scale factor with time for the different epochs.	25
1.3	Perturbations growth	28
1.4	Power spectrum	29
1.5	Evolution of a spherical perturbation in linear and non-linear theory	30
1.6	Halo mass function	34
1.7	Constraints on the cosmological parameters from galaxy cluster abundances and WMAP CMB data	35
1.8	Predicted halo mass thresholds as a function of cumulative number counts	36
1.9	Combined constraints on the cosmological parameters from different methods	39
1.10	Selection function of the next generation surveys	41
2.1	Scheme of a typical lensing system	48
2.2	Sketch of the effect of the convergence and shear on the image of a round source	52
2.3	Tangential and cross components of the shear	53
2.4	Shape of the image of a circular source, as a function of the ellipticity components	55
2.5	Reconstruction of the radial surface density contrast	61
2.6	Miscentering parameters from van Uitert et al. (2016)	64
2.7	Mass-richness relation from van Uitert et al. (2016)	65
2.8	Mass-concentration relation from van Uitert et al. (2016)	66
2.9	Shear peak counts	68
2.10	Illustration of simulations for peak counts prediction	68
2.11	Constraints on cosmological parameters from peak counts statistics, power spectrum, and joint analysis	69

2.12	CMB lensing power spectrum measured from different surveys with increasing significance	72
2.13	Illustrative example of the effects of shear, seeing, pixelization and noise on the image of a galaxy	73
2.14	Scheme of the different ingredients involved in weak lensing analysis	76
2.15	Multiplicative and additive calibration corrections of lensfit ellipticity measurements	77
2.16	Constraints on cosmological parameter obtained with different photometric redshift uncertainty and calibration methods. . .	77
2.17	Comparison of low resolution images from ground based telescopes with high resolutions ones from space telescopes	79
2.18	The tension between Planck CMB and KiDS lensing	81
3.1	Illustration of the bootstrap method	85
3.2	Burn in and converge of MCMC chain	87
3.3	Example of a skewed probability density	89
3.4	Representation of a step of the Stretch Move	90
4.1	Lensing efficiency as a function of cluster redshift, for sources at $z = 1$	102
4.2	The richness and redshift distributions of the RedGOLD CFHT-LS W1, NGVS5, and NGVS4	103
4.3	The distribution of the offsets between the RedGOLD, X-ray and simulation cluster centers	111
4.4	MCMC corner plot	116
4.5	Comparison of the mass-richness relation with that of Ford et al. (2015)	119
4.6	Comparison of the miscentering parameters with those derived by Ford et al. (2015)	120
4.7	The percentage of selected background sources, and the percentage of wrong selections, as a function of the cluster redshift	123
4.8	Mass-richness relations obtained using the different selection criteria	126
4.9	Masses inferred fitting individual clusters with $\lambda > 50$	127
4.10	Number density of background sources as a function of redshift	127
4.11	Mean number density of background sources as a function of redshift and richness.	128
4.12	Mass-richness relations obtained fitting different λ bins	128
4.13	Shear field maps for the stacking of 50, 100, 150 clusters . . .	130
4.14	Tangential and cross shear components profiles	131

4.15	Masses of individual clusters obtained with the miscentering correction, and without	132
4.16	Lensing S/N ratio map of simulations with and without the intrinsic ellipticity	133
4.17	Convergence and S/N ratio map of a simulated cluster	135
4.18	Optical images and lensing S/N maps of some of the most massive RedGOLD clusters, with centers in good agreement	137
4.19	Optical images and lensing S/N maps of some of the most massive RedGOLD clusters, with centers not in agreement	138
4.20	Comparison of the shear profiles measured with the CFHT-LS W1 + NGVS5, NGVS4, and CFHT-LS W1 + NGVS5 + NGVS4	142
4.21	Shear profiles measured with the CFHT-LS W1 + NGVS5 + NGVS4, and the corresponding lensing signal-to-noise ratio maps	144
4.22	Signal contribution to the shear profile	145
4.23	The weak lensing mass-richness relations obtained with the complete sample CFHT-LS W1 + NGVS5 + NGVS4, using the three different models	147
4.24	Effect of the a posteriori intrinsic scatter correction	149
4.25	Comparison of the mass-richness relations derived with and without scatter in the c-M relation	149
4.26	Normalized difference between X-ray masses and lensing masses	151
4.27	Comparison between X-ray masses and lensing masses	152
4.28	Mass-luminosity and mass-temperature relations	153
5.1	Comparison of the mass-richness relation derived from the Two Component Model, with the a posteriori intrinsic scatter correction, with others in literature	159
5.2	Comparison of RedGOLD and redMaPPer richnesses as a function of redshift	161
6.1	Stellar mass versus halo mass relation	174
6.2	Optimal filter from Maturi et al. (2005)	176
6.3	Effective convergence power spectrum	177
6.4	Comparison of lensing center estimates	177

LIST OF TABLES

4.1	MCMC priors for the fit of the shear profiles	115
4.2	Mass-richness relation parameters obtained with the different background selection criteria	124
4.3	Difference between the mass-richness relation parameters obtained with the different selection criteria	124
4.4	Range in λ , the number of clusters, and the mean λ , for each bin in the different λ binnings	129
4.5	MCMC priors for the joint fit of the shear profiles	139
4.6	Parameters derived for the five models of the joint fit	140
4.7	Stacking background source number density	143
4.8	Parameters derived from the fit of the <i>Basic Model</i> , the <i>Added Scatter Model</i> , and the <i>Two Component Model</i> shear profiles to the measurements	146
4.9	The results of the fit of the mass-richness relation, the normalized average difference between lensing and X-ray masses, and the average ratio of the two	148
4.10	Results of the fit of the weak lensing mass versus X-ray mass and mass proxy relations	156
4.11	Comparison of the mass-temperature and mass-luminosity relations with others in literature	157

ABSTRACT

Galaxy clusters are essential cosmological and astrophysical tools, since they represent the largest and most massive gravitationally bound structures in the Universe. Their number and distribution permit us to probe the predictions of cosmological models and structure formation scenarios. Through the study of their mass function, of their correlation function, and of the scaling relations between their mass and different observables, we can infer the cosmological parameters and constrain them. Galaxy clusters are also interesting laboratories that allow us to study galaxy formation and evolution, and their interactions with the intra-cluster medium, being the densest environment that we can find in the Universe.

For all of these goals, an accurate estimate of the cluster mass is of fundamental importance. Since it cannot be measured directly, we need to rely on mass proxies. Studying galaxy clusters radiation at different wavelengths, we can estimate their mass using different tracers.

The cluster mass can be derived from X-ray observations of the cluster gas, measuring its temperature under the assumption of hydrostatic equilibrium (Sarazin, 1988). Studying the emission in the millimeter of the intra-cluster medium, we can measure the total cluster mass through the thermal Sunyaev-Zel'dovich effect (S-Z effect; Sunyaev & Zeldovich, 1972). In the optical and in the infrared, we can use the starlight emission of cluster galaxies. In fact, we can relate the velocity dispersion of cluster members to the cluster mass through the virial theorem, assuming that the cluster is in dynamical equilibrium. Also the cluster's total optical or infrared luminosity can be used as a mass proxy. Postman et al. (1996), for example, defined the *richness* parameter, introduced by Abell (1958), as the number of cluster galaxies brighter than the characteristic luminosity of the Schechter (1976) profile, L_* .

Gravitational lensing is another tool that can be used to measure cluster masses. Strong and weak gravitational lensing produce a distortion of the image of the background sources that it's proportional to the total cluster mass. In the *strong lensing* regime, this distortion can be so intense that it creates multiple-image systems or image deformations that can be seen by eye, like *Einstein's rings* or *arcs* in galaxy clusters. On the other hand, in the weak lensing regime, the cluster gravitational potential produces small distortions in the observed shape of the background field galaxies, creating the so-called shear field. Because the shear is small relative to the intrinsic ellipticity of the galaxies (due to their random shape and orientation), a statistical approach is required to measure it and the signal is averaged over a large number of background sources to increase the signal-to-noise ratio

(Schneider, 2005).

Different mass proxies usually lead to mass estimations that are affected by different systematics. X-ray mass measurements are not reliable in systems for which the assumption of the hydrostatic equilibrium is not valid, such as clusters in merging process or in the central regions of clusters with strong AGN feedback. The S-Z method allows us to perform mass measurements at high redshifts, but it is subjected to projection effects. Velocity dispersion measurements are not affected by forms of non-thermal pressure such as magnetic fields, turbulence and cosmic ray pressure, as X-ray and S-Z mass measurements, but they are sensitive to triaxiality and projection effects, and constrained to the assumption of dynamical equilibrium. Gravitational lensing, on the other hand, does not require any assumption on the dynamical state of the cluster and it is sensitive to the projected mass along the line of sight, representing a more reliable tool to determine total cluster masses (Meneghetti et al., 2010; Allen, Evrard & Mantz, 2011; Rasia et al., 2012).

Every method as its advantages and disadvantages but optical and infrared detection methods are particularly important since, in the future, large scale surveys at these wavelengths, such as LSST¹ and Euclid² will be able to identify clusters that will not be detected with other methods.

Several works in the literature have proven that the optical richness shows a good correlation with the cluster total masses derived from weak lensing (Johnston et al., 2007; Covone et al., 2014; Ford et al., 2015; van Uitert et al., 2015; Simet et al., 2016; Melchior et al., 2016). The typical mass uncertainty at a given richness is of $\sim 10 - 25\%$ including statistical and systematic errors, in the mass range $6 \times 10^{12} M_{\odot} \lesssim M \lesssim 10^{15} M_{\odot}$ and in the redshift range $0.1 \lesssim z \lesssim 0.9$.

Rykoff et al. (2014) built an optical cluster finder based on the red-sequence finding technique, redMaPPer, and applied it to the Sloan Digital Sky Survey (SDSS; York et al., 2000). This technique detects galaxy clusters looking for overdensities of early type galaxies (ETGs). It relies on the observational evidence that cluster inner regions host a large population of this kind of galaxies, which are tightly distributed on a red-sequence on the color-magnitude diagram (Gladders & Yee, 2000). redMaPPer richness is computed using optimal filtering, as a sum of probabilities and depends on three filters based on colors, positions and luminosity (Rozo et al., 2009a; Rozo & Rykoff, 2014; Rykoff et al., 2012, 2014, 2016).

Licitra et al. (2016a,b) introduced a simplified definition of cluster rich-

¹<http://www.lsst.org>

²<http://euclid-ec.org>

ness based on the redMaPPer richness measurement, within their detection and cluster selection algorithm RedGOLD.

This algorithm is based on a revised red-sequence technique. It assigned to each detection the center coordinates, the redshift, a significance parameter, and a richness. RedGOLD richness quantifies the number of red, passive ETGs brighter than $0.2L_*$, inside a given radius. It is optimized to detect massive galaxy clusters ($M_{200} > 10^{14}M_\odot$), and to produce optical cluster catalogs with high completeness and purity. When compared to X-ray mass proxies, the RedGOLD richness leads to scatters in the X-ray temperature-richness relation similar to those obtained with redMaPPer (Rozo & Rykoff, 2014), which is very promising since RedGOLD was applied to a lower richness threshold (i.e. lower cluster mass).

The goal of my thesis was to measure cluster masses using weak lensing, and derive scaling relations with optical and X-ray mass proxies. This permitted me to calibrate and evaluate the precision of the RedGOLD richness as a cluster mass proxy. Using the mean lensing cluster masses calculated stacking clusters in bins of richness, I inferred the mass-richness relation. I then compared the weak lensing masses with X-ray masses, luminosity, and temperature.

For this work, I used the RedGOLD cluster catalogs of the Canada-France-Hawaii Telescope Legacy Survey (CFHT-LS; Gwyn, 2012) Wide 1 (W1) field and of the Next Generation Virgo Cluster Survey (NGVS; Ferrarese et al., 2012), obtained by Licitra et al. (2016a,b). The algorithm detected 652 clusters on the CFHTLS W1, and 279 and 1704 clusters on the $\sim 20deg^2$ of the NGVS covered by 5 bands and on the entire NGVS without the r -band coverage, respectively. For the weak lensing analysis, I selected a subsample of 1323 clusters with a threshold in significance of $\sigma_{\text{det}} \geq 4$, with richness $10 < \lambda < 70$, and redshift $0.2 \leq z \leq 0.5$. Using this selection, the published catalogs are $\sim 100\%$ complete and $\sim 80\%$ pure Licitra et al. (2016a).

I used the photometric redshift catalogs obtained by Raichoor et al. (2014), with the Bayesian softwares *LePhare* (Arnouts et al., 1999; Arnouts et al., 2002; Ilbert et al., 2006) and BPZ (Benítez, 2000; Benítez et al., 2004; Coe et al., 2006). They found a bias $-0.05 < \Delta z < 0.02$, scatter values in the range $0.02 < \sigma < 0.06$, and 5 – 15% of outliers, for $i' < 23$ mag.

For the shear analysis, I used the CFHTLenS and the NGVSLenS shear catalogs, based on an improved data reduction, compared to the standard THELI pipeline (Erben et al., 2005, 2009, 2013), performed by Raichoor et al. (2014). Galaxy shape measurements were obtained applying the Bayesian *lensfit* algorithm (Miller et al., 2013).

For the X-ray comparison, I used Gozaliasl et al. (2014), Mehrrens et al.

(2012), and Piffaretti et al. (2011) X-ray catalogs.

In order to infer weak lensing masses, using the cluster, photometric redshift, and shear catalogs, I developed and optimized my own weak lensing analysis pipeline. The code starts with the selection of the background galaxy field inside a circular area of a given radius around each cluster in the sample, through a photometric redshift selection. The algorithm stacks clusters according to their richness, and calculates the radial shear profiles, averaging the tangential shear in logarithmic radial bins around the center of the stacked samples. It applies lens-source pairs weights (that depend on the lensing efficiency and on the quality of background galaxy shape measurements), and the *lensfit* calibration corrections. The algorithm then calculates the covariance matrices, using the bootstrap method (Efron, 1979), taking clusters with replacements in each richness bin, in order to assign error bars to each point of the radial shear profile. For each stack of clusters, a signal-to-noise ratio map is calculated using aperture mass statistics (Schneider, 1996; Schirmer et al., 2006; Du & Fan, 2014).

Once I obtained the shear profiles for each stack of clusters, I fitted them using Markov Chains Monte Carlo (MCMC; Metropolis et al., 1953). This method allowed me to efficiently sample the model likelihood distribution, from which I obtained the estimation of the error bars on the fitting parameters and of the confidence regions for each couple of parameters.

I matched the observed profiles with three analytic models. The *Basic Model*, which consists of a halo model (Seljak, 2000), with an NFW (Navarro, Frenk & White, 1996) surface density contrast and correction terms that take into account cluster miscentering (Johnston et al., 2007; George et al., 2012), non-weak shear (Mandelbaum et al., 2006; Johnston et al., 2007) and the two halo term (Seljak, 2000; Seljak & Warren, 2004; Johnston et al., 2007). The free parameters of this model are r_{200} , from which I calculate the mass M_{200} , and the miscentering parameters p_{cc} , and σ_{off} . I then added to this model an additional free parameter, $\sigma_{M|\lambda}$, the intrinsic scatter in the mass-richness relation (hereafter *Added Scatter Model*). Finally, I took into account the contribution from the Brightest Central Galaxy (BCG) mass M_{BCG} , adding this parameter to the *Basic Model* (hereafter *Two Component Model*).

For the three models, I obtained the mass-richness relation fitting the lensing mass values recovered for each richness bin.

I validated my code comparing my results with those of Ford et al. (2015), obtained in an independent way, using the entire CFTHLS W1, W2, W3, W4, and the public cluster catalog of Milkeraitis et al. (2010), and performed several tests to estimate possible biases in the results. I tested different kinds of background sample selection and source magnitude cuts. I tested the redshift selection and different binnings in richness of the cluster sample. I

checked that the behavior of the tangential and cross components of the shear profiles were as expected from theory. I compared masses estimated with and without the miscentering correction, in order to evaluate the contribution of this correction term. I used aperture mass statistics to test the identification of cluster centers through the lensing signal, using simulated shear maps, simulated clusters, and observed RedGOLD clusters. In order to check that fitting the profile of each richness bin individually does not introduce a bias in the determination of the mass-richness relation parameters, I tested a *joint fit* (i.e. the fit of the profiles associated to all richness bin simultaneously).

From the tests that I performed, I concluded that : (1) the joint and individual fitting techniques are equivalent. (2) The miscentering correction is the one that most affects the halo mass measurements. (3) The BCG mass and the intrinsic scatter in the mass-richness relation are not constrained by the data. (4) The BCG mass addition in the model doesn't affect the recovered halo mass.

For these reasons, I decided to use the mass-richness relation inferred from the *Two Component Model*, with an a posteriori intrinsic scatter correction (Ford et al., 2015) *Final Model*. With this model, I obtained a mass-richness relation of $\log M_{200}/M_{\odot} = (14.46 \pm 0.02) + (1.04 \pm 0.09) \log(\lambda/40)$ (statistical uncertainties). This result is consistent within $1 - 2\sigma$ with the lensing mass-richness relations obtained by Rykoff et al. (2012), Saro et al. (2015), Simet et al. (2016), Farahi et al. (2016) and Melchior et al. (2016), using the SDSS and DES redMaPPer cluster samples.

For the lensing mass vs X-ray luminosity relation I found $\log\left(\frac{M_{200}E(z)}{8 \times 10^{13} h^{-1} M_{\odot}}\right) = (0.10 \pm 0.03) + (0.61 \pm 0.12) \log\left(\frac{L_X}{5.6 \times 10^{42} h^{-2} \text{erg/s} E(z)}\right)$. For the lensing mass vs X-ray temperature relation I obtained $\log\left(\frac{M_{200}E(z)}{6 \times 10^{13} h^{-1} M_{\odot}}\right) = (0.23 \pm 0.03) + (1.46 \pm 0.28) \log\left(\frac{T_X}{1.5 \text{KeV}}\right)$. These results are consistent with those of Leauthaud et al. (2010), Kettula et al. (2015), Mantz et al. (2016). For all three relations, I found a scatter of 0.20 dex, consistent with redMaPPer scatters.

In the remaining months of my PhD, I will focus on projects that are complementary to what I've done so far. I will study the relation between the lensing halo mass and the BCG stellar mass. I will check how different kinds of BCG selection affect the estimated lensing masses, and calculate the stellar-to-halo mass ratio for cluster central galaxies. I will also be able to infer an optical mass-luminosity relation, with the information on the b rest frame luminosity of central galaxies and of the entire cluster.

On the other hand, I would like to study in more detail the miscentering problem to see how different center choices would affect the shear profiles and the mass measurements of stacked or individual massive clusters. I

would like to expand the work of George et al. (2012) and include in the comparison also centers based on the peak of the weak lensing signal and on the hybrid approach between galaxy centers and centroids (used for example in RedGOLD), not considered in the cited work.

For these new projects I will use the new self calibrating version of the *lensfit* algorithm, and refined photometric redshift estimations on the CFHTLS W1 and on entire NGVS.

Next generation space surveys as *Euclid* and WFIRST³ will have a huge impact on the kind of weak lensing analysis that I performed for my thesis work, giving access to a cluster sample of one order of magnitude bigger. Also, the next generation radio surveys such as SKA⁴ will allow us to extend weak lensing measurements to the radio band, and to even larger scales.

The aim for future analysis is to reach an accuracy of 1% in cluster mass measurements. The main challenge in weak lensing analysis comes from the photometric redshift estimation that is linked to the selection of background source samples and to the weights assigned to each lens-source pair. In my future work I would like to study how the use of the photometric redshift distribution derived with different calibration methods affect the measurement of weak lensing masses and of cluster lensing centers.

The thesis is organized as follows: in Chapter 1, I will discuss galaxy clusters from a theoretical and observational point of view. I will describe the standard cosmological model, the structure formation mechanism, the most used cluster mass profiles, and the cluster mass function. I will also talk about how we can detect galaxy clusters and estimate their mass using different mass proxies, and the importance of scaling relations. In Chapter 2, I will summarize the theoretical principles of weak lensing, and discuss its possible applications. In Chapter 3, I will explain the statistical methods that I used for my analysis and the way that I applied them to the data. In Chapter 4, I will describe in detail the analysis and the tests that I performed. Finally, in Chapter 6, I will summarize the main results of my thesis work, discuss my future projects, and the perspectives of the weak lensing field.

³<http://wfirst.gsfc.nasa.gov>

⁴<http://www.skatelescope.org>

RÉSUMÉ

Les amas de galaxies sont des outils cosmologiques et astrophysique essentiels, car ce sont les objets les plus grands et les plus massifs gravitationnellement liés dans l'Univers. Leur nombre et leur distribution nous permettent de tester les prévisions des modèles cosmologique et les scenarii de formation des structures. Par l'étude de leur fonction de masse, de leur fonction de corrélation et des relations d'échelle entre leur masse et différentes observables, nous pouvons contraindre les paramètres cosmologiques de façon toujours plus stricte. En tant qu'environnements les plus denses qu'y soit dans l'Univers, les amas de galaxies sont aussi d'intéressants laboratoires pour l'étude de la formation et de l'évolution des galaxies, et de leur interactions avec le milieu qui les entourent.

Pour y parvenir, estimer précisément leur masse revêt une importance fondamentale. Puisqu'elle ne peut pas être mesurée directement, nous devons compter sur d'autres observables appelés alors *mass proxy*.

Avec les différentes longueurs d'onde auxquelles l'amas est observée viennent différents *mass proxy*. La masse d'un amas peut être dérivée de l'observation du gaz de l'amas en rayon X, en mesurant sa température avec l'hypothèse que ce dernier est en équilibre hydrostatique (Sarazin, 1988). En étudiant l'émission millimétrique du milieu intra-amas, nous pouvons mesurer la masse totale à l'aide de l'effet Sunyaev-Zel'dovich thermique (effet S-Z; Sunyaev & Zeldovich, 1972). En optique et en infra-rouge, c'est l'émission des étoiles de l'amas qui nous renseigne : la mesure de la dispersion de vitesse des membres de l'amas et la masse totale peut être mis en relation, lorsque celui ci s'applique, avec le théorème du viriel. La luminosité en optique et en infra-rouge peuvent aussi être utilisés comme de *mass proxy*. On définit alors, à la manière de Abell (1958) et Postman et al. (1996) par exemple, le paramètre de *richesse* comme le nombre de galaxies d'amas plus brillantes que la luminosité caractéristique du profil de Schechter (1976), L_* .

L'effet de lentille gravitationnelle est un autre outil qu'on peut utiliser pour mesurer la masse des amas. L'effet de lentille gravitationnelle fort et l'effet de lentille gravitationnelle faible (*i.e. strong lensing* et *weak lensing*, respectivement), produisent une distorsion de l'image des sources en arrière plan proportionnelle à la masse totale de l'objet d'avant plan, ici un amas de galaxies. Dans le régime de *strong lensing* d'une part, cette distorsion peut être si intense qu'elle crée un système d'images répliquées ou une déformation de l'image qui peuvent être aisément identifiées à l'œil, comme les anneaux d'Einstein ou les arcs dans les amas de galaxies. Dans le régime du *weak lensing* d'autre part, le potentiel gravitationnel produit de plus faibles distorsions qui affectent la forme observée de la galaxie d'arrière plan. Ces

déformations sont quantifiées par le biais de ce que l'on nomme champ de *shear*. Comme ce dernier est faible devant la grande diversité de morphologie et d'orientation des galaxies, il faut adopter une approche statistique pour le mesurer et ainsi calculer la moyenne sur un grand nombre de sources d'arrière plan (Schneider, 2005).

Différents *mass proxy* mènent généralement à des estimations de masse qui sont affectées par des différences systématiques. Les mesures de masse en rayon X faillissent dans les systèmes où l'hypothèse d'équilibre hydrostatique n'est pas applicable, comme les amas en cours de fusion ou dans les régions centrales lorsque l'effet d'un noyau actif de galaxie (*AGN*) est important. La méthode S-Z quant à elle, nous permet de faire des mesures de masse à haut décalage spectral (*redshift*), mais elle est affectée par des effets de projection. Contrairement aux deux méthodes précédentes, les mesures de dispersion de vitesse ne sont pas impactées par les formes de pression non-thermique comme les champs magnétiques, la turbulence et la pression des rayons cosmiques, mais elle sont sensibles à l'asymétrie du potentiel et aux effets de projection en plus de reposer sur l'hypothèse que le système est à l'équilibre dynamique. L'effet de lentille gravitationnelle, par contre, ne souffre d'aucun de ces écueils. Il est directement sensible à la masse totale projetée sur la ligne de visée, et représente donc un outil fiable pour la détermination de la masse totale des amas (Meneghetti et al., 2010; Allen, Evrard & Mantz, 2011; Rasia et al., 2012).

Chacune de ces méthodes offre des avantages et présente des inconvénients mais les méthodes de détection en optique et en infra-rouge sont particulièrement importantes car, dans le future, les programmes d'observations à grande échelle dans ces longueurs d'onde, comme LSST et *Euclid*, seront capables d'identifier des amas qui ne sauraient être détectés autrement.

Plusieurs travaux ont démontré que la richesse optique présente une bonne corrélation avec la masse totale de l'amas mesurée avec le *weak lensing* (Johnston et al., 2007; Covone et al., 2014; Ford et al., 2015; van Uitert et al., 2015; Simet et al., 2016; Melchior et al., 2016). L'incertitude caractéristique sur la masse, à richesse fixée, est de $\sim 10 - 25\%$, cela inclue les erreurs statistiques et systématiques, dans l'intervalle de masse $6 \times 10^{12} M_{\odot} \lesssim M \lesssim 10^{15} M_{\odot}$ et dans l'intervalle de *redshift* $0.1 \lesssim z \lesssim 0.9$.

Rykoff et al. (2014) ont développé redMaPPer, un algorithme optique de détection d'amas basé sur la technique de la séquence rouge, algorithme qu'ils ont appliqué aux *Sloan Digital Sky Survey* (SDSS; York et al., 2000). Cette méthode identifie les amas de galaxies en détectant les surdensités de galaxies *early type* (ETGs). Les observations montrent en effet que la région centrale d'un amas accueille un grand nombre de galaxies de ce type, ces dernières sont, lorsqu'on les placent dans un diagramme couleur - magnitude,

distribuées dans une étroite région appelée la séquence rouge. La richesse de redMaPPer est définie comme une somme de probabilité et utilise un filtrage en couleur, position et luminosité (Rozo et al., 2009a; Rozo & Rykoff, 2014; Rykoff et al., 2012, 2014, 2016).

Licitra et al. (2016a,b) ont par la suite présenté une définition simplifiée de la richesse basée sur celle de redMaPPer et l’ont utilisé pour bâtir RedGOLD, leur algorithme de détection d’amas.

Cet algorithme est fondé sur une technique de séquence rouge révisée; il estime à chaque détection d’un amas les coordonnées de son centre, son *redshift*, un paramètre dit de confiance et sa richesse. La richesse de RedGOLD quantifie le nombre de ETGs rouge et passives, plus brillantes que $0.2L_*$, dans un rayon donné. Il est optimisé pour détecter des amas de galaxies massifs ($M_{200} > 10^{14}M_\odot$), et pour produire des catalogues optiques complets et purs. Comparés aux résultats obtenues via des observations en rayon X, la richesse définie dans RedGOLD conduit à des dispersions dans la relation température X - richesse qui sont similaires à celles obtenues avec redMaPPer (Rozo & Rykoff, 2014), ce qui est très prometteur étant donné que RedGOLD a été appliqué avec un seuil en richesse inférieur (soit sur des amas de masse inférieure).

L’objectif de mon travail de thèse était de mesurer des masses d’amas en utilisant le *weak lensing* ainsi d’établir les relations entre la masse totale d’une part et la richesse, la luminosité X, la température X et la masse X d’autre part. On parle alors de relation d’échelle. Cela m’a permis de calibrer et valider la précision de la richesse de RedGOLD en tant que *mass proxy*. J’ai inféré la relation masse - richesse, en utilisant les masses *weak lensing* moyennes calculées en empilant les amas en groupes de richesse. Ensuite j’ai comparé mes masse *weak lensing* avec de masse, luminosités et températures en rayon X.

Pour ce travail, j’ai utilisé les catalogues d’amas de RedGOLD des campagnes d’observations du Canada-France-Hawaii Telescope Legacy Survey (CFHT-LS; Gwyn, 2012) Wide 1 (W1) et Next Generation Virgo Cluster (NGVS; Ferrarese et al., 2012), obtenus par Licitra et al. (2016a,b). L’algorithme a détecté 652 amas dans le CFHTLS W1 et, pour le NGVS, 279 amas dans la portion de ~ 20 degrés carrés observée dans 5 bandes et 1704 dans l’intégralité du champ observé sans la bande r. Pour l’analyse *weak lensing*, j’ai sélectionné un échantillon de 1323 amas, au dessus d’un seuil de détection $\sigma_{\text{det}} \geq 4$, dans l’intervalle de richesse $10 < \lambda < 70$ et de *redshift* $0.2 \leq z \leq 0.5$. En utilisant cette sélection, les catalogues publiés sont $\sim 100\%$ complets et $\sim 80\%$ purs (Licitra et al., 2016a).

J’ai utilisé les catalogues de *redshift* photométriques obtenus par Rai-choor et al. (2014), avec les logiciels bayésiens *LePhare* (Arnouts et al.,

1999; Arnouts et al., 2002; Ilbert et al., 2006) et BPZ (Benítez, 2000; Benítez et al., 2004; Coe et al., 2006). Ces derniers ont déterminé un biais $-0.05 < \Delta z < 0.02$, une valeur de dispersion $0.02 < \sigma < 0.06$, et 5 – 15% de points aberrants, pour $i' < 23$ magnitude.

Pour mon analyse, j’ai utilisé les catalogues de *shear* CFHTLenS et NGVSLenS, basés sur une analyse de données plus sophistiquée comparée à la procédure THELI standard (Erben et al., 2005, 2009, 2013), réalisée par Raichoor et al. (2014). Les mesures de formes des galaxies ont été ensuite obtenues en appliquant l’algorithme bayésien *lensfit* (Miller et al., 2013).

Pour effectuer la comparaison avec les observations en rayon X, j’ai utilisé les catalogues de Gozaliasl et al. (2014) et Mehrrens et al. (2012).

Pour obtenir les masses *weak lensing* à partir de catalogues d’amas, de *redshift* photométriques et de *shear*, j’ai développé et optimisé ma propre procédure d’analyse. Tout d’abord, l’algorithme fait la sélection des galaxies d’arrière plan dans une région circulaire de rayon donné autour du centre de chaque amas de l’échantillon à l’aide des *redshift* photométriques. L’algorithme empile ensuite les amas selon leur richesse et il calcule les profils de *shear* radiaux, en faisant la moyenne des *shear* tangentielles dans des intervalles logarithmiquement espacés autour du centre de l’échantillon empilé. Cette moyenne inclue des coefficients qui dépendent de l’efficacité de l’effet de lentille produit par l’amas, de la qualité des mesures des déformations subit par l’image de la source d’arrière plan ainsi que de corrections de calibration opérées par *lensfit*. Ensuite mon logiciel calcule les matrices de covariance, par la méthode dite de *bootstrap* (Efron, 1979), qui consiste à réaliser un tirage avec remise d’amas dans chaque intervalle de richesse afin d’assigner une barre d’erreur à chaque point du profil radial de *shear*. Pour chaque regroupement d’amas, une carte du rapport signal sur bruit est produite en utilisant la statistique dite d’*aperture mass* (Schneider, 1996; Schirmer et al., 2006; Du & Fan, 2014).

Une fois les profils de *shear* obtenus pour chaque pile d’amas, j’ajuste un modèle sur chacun grâce à un algorithme de chaînes de Markov Monte Carlo (MCMC; Metropolis et al., 1953). Cette méthode me permet d’échantillonner efficacement la distribution de vraisemblance du modèle, de laquelle je tire une estimations et une barre d’erreur pour chaque paramètre ainsi que des intervalles de confiance pour chaque couple de paramètres.

Dans un premier temps, j’ajuste aux profils observés un modèle basique (ci-après *Basic Model*) qui consiste en un modèle de halo (Seljak, 2000), avec un contraste de densité superficiel NFW (Navarro, Frenk & White, 1996) et un termes de correction qui tient compte de l’erreur sur le centrage de l’amas (miscentering; Johnston et al., 2007; George et al., 2012), les *non-weak shear* (Mandelbaum et al., 2006; Johnston et al., 2007) et le *two-halo term* (Seljak,

2000; Seljak & Warren, 2004; Johnston et al., 2007). Les paramètres libres de cette modèle sont r_{200} (duquel je déduit la masse M_{200}), le paramètre dit de *miscentering*, p_{cc} et σ_{off} .

À ce premier modèle, j'ai ensuite ajouté un paramètre supplémentaire, $\sigma_{\ln M|\lambda}$, qui caractérise la dispersion intrinsèque dans la relation masse-riche. Cela donne le *Added Scatter Model*.

Indépendamment, j'ai pris en compte la contribution de la galaxie la plus brillante (nommé BCG) à la masse totale, et ajouté pour ce faire le paramètre libre M_{BCG} au *Basic Model* pour obtenir le *Two Component Model*.

La masse prédite pour chaque regroupement d'amas par chacun des trois modèles me permet ensuite d'établir une relation entre masse et richesse.

J'ai ensuite validé mon code en comparant mes résultats avec ceux de Ford et al. (2015), obtenus de façon indépendante, en utilisant le CFHTLS W1, W2, W3, W4 entier, et le catalogue d'amas publique de Milkeraitis et al. (2010). J'ai effectué plusieurs tests afin d'écarter d'éventuels biais dans mes résultats. J'ai notamment testé différents critères de sélection pour l'échantillon de sources d'arrière plan et différentes limites en magnitude. J'ai vérifié la sélection en *redshift* et la façon d'échantillonner les amas en fonction de leur richesse. J'ai contrôlé que le comportement des composantes ortho-radiales du *shear* étaient conforme aux prédictions théoriques. J'ai comparé les masses estimées avec et sans la correction de *miscentering* afin d'évaluer sa contribution. J'ai utilisé la statistique d'*aperture mass* pour tester l'identification des centres des amas à l'aide du signal de *lensing*, en utilisant des cartes de *shear* simulées, d'amas simulés et d'amas observés par RedGOLD. Afin de vérifier qu'en ajustant le profil de chaque intervalle de richesse individuellement nous n'introduisons pas un biais dans la détermination des paramètres de la relation masse - richesse, j'ai essayé d'ajuster l'ensemble des intervalles de richesses simultanément.

Mes tests m'ont permis de conclure que : (1) les techniques d'ajustement individuel et simultané sont équivalentes. (2) La correction de *miscentering* est celle dont l'impact sur la mesure de la masse est le plus grand. (3) La masse de la galaxie centrale (BCG) et la dispersion intrinsèque dans la relation masse - richesse ne sont pas contraintes par les données. (4) L'ajout de la masse de la BCG dans le modèle n'affecte pas l'estimation de la masse totale de l'amas.

Pour cette raison, j'ai décidé d'utiliser la relation masse - richesse inférée par le *Two Component Model*, avec une correction *a posteriori* pour la dispersion intrinsèque (Ford et al., 2015) (*Final Model*). Avec ce modèle, j'ai obtenu la relation masse-riche $\log M_{200}/M_{\odot} = (14.46 \pm 0.02) + (1.04 \pm 0.09) \log(\lambda/40)$ (erreurs systématiques). Ce résultat est cohérent à $1 - 2\sigma$ avec les relations masse - richesse *lensing* obtenues par Rykoff et al. (2012),

Saro et al. (2015), Simet et al. (2016), Farahi et al. (2016) et Melchior et al. (2016), en utilisant les échantillons d'amas obtenus par redMaPPer avec le SDSS et le DES.

Pour la relation $M_{200}^{lens} - M_{200}^X$, pour une pente unitaire fixé, j'ai obtenu $\log M_{200}^{lens} = (0.20 \pm 0.03) \log M_{200}^X$. Pour la relation masses *lensing* - luminosité en rayons X j'ai trouvé $\log \left(\frac{M_{200} E(z)}{8 \times 10^{13} h^{-1} M_{\odot}} \right) = (0.10 \pm 0.03) + (0.61 \pm 0.12) \log \left(\frac{L_X}{5.6 \times 10^{42} h^{-2} \text{erg/s} E(z)} \right)$. Pour la relation masses *lensing* - température en rayons X j'ai obtenu $\log \left(\frac{M_{200} E(z)}{6 \times 10^{13} h^{-1} M_{\odot}} \right) = (0.23 \pm 0.03) + (1.46 \pm 0.28) \log \left(\frac{T_X}{1.5 \text{KeV}} \right)$. Ces résultats sont en accord avec ceux de Leauthaud et al. (2010), Kettula et al. (2015), Mantz et al. (2016). Pour ces trois relations, j'ai trouvé une dispersion de 0.20 dex, ce qui est compatible avec les dispersions de redMaPPer.

Au cours des derniers mois de mon doctorat, je me concentrerai sur des projets complémentaires à ce que j'ai fait jusqu'ici. J'étudierai la relation entre les masses *lensing* des halos et les masses stellaires des BCG. Je vérifierai comment différents critères de sélection de la galaxie BCG affectent les masses estimées avec le *lensing*, et je calculerai le rapport masse du halo sur masse stellaire pour les galaxies centrales des amas. Je serai aussi en mesure de déduire la relation masse - luminosité optique avec la luminosité en bande b soit pour l'objet central soit pour l'ensemble de l'amas.

D'un autre côté, j'aimerais étudier plus en détail le problème du *miscentering* pour voir comment différents choix de centrage affectent les profils de *shear* et les mesures de masse d'amas massifs, individuels ou empilés. J'aimerais étendre le travail de George et al. (2012) et y inclure une comparaison avec une technique de centrage utilisant le *weak lensing* et une reposant sur une approche hybride entre l'utilisation de galaxies et de centroïdes comme centres (utilisé par exemple dans RedGOLD), méthodes non considérées dans le travail cité.

Pour ces nouveaux projets, j'utiliserai la nouvelle version auto calibrante de l'algorithme *lensfit*, et des estimations raffinées de *redshifts* photométriques de CFTHLS W1 et de l'intégralité de NVGS.

Les programmes d'observations spatiaux de nouvelle génération comme *Euclid* et WFIRST auront un énorme impact sur les analyses de données de *weak lensing* telles que les ai conduites au cours de mon travail de thèse. Ils donneront accès à un échantillon d'amas un ordre de grandeur plus important. Sans compter les campagnes en radio de nouvelle génération tel que SKA qui permettront d'étendre les mesures de masses *weak lensing* en bande radio à des échelles spatiales plus grande encore.

Le but des analyses futures est de parvenir à une précision de l'ordre du

pourcent sur les mesures de masses des amas. Le principal défi dans le traitement des données issues du *weak lensing* vient de l'estimation du *redshift* photométriques qui est liée à la sélection de l'échantillon de sources d'arrière plan et aux coefficients assignés à chaque paire lentille-source. Dans mon travail futur j'aimerais étudier comment l'utilisation de la distribution de *redshift* photométriques obtenue par différentes méthodes de calibration affecte les mesures de masse *weak lensing* et la position estimée du centre des amas.

Cette thèse est organisée comme suit : dans le Chapitre 1, je présenterai les amas de galaxies d'un point de vue théorique et observationnel. Je décrirai le modèle cosmologique standard, le mécanisme de formation des structures, les profils de masse les plus couramment utilisés, et la fonction de masse des amas. Je discuterai aussi des techniques employées pour détecter les amas de galaxies et estimer leur masse en utilisant différents estimateurs (*mass proxy*), ainsi que l'importance des relations d'échelle. Dans le Chapitre 2, je résumerai les principes théoriques du *weak lensing*, et je présenterai ces applications possibles. Dans le Chapitre 3, j'expliquerai les méthodes statistiques que j'ai mises à profit pour mon analyse et la manière dont je les ai appliquées aux données. Dans le Chapitre 4, je discuterai en détail l'analyse et les tests que j'ai réalisés. Enfin dans le Chapitre 6, je résumerai les principaux résultats de mon travail de thèse, je discuterai mes projets futurs et les perspectives du domaine d'étude des lentilles gravitationnelles faibles.

GALAXY CLUSTERS

Galaxy clusters are the the largest and the most massive gravitationally bound systems in the Universe. They have proven to be important tools to probe the predictions of cosmological models and structure formation scenarios. They also permit us to study galaxy formation and evolution, and their interactions with the intra-cluster medium, in a dense environment. Their number and distribution allows us to study the mass function and the correlation function, from which we can infer the cosmological parameters. Studying with accuracy the scaling relations between cluster mass, and different observables, we can put even tighter constrains on the cosmological model.

In this chapter, I will start by describing the standard cosmological model and the evolution of its components. I will explain the process of cluster formation through the growth of the density perturbations in non linear regime. I will discuss clusters from a theoretical point of view, their profile and mass function, and from an observational point of view, reviewing the main methods to detect them and infer their masses through mass proxies.

1.1 Theory

1.1.1 Cosmological model

Cosmology is the study of the Universe and of the formation, evolution, and interaction of its components, from galaxies and clusters to the large scale structure.

Modern cosmology is based on the *cosmological principle* that states that the Universe is homogeneous and isotropic at scales larger than $\sim 100Mpc$.

This means that at large scales the Universe appears the same in all directions, and therefore doesn't have a center and neither a privileged observing position.

In the context of General Relativity, such a universe can be described by the *Friedmann-Robertson-Walker metric*:

$$ds^2 = c^2 dt^2 - a(t)^2 [dr^2 + S_k(r)^2 d\Omega^2]$$

with $d\Omega^2 \equiv d\theta^2 + \sin^2 \theta d\phi^2$ and S_k a function of the curvature of space-time:

$$S_k(r) = \begin{cases} R \sin(r/R) & \text{for } k = +1 \\ r & \text{for } k = 0 \\ R \sinh(r/R) & \text{for } k = -1 \end{cases}$$

where k is the *curvature constant* (that corresponds, for the three cases listed, to a positively curved, flat and negatively curved space, respectively) and R is the curvature radius.

$a(t)$ is the *scale factor* that describes how distances expand or contract as a function of time, in an homogeneous and isotropic universe.

In 1929, in fact, Hubble discovered that the Universe is expanding. Considering that the light emitted by galaxies is shifted toward longer wavelengths when observed by us, the *redshift* of a galaxy can be defined as:

$$z \equiv \frac{\lambda_{ob} - \lambda_{em}}{\lambda_{em}}$$

Hubble derived a linear relation between redshift and distance, known today as the *Hubble's law*:

$$z = \frac{H}{c} r$$

where $H = \dot{a}/a$ is the *Hubble constant* and $a(t)$ is the scale factor introduced above that, at present time is equal to one. In an homogeneous and isotropic universe in expansion, the scale factor ensures that relative distances are preserved.

We can also define the *Hubble distance* as $D_H = c/H$ that is a good approximation of the *horizon*, the maximum distance that a photon can travel during the age of the universe.

In 1922, Friedmann derived an equation to describe such a universe in expansion using Einstein's field equation:

$$\left(\frac{\dot{a}}{a}\right)^2 = \frac{8\pi G}{3} \rho - \frac{kc^2}{a^2} + \frac{\Lambda c^2}{3}$$

$$\frac{\ddot{a}}{a} = -\frac{4\pi G}{3} \left(\rho + \frac{3p}{c^2} \right) + \frac{\Lambda c^2}{3}$$

where ρ and p are the density and the pressure of the fluid, G is the gravitational constant, c is the speed of light, and Λ is the cosmological constant.

Considering a flat universe composed by radiation, matter, and a cosmological constant, we can rewrite Friedmann's equation as:

$$\left(\frac{\dot{a}}{a} \right)^2 = \frac{8\pi G}{3} (\rho_m + \rho_r + \rho_\Lambda)$$

with $\rho_m = \rho_{DM} + \rho_b$, meaning that the matter component is composed by dark matter and baryons. The densities $\rho_m, \rho_r, \rho_\Lambda, \rho_{DM}, \rho_b$ are the densities of matter, radiation, dark energy, dark matter, and baryons, respectively.

Furthermore, defining the Hubble constant at present time as $H_0 = (\dot{a}/a)_{t=t_0}$, and the critical density of the universe as $\rho_{c,0} = 3H_0^2/8\pi G$, the equation takes the form:

$$\frac{H^2}{H_0^2} = \frac{\Omega_m}{a^3} + \frac{\Omega_r}{a^4} + \Omega_\Lambda$$

where the *density parameter* for each component x is $\Omega_x = \rho_{x,0}/\rho_{c,0}$, and their sum is $\Omega = \Omega_m + \Omega_r + \Omega_\Lambda = 1$. The evolution of the density as a function of the scale factor is given by the *continuity equation*:

$$\rho(a) = \frac{\rho_0}{a^{3(1+w)}}$$

and

$$w = \begin{cases} 0 & \text{matter} \\ 1/3 & \text{radiation} \\ -1 & \Lambda \end{cases}$$

The standard cosmological model assumed today is the $\Lambda - CDM$. It's a spatially flat model that contains baryonic and dark matter, radiation and a dark energy (whose impact on the Universe dynamic is quantified by the cosmological constant), with the Hubble constant assumed to be $H_0 = 70 \text{ km s}^{-1} \text{ Mpc}^{-1}$.

The total matter density parameter is $\Omega_m \sim 0.3$ and includes contributions from both dark matter and baryons, where the density parameter of the first is ~ 6 times greater than the second.

The radiation density parameter is $\Omega_r \sim 10^{-5}$ and includes neutrinos and photons.

List of Ingredients	
photons:	$\Omega_{\gamma,0} = 5.0 \times 10^{-5}$
neutrinos:	$\Omega_{\nu,0} = 3.4 \times 10^{-5}$
total radiation:	$\Omega_{r,0} = 8.4 \times 10^{-5}$
baryonic matter:	$\Omega_{\text{bary},0} = 0.04$
nonbaryonic dark matter:	$\Omega_{\text{dm},0} = 0.26$
total matter:	$\Omega_{m,0} = 0.30$
cosmological constant:	$\Omega_{\Lambda,0} \approx 0.70$

Important Epochs		
radiation-matter equality:	$a_{rm} = 2.8 \times 10^{-4}$	$t_{rm} = 4.7 \times 10^4 \text{ yr}$
matter-lambda equality:	$a_{m\Lambda} = 0.75$	$t_{m\Lambda} = 9.8 \text{ Gyr}$
Now:	$a_0 = 1$	$t_0 = 13.5 \text{ Gyr}$

event	redshift	temperature (K)	time (megayears)
radiation-matter equality	3570	9730	0.047
recombination	1370	3740	0.24
photon decoupling	1100	3000	0.35
last scattering	1100	3000	0.35

Figure 1.1 – In the table on the top, the density parameter of the different components of the $\Lambda - \text{CDM}$ model. In the table on the bottom, the scale factor, time, redshift, and temperature at which the main events took place (Ryden, 2006).

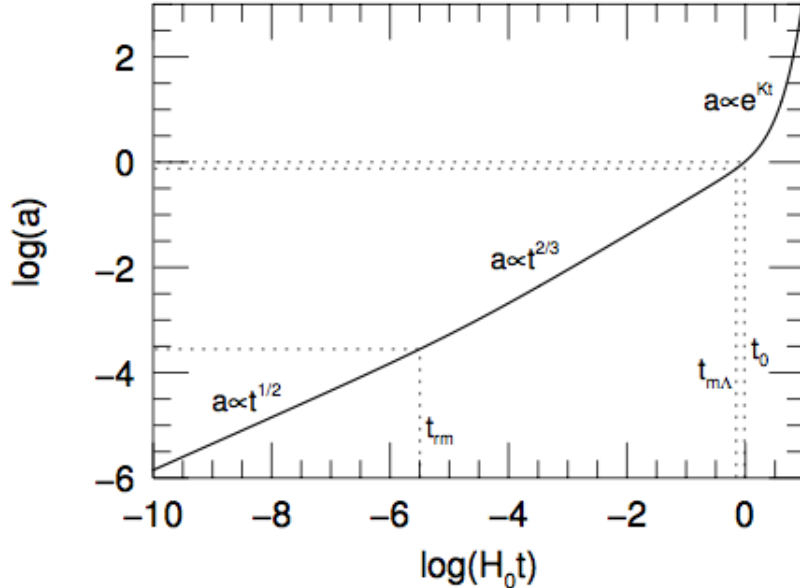


Figure 1.2 – Dependence of the scale factor with time for the different epochs. t_{rm} is the radiation-matter equality, $t_{\text{m}\Lambda}$ is the matter- Λ equality, and t_0 is the present time (Ryden, 2006).

Finally the cosmological constant density parameter is $\Omega_\Lambda \sim 0.7$.

In Figure 1.1, we find the density parameter values of the different components and the scale factor, time, redshift, and temperature at which the main events took place. In Figure 1.2, we can see how the scale factor, and thus the expansion of the Universe, depends on time in the different epochs: radiation, matter, Λ and present time.

Given a cosmological model, there are several ways to measure cosmological distances.

Following Hogg (2000), we define the *comoving line-of-sight distance* to an object at redshift z as:

$$D_C = D_H \int_0^z \frac{dz'}{E(z')} \quad (1.1)$$

where $E(z) \equiv H(z)/H_0(z) = \sqrt{\Omega_m(1+z)^3 + \Omega_k(1+z)^2 + \Omega_\Lambda}$, D_H is the Hubble distance previously defined, and $\Omega_k = 1 - \Omega_m - \Omega_r - \Omega_\Lambda$ is the density parameter associated to the curvature constant.

The *transverse comoving distance* is defined as:

$$D_M = \begin{cases} D_H \frac{1}{\sqrt{\Omega_k}} \sinh(\sqrt{\Omega_k} D_C / D_H) & \text{for } \Omega_k > 0 \\ D_C & \text{for } \Omega_k = 0 \\ D_H \frac{1}{\sqrt{\Omega_k}} \sin(\sqrt{\Omega_k} D_C / D_H) & \text{for } \Omega_k < 0 \end{cases} \quad (1.2)$$

so that the comoving distance between two objects at the same redshift, separate on the sky by an angle $\delta\theta$ will be $D_M \delta\theta$.

The *angular diameter distance* of a given object is defined as the ratio of its physical transverse size, l , to its angular size in radians, θ , and it is related to the transverse comoving distance:

$$D_A \equiv l/\theta = \frac{D_M}{(1+z)} \quad (1.3)$$

Finally, the *luminosity distance* is defined as the relation between the bolometric (i.e. integrated over all frequency) luminosity L , and the bolometric flux S , of an object. It is related to the transverse comoving distance and to the angular diameter distance:

$$D_L \equiv \sqrt{\frac{L}{4\pi S}} = (1+z)D_M = (1+z)^2 D_A \quad (1.4)$$

1.1.2 Density perturbations and structure formation

In the standard model, the primordial Universe was very dense and hot ($T \gg 10^4 K$) so that the baryonic matter was completely ionized, and the photons scattering by free electrons made it completely opaque. In the very first phases of its evolution its density was dominated by the radiation density, then, as it expanded the matter density dominated and finally the dark energy density, which is the dominant component today.

While expanding, the average Universe temperature cooled to $\sim 3000K$ and, at this point, ions and electrons combined to form neutral atoms (*recombination* epoch), photons started to stream freely from the so called *last scattering surface*, decoupling from the electrons, and the Universe became transparent. We observe the photons from the *last scattering surface* as a Cosmic Microwave Background (CMB; Penzias & Wilson, 1965) with a black body distribution at a temperature of $\sim 2.7K$. The CMB shows temperature fluctuations that correspond to matter density perturbations (Planck Collaboration IX, 2016).

Cosmic structures form from gravitational instability and the subsequent growth of these primordial density perturbations. The study of the large

scale structure in the Universe and its formation is linked to the study of the statistical properties of the overdensity field:

$$\delta(\vec{x}) = \frac{\rho(\vec{x}) - \rho_b}{\rho_b}$$

where ρ_b is the average density of the universe.

Assuming that $\delta(\vec{x})$ is an homogeneous and isotropic Gaussian random field, we can think of our Universe as a statistical realisation of the overdensity field, and of its unperturbed density as the mean over the statistical ensemble, $\rho_b \equiv \langle \rho(\vec{x}) \rangle$. Moreover, the Gaussian assumption implies that to completely describe the field, we only need its variance.

In practice, with the *ergodic hypothesis*, we can calculate ρ_b averaging the overdensity field in finite volumes of the Universe that are sufficiently distant to be considered independent (Coles & Lucchin, 2002).

Averaging in a finite volume V is equivalent to filter the overdensity field on a given scale R (Voit, 2005):

$$\delta_M(\vec{x}) \equiv \frac{\delta M(\vec{x})}{M} = \delta(\vec{x}) * W(\vec{x}; R)$$

where $W(\vec{x}; R)$ is a generic window function, and δ_M is the mass fluctuation. Considering that luminous matter traces the total matter distribution, we can link the number of galaxies in a given volume V with the corresponding total mass fluctuation in the same volume through the *bias* parameter b, so that $\delta_g \equiv b\delta_M$.

We can then write the mass variance as:

$$\sigma^2 \equiv \langle \delta^2(\vec{x}) \rangle = \frac{1}{(2\pi)^3} \int P(k) |W(kR)|^2 d^3k$$

where $P(k)$ is the power spectrum, the Fourier transform of the correlation function $\xi(r) \equiv \langle \delta(\vec{x})\delta(\vec{x} + \vec{r}) \rangle$.

Assuming that the power spectrum has a power-law form, $P(k) \sim k^n$ and that the window function is a spherical one, we have:

$$\sigma^2 \sim k^{n+3} \rightarrow \frac{\delta M}{M} \sim M^{-(n+3)/6}$$

The growth of the perturbations doesn't depend on the scale and they all grow in unison until they are outside of the horizon, where the only important effect is gravity. In this regime, the different components of the Universe are coupled to the dominant one, so in the radiation dominated epoch $\delta \propto \delta_r \propto a^2$ and in the matter dominated epoch $\delta \propto \delta_{dm} \propto a$.

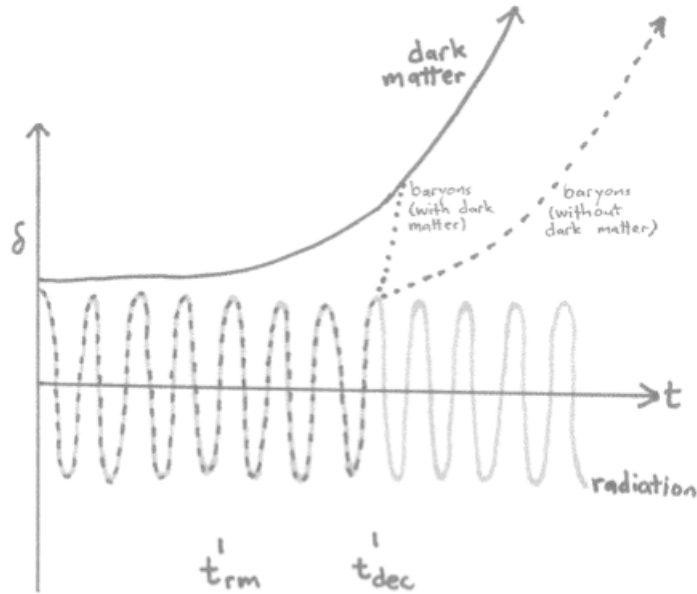


Figure 1.3 – *Growth of the perturbations inside the horizon, as a function of time (Ryden, 2006).*

As time passes and perturbations of larger scales enter in the horizon, new physical effects that modify the scale-free nature of the initial power spectrum need to be taken into account. As we can see in Figure 1.3, before the radiation-matter equality (t_{rm}) and inside the horizon, the dominant component is the radiation, and the baryonic component is coupled to it. Radiation pressure resists gravitational compression, inhibiting the growth of the perturbations. The photo-baryonic fluid oscillates as acoustic waves, and eventually damps because of photon diffusion, while the dark matter component stalls at the amplitude at which it entered the horizon.

After the radiation-matter equality, when the Universe becomes matter dominated, dark matter perturbations start to grow again. The baryons, after decoupling from the photons (t_{dec}), are attracted by the gravitational wells of dark matter, and catch up with the perturbation growth of this component, while radiation continues to oscillate.

All the alterations that these effects produce on the original power spectrum, until we are in linear regime, can be described by the *transfer function* (Voit, 2005):

$$T(k) \equiv \frac{\delta_k(z=0)}{\delta_k D(z)}$$

where $D(z)$ is the *growth function*:

$$D(a) \propto \frac{\delta\rho}{\rho} \propto \frac{\dot{a}}{a} \int_0^a \frac{da}{\dot{a}^3} \quad a = \frac{1}{(1+z)}$$

If the primordial power spectrum has a power law index of $n=1$, the power spectrum of linear perturbations is $P(k) \propto k^n T^2(k)$, at $z=0$ (Voit, 2005).

In the Λ -*CMD* model, structure formation is driven by the growth of the dark matter density perturbations and it leads to a hierarchical or *bottom-up* scenario, in which small scale perturbations reach the nonlinear regime before larger-scale ones (Ryden, 2006). This can be explained by the fact that, before the radiation-matter equality, dark matter perturbations with wavelengths greater than the Hubble distance (small scales in the Fourier space) will be free to grow, while perturbations with smaller wavelengths that are then inside the horizon (large scales in the Fourier space), will stall until the matter dominated epoch.

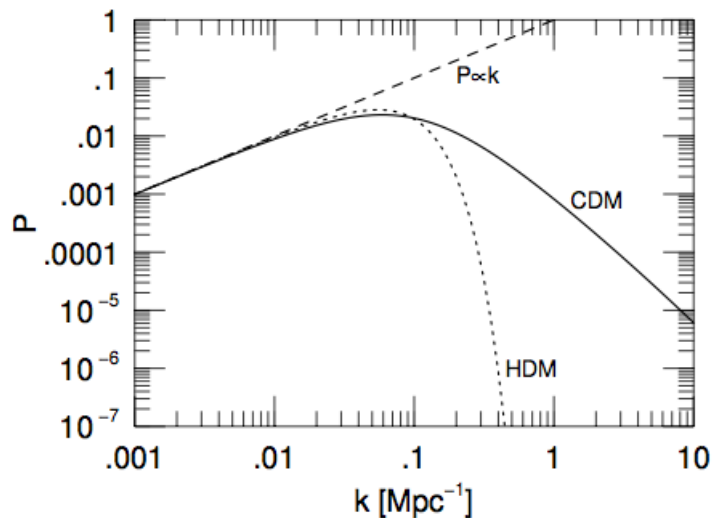


Figure 1.4 – *Power spectrum at the radiation-matter equality for a cold dark matter model (CDM), and for a hot dark matter model (HDM), compared with the scale free power spectrum, $P \propto k$ (Ryden, 2006).*

In Figure 1.4, we can see that the power spectrum at the time of radiation-matter equality is suppressed in amplitude for large wavenumbers. This means that galaxies form first, then clusters, and then the large scale structure. This scenario is consistent with the observed ages of galaxies and clusters.

1.1.3 Cluster formation

As small clumps of matter merge and coalesce to form larger structures, perturbations reach the nonlinear regime with $\delta \sim 1$. At this point is no longer possible to study the evolution of the perturbations in linear regime and we need to rely on numerical simulations. In a simplified way though, cluster formation can also be studied assuming a spherically symmetric model as the *spherical top-hat*.

In this model, the radius of a mass shell with constant density has a parametric solution:

$$r = r_{ta} \frac{(1 - \cos \theta)}{2}$$

where r_{ta} is the turnaround radius at which the expansion stops, and the collapse starts. The behavior of the radius of a nonlinear perturbation is shown in Figure 1.5.

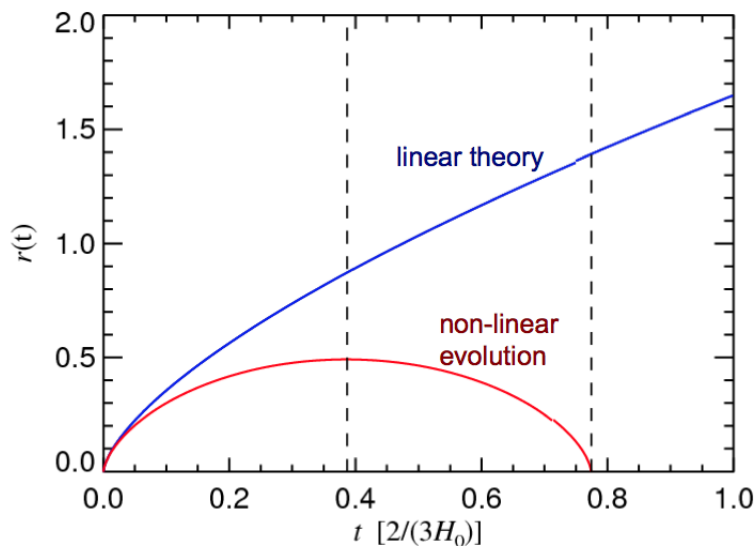


Figure 1.5 – *Evolution of the radius of a non-linear spherical perturbation, in red, compared with the evolution in linear theory, in blue (Springel, V., Dark Matter, Cosmology & Structure Formation, ISAPP, Heidelberg 2011).*

The radius of the collapsed object is the cluster’s outer boundary. This radius satisfies the virial theorem and corresponds to half the turnaround radius. In a matter dominated universe, the virial radius can be estimated as $\sim 178\rho_c$ (Voit, 2005). Even though it’s possible to perform more accurate numerical calculations, a value that is often used is the scale radius r_{200} , that corresponds to a density of $200\rho_c$, as we will see in the next paragraph.

1.1.4 Mass profile

Observations have shown that the velocity dispersion of cluster galaxies is almost constant with the distance from the cluster center (Voit, 2005). A simple analytical model that fits this behavior is the *singular isothermal sphere*, that has a density profile of the form:

$$\rho(r) = \frac{\sigma_v^2}{2\pi G r^2}$$

with σ_v constant and isotropic at every point.

Numerical simulations (e.g. Navarro, Frenk & White, 1996; Moore et al., 1998; Rasia et al., 2003) though have shown that the density profile of a dark matter halo should be shallower at small radii and steeper at large radii, fitting better with the generic form:

$$\rho(r) \propto r^{-p}(r + r_s)^{p-q}$$

Today the most used fitting formula is the Navarro, Frenk and White profile (Navarro, Frenk & White, 1996), that has $p = 1$ and $q = 3$. Slightly different values are also possible and consistent with both simulations and optical and X-ray observations.

In a more complete form, the NFW profile is usually written as:

$$\rho(r) = \frac{\delta_c \rho_c}{\left(\frac{r}{r_s}\right)\left(1 + \frac{r}{r_s}\right)^2} \quad (1.5)$$

$$\rho_c = \frac{3H(z)^2}{8\pi G} \quad (1.5a)$$

$$r_s = \frac{r_{200}}{c} \quad (1.5b)$$

$$\delta_c = \frac{200}{3} \frac{c^3}{\ln(1+c) - \frac{c}{1+c}} \quad (1.5c)$$

where we can see that the scale radius r_s depends on the radius r_{200} introduced in the last paragraph; c , is the concentration parameter; δ_c is a dimensionless parameter that depends only on the concentration.

The mass M_{200} is defined as the mass of a sphere of radius r_{200} and density $200\rho_c$:

$$M_{200} = M(r_{200}) = \frac{800\pi}{3} \rho_c r_{200}^3 \quad (1.6)$$

Simulations have also shown that there is a relation between M_{200} and c (e.g. Navarro, Frenk & White, 1996; Bullock et al., 2001). Given the hierarchical model of structure formation, lower mass objects formed before than higher

mass ones, when the Universe was more dense, and therefore have higher halo concentration values. Typical values are $c \sim 4 - 10$.

Cluster mass can be defined also at other overdensity values. For example in X-ray observation, M_{500} is commonly used because simulations have shown that clusters are considerably more relaxed in the region within r_{500} , making it easier to observe them. Knowing the concentration values though, it is possible to convert masses from a definition to another:

$$\frac{M_{\Delta_1}}{M_{\Delta_2}} = \frac{\Delta_1}{\Delta_2} \left(\frac{c_{\Delta_1}}{c_{\Delta_2}} \right)^3$$

with Δ_1 and Δ_2 , two different overdensity values.

1.1.5 Mass function

The cluster mass function $n(M)$ is defined as the number density of clusters with a mass greater than M in a given volume. It is an important tool to constrain the cosmological model parameters.

The first to find an analytical form for the mass function, assuming the spherical top-hat model and the linear growth function, were Press & Schechter (1974). If perturbations are assumed to grow according to the linear growth function, even when they reach the nonlinear regime, the variance on mass scale M can be written as:

$$\sigma^2(M, z) = \frac{D^2(z)}{(2\pi)^3} \int P(k) |W_k(M)|^2 d^3k$$

Perturbations then collapse and virialize when they exceed the threshold δ_c . Assuming a flat universe with $\Omega_m = 1$ and the parametric solution for the radius of a spherical perturbation in the top-hat model (described above), leads to a value of $\delta_c \sim 1.686$.

The mass function can be then written as:

$$\frac{dn}{d \ln \sigma^{-1}} = \sqrt{\frac{2}{\pi}} \frac{\Omega_m \rho_{c,0} \delta_c}{M} \frac{\delta_c}{\sigma} \exp \left[-\frac{\delta_c^2}{2\sigma^2} \right]$$

Measuring this function, we can put constraints on the values of Ω_m and σ_8 , the normalization of the power spectrum, defined as the variance at which $\delta M/M \sim 1$ within a radius of $8h^{-1} Mpc$.

Press & Schechter (1974) mass function agrees rather well with the results of N-body simulations, and has been widely used for its simplicity despite its limitations. In particular, the Press & Schechter (1974) formalism doesn't

take into account the so-called *cloud-in-cloud* problem, which is the possibility that an object that is underdense for a given filtering mass scale could end up in a collapsed halo of larger mass. Not considering properly the underdense regions, Press & Schechter (1974) accounted only for half of the mass, and corrected their result multiplying it by a factor 2, without a rigorous justification. Also this approach is merely statistical, and doesn't take into account the detailed evolution of individual objects.

The Press & Schechter (1974) model has been refined and extended during the years. Bond et al. (1991) and Lacey & Cole (1993) used predictions from the merger histories of dark matter haloes to identify those objects that were neglected in the *cloud-in-cloud* problem, and explained how the factor 2 can arise for a particular filter choice. Sheth & Tormen (1999) improved the model replacing the spherical collapse with an ellipsoidal one. Using larger and more detailed simulations, the accuracy in the mass function determination increased from 30% to 1% (Jenkins et al., 2001; Tinker et al., 2008; Crocce et al., 2010; Bhattacharya et al., 2011; Angulo et al., 2012; Watson et al., 2013; Fosalba et al., 2015; Bocquet et al., 2016)

In Figure 1.6, we can see the predicted halo mass function for the standard $\Lambda - CDM$ model and, in the bottom panel, the fractional changes induced by adopting different cosmological models (Weinberg et al., 2013).

1.1.6 Cluster mass and cosmology

The cosmological model can be constrained using different and complementary methods.

Type Ia supernovae (SN Ia) can be considered standard candles since they show a tight correlation between their peak luminosity and the shape of their light curves (Phillips, 1993). Comparing the peak apparent magnitude of distant SN to those of local ($z < 0.1$) calibrators with distances inferred from the distance scale ladder, we can measure the luminosity distance $D_L(z)$, which is related to the cosmological parameters by Equations 1.1-1.4 (Weinberg et al., 2013).

CMB anisotropies can provide strong constraints on Ω_m , Ω_b and Ω_k . In fact, the amplitudes of the acoustic peaks in the CMB angular power spectrum depend on the matter and baryon densities, while the locations of the peaks depend on spatial curvature (Weinberg et al., 2013).

The ratio between baryonic and total mass in massive galaxy clusters is expected to match the ratio of the cosmological parameters Ω_b/Ω_m . The combination of X-ray gas mass fraction measurements in clusters with the determination of Ω_b from CMB data can be used to put tighter constraints on Ω_m (Allen et al., 2013).

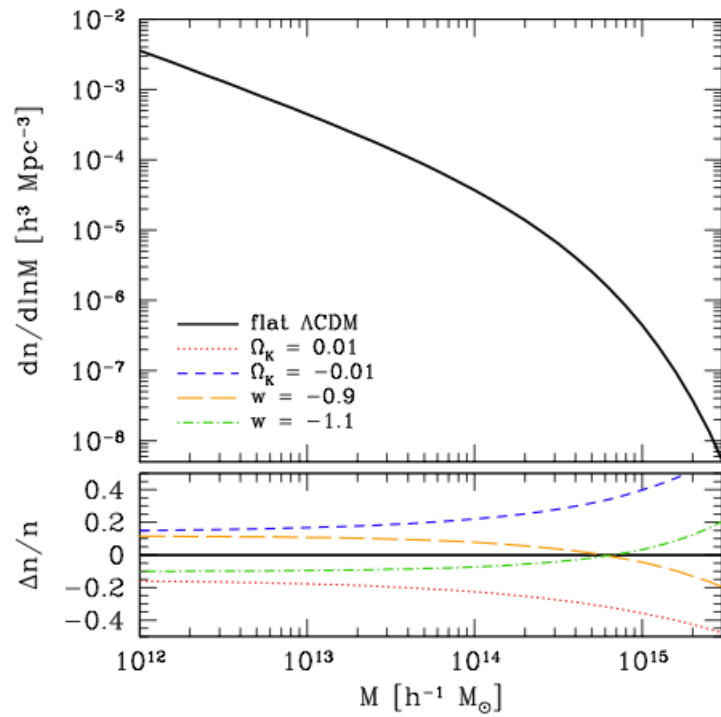


Figure 1.6 – Halo mass function for the standard Λ – CDM model and fractional changes induced by varying the w and Ω_k cosmological parameters (Weinberg et al., 2013).

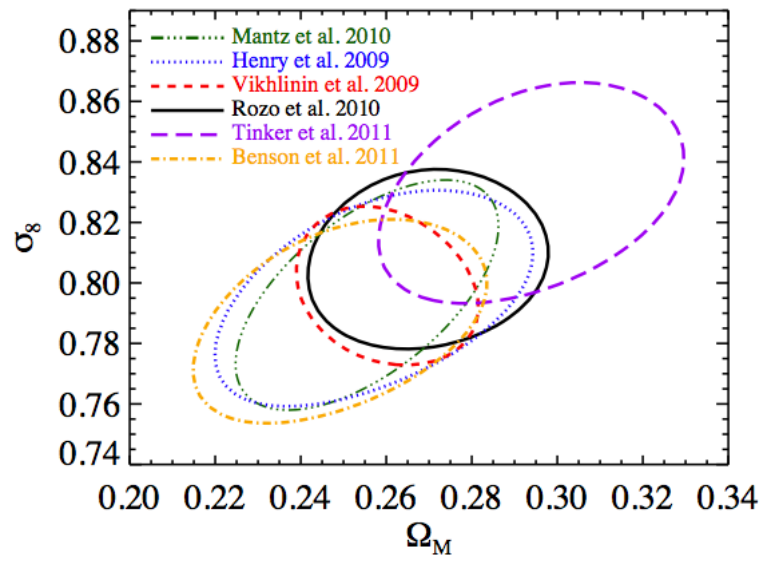


Figure 1.7 – Constraints on the cosmological parameters σ_8 and Ω_m derived from galaxy cluster abundances and WMAP CMB data. Mantz et al. (2010), Henry et al. (2009), and Vikhlinin et al. (2009) used X-ray measurements. Rozo et al. (2010) used optically selected clusters and performed a stacked weak lensing mass calibration. Tinker et al. (2012) used galaxy clustering and mass-to-number ratios. Benson et al. (2011) used SZ measurements (Weinberg et al., 2013).

The baryonic acoustic oscillation (BAO) method is based on the calculation of the acoustic length scale, the comoving distance that the sound waves produced by the oscillations of the photo-baryonic fluid in the early universe could travel from the Big Bang until the recombination epoch (Hu & Sugiyama, 1996; Eisenstein & Hu, 1998):

$$r_s = \int_0^{t_{rec}} \frac{c_s(t)}{a(t)} dt = \int_{z_{rec}}^{\infty} \frac{c_s(z)}{H(z)} dz \quad (1.7)$$

where c_s is the speed of sound. The acoustic scale can be known, to better than 1% accuracy, measuring the relative heights of the acoustic peaks in the CMB anisotropy power spectrum, and can therefore be considered as a standard ruler. Using the BAO method is possible to calculate cosmic distances, in fact the separation along the line of sight is related to $H(z)r_s$, and the separation transverse to the line of sight is proportional to $D_A(z)/r_s$ (Weinberg et al., 2013).

The combination of the galaxy power spectrum with the CMB power spectrum can be used to put even tighter constraints on the cosmological parameters, especially on the Hubble constant (Weinberg et al., 2013).

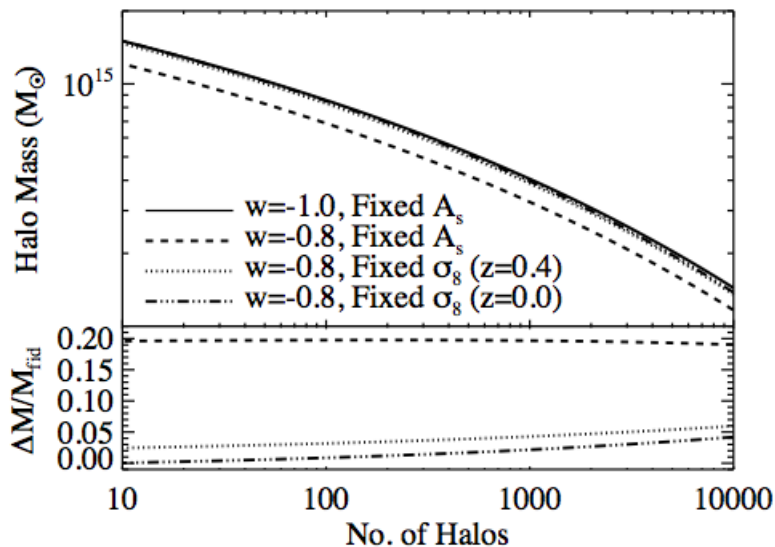


Figure 1.8 – Halo mass thresholds as a function of cumulative number counts predicted for a 10^4deg^2 survey at redshift $z = 0.4 \pm 0.05$, and fractional changes obtained using different cosmological models (Weinberg et al., 2013).

Also, as I will discuss in greater detail in Chapter 2, there are several

methods in which gravitational lensing can be used to constrain the cosmological model.

Finally, cluster abundances can be used for cosmological studies, comparing the predicted mass function with the observed one, obtained measuring cluster masses with different methods. Cluster masses cannot be measured directly but we need to rely on different observables, at different wavelengths, that correlate with the halo mass.

Halo abundance studies allow us to measure the amplitude of the matter power-spectrum, σ_8 , and Ω_m . In fact, clusters form from the gravitational collapse of fluctuations of σ_8 scale ($8h^{-1}Mpc \sim 2 \times 10^{14}M_\odot$), and the total mass of each collapsed volume scales linearly with Ω_m . Since these two parameters are degenerate, it is necessary to measure abundances at different masses (Weinberg et al., 2013).

In figure 1.7, we can see the constraints on these two parameters, obtained from galaxy cluster abundance studies performed using cluster samples selected in different ways. Mantz et al. (2010), Henry et al. (2009), and Vikhlinin et al. (2009) used X-ray measurements. Rozo et al. (2010) used optically selected clusters and performed stacked weak lensing mass measurements, which is the method used that I used for my thesis work. Tinker et al. (2012) used optically selected clusters and galaxy clustering. Benson et al. (2011) used South Pole Telescope (SPT) selected clusters (Weinberg et al., 2013).

More recently, Mantz et al. (2015) used weak lensing mass measurements from Weighing the Giants of the X-ray selected cluster sample in the ROSAT All-Sky Survey to constrain the matter density parameter and the normalization of the power spectrum. They found results in agreement with CMB data, both from WMAP and Planck. Pacaud et al. (2016) used the bright cluster sample from the XMM-Newton XXL Survey to put constraints on the cosmological parameters, comparing the X-ray luminosity-temperature relation with predictions from different cosmological models.

Bocquet et al. (2015) calibrated the SPT-SZ cluster sample using velocity dispersion measurements, and compared the SPT cluster abundances with what expected from WMAP9 and Planck+WMAP9 cosmology. de Haan et al. (2016) performed a similar analysis but using X-ray and weak lensing calibrations. Planck Collaboration XXIV (2016) presented constraints on the cosmological parameters from cluster counts of the full-mission SZ catalog PSZ2 (Planck Collaboration XXVII, 2016).

In order to avoid the systematics related to the halo mass calibration in cluster abundances studies, Caldwell et al. (2016) directly compared the predicted and observed cluster counts as a function of cluster velocity dispersion measurements.

Finally, Liu, X., et al. (2015); Liu, J., et al. (2015); Hamana et al. (2015) used weak lensing cluster counts, obtained from shear peaks analysis, to constrain the Ω_m and σ_8 parameters.

The calibration of the scaling relations between cluster observables and halo masses is fundamental to achieve high precision in cluster cosmology. In Figure 1.8, we can see the halo mass thresholds as a function of cumulative number counts predicted for a 10^4 deg^2 survey at redshift $z = 0.4 \pm 0.05$, and different cosmological models. Changing w and keeping fixed the primordial power spectrum amplitude, A_s , changes the predicted abundances by 30 – 60%, while the corresponding mass threshold changes only by $\sim 20\%$. Keeping σ_8 fixed, the change in abundance is $\sim 15\%$ and corresponds to a change in mass threshold $\sim 2.5\% - 6\%$ (Weinberg et al., 2013). For this reason, it is important to calibrate the cluster mass-observable relations with the highest possible accuracy, and ideally measure cluster masses at $\sim 1\%$ precision.

In Figure 1.9, we can see how all the methods described can be combined to put much tighter constraints on the cosmological parameters (Allen et al., 2013).

In Section 1.2, I will describe in detail the techniques that can be used to detect galaxy clusters and the different observables that allow us to measure cluster masses (i.e. mass proxies).

1.2 Observations

1.2.1 Detection and catalog creation

Galaxy clusters can be detected using different techniques based on their emission at different wavelengths.

Cluster can be easily identified through their X-ray emission. The potential well of galaxy clusters compresses the baryon gas to virial temperatures of $10^7 - 10^8 K$. At these temperatures, atoms are ionized and the bremsstrahlung radiation, the free-free emission due to collisions between ions and electrons in the intra cluster medium (ICM), causes clusters to emit in X-ray. This method selects preferentially relaxed, gas-rich systems, while gas-poor filamentary or assembling structures are not recovered. X-ray catalogs are therefore incomplete for systems with an X-ray emission below the survey detection limit.

The ICM electrons also interact with the CMB photons through inverse Compton scatter. CMB photons are shifted to higher energies as they pass through the hot ICM and collide with its free electrons, distorting the CMB

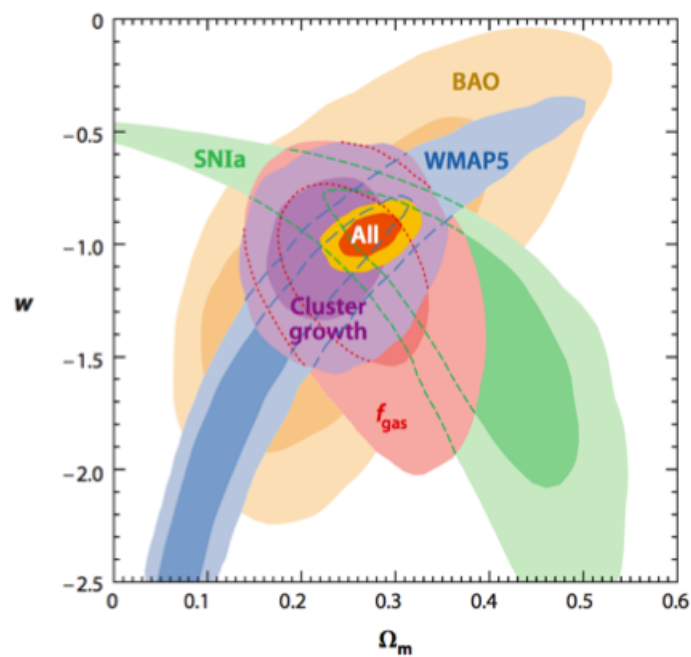


Figure 1.9 – Constraints on the dark energy equation of state, w , and on the mean matter density Ω_m , from the observed abundance and growth of galaxy clusters, from cluster X-ray gas fraction measurements, from WMAP CMB measurements, from type Ia supernovae, and from baryonic acoustic oscillations (BAO), for spatially flat, constant w models (Allen et al., 2013).

black body spectrum in a frequency dependent way. This process is known as the thermal Sunyaev-Zel'dovich effect (S-Z effect; Sunyaev & Zeldovich, 1972). Unlike the X-ray surface brightness, the S-Z mass selection function is almost redshift independent and reaches lower masses at high redshifts (Figure 1.10). Selecting clusters based on their S-Z emission allows us to detect clusters at higher redshift, compared to other techniques. As in X-ray surveys, the S-Z detected clusters are massive relaxed systems.

In principle gravitational lensing could be used to detect massive galaxy clusters, using aperture mass statistics that associates high S/N peaks in lensing maps with massive structures along the line of sight (Wittman et al., 2001, 2003; Dahle et al., 2003; Schirmer et al., 2003). This method though suffers of projection effects that give rise to non physical low and medium S/N peaks that contaminate the measurements (Kratochvil et al., 2010; Yang et al., 2011). On the other hand, since weak lensing peak abundance is related to the mass function of dark matter halos, peak counts can be used to constraint the cosmological model and to study the non-gaussian information that is inaccessible with two-point correlation analysis (Liu, J., et al., 2015; Martinet et al., 2015).

Using optical and infrared data, it is possible to detect galaxy clusters tracing their stellar component. There several techniques that can be applied to this purpose. *Matched filter* techniques detect galaxies in one band and assume some a priori model profiles to fit the data, such as a luminosity profile or a radial profile (Postman et al., 1996; Olsen et al., 2007; Grove et al., 2009; Milkeraitis et al., 2010). *Adaptive kernel* methods are based on the detection of the most significant peaks in galaxy density maps (Shectman, 1985; Mazure et al., 2007; Durret et al., 2011). *Friends-of-Friends* is an algorithm that searches for galaxy structures, iteratively linking together objects with a spatial difference smaller than a fixed value, called *linking length* (Huchara & Geller, 1982). The *red-sequence* based algorithms look for overdensities of red early type galaxies in the color magnitude diagram, based on the observational evidence that large populations of this kind of objects can be found in the inner regions of galaxy clusters (Gladders & Yee, 2000; Thanjavur et al., 2009; Licitra et al., 2016a,b).

Every method as its advantages and its disadvantages but optical and infrared detection methods are particularly important since, in the future, large scale surveys at these wavelengths, such as LSST and Euclid will be able to identify clusters that won't be detected with other methods. The limiting cluster mass for a 3σ detection for Euclid will be $\sim 8 \times 10^{13} M_{\odot}$, up to $z < 2$ (Sartoris et al., 2016). Imposing completeness and purity rates $> 80\%$ the limiting cluster mass will be $< 2 \times 10^{14} M_{\odot}$ up to $z < 1.5$ for Euclid, and even lower for LSST, up to $z < 0.8$ (Ascaso et al., 2016). As shown in

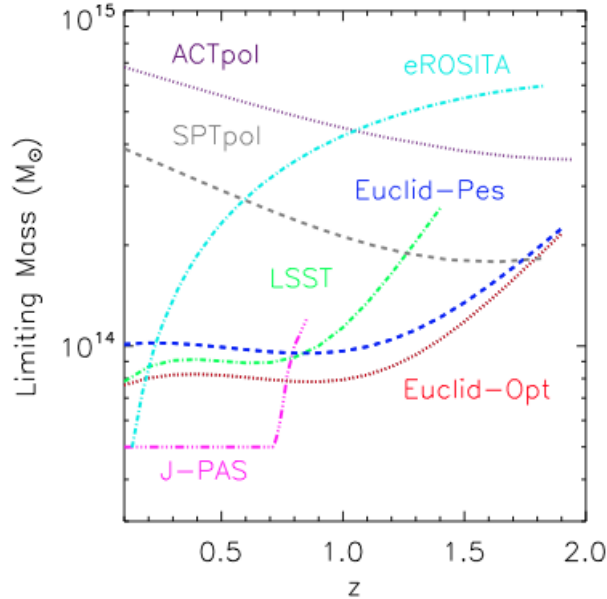


Figure 1.10 – Selection function of the next generation surveys (Ascaso et al., 2016).

Figure 1.10 (Ascaso et al., 2016), the selection function of the e-Rosita X-ray survey (Merloni et al., 2012) will be comparable with the optical ones only at $z < 0.2$, while the limiting cluster mass for the SPTpol (Carlstrom et al., 2011) and ACTpol (Marriage et al., 2011) S-Z survey at the same redshift will be $\sim 4 \times 10^{14} M_{\odot}$ and $\sim 7 \times 10^{14} M_{\odot}$, respectively. This means that optical and near-infrared surveys will be of fundamental importance to detect low mass galaxy clusters at low to medium redshift.

1.2.2 Mass proxies

The cluster mass is not a direct measurement and is inferred using several mass proxies. Galaxy clusters emit radiation in different wavelengths and their mass can be estimated using different tracers. Different mass proxies usually lead to mass estimations that are affected by different systematics.

The X-ray temperature is related to the cluster’s gravitational potential and, consequently, to its mass. Assuming that the ICM is isothermal and at hydrostatic equilibrium, the X-ray density and temperature profiles can be related to the total mass (Sarazin, 1988). X-ray mass measurements are less subjected to projection and triaxiality effects compared to the optical ones. On the other hand, this method cannot be applied if we can’t assume

hydrostatic equilibrium, as in systems undergoing mergers, or in the central regions of clusters with strong AGN feedback (Allen, Evrard & Mantz, 2011).

The S-Z effect is proportional to the line of sight integral of the product of the cluster gas density and temperature and it's related to the total cluster mass. The S-Z mass selection is almost redshift independent at $z > 0.5$, and reaches lower masses when compared to the steep X-ray survey selection function (Figure 1.10). For the same reason, though, the method is also subjected to projection effects due to the overlap of all the groups and clusters along the line of sight (Voit, 2005).

In galaxy clusters, the majority of optical and near infra-red emission comes from starlight. At these wavelengths, we observe the number density, luminosity and velocity dispersion profiles. If a cluster is at dynamical equilibrium, the velocity distribution of its galaxies is expected to be gaussian and the velocity dispersion can be directly linked to its mass through the virial theorem. An advantage of this method is that, unlike X-ray and S-Z mass measurements, it's not affected by forms of non-thermal pressure such as magnetic fields, turbulence and cosmic ray pressure. As a downside, it is sensitive to triaxiality and projection effects, the precision of the measurements is limited by the finite number of galaxies and the assumption of dynamical equilibrium it's not always possible (Allen, Evrard & Mantz, 2011).

Also, considering that light traces mass, the total optical luminosity of a cluster is another indicator of its mass. Abell (1958) defined a *richness* class to categorize clusters based on the number of member galaxies brighter than a given magnitude limit. The luminosity distribution function of cluster galaxies, though, is well described by the Schechter (1976) profile and the observation of the high luminosity tip of this distribution allows us to better constrain cluster masses. Postman et al. (1996), for example, defined the richness parameter as the number of cluster galaxies brighter than the characteristic luminosity of the Schechter (1976) profile, L_* . Different definitions are possible and intrinsically related to the technique used to optically detect galaxy clusters.

The total cluster mass can also be derived by its strong and weak gravitational lensing of background sources. In the weak lensing regime, the gravitational potential of clusters of galaxies produces small distortions in the observed shape of the background field galaxies, creating the so-called shear field, which is proportional to the cluster mass. Being the shear much smaller compared to the intrinsic ellipticity of the galaxies (due to their random shape and orientation), a statistical approach is required to measure it and the signal is averaged over a large number of background sources to increase the signal-to-noise ratio (Schneider, 2005). Gravitational lensing

doesn't require any assumption on the dynamical state of the cluster and it is sensitive to the projected mass along the line of sight, representing a reliable tool to determine total cluster masses (Allen, Evrard & Mantz, 2011).

1.2.3 Scaling relations

Considering all the mass proxies described above, it is important to study the relation between the cluster mass and different observables that correlate with it, with the aim of identifying systematics and converge towards an estimation of the cluster true mass.

The study of scaling relations is useful because, given a cluster mass estimated with a certain method, it is possible to calculate other parameters linked to it. On the other hand, comparing different masses we can study the systematics related to the methods used. Also, the study of the scaling relations as a function of the redshift can give us informations on the cluster evolution. Moreover, scaling relations can help us to put tighter constraints on the cosmological parameters, through the reconstruction of the mass function.

The advantages and the systematics of the different mass proxies are found in the respective scaling relations.

For example, assuming a singular isothermal sphere at hydrostatic equilibrium, the relation between the true cluster mass and its X-ray temperature can be written as:

$$k_B T_{200} = (8.2 \text{keV}) \left(\frac{M_{200}}{10^{15} h^{-1} M_\odot} \right)^{2/3} \left[\frac{H(z)}{H_0} \right]^{2/3}$$

Since clusters are not perfectly isothermal though, it's important how we define the cluster temperature. A definition often used is the luminosity weighted mean temperature, in which each component is proportional to its photon flux in the overall spectrum. The normalization of the mass-temperature relation can change if galaxy formation is taken into account or not. This can lead to a discrepancy between observed and theoretical masses of $\sim 30 - 60\%$. The discrepancy could be explained by systematic errors in the determination of the cluster mass from observations. The assumption of hydrostatic equilibrium, in fact, can lead to a mass underestimation of a factor $\sim 10 - 15\%$ (Voit, 2005).

X-ray luminosity is easier to measure than the temperature but it correlates less tightly with mass, with a scatter of $\sim 50\%$. Also, even more than in the case of the mass-temperature relation, the slope and normalization of the mass-luminosity relation depend greatly on the model of galaxy formation assumed. A way to calibrate the mass-luminosity relation is to combine

the mass-temperature relation with the observed luminosity-temperature relation. If the density distribution of the intracluster gas within r_{200} was independent of cluster mass, then we would expect $L \propto T^2$. The observed slope though is steeper, indicating that non gravitational processes raised the entropy of the intracluster gas and, making it hard to compress, lowered its mean density and luminosity. Excising the central regions of a cluster can reduce the scatter in the relation, since cooling and non gravitational heating processes alter the temperature and luminosity of these regions in different ways from cluster to cluster (Voit, 2005).

Clusters in optical surveys are selected as galaxy overdensities, which can be biased by line-of-sight projections (Cohn et al., 2007). Richness is found to correlate quite well with X-ray observables even though the scatter is large (Donahue et al., 2001, 2002; Yee & Ellingson, 2003; Kochanek et al., 2003; Gilbank et al., 2004). Galaxy concentrations projected along the line of sight can lead to an overestimation of the cluster mass, especially when their redshifts is not precisely known. The intrinsic scatter between true cluster mass and richness, leads to an overestimation of the normalization of the mass function. Because the low mass clusters that are scattered to higher masses are far more than the low mass clusters scattered in the opposite way, mean cluster masses will be on average biased high. Underestimating this scatter leads also to a bias in the cosmological parameters estimation (Roza et al., 2009a,b).

Galaxy velocity dispersion in clusters has shown to correlate well with cluster mass (Xue & Wu, 2000; Munari et al., 2013). Velocity dispersion in the optical traces the X-ray temperature of the cluster but the masses inferred from those measurements are larger than the X-ray counterparts (Reiprich & Böhringer, 2002). This discrepancy can be explained considering the intrinsic scatter in the velocity dispersion-mass relation but also by cut-off and projection effects in the measurements of the one-dimensional velocity dispersion (Voit, 2005).

WEAK LENSING

As predicted by General Relativity, gravitational lensing is a phenomenon in which a mass concentration creates a curvature of space time, and deflects the light rays that propagate along the geodesic lines, causing the distortion of the image of the emitting source.

In the *strong lensing* regime, this distortion can be so intense that multiple light rays can travel from the source to the observer creating multiple-image systems or image deformations that can be seen by eye, like *Einsteins rings*, when the source and the lens are perfectly aligned, or *arcs* in galaxy clusters.

On the other hand, in the *weak lensing* regime, this effect can't be detected on single sources, and a statistical approach is needed to access the information on the mass distribution of the lens. Galaxies, in fact, are not perfectly circular and the shape distortion due to lensing, called *shear*, can't be distinguished from their intrinsic ellipticity. Assuming that galaxies are randomly oriented in the universe though, it's possible to extract the shear signal averaging over a large sample of background sources as the expected value of the intrinsic ellipticity will be zero.

Moreover, since the deflection angle of the light rays, and thus the shape distortion of the background galaxies, depends only on the gravitational potential of the lens, and not on the nature or the physical state of the matter, gravitational lensing probes the total mass distribution and no assumption is required regarding the dynamical state of the lensing object, unlike other methods that imply the condition of hydrostatic equilibrium and the application of the virial theorem.

For these reasons, weak lensing can be considered a powerful tool to constrain the cosmological model with different kind of applications, ranging from the study of the large scale structure, through *cosmic shear* and *CMB lensing* that, for example, allow to measure the cosmological parameters from

the power spectrum, to the estimation of the mass of galaxy clusters and galaxies, and of the various observable-mass relations from the reconstruction of their shear radial profiles. *Galaxy-galaxy lensing* and *galaxy clusters lensing* can lead then to the comparison of the observed mass function with the theoretical models from simulations and to the study of the formation and evolution of these gravitationally bound systems and their environment.

In this chapter, I will describe the lensing formalism and I will review in more detail the lensing applications cited above, then I will discuss what kind of data is required for these analysis, and the different tools developed to adequately process them, alongside with the main results and the challenges for the future of the lensing field. This synthesis is based mainly on three reviews: Wright & Brainerd (2000), Bartelmann & Schneider (2001), and Bartelmann & Maturi (2016). I refer the reader to these works for a complete reference review of weak lensing.

2.1 Theory

2.1.1 Lens equation

In General Relativity, light deflection can be calculated starting from the *Fermat principle* that states that a light ray travels along a path along which the travel time is extremal. We have to consider the path for which, given two fixed points A and B, we have:

$$\delta \int_A^B n[\vec{x}(l)dl] = 0 \quad (2.1)$$

where n is the refraction index. In order to calculate n , we can use the weak field approximation, $\frac{\phi}{c^2} \ll 1$.

The lens causes a perturbation of the Minkowski space-time:

$$ds^2 = g_{\mu\nu}dx^\mu dx^\nu = (1 + \frac{2\phi}{c^2})c^2dt^2 - (1 - \frac{2\phi}{c^2})d\vec{x}^2 \quad (2.2)$$

and since for a light ray $ds^2 = 0$, we can calculate the speed of light reduced by the gravitational field of the lens:

$$c' = \frac{d\vec{x}}{dt} \simeq c(1 + \frac{2\phi}{c^2}) \quad (2.3)$$

The refraction index then will be:

$$n = \frac{c}{c'} \simeq 1 - \frac{2\phi}{c^2} \quad (2.4)$$

If we assume that the integral line of Equation 2.1 is parametrized by an arbitrary parameter λ , we can write:

$$\delta \int_{\lambda_A}^{\lambda_B} d\lambda n[\vec{x}(\lambda)] \left| \frac{d\vec{x}}{d\lambda} \right| = 0 \quad (2.5)$$

Using Euler equations and the refraction index previously calculated, we can write the total deflection angle as:

$$\widehat{\vec{\alpha}} = \frac{2}{c^2} \int_{\lambda_A}^{\lambda_B} \vec{\nabla}_{\perp} \phi d\lambda = \frac{4GM}{Rc^2} \quad (2.6)$$

where $\vec{\nabla}_{\perp}$ is the gradient with respect to the normal direction.

The deflection angle is a linear function of the lens mass. If we suppose to have a distribution of N point masses on a plane, with masses M_i and positions ξ_i , the deflection angle will be the linear superposition of the angle due to each lens:

$$\widehat{\vec{\alpha}}(\vec{\xi}) = \sum_i \widehat{\vec{\alpha}}_i(\vec{\xi} - \vec{\xi}_i) = \frac{4G}{c^2} \sum_i M_i \frac{\vec{\xi} - \vec{\xi}_i}{|\vec{\xi} - \vec{\xi}_i|^2} \quad (2.7)$$

Since the physical size of the lens is usually much smaller compared to the distance between lens and observer, the deflection takes place on a short path, and the lens can be approximated with a planar matter distribution, the so called *lens plane*, while the sources will be distributed on their on place, as shown in Figure 2.1.

$$\Sigma(\vec{\xi}) = \int \rho(\vec{\xi}, z) dz \quad (2.8)$$

The deflection angle can then be rewritten as:

$$\widehat{\vec{\alpha}}(\vec{\xi}) = \frac{4G}{c^2} \int \frac{(\vec{\xi} - \vec{\xi}') \Sigma(\vec{\xi}')}{|\vec{\xi} - \vec{\xi}'|^2} d^2 \xi' \quad (2.9)$$

In Figure 2.1, we find the observer, the lens plane, the source plane, and the respective angular diameter distances. D_L is the distance between the observer and the lens, D_S is the distance between the observer and the source, and D_{LS} is the distance between the lens and the source. Since we are dealing with angular distances, $D_L + D_{LS} \neq D_S$.

The dashed vertical line represents the optical axis from which we measure the angular position of the lens and of the source. If the source is at distance $\vec{\eta} = \vec{\beta} D_S$ from the optical axis, the impact parameter on the lens plane is $\vec{\xi} = \vec{\theta} D_L$.

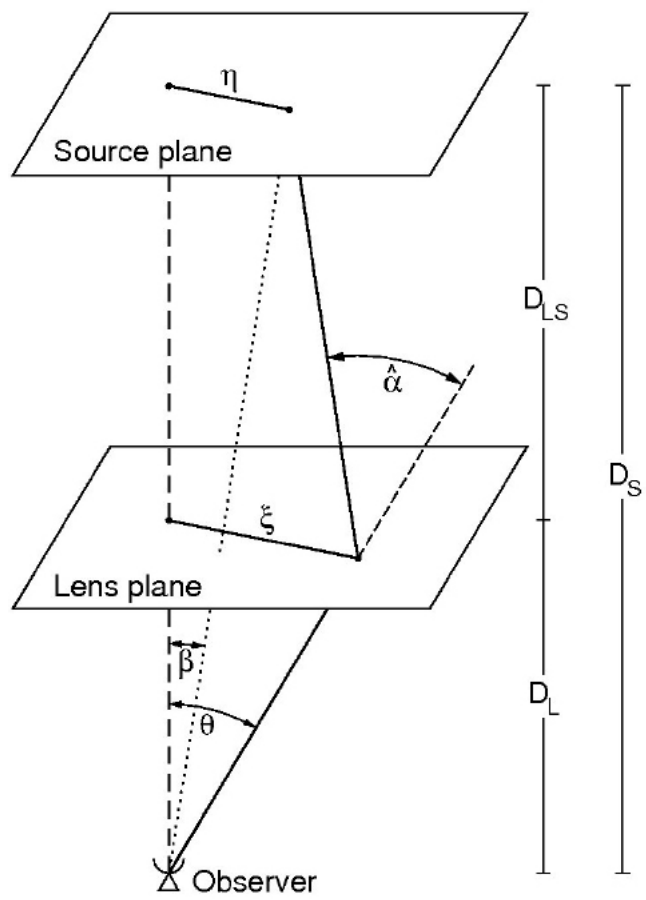


Figure 2.1 – Scheme of a typical lensing system (Bartelmann & Schneider, 2001).

If $\vec{\theta}$, $\vec{\beta}$, and $\widehat{\alpha}$ are small, the true and the observed position of the source are linked by a simple equation:

$$\vec{\theta}D_S = \vec{\beta}D_S + \widehat{\alpha}D_{LS} \quad (2.10)$$

Defining the reduce deflection angle as $\vec{\alpha}(\vec{\theta}) \equiv \frac{D_{LS}}{D_S}\widehat{\alpha}(\vec{\theta})$, we can write the *lens equation*:

$$\vec{\beta} = \vec{\theta} - \vec{\alpha}(\vec{\theta}) \quad (2.11)$$

Defining a scale length ξ_0 , such that $\mu_0 = \xi_0 D_S / D_L$, we can write:

$$\vec{x} \equiv \frac{\vec{\xi}}{\xi_0}, \quad \vec{y} \equiv \frac{\vec{\mu}}{\mu_0}, \quad \vec{\alpha}(\vec{x}) = \frac{D_L D_{LS}}{\xi_0 D_S} \widehat{\alpha}(\xi_0 \vec{x}) \quad (2.12)$$

We obtain the dimensionless lens equation:

$$\vec{y} = \vec{x} - \vec{\alpha}(\vec{x}) \quad (2.13)$$

2.1.2 Lensing potential

An extended matter distribution is characterized by an effective lensing potential. It can be calculated projecting the tridimensional Newtonian potential on the lens plane, applying a convenient scaling:

$$\widehat{\Psi}(\vec{\theta}) = \frac{D_{LS}}{D_L D_S} \frac{2}{c^2} \int \phi(D_L, \vec{\theta}, z) dz \quad (2.14)$$

Imposing $\Psi = \frac{D_L^2}{\xi_0^2} \widehat{\Psi}$.

Two important properties of the lensing potential are:

- The gradient of Ψ gives the scaled deflection angle:

$$\vec{\nabla}_x \Psi(\vec{x}) = \vec{\alpha}(\vec{x}) \quad (2.15)$$

- The Laplacian of Ψ is twice the *convergence*:

$$\Delta_x \Psi(\vec{x}) = 2k(\vec{x}) \quad (2.16)$$

where the convergence $k(\vec{x})$ is defined as a dimensionless surface density:

$$k(\vec{x}) \equiv \frac{\Sigma(\vec{x})}{\Sigma_{cr}} \quad (2.17)$$

and Σ_{cr} , is the critical surface density. It is a quantity that characterizes the lensing system, and is a function of the angular diameter distance of the lens and of the source:

$$\Sigma_{cr} = \frac{c^2}{4\pi G} \frac{D_S}{D_L D_{LS}} \quad (2.18)$$

Equation 2.16 can be demonstrated using Poisson's equation:

$$\Delta\phi = 4\pi G\rho \quad (2.19)$$

to rewrite the surface density as:

$$\Sigma(\vec{x}) = \int_{-\infty}^{+\infty} \rho dz = \frac{1}{4\pi G} \int_{-\infty}^{+\infty} \Delta\phi dz \quad (2.20)$$

Inserting it in Equation 2.17, along with Equation 2.18, we find:

$$k(\vec{x}) = \frac{D_L D_{LS}}{D_S c^2} \int_{-\infty}^{+\infty} \Delta\phi dz \quad (2.21)$$

The total Laplacian can be written as:

$$\Delta = \frac{1}{\xi_0^2} \Delta_x + \frac{\partial^2}{\partial z^2} \quad (2.22)$$

So we obtain:

$$k(\vec{x}) = \frac{D_L D_{LS}}{D_S c^2 \xi_0^2} \left[\int_{-\infty}^{+\infty} \Delta_x \phi dz + \int_{-\infty}^{+\infty} \frac{\partial^2 \phi}{\partial z^2} dz \right] \equiv \frac{1}{2} \Delta_x \Psi(\vec{x}) \quad (2.23)$$

since the second integral, taken at the end points of the line-of-sight, is zero if the mass distribution is small compared to the distances characterizing the system.

2.1.3 Shear and convergence

In principle, the image of the source can be determined solving the lens equation in every point of the extended surface. If the lens is much smaller compared to the angular scale in which its physical property change, the distortion of the image can be described by the Jacobian matrix A :

$$A \equiv \frac{\partial \vec{y}}{\partial \vec{x}} = \left(\delta_{ij} - \frac{\partial \alpha_i(\vec{x})}{\partial x_j} \right) = \left(\delta_{ij} - \frac{\partial^2 \Psi(\vec{x})}{\partial x_i \partial x_j} \right) \equiv (\delta_{ij} - \Psi_{ij}) \quad (2.24)$$

Considering the anisotropic part of the Jacobian matrix, we have:

$$(A - \frac{1}{2}TrA \cdot I)_{ij} = \begin{pmatrix} -\frac{1}{2}(\Psi_{11} - \Psi_{22}) & -\Psi_{12} \\ -\Psi_{21} & \frac{1}{2}(\Psi_{11} - \Psi_{22}) \end{pmatrix} \quad (2.25)$$

This symmetric matrix with null trace is called *shear*. It quantifies the gradient of the gravitational force that describes the distortion of the background sources.

The shear field γ is defined as:

$$\vec{\gamma} = (\gamma_1, \gamma_2), \quad \gamma_1(\vec{x}) = \frac{1}{2}(\Psi_{11} - \Psi_{22}), \quad \gamma_2(\vec{x}) = \Psi_{12} = \Psi_{21} \quad (2.26)$$

The shear is actually a pseudo vector. In fact, defining the eigenvectors of the shear matrix as $\pm\sqrt{\gamma_1^2 + \gamma_2^2} = \pm\gamma$, it exist a coordinate rotation of an angle ϕ such that:

$$\begin{pmatrix} \gamma_1 & \gamma_2 \\ \gamma_2 & -\gamma_1 \end{pmatrix} = \gamma \begin{pmatrix} \cos 2\phi & \sin 2\phi \\ \sin 2\phi & -\cos 2\phi \end{pmatrix} \quad (2.27)$$

where the factor 2 indicates that the shear components are elements of a 2x2 tensor.

Consider the isotropic part of the Jacobian matrix, we find:

$$\frac{1}{2}TrA \cdot I = [1 - \frac{1}{2}(\Psi_{11} + \Psi_{22})]\delta_{ij} = (1 - \frac{1}{2}\Delta\Psi)\delta_{ij} = (1 - k)\delta_{ij} \quad (2.28)$$

with k , the convergence previously defined.

The Jacobian matrix can be then rewritten as:

$$A = \begin{pmatrix} 1 - k - \gamma_1 & -\gamma_2 \\ -\gamma_2 & 1 - k + \gamma_1 \end{pmatrix} = \begin{pmatrix} -\gamma_1 & -\gamma_2 \\ -\gamma_2 & \gamma_1 \end{pmatrix} + (1 + k) \begin{pmatrix} 1 & 0 \\ 0 & 1 \end{pmatrix} \quad (2.29)$$

As shown in Figure 2.2, the convergence scales the images of a constant factor in every direction, while the shear distorts the image in a privileged direction.

The *magnification* is related to the convergence. Through the lens equation, we have $\delta\beta^2 \rightarrow \delta\theta^2$, but since there is no photon emission or absorption during the lensing process, the surface brightness of the lensed source is conserved. The change of solid angle therefore implies that the received flux will be magnified or demagnified.

Defining the magnification tensor as $M = A^{-1}$, we can define the magnification factor μ :

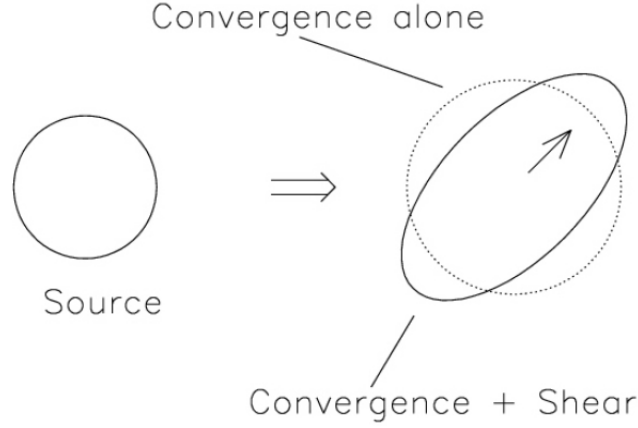


Figure 2.2 – Sketch of the effect of the convergence and shear on the image of a round source (Bartelmann & Schneider, 2001).

$$\mu = \det M = \frac{1}{\det A} = \frac{1}{(1-k)^2 - \gamma^2} \quad (2.30)$$

$$\mu_t = \frac{1}{\lambda_t} = \frac{1}{1-k-\gamma}, \quad \mu_r = \frac{1}{\lambda_r} = \frac{1}{1-k+\gamma} \quad (2.31)$$

Imposing the eigenvalues as $\lambda_t = \lambda_r = 0$, we can define two curves on the lens plane, called tangential and radial critical lines, which ideally have infinite magnification. If an image forms along the tangential critical line, it will be distorted in its direction. If the image forms near the radial critical line, it will be elongated in the direction perpendicular to it. The critical lines mapped on the source plane are called caustics.

The shear can be written in complex form:

$$\gamma = \gamma_1 + i\gamma_2 = |\gamma|e^{2i\phi} \quad (2.32)$$

The amplitude describes the amount of distortion, and the phase indicates the distortion direction.

We can also define a tangential and a cross component relative to the direction ϕ :

$$\gamma_t = -Re[\gamma e^{-2i\phi}], \quad \gamma_\times = -Im[\gamma e^{-2i\phi}] \quad (2.33)$$

where the factor 2 again reminds us that the shear is not a vector but a tensor defined by the trace-free part of the symmetric Jacobian matrix A .

This definition is useful in case of a spherically symmetric matter distribution. In this case, in fact, the shear will be always positive and oriented tangentially respect to the center of symmetry, while the cross component will always be null.

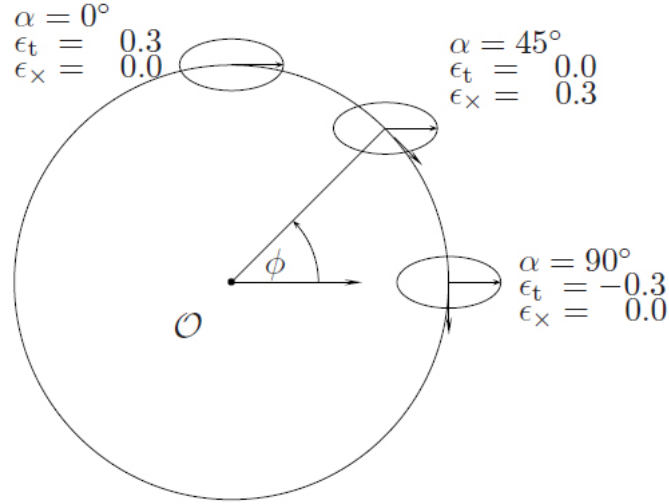


Figure 2.3 – Representation of the tangential and cross components of the shear, for an image with $\epsilon_1 = 0.3$ and $\epsilon_2 = 0$, and three different ϕ directions (Meneghetti, M., 2009, "Weak Lensing by Galaxy Clusters").

In Figure 2.3, we can see how the tangential and cross components change along with the direction considered, for an image with the same values of ϵ_1 e ϵ_2 , in all three cases.

2.1.4 Ellipticity definition

If we define the *reduce shear* as:

$$g(\vec{\theta}) = \frac{\gamma(\vec{\theta})}{1 - k(\vec{\theta})} \quad (2.34)$$

we can rewrite the Jacobian matrix:

$$A(\vec{\theta}) = (1 - k) \begin{pmatrix} 1 - g_1 & -g_2 \\ -g_2 & 1 + g_1 \end{pmatrix} \quad (2.35)$$

with g_1 and g_2 , the components of the reduced shear.

The image distortion can be described also through the surface brightness, considering the lens equation locally linearized:

$$\vec{\beta} - \vec{\beta}_0 = A(\vec{\theta}_0) \cdot (\vec{\theta} - \vec{\theta}_0) \quad (2.36)$$

where $\vec{\beta}_0 = \vec{\beta}(\vec{\theta}_0)$. Considering the invariance of the surface brightness respect to the gravitational deflection of the light, $I(\vec{\theta}) = I^{(s)}[\vec{\beta}(\vec{\theta})]$, we find:

$$I(\vec{\theta}) = I^{(s)}(\vec{\beta}_0 + A(\vec{\theta}_0) \cdot (\vec{\theta} - \vec{\theta}_0)) \quad (2.37)$$

Considering an isolated image with surface brightness $I(\vec{\theta})$, we can define its center as:

$$\vec{\theta} \equiv \frac{\int d^2\theta I(\vec{\theta}) q_I[I(\vec{\theta})] \vec{\theta}}{\int d^2\theta I(\vec{\theta}) q_I[I(\vec{\theta})]} \quad (2.38)$$

where $q_I(I)$ is an appropriate weight function.

We then define the second moment tensor of the brightness:

$$Q_{ij} = \frac{\int d^2\theta I(\vec{\theta}) q_I[I(\vec{\theta})] (\theta_i - \bar{\theta}_i) (\theta_j - \bar{\theta}_j)}{\int d^2\theta I(\vec{\theta}) q_I[I(\vec{\theta})]}, \quad i, j \in \{1, 2\} \quad (2.39)$$

The trace of Q describes the size of the image, the traceless part of Q_{ij} contains informations on the ellipticity. From Q_{ij} , we can define two complex ellipticities:

$$\chi \equiv \frac{Q_{11} - Q_{22} + 2iQ_{12}}{Q_{11} + Q_{22}}, \quad \epsilon \equiv \frac{Q_{11} - Q_{22} + 2iQ_{12}}{Q_{11} + Q_{22} + 2(Q_{11}Q_{22} - Q_{12}^2)^{1/2}} \quad (2.40)$$

Both have the same phase but a different absolute value. We can easily pass from a definition to another if one appear more convenient in the context in which is used.

In Figure 2.4, we can see the shape of the images as a function of their complex ellipticity χ .

We can define the same quantities for a non lensed source:

$$Q_{ij}^{(s)} = \frac{\int d^2\beta I^{(s)}(\vec{\beta}) q_I[I^{(s)}(\vec{\beta})] (\beta_i - \bar{\beta}_i) (\beta_j - \bar{\beta}_j)}{\int d^2\beta I^{(s)}(\vec{\beta}) q_I[I^{(s)}(\vec{\beta})]} \quad i, j \in \{1, 2\} \quad (2.41)$$

Considering that:

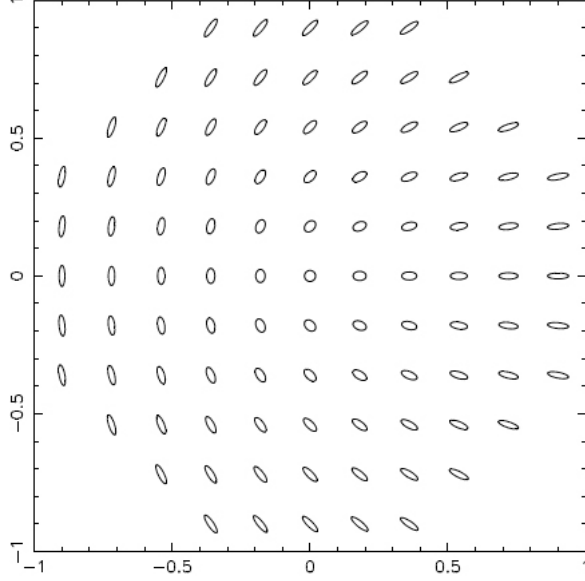


Figure 2.4 – Shape of the image of a circular source, as a function of the ellipticity components χ_1 and χ_2 (Meneghetti, M., 2009, "Weak Lensing by Galaxy Clusters").

$$d^2\beta = \det A d^2\theta \quad (2.42)$$

$$\vec{\beta} - \vec{\beta} = A(\vec{\theta} - \vec{\theta}) \quad (2.43)$$

$$Q^{(s)} = AQA^T = AQA \quad (2.44)$$

and using the definition of complex ellipticity, we can write:

$$\chi^{(s)} = \frac{\chi - 2g + g^2\chi^*}{1 + |g|^2 - 2\text{Re}(g\chi^*)}, \quad \epsilon^{(s)} = \begin{cases} \frac{\epsilon - g}{1 - g^*\epsilon} & \text{se } |g| \leq 1 \\ \frac{1 - g\epsilon^*}{\epsilon^* - g^*} & \text{se } |g| > 1 \end{cases} \quad (2.45)$$

In order to estimate the shear, since there isn't a privileged direction in the Universe, we assume that galaxies are randomly oriented:

$$E(\chi^{(s)}) = 0 = E(\epsilon^{(s)}) \quad (2.46)$$

This implies that averaging over the formula shown so far:

$$E(\epsilon) = \begin{cases} g & \text{se } |g| \leq 1 \\ 1/g^* & \text{se } |g| > 1 \end{cases} \quad (2.47)$$

This is a fundamental result, since it shows that the ellipticity is an estimation of the local reduced shear. The noise of this measurement is given by intrinsic ellipticity dispersion:

$$\sigma_\epsilon = \sqrt{\langle \epsilon^{(s)} \epsilon^{(s)*} \rangle} \quad (2.48)$$

This means that averaging over a large number of galaxies affected by the same shear, we get σ_ϵ/\sqrt{N} . Actually, since the region in which the shear can be considered constant is very small, we need to rely on very deep surveys to increase the number density of the background sources. Alternatively, we can use wide surveys and stack the background samples of lenses with similar characteristics.

The background sources used so far in weak lensing studies are distant galaxies observed in the optical or near-infrared. In order to obtain a very high number density of sources, it's necessary to study also very distant and faint galaxies. These objects have a small size and are then greatly affected by the Point Spread Function (PSF), caused by the atmospheric *seeing*, and by the instrumentation.

Taking into account the seeing, the observed ellipticity is then:

$$\epsilon_{oss} = (\epsilon_{intr} + \gamma) \otimes PSF \quad (2.49)$$

This represents the sum of the intrinsic ellipticity, due to the shape of a galaxy, and of the gravitational shear, convolved with the PSF. To accurately perform shape measurements is therefore important to study in detail the PSF to adequately correct the images.

2.1.5 Lens models

a) Point mass

The simplest lens model is a point mass lens. For this object, the lens equation can be written as:

$$\beta = \theta - \frac{4GM}{c^2 D_L \theta} \frac{D_{LS}}{D_S} \quad (2.50)$$

Defining the Einstein radius, we can rewrite it as:

$$\theta_E \equiv \sqrt{\frac{4GM}{c^2} \frac{D_{LS}}{D_S}} \quad (2.51)$$

$$\beta = \theta - \frac{\theta_E^2}{\theta} \quad (2.52)$$

b) Extended surface mass density

If we consider instead an extended surface with axial symmetry, we can choose the optical axis in such a way that it intercepts the lens plane, passing through the center of the lens. In this case, $\Sigma(\vec{\xi}) = \Sigma(|\vec{\xi}|)$, and the lens equation can be written as:

$$y = x - \frac{m(x)}{x} \quad (2.53)$$

where $m(\vec{x})$ the dimensionless mass, from which we can calculate the deflection angle:

$$\vec{\alpha}(\vec{x}) = \frac{m(\vec{x})}{x^2} \vec{x} \quad (2.54)$$

Differentiating $\vec{\alpha}(\vec{x})$, we can reconstruct the elements of the Jacobian matrix A and, from that, calculate the convergence $k(x)$, and the shear components $\gamma_1(x)$ e $\gamma_2(x)$.

c) SIS

Another lens model that we can consider is the Singular Isothermal Sphere (SIS). Assuming that the matter of which the lens is composed behaves as an ideal gas confined in a spherically symmetric gravitational potential at thermal and hydrostatic equilibrium, we find:

$$\rho(r) = \frac{\sigma_v^2}{2\pi G r^2} \quad (2.55)$$

where σ_v is the velocity dispersion of the gas particles, and r is the distance from the center of the sphere.

We can calculate the surface density, projecting the tridimensional density along the line of sight:

$$\Sigma(\xi) = 2 \frac{\sigma_v^2}{2\pi G} \int_0^\infty \frac{dz}{\xi^2 + z^2} = \frac{\sigma_v^2}{2G\xi} \quad (2.56)$$

Choosing a scale length ξ_0 , we can write:

$$\Sigma(x) = \frac{1}{2x} \Sigma_{cr} \quad (2.57)$$

Then we can calculate the convergence, the potential and the deflection angle:

$$k(x) = \frac{1}{2x}, \quad \Psi(x) = |x|, \quad \alpha(x) = \frac{x}{|x|} \quad (2.58)$$

and the lens equation will be:

$$y = x - \frac{x}{|x|} \quad (2.59)$$

In order to calculate the shear components, we need the derivatives of Ψ :

$$\frac{\partial \Psi}{\partial x_i} = \frac{x_i}{|x|}$$

$$\frac{\partial \Psi}{\partial x_i \partial x_j} = \frac{\delta_{ij} x^2 - x_i x_j}{x^3}$$

Then we get:

$$\Psi_{11} = \frac{x_2^2}{x^3}$$

$$\Psi_{12} = -\frac{x_1 x_2}{x^3}$$

$$\Psi_{22} = \frac{x_1^2}{x^3}$$

The shear components will be:

$$\gamma_1 = \frac{1}{2}(\Psi_{11} - \Psi_{22}) = -\frac{1}{2} \frac{\cos 2\phi}{x}$$

$$\gamma_2 = \Psi_{12} = -\frac{1}{2} \frac{\sin 2\phi}{x}$$

d) NFW

Finally, I will described an NFW lens model, the one that is most commonly assumed in weak lensing by galaxy clusters analysis.

Integrating the density profile along the line of sight, as for the previous model, and imposing $\xi_0 = r_s$, we find the surface density:

$$\Sigma = \frac{2r_s \delta_c \rho_c}{x^2 - 1} f(x) \quad (2.60)$$

where:

$$f(x) = \begin{cases} 1 - \frac{2}{\sqrt{x^2-1}} \arctan \sqrt{\frac{x-1}{x+1}} & x > 1 \\ 0 & x = 1 \\ 1 - \frac{2}{\sqrt{1-x^2}} \arctan h \sqrt{\frac{1-x}{1+x}} & x < 1 \end{cases} \quad (2.61)$$

The lensing potential will be:

$$\Psi(x) = \frac{4r_s \delta_c \rho_c}{\Sigma_{cr}} g(x) \quad (2.62)$$

where:

$$g(x) = \frac{1}{2} \ln^2 \frac{x}{2} + \begin{cases} 2 \arctan^2 \sqrt{\frac{x-1}{x+1}} & x > 1 \\ 0 & x = 1 \\ -2 \arctan h^2 \sqrt{\frac{1-x}{1+x}} & x < 1 \end{cases} \quad (2.63)$$

The deflection angle will be:

$$\alpha(x) = \frac{4r_s \delta_c \rho_c}{\Sigma_{cr} x} h(x) \quad (2.64)$$

where:

$$h(x) = \ln \frac{x}{2} + \begin{cases} \frac{2}{\sqrt{x^2-1}} \arctan \sqrt{\frac{x-1}{x+1}} & x > 1 \\ 1 & x = 1 \\ \frac{2}{\sqrt{1-x^2}} \arctan h \sqrt{\frac{1-x}{1+x}} & x < 1 \end{cases} \quad (2.65)$$

Finally, for the shear we can write:

$$\gamma(x) = \begin{cases} \frac{r_s \delta_c \rho_c}{\Sigma_{cr}} g_>(x) & x > 1 \\ \frac{r_s \delta_c \rho_c}{\Sigma_{cr}} [\frac{10}{3} + 4 \ln \frac{1}{2}] & x = 1 \\ \frac{r_s \delta_c \rho_c}{\Sigma_{cr}} g_<(x) & x < 1 \end{cases} \quad (2.66)$$

where:

$$g_>(x) = \frac{8 \arctan \sqrt{\frac{x-1}{x+1}}}{x^2 \sqrt{x^2-1}} + \frac{4}{x^2} \ln \frac{x}{2} - \frac{2}{x^2-1} + \frac{4 \arctan \sqrt{\frac{x-1}{x+1}}}{(x^2-1)^{3/2}} \quad (2.67)$$

$$g_<(x) = \frac{8 \arctan h \sqrt{\frac{1-x}{1+x}}}{x^2 \sqrt{x^2-1}} + \frac{4}{x^2} \ln \frac{x}{2} - \frac{2}{x^2-1} + \frac{4 \arctan h \sqrt{\frac{1-x}{1+x}}}{(x^2-1)(1-x^2)^{1/2}} \quad (2.68)$$

2.2 Applications

2.2.1 Galaxy-galaxy lensing

Unlike the case of single massive galaxy cluster, the lensing signal from a single galaxy is too small to be detected on the background sources sample, even for the most massive objects. Besides averaging over a large number of background galaxies, it's therefore necessary to stack many foreground galaxies, acting as lenses, selecting and binning them according to some observable that correlates well with their total mass (e.g. luminosity, stellar mass).

Galaxy-galaxy lensing can be applied to field and cluster galaxies, measuring the stacked tangential radial shear profile around these objects and inferring their masses with a fit to a chosen model. In the second case, on first approximation, the aperture around the lenses needs to be small enough not to include the contribution from the host halo and neighboring cluster galaxies, while in a more detailed analysis is necessary to model these supplementary signals.

In Figure 2.5¹, we can see an example of a shear profile reconstruction. The same method can be applied in case of cluster lensing. We find, on

¹All figures cited as *Gravlens 2016* were taken from talks presented at the conference "From theory to applications: celebrating a century of gravitational lensing", 11-15 July 2016, Leiden, the Netherlands. The complete pdf presentations can be found at <http://home.strw.leidenuniv.nl/~gravlens2016/Talks/talks.html>

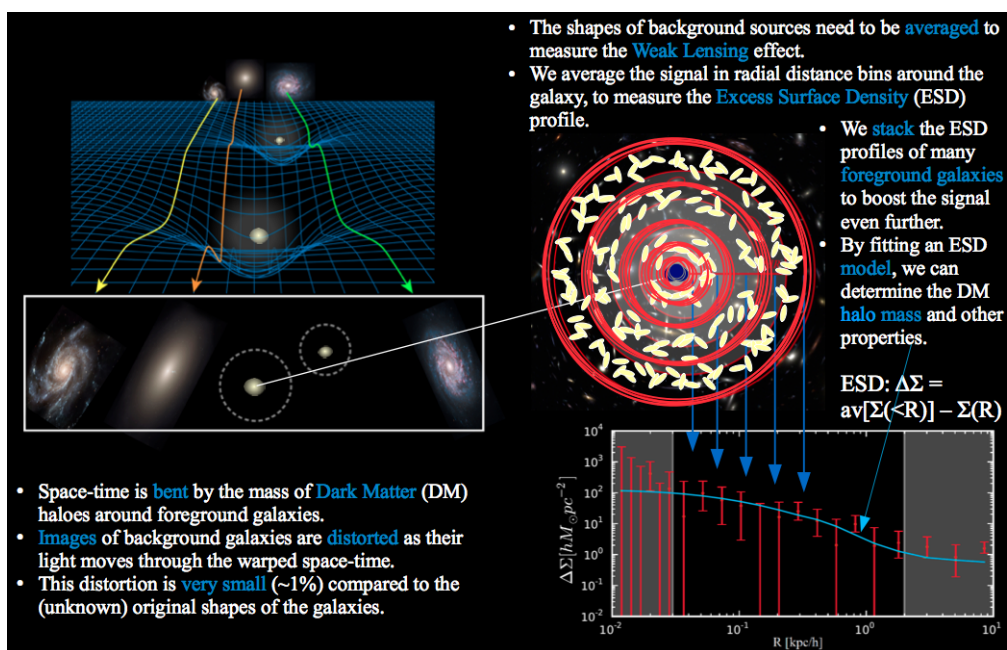


Figure 2.5 – The images of the background sources are distorted by the foreground objects. Averaging the shear signal in concentric annuli around the lens, it's possible to reconstruct the radial surface density contrast (Brouwer, M., Gravlens 2016).

the left, a drawing representing the bending of the space time caused by the foreground mass concentration, and the path followed by the light emitted by the background sources, whose image is distorted. On the right, we have a representation of the annular binning around the lens. Galaxy ellipticities are averaged inside each annulus to calculate the shear radial profile, shown in the bottom right.

With this kind of analysis, it's possible to infer the stellar-to-subhalo mass ratio and different observable-halo mass relations (Coupon et al., 2015; Sifón et al., 2015; van Uitert et al., 2016) and, for example, compare these results with abundance matching (Li et al., 2014). The abundance matching technique it's based on the assumption of a monotonic relation between a (sub)halo property (i.e. mass or velocity) and an observed galaxy property (i.e. luminosity or mass). It consist in the match between an halo mass function from simulations with a luminosity or stellar mass function from observations, so that the most massive or the most luminous galaxy will reside in the most massive halo. This technique offers a very simple prediction of the stellar-to-subhalo mass ratio that can be tested against observations, using for example this kind of lensing measurements.

Dividing cluster galaxies into satellites and centrals, it's also possible to study the interaction between the host halo and the subhalos, binning them according to their distance from the cluster center (Li et al., 2016). The mass loss as a function of the halo centric radius can give evidence of tidal stripping and allows us to constrain galaxy formation models, comparing the results with simulations. (Li et al., 2016) found that the subhalo-to-stellar mass ratio of satellite galaxies increases as a function of the halo-centric radius, as predicted from simulations. In fact, when a small halo merges to a larger system, becoming a subhalo, it starts to suffer from environmental effects such as tidal stripping, ram-pressure, and dynamical friction. The infalling subhalos will mainly loose dark matter rather than luminous matter, since the mass distribution of the latter is much more concentrated compared to the more extended profile of the first.

2.2.2 Galaxy cluster lensing

Galaxy cluster masses can be inferred with different methods (i.e. X-ray flux and temperature, S-Z effect, dynamics) but as stated before, unlike gravitational lensing, they have to rely on the assumption of hydrostatic equilibrium. The simulations of Rasia et al. (2012) showed that the bias on weak lensing derived masses is $\sim 5 - 10\%$, while for X-ray masses it increases to $\sim 25 - 30\%$. The X-ray bias is mainly due to the lack of hydrostatic equilibrium, presence of clumps, and temperature inhomogeneity.

Hoekstra (2003) showed that the relative accuracy on individual cluster mass measurements, leaving the concentration as a free parameter, goes from $\sim 30\%$ to $\sim 15\%$ for masses between $\sim 7 \times 10^{14} M_{\odot}$ and $\sim 3 \times 10^{15} M_{\odot}$. Clusters less massive than $\sim 7 \times 10^{14} M_{\odot}$ need then to be stacked to allow the shear signal to emerge from the noise of the intrinsic ellipticity of the background sources and, in this case, the profile obtained will give a mean lensing mass.

There are two different methods to infer cluster masses from the lensing signal, either using single clusters or stacking them, that have been largely used so far. I will discuss this methods briefly, and I refer the reader to Hoekstra et al. (2013) for a more comprehensive review on cluster mass estimation from weak lensing measurements.

Aperture mass measurements, first introduced by Schneider (1996), are based on the computation of the amount of tangential shear inside a fix aperture radius, filtered by a function that maximizes the signal-to-noise ratio for a given lens model. In Hoekstra (2001), two different filters are used, one corresponding to a SIS lens model and one based on the ζ -*statistic* (Fahlman et al., 1994), which is independent of the mass distribution. In the same paper, the contribution from the large scale structure is also addressed and considered as an additional statistical source of error, estimated integrating the power spectrum. Hoekstra et al. (2012) measured masses of single X-ray selected clusters (from Chandra and XMM-Newton; Mahdavi et al., 2012) using this technique and compared the results with S-Z mass estimates (from OVRO and BIMA; Bonamente et al., 2006), finding good agreement between the two.

Israel et al. (2010) also measured single cluster masses with aperture mass statistics. He used a different filter, first introduced by Schirmer et al. (2006), which corresponds to an NFW lens model. In the same work, this method is used to identify cluster centers, and the results are compared with X-ray centers.

In principle, aperture mass statistic could be then used to detect galaxy cluster and their center using only their shear signal but this is possible only for very massive clusters that give rise to high S/N peaks that can be distinguished from spurious low peaks.

Another way in which cluster masses can be inferred is to assume a semi-analytic model for the lens, called halo model and first introduced by Seljak (2000). The idea is that all the matter in the universe is confined in spherical halos that are clustered according to their mass. As a first approximation then, a galaxy cluster can be modeled with an NFW profile, and the contribution from neighboring halos and filaments can be included in a second term (i.e. two-halo term), proportional to the linear matter bias and correlation

function. Assuming this model, it is possible to relate the measured shear radial profile (the tangential shear averaged in annuli around the center of the lens or the stack of lenses, as explained in the case of galaxy-galaxy lensing in Figure 2.5) to the surface density contrast, and perform a fit to evaluate the parameters of interest, the radius r_{200} , and optionally the concentration c_{200} .

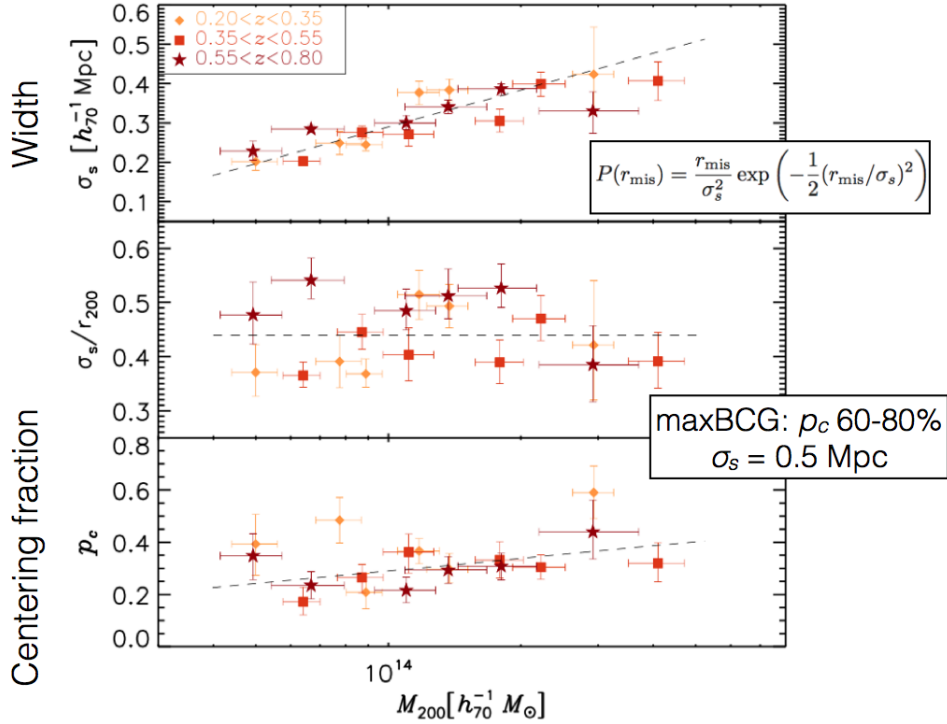


Figure 2.6 – Example of miscentering parameters from van Uitert et al. (2016) as a function of the halo mass in each richness bin. In the top plot, the width of the miscentering distribution $P(r_{\text{mis}})$. In the middle, the width normalized by the radius r_{200} . In the bottom, the percentage of correctly centered clusters in each bin. The different colors represent different redshift bins. There is no evidence of redshift evolution.

Additional terms can be included in the model to take into account, for example, the contribution from the cluster BCG or non-weak shear effects in the innermost regions. The most important term is the one that corrects for errors in the determination of the true cluster center. George et al. (2012) performed an analysis on miscentering that resulted in an underestimation of the mass by 5 – 30%, depending on the centering method. They tested galaxy candidate centers (the galaxy with the greatest stellar mass within a given radius from the X-ray centroid, the galaxy with the greater stellar

mass within r_{200} , the brightest galaxy within a given radius from the X-ray centroid, and the brightest galaxy within r_{200}), and centroid candidate centers (the centroid of member galaxies, the centroid of member galaxies weighted by stellar mass, the centroid of member galaxies weighted by flux, and the X-ray centroid). Based on the recovered weak lensing signal, the brightest or the most massive galaxy near the X-ray centroid resulted to be the best cluster center tracer.

Johnston et al. (2007) found from simulations that the distribution of center offsets can be modeled as a Reyleigh distribution that, when applied to the shear radial profile, creates a smoothing responsible for the mass underestimation. In order to add this effect in the analytic model is therefore necessary to add some parameters, usually the width of the offset distribution and the percentage of correctly centered clusters.

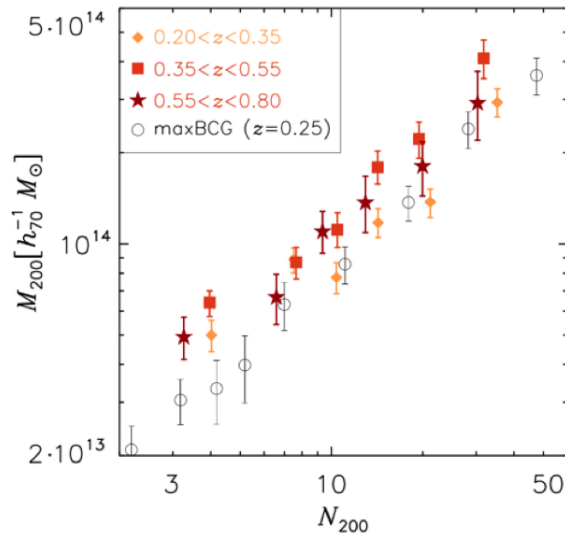


Figure 2.7 – Mass-richness relation inferred with shear profile fitting from van Uitert et al. (2016), compared with the results of Johnston et al. (2007), in back. The different colors represent different redshifts bins. The normalization of the mass richness relation increases with redshift.

Johnston et al. (2007), and more recently Ford et al. (2015) and van Uitert et al. (2016), applied this technique, stacking clusters in richness and luminosity bins and evaluating the mean mass M_{200} , with other interesting parameters such as the linear bias, the concentration, the miscentering parameters, and mass of the BCG, deriving also the corresponding scaling relations.

As an example, I show the results of van Uitert et al. (2016). In Figure

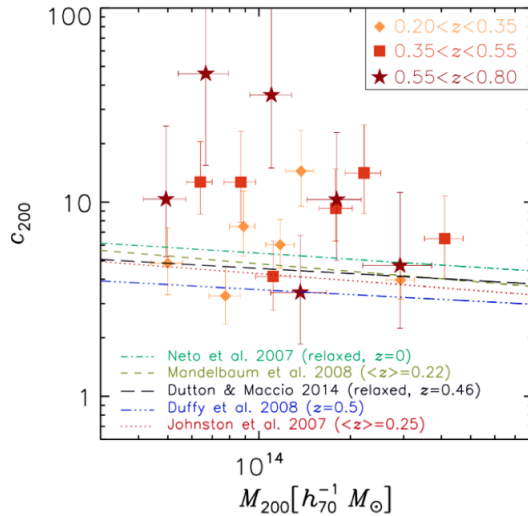


Figure 2.8 – *Mass-concentration relation inferred with shear profile fitting from van Uitert et al. (2016), compared with others in literature. The different colors represent different redshift bins. The uncertainties are too high to constrain redshift evolution.*

2.6, we can see the recovered miscentering parameters, as a function of the mean halo mass in each bin. From top to bottom, we find the width of the miscentering distribution, the width over the radius r_{200} , and the percentage of correctly centered clusters in each bin. Different colors correspond to different redshift bins. They found that the miscentering parameters increase with the cluster mass, with no evidence of evolution with redshift of these relations. In Figure 2.7, we can see the mass-richness relation that they inferred, for different redshifts bins, compared to the results of Johnston et al. (2007), in black. They found that the normalization of the mass-richness relation increases with redshift. This is the opposite of what we would expect, since M_{200} masses are defined with respect to the critical density of the universe, they should increase for lower redshifts, as the background density decrease. They justify the unexpected trend that they found with the evolution of richness with redshift. Since the richness quantifies the number of red passive galaxies in a cluster, its value will increase for lower redshift, as tidal and ram pressure stripping will quench the galaxy star formation. In Figure 2.8, we find their mass-concentration relation. The uncertainties on the concentration parameter are large, as it is generally the case with this kind of analysis (e.g. Johnston et al., 2007; Mandelbaum et al., 2008; Covone et al., 2014). The concentration parameter, in fact, it's usually not well constrained

by the data since it's degenerate with the miscentering parameters.

Simet et al. (2016) performed the same kind of analysis but with a different choice of parametrization, studying extensively the systematic error budget, taking into account photo-z and shape measurements, miscentering, cluster projections, halo triaxiality and baryonic effects and deriving an updated mass-richness relation. Unlike van Uitert et al. (2016), they didn't calculate the fit parameters in each richness bin, but performed a simultaneous fit of all the shear profiles, inferring directly the slope and normalization of the mass-richness relation, and the mean values of the miscentering parameters. They found results in good agreement with others in literature.

Kettula et al. (2015), on the other hand, used the same method on individual X-ray detected clusters to correlate lensing masses with X-ray (XMM-Newton) luminosity and temperature. They divided their sample in relaxed and merging clusters, based on the offset between the X-ray peak and the BCG position. They found that the scatter in T_X at fixed mass is lower than that of L_X . For the mass-luminosity and mass-temperature relations, they found that merging cluster sample shows a greater scatter, compared to the relaxed samples. They also performed a X-ray cross calibration between XMM-Newton and Chandra, and found that the slopes of the luminosity-temperature, and mass-temperature relations are flatter using Chandra calibration, while the mass-luminosity relation is not affected.

2.2.3 Peak statistics

High S/N peaks in lensing maps are expected to be associated with massive structures along the line of sight. Theoretically then, weak lensing peak abundance is related to the mass function of dark matter halos and peak counts can be used to constrain the cosmological model and also to study the non-gaussian information that is inaccessible with the reconstruction of the convergence power spectrum alone, in two-point correlation analysis (Figure 2.9).

As we said in the previous chapter, it's possible to detect galaxy cluster using aperture mass measurements. The problem though is that, while high S/N peaks are actually associated with a single massive collapsed halo, the nature of low and medium peaks has to be interpreted differently. Kratochvil et al. (2010) and Yang et al. (2011) reconstructed convergence maps from ray tracing simulations (Figure 2.10) to investigate the nature of these peaks. They found that they arise from the projection of multiple halos along the line of sight and by random galaxy shape noise. They also reached the counter intuitive conclusion that noise can increase the peak counts, simulating low peaks, since it doesn't add linearly to the lensing signal.

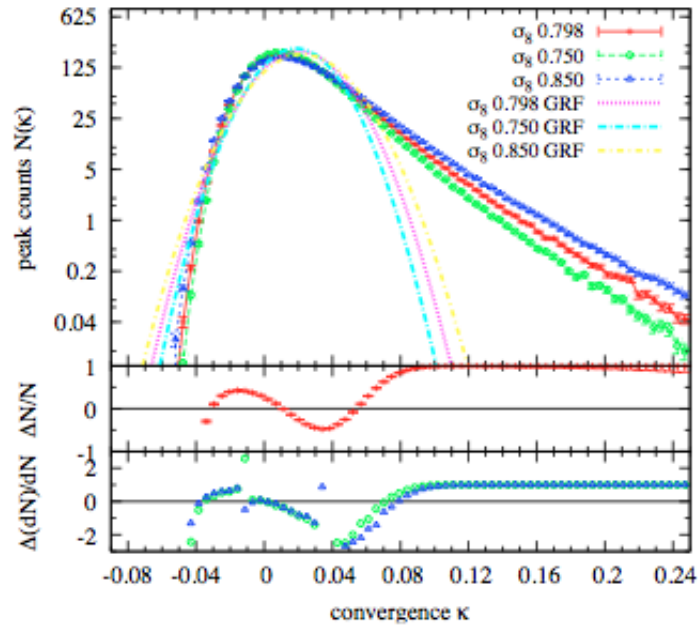


Figure 2.9 – Peak counts from different cosmological simulations and compared with those expected for Gaussian Random Fields (GRF). Peak statistics is highly non Gaussian (Yang et al., 2011).

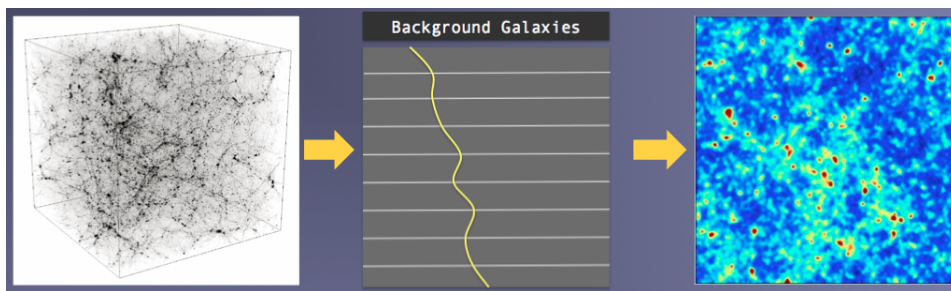


Figure 2.10 – *Illustration of simulations for peak counts prediction. Starting from N-body simulations, ray tracing is applied to get a full cosmological simulation (Haiman, Gravens2016).*

Liu, X., et al. (2015) applied peaks statistics to observed data, reconstructing convergence maps and scanning the pixels to look for maxima. Cosmological parameters were then inferred applying a fit to a theoretical model of peak abundance.

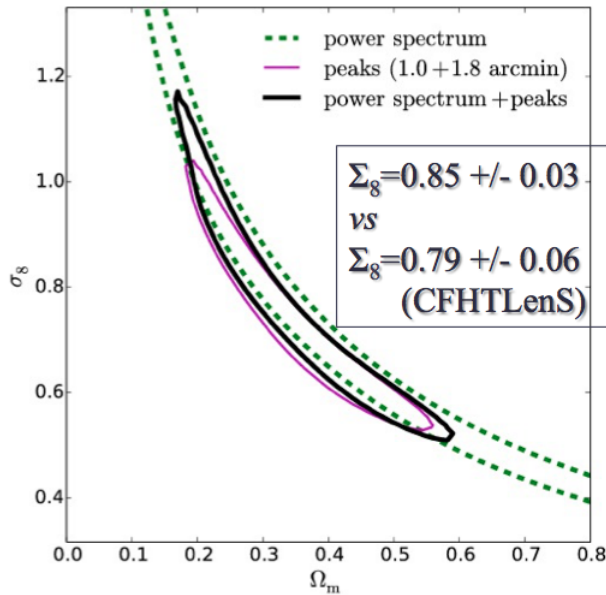


Figure 2.11 – Constraints on cosmological parameters from peak counts statistics, power spectrum, and joint analysis (Liu, J., et al., 2015).

Liu, J., et al. (2015) performed a similar analysis on another sample of observed data, calculating also the convergence power spectrum from the Fourier transform of the convergence maps. The results were then compared with a set of ray tracing simulations for different cosmological models. The constraints derived are tighter when using the power spectrum and peak counts combined (Figure 2.11).

Martinet et al. (2015) on the other hand, applied the peak statistics directly on shear maps, instead of performing the convergence map reconstruction. Peaks were identified using the aperture mass technique using a particular filter (not associated with the physical mass of the dark matter halos), on simulated shear maps for different kind of cosmologies.

2.2.4 LSS lensing

Lensing by Large Scale Structure was first probed by Bacon et al. (2000) and called *cosmic shear*. It has proven to be an important tool to directly

measure the projected matter power spectrum, and cosmological parameters such as the matter density and the amplitude of the power spectrum. It has been used also to constrain neutrino mass and dark energy, especially if used in combination with other measurements (for example those from CMB lensing).

Bacon et al. (2000) calculated the two-dimensional power spectrum to differentiate between different cosmological models, averaging the shear in cells to minimize cosmic variance. Their results are consistent with Λ -CDM models. In particular, for a Λ -CDM model with $\Omega_m=0.3$, they found $\sigma_8 = 1.5 \pm 0.7$, consistent with the value derived from cluster abundance.

Hoekstra et al. (2005) used different two-point statistics to calculate the correlation functions. In particular, the ellipticity correlation function allows us to separate the signal into E-mode and B-mode. The latter should be zero and its amplitude provides an estimate of the residual systematics. They also used the aperture mass statistics as two-point statistics to calculate the aperture mass variance. The observed two-point statistics can be related to the matter power spectrum to infer the cosmological parameters of interest. They found $\sigma_8 = 0.85 \pm 0.06$, and $w_0 < -0.8$ at 68% confidence, in agreement with previous results.

Becker et al. (2016) also performed two-point statistics on Dark Energy Survey Science Verification (DES VS) data in both, real and Fourier space, extensively testing for systematics using simulations, including B-modes contamination and dependence on observing conditions and galaxy properties. The constraints on the cosmological parameters inferred with these data are presented in the companion paper Dark Energy Survey Collaboration (2016). They found $\sigma_8 (\Omega_m/0.3)^{0.5} = 0.81 \pm 0.06$. This result is in agreement with cosmic shear studies from the CFHTLenS and Planck CMB data. The $\sim 20\%$ of the error budget comes from photometric redshift calibration uncertainties.

2.2.5 CMB lensing

Gravitational lensing has different effects on the Cosmic Microwave Background radiation, introducing correlations in the temperature fluctuation modes. This distorts the local 2-D power spectrum (as it happens on galaxy images) and smears its peaks. While cosmic variance creates fluctuations in the power spectrum that can't be distinguished from lensing effects, the B-mode polarization on small scales is due to lensing alone and constitutes noise for the inflation B-modes (Lewis, Challinor & Lasenby, 2000).

CMB lensing can be used to study structure formation at high redshift, probing the sum of neutrino masses, and to measure the gravitational potential on very large scales, constraining curvature, dark energy and modified

gravity.

While previously CMB observation alone lacked of the sensitivity and resolution to detect lensing, and had to be studied in cross correlation with galaxy distributions from other data, van Engelen et al. (2012) used a quadratic estimator to reconstruct the lensing power spectrum with SPT data, measuring its amplitude and constraining other cosmological parameters, studying in detail the systematics due to noise and foreground.

POLARBEAR Collaboration (2014), in the POLARBEAR Collaboration, used again the four-point correlation function, detecting for the first time evidence of CMB lensing polarization with CMB information alone, and measuring the amplitude of matter fluctuations and lensing B-modes.

Planck Collaboration XV (2016), performed the most significant detection of the CMB lensing potential using temperature and polarization data. They estimated the lensing potential power spectrum finding good agreement with Planck temperature and polarization power spectra. They combined this information with E-mode polarization to have an estimate of the B-mode, and detected cross-correlation of this signal with large scale temperature anisotropies.

In Figure 2.12, we can see the lensing power spectrum measured by Planck, POLARBEAR and other surveys. The significance of the measurement grew from $\sim 3\sigma$ to almost 50σ .

Melin & Bartlett (2015) proposed a different use of CMB lensing data. They used simulations of Planck observations to demonstrate that it's possible to measure cluster masses, even in low S/N conditions, analyzing the distortions of the CMB anisotropies caused by the lens gravitational potential. After removing the tSZ signal, a map of the cluster gravitational potential is reconstructed applying a quadratic estimator on the background CMB temperature map. Then a matched filter is used to extract the lens mass, assuming an NFW profile. They first simulated 62 observations of A2163, one of the most massive clusters known, with $M_{500}^X = 1.9 \times 10^{15} M_\odot$, and $z = 0.203$. They found $M_{500}^{lens}/M_{500}^X = 1.01 \pm 0.13$, which results in an unbiased recovery of the sample mass scale with 13% of uncertainties. Then they simulated 62 clusters from a mock of the Planck Early Sunyaev-Zeldovich sample with good X-ray observations (ESZ-XMM), with masses in the range $2 \times 10^{14} M_\odot - 2 \times 10^{15} M_\odot$. They found an unbiased estimate of the mass scale $M_{500}^{lens}/M_{500}^X = 0.99 \pm 0.28$. The larger uncertainty in this case is due to the larger range of masses used.

This method could be complementary to the other methods described for cluster lensing, based on the use of shear measurements on background galaxies. The use of the CMB as source plane, in fact, allows us to extend this analysis to much higher redshifts and to infer mass-SZ relations.

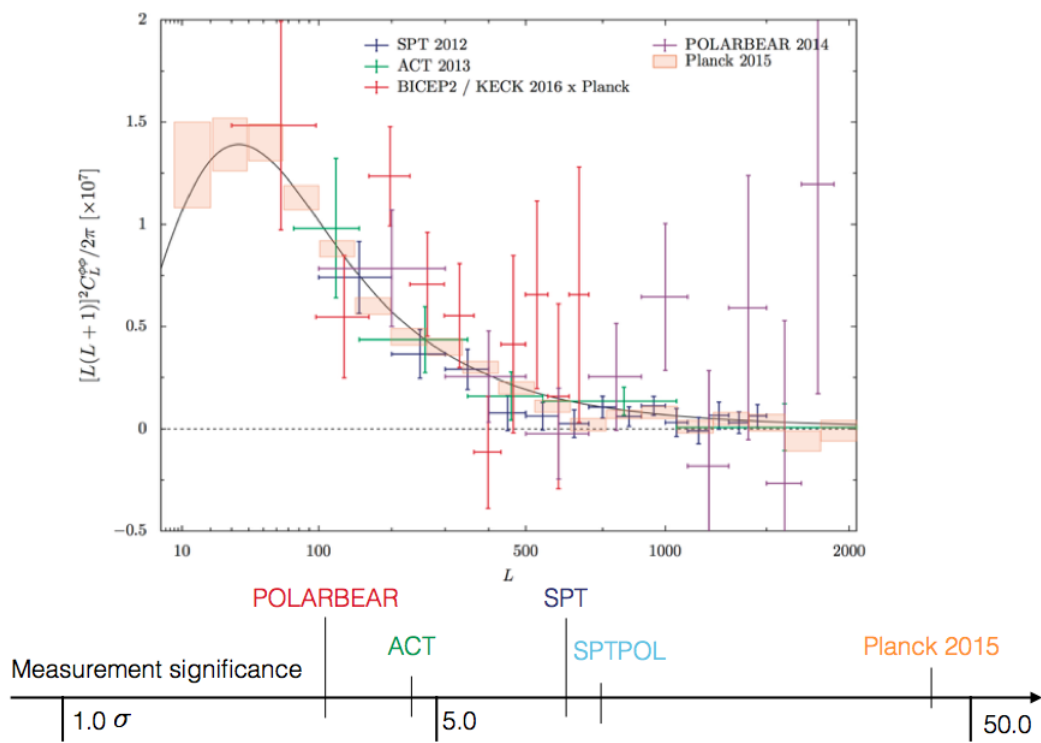


Figure 2.12 – CMB lensing power spectrum measured from different surveys with increasing significance (Carron, J., Gravlens 2016).

2.3 Data and tools

For weak lensing studies, very accurate shape measurements of the background sources are required, and have been performed so far using optical images obtained from ground based telescopes in optimal seeing conditions for wide field surveys (e.g. CFHTLS², SDSS³ and ongoing and future KiDS⁴, LSST⁵, DES⁶, HSC⁷) or space telescopes for single clusters observations (e.g. HST Frontier Fields⁸). In the upcoming future though, thousands of square degrees of the sky will be covered from space surveys such as *Euclid*⁹ and WFIRST¹⁰, and this will have a huge impact on this kind of work. Also, the next generation radio surveys such as SKA¹¹ will allow us to extend weak lensing measurements to the radio band, giving access to even larger scales.

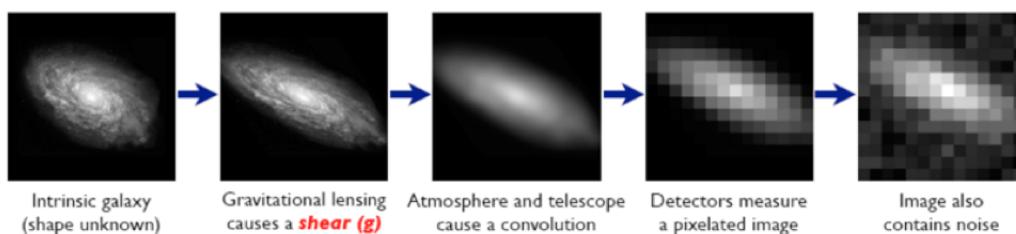


Figure 2.13 – *Illustrative example of the effects of shear, seeing, pixelization and noise on the image of a galaxy (von der Linden, Gravlens2016).*

In Figure 2.13, we can see an example of how the image of a background galaxy is modified by the effect of the shear, the PSF, the pixelization, and the noise, in a typical ground based survey.

Some of the tools developed for the purpose of measuring galaxy ellipticity are:

- *lensfit* (Miller et al., 2013): a Bayesian code that fits a two component (bulge plus disk) galaxy model, convolved with pixel-based models of the PSF for each image, marginalizing over nuisance parameters of galaxy position, size, brightness and bulge fraction.

²<http://www.cfht.hawaii.edu/Science/CFHTLS/>

³<http://www.sdss.org>

⁴<http://kids.strw.leidenuniv.nl>

⁵<http://www.lsst.org>

⁶<http://www.darkenergysurvey.org>

⁷<http://subarutelescope.org/Projects/HSC>

⁸<http://www.stsci.edu/hst/campaigns/frontier-fields/>

⁹<http://euclid-ec.org>

¹⁰<http://wfirst.gsfc.nasa.gov>

¹¹<http://www.skatelescope.org>

- im3shape (Zuntz et al., 2103): a model fitting code similar to *lensfit*. It uses a sum of two Sersic profiles for the galaxy model, and a Moffat profile for the PSF.
- ngmix (Sheldon, 2014): another model fitting method that, unlike the previous two, is not based on a point estimate of the shear (the expectation value of the galaxy ellipticity). It relies on the fact that the mean shear estimated from a large ensemble of galaxy images has a posterior distribution that approaches a Gaussian. The code uses then sums of Gaussians to model galaxies convolved with a round Gaussian PSF.
- SExtractor + PSFEx (Bertin, 2011): this method relies on SExtractor’s two-dimensional model fitting capabilities, and the convolution with the PSF modeled by the integrated companion code PSFEx, which uses a linear combination of basis vectors, that can be the pixel basis, the Gauss-Laguerre basis, or any other user-provided basis.

Alongside shape measurements, it’s important to have redshift estimations as accurate as possible since they are used to select background sources samples. Contaminations from foreground galaxies will lead to not negligible biases in mass profile reconstructions.

Because spectroscopic redshifts measurements are subjected to instrument limitations, they can’t be performed on very faint galaxies (i.e. fainter than $mag_{AB} = 24$) and very large sky areas. In fact, spectroscopic surveys can’t be as wide and deep as required by weak lensing studies, and we have to rely on photometric redshift (photo-z) estimations (Newman et al., 2015).

Even though photo-zs measurements are still not considered completely reliable and further improvements are needed in the future to reach the goal of 1% accuracy in mass estimations, the use of the complete $P(z)$ distributions has proven to lead to almost unbiased results compared to the use of a single photo-z for each galaxy, when applied to cosmological analysis (Mandelbaum et al., 2008).

Commonly used softwares for photo-zs estimations, that rely on accurate multi band photometry, are:

- BPZ (Benítez, 2000): a Bayesian code that assumes an empirical prior for the expected redshift distribution for galaxies of a given spectral type as a function of magnitude, derived from objects with spectroscopic redshifts in the HDF-N. A marginalization over a library of SED templates is then performed.

- lePhare (Ilbert et al., 2006): this code applies a simple χ^2 fit of the input photometry to various SED templates redshifted by different amounts. Varying both redshift and spectral type, a likelihood distribution can be obtained for each object.
- zebra (Feldmann et al., 2006): this code produces two estimates for the photometric redshift of each galaxy, a Maximum Likelihood one and a Bayesian one, using both the approaches described above with some improvements: SED models are corrected with an iterative technique and a training set of spectroscopic redshifts can optionally be used to optimize the initial set of galaxy templates.
- EAZY (Brammer, van Dokkum & Coppi, 2008): this algorithm is optimized for studies in which the spectroscopic redshifts are not available, or they are biased by the sample selection. In fact, the templates used in this code are not based on spectroscopic samples, but on a semi analytic model that uses galaxy synthetic photometry. It offers the possibility of performing a χ^2 minimization of linear combinations of templates, and of using bayesian priors.

In Figure 2.14, we can see a scheme that represents the different stages that are typical of a weak lensing analysis. Starting from high resolution and multi-band imaging we can identify and separate galaxies and stars, then we measure ellipticities and photometric redshift with the methods described above, performing calibration through simulations and overlapping spectroscopic redshifts samples. Depending on the kind of analysis, and lensing objects involved, we use a different statistics and compare the results with analytic models, or N-body simulations to infer the parameters of interest.

2.4 Challenges for the future

Concerning cluster and galaxy lensing, the aim for future analysis is to reach an accuracy of 1% in mass measurements. At present, the main challenge in this context, comes from the photometric redshift estimation. While we can be satisfied with our knowledge of the calibration biases in shear measurements, further improvements need to be made for photo-zs calibration to avoid the contamination of background sources samples from foreground galaxies. For example, the ellipticity estimates performed by *lensfit* are characterized by a multiplicative bias, m , that is inversely proportional to the size and detection signal-to-noise ratio of the galaxy, and by an additive bias, c , that increases for the smallest brightest objects. In Figure 2.15, we find the m

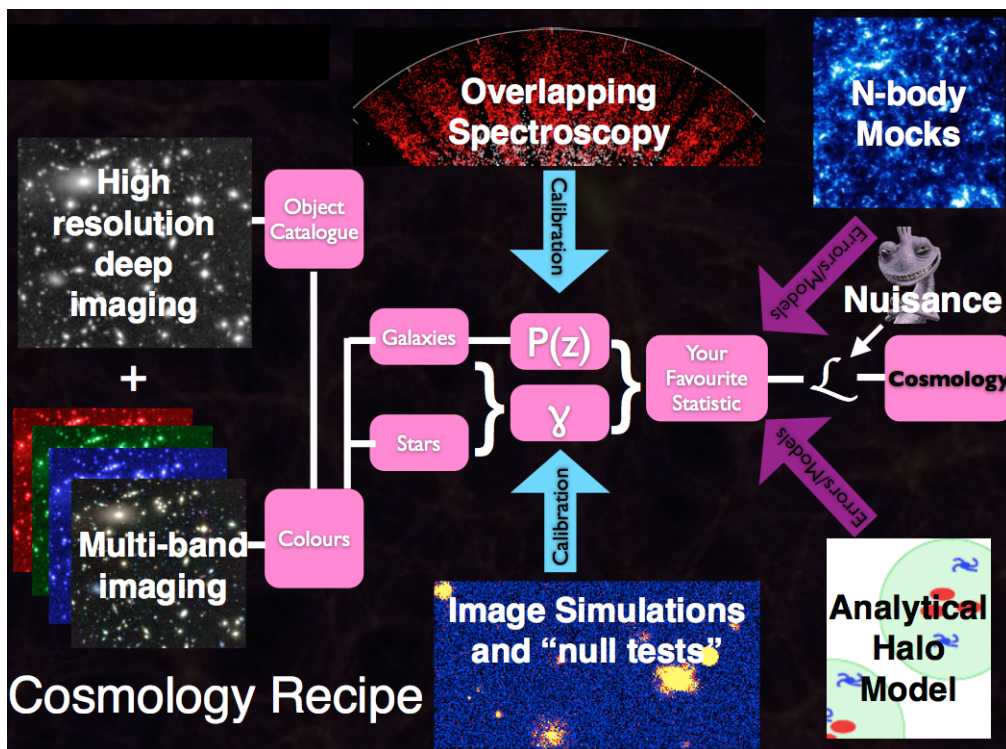


Figure 2.14 – Scheme of the different ingredients involved in weak lensing analysis (Heymans, C., Gravlens 2016).

and c calibration biases, as a function galaxy ellipticity for different redshift bins, calculated by Fenech Conti et al. (2016) from simulations. They found an average multiplicative bias $\sim 2\%$, and an average additive bias $\sim 5^{-4}$.

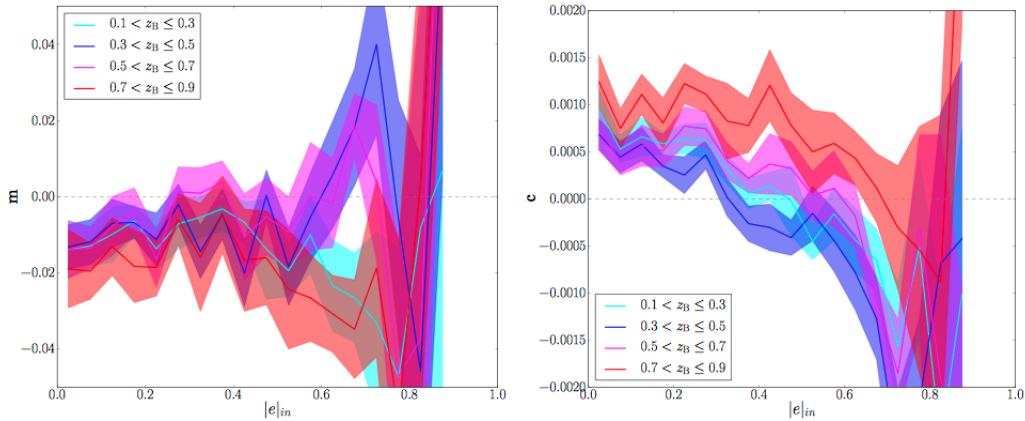


Figure 2.15 – *Multiplicative and additive calibration corrections of lensfit ellipticity measurements as a function of the galaxy ellipticity, for different redshift bins, calculated from simulations (Fenech Conti et al., 2016).*

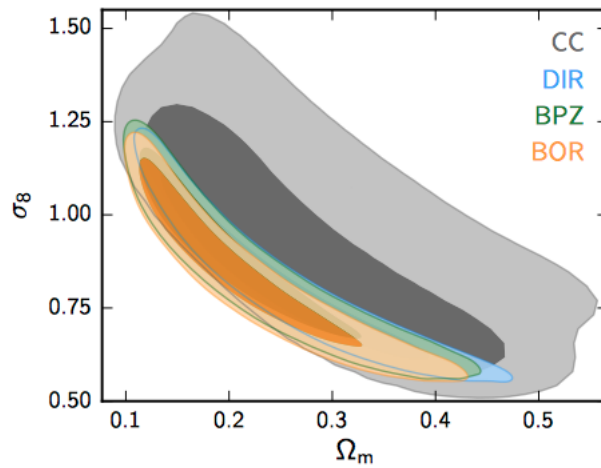


Figure 2.16 – *Constraints on cosmological parameter obtained with different redshift uncertainty and calibration methods. Weighted direct calibration in blue, cross correlation calibration in grey, original $P(z)$ from BPZ in green and recalibrated version in orange (Hildebrandt et al., 2016).*

In Figure 2.16, we can see the impact of various calibration methods for photometric redshifts estimations on the derived constraints on the cosmological parameters, through the tomographic weak lensing analysis of the

KiDS-450 data. They used three different kind of photometric redshift calibrations: a weighted direct calibration that consists in the use of the distribution of spectroscopic redshifts of object selected in the same way as the photometric sample that we want to analyze (DIR); an indirect method based on the angular cross-correlation function between the photometric and spectroscopic samples (CC); the recalibration of the original photometric $P(z)$ (BPZ) through its integration over the spectroscopic redshift range for each spectroscopic training object (BOR). We can see that the DIR method provides the best fit to the data. with uncertainties that are subdominant compared to the measurements errors. The CC method, on the other hand, provides much larger constraints, due to the limited coverage of the used spectroscopic sample. Even though all four methods shown give consistent results, it will be fundamental to further reduce the statistical uncertainties in the calibration to fully exploit the shear measurements in cosmological studies (Hildebrandt et al., 2016).

It is also important to increase the number density of background sources to achieve an higher S/N ratio in shear profile measurements. This will be possible thanks to the upcoming space missions, as *Euclid* and WFIRST that will produce optical images, and the ground based SKA radio survey, that will give access to a new order of magnitude in sky coverage.

In Figure 2.17, we can see a clear illustrative example of the different resolution achieved by ground based telescopes, on the top, and by space telescopes, on the bottom.

Regarding CMB lensing, future studies will focus on the informations accessible through polarization, to constrain neutrino masses and to probe lensing B-modes that represent noise for the measure of inflation B-modes. It is then necessary to study CMB delensing techniques to clean the signal enough to probe B-modes from primordial gravitational waves.

In cosmic shear studies and peak counts statistics it will be interesting to analyze non Gaussianity in more depth, to see if we can have access to new kind of informations that will allows us to put even tighter constraints on the cosmological model parameters.

Finally, as we can see in Figure 2.18, while the results from CMB lensing with Planck and those from clustering, galaxy-galaxy lensing, and cosmic shear with DES are in good agreement with what obtained with Planck CMB (top and middle plots), there is still a $2-3\sigma$ tension with KiDS measurements that needs to be further investigated (bottom plot). In fact, using KIDS-450 data, Hildebrandt et al. (2016) found $S_8 \equiv \sigma_8 \sqrt{\Omega_m/0.3} = 0.745 \pm 0.039$, consistent with several previous cosmic shear analysis, but inconsistent within $2-3\sigma$ with Planck 2015 results. They found evidence of low-level shear B modes that suggests the presence of some unaccounted systematics in the

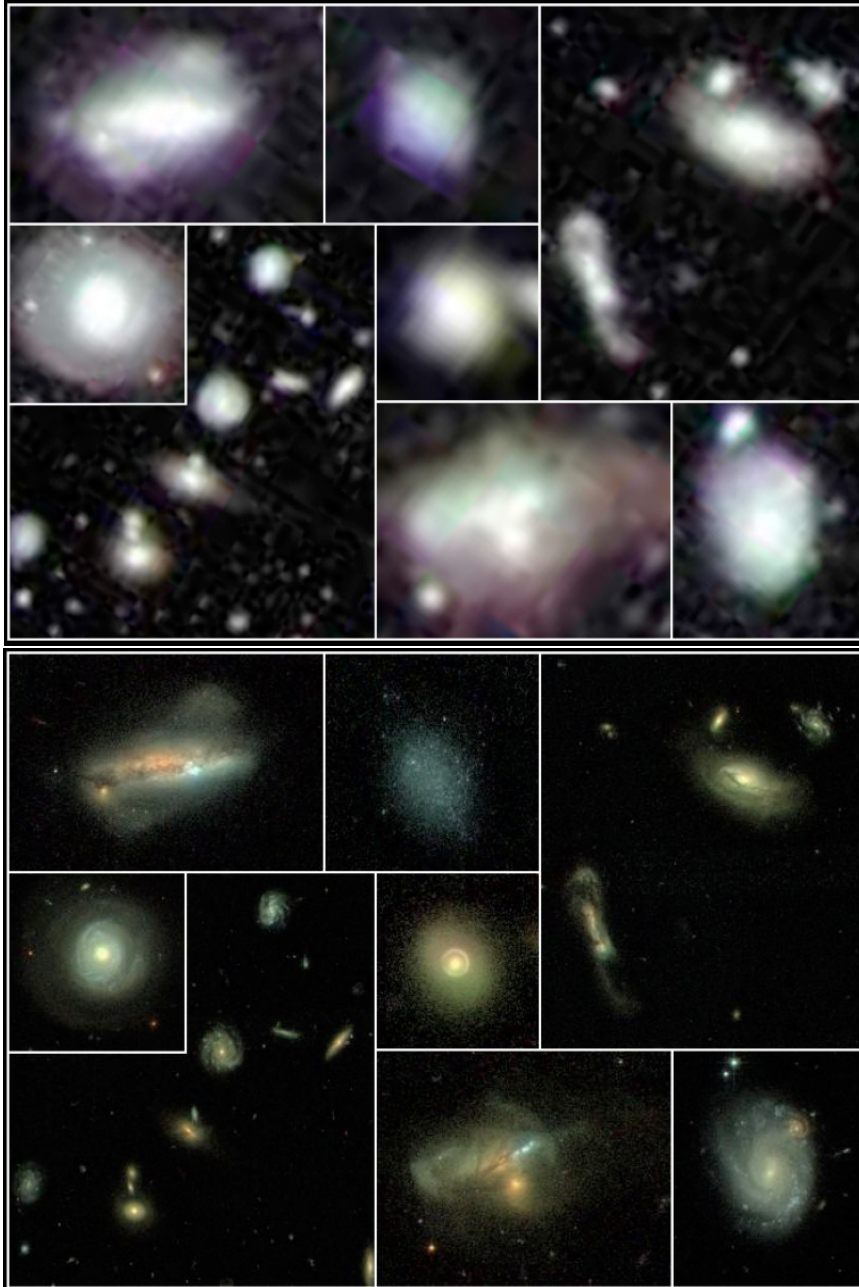


Figure 2.17 – *Low resolution images from ground based telescopes on the top, compared with high resolutions ones from space telescopes on the bottom (Heymans, C., Gravlens 2016).*

data that, however, do not affect the constraints on the cosmological parameters. In particular, the correction for B modes increases the tension with Planck results. Despite the increasingly accurate corrections for systematic errors, the nature of this tension is still unknown.

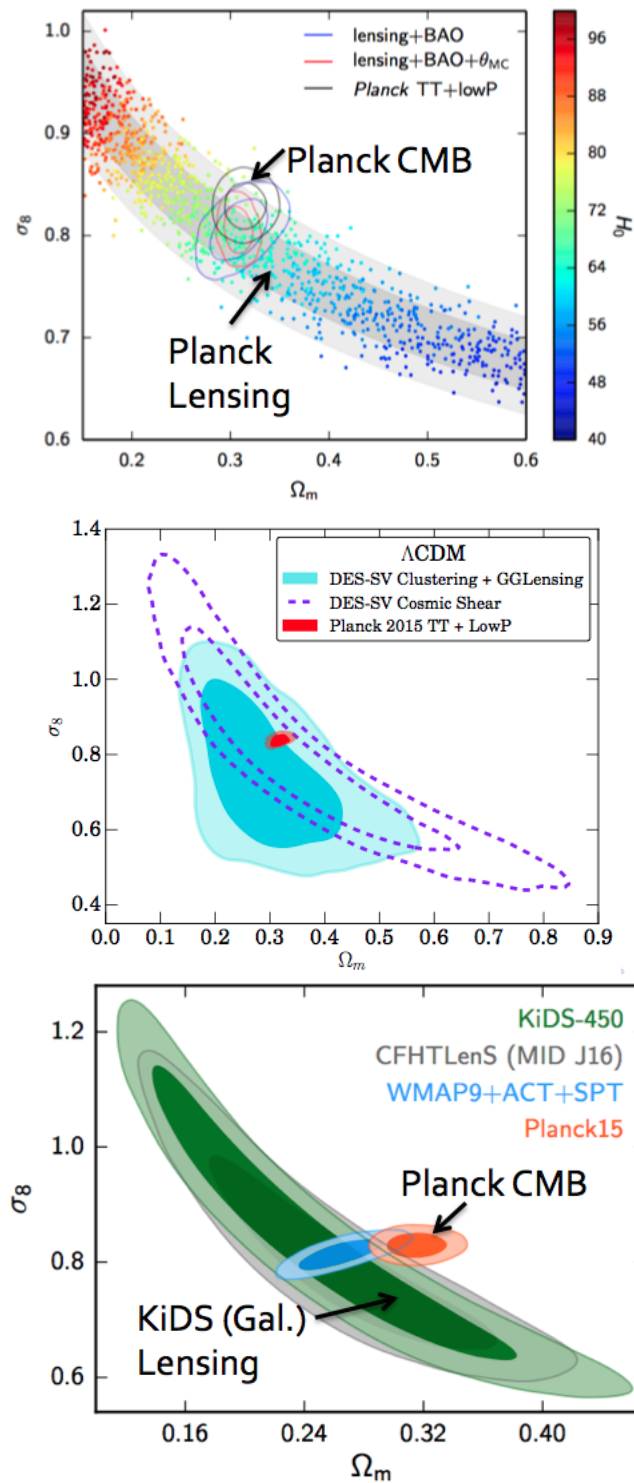


Figure 2.18 – *Planck CMB lensing and DES lensing are in agreement with Planck CMB, while there is a 2–3 σ tension with KiDS lensing (Sherwin and Kwan, Gravlens 2016).*

STATISTICAL ANALYSIS

In this chapter, I will explain the theory behind the statistical methods that I used in the weak lensing analysis that I performed. I will describe the bootstrap, the Markov Chain Monte Carlo (MCMC), and the aperture mass statistics, and how I applied them to my work in order to estimate the errors on the shear profiles, the errors on the fit parameters, and the lensing S/N ratio for individual and stacked clusters, respectively.

3.1 Bootstrap theory

The idea of bootstrap was first introduced by Efron (1979) and presented as a more general technique compared to Quenouille - Tukey jackknife method. The bootstrap allows us to make inference about a population characteristic, sampling from an approximating distribution. This makes it particularly useful when the theoretical distribution is unknown or when the sample size is insufficient to be fully representative of the population.

In order to understand how the bootstrap works, we first need to clarify the notation used in Efron (1979), and briefly introduce the theory of inferential statistics.

A sample (X_1, \dots, X_n) is a *probability sample* if the probability of each unit of the population of interest being selected is known, and greater than zero. Before the n units are drawn, the sample (X_1, \dots, X_n) is a random variable, formed by independent and identically distributed random variables (*i.i.d.*). After the selection, the sample won't be a random variable anymore, and it will contain the observed realization of the n units (x_1, \dots, x_n) , so that $(X_1 = x_1, \dots, X_n = x_n)$.

We generally denote by θ the population characteristic that we are interested in, and by T , the estimator that we use to make inference about θ . Before the sample is drawn, the statistic $T(X_1, \dots, X_n)$ is a random variable while after the selection, $T(x_1, \dots, x_n) = t$, where t is the value in the observed sample.

The probability that a random variable X will fall within a particular range of values is given by the integral of its *probability density function* (PDF) over that range. If we denote the PDF by f , for an absolutely continuous univariate distribution we'll have:

$$Pr(a \leq X \leq b) = \int_a^b f(x)dx \quad (3.1)$$

We can then denote the *cumulative distribution function* (CDF) by F . The CDF gives the probability that the random variable X will take a value less than, or equal to x . It can be expressed as the integral of the PDF:

$$F(x) = P(X \leq x) = \int_{-\infty}^x f(y)dy \quad (3.2)$$

When f is fully determined by a particular mathematical model with adjustable constants or parameters, the statistical methods based on this model are said *parametric*, while if no such mathematical model is used, the statistical analysis is *nonparametric*.

In case of nonparametric analysis, an important role is played by the *empirical distribution function* (EDF), denoted by \hat{F} , which estimates F . It is defined as the CDF that puts equal probability $1/n$ at each sample value x_i :

$$\hat{F}(x) = \frac{1}{n} \sum_{i=1}^n H(x - x_i) \quad (3.3)$$

where $H(n)$ is the Heaviside step function

$$H(n) = \begin{cases} 0, & n < 0 \\ 1, & n \geq 0 \end{cases}$$

At any fixed value of x

$$E\{\hat{F}(x)\} = F(x)$$

$$Var\{\hat{F}(x)\} = \frac{1}{n}F(x)(1 - F(x))$$

and this implies that $\hat{F}(x) \rightarrow F(x)$ with probability 1.

Given this notation and following Efron (1979), we want to estimate the sampling distribution of a random variable $R(X, F)$, with F unknown, on the basis of the observed sample x .

To apply the bootstrap method we need the \hat{F} and, keeping it fixed, we draw a sample of size n from it:

$$(X_1^* = x_1^*, \dots, X_n^* = x_n^*), \quad (X_1^*, \dots, X_n^*) \stackrel{i.i.d.}{\sim} \hat{F}$$

where the values of X^* are selected with replacements from the observed sample x (while with jackknife we would draw a sample of size $n - 1$ without replacements).

We can then approximate the sampling distribution of $R(X, F)$ by the *bootstrap distribution*:

$$R^* = R(X^*, \hat{F})$$

To calculate R^* , there are three methods: direct theoretical calculation, which is not always possible; Monte Carlo approximation; Taylor series expansion. We will focus on the second one.

To approximate the bootstrap distribution with a Monte Carlo approach, we can generate N different realization of X^* , always drawing random samples of size n from \hat{F} , and use the histogram of the values:

$$(R(x^{*1}, \hat{F}), \dots, R(x^{*N}, \hat{F}))$$

In Fig. 3.1 we can see a scheme that illustrates this process. In this case, B samples of size n are drawn with replacements from the original observed sample (x_1, \dots, x_n) and, for each of those, the statistic $T(x^{*i})$ is calculated, creating the bootstrap distribution (T_1, \dots, T_B) .

As we will see in the chapter dedicated to the weak lensing analysis, when applying this method to shear data, the original observed sample (x_1, \dots, x_n) will be the stacked cluster in a given richness bin, and the statistic $T(x^{*i}) = \Delta\Sigma(R)$ will be the shear estimator. For each richness bin, I will draw with replacements n clusters from the stack and repeated this process $B = 100$ times, calculating each time $\Delta\Sigma(R)$. In the end, I obtained the bootstrap distribution $(\Delta\Sigma(R)_1, \dots, \Delta\Sigma(R)_B)$ of the shear estimator. From that, I was able to calculate the covariance matrix using the value of $\Delta\Sigma(R)$ in each bootstrap realization, and the mean over all the bootstrap samples.

Graphical Illustration of Bootstrap

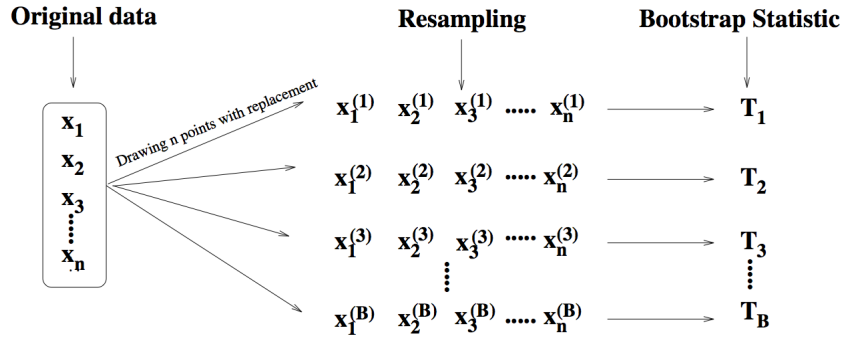


Figure 3.1 – The statistic T is calculated for each of the B samples of size n drawn with replacements from the original observed sample, creating the bootstrap distribution (Li, L., "Calculating the Confidence Intervals Using Bootstrap", 2004).

3.2 MCMC theory

Markov chain Monte Carlo methods (MCMC; Metropolis et al., 1953) allow us to efficiently sample from a posterior PDF, even when the assumed model has a large number of parameters and it's computationally expensive, by constructing a Markov chain that has the target posterior distribution as its equilibrium distribution.

To understand how these algorithms work, we first need to introduce the concept of Bayesian inference through *Bayes' Theorem*. Following (Gilks, Richardson & Spiegelhalter, 1996), given a model that depends on some parameters θ and a series of observed data D , we define:

- the prior probability* $P(\theta)$, the probability of model θ before D is observed.
- the posterior probability* $P(\theta|D)$, the probability of the model θ having observed D .
- the likelihood* $P(D|\theta)$, the probability of observing D given the model θ .
- the marginal likelihood* $P(D) = \int P(D|\theta)P(\theta)d\theta$, the probability of observing D for any model. It can be considered as a normalization constant.

Bayes' Theorem states that the probability of the model θ given the observed data D (the posterior) is proportional to the inherent likeliness of the model (the prior) and to the compatibility of the observed data with the model (likelihood):

$$P(\theta|D) = \frac{P(D|\theta)P(\theta)}{P(D)} = \frac{P(D|\theta)P(\theta)}{\int P(D|\theta)P(\theta)d\theta} \propto P(D|\theta)P(\theta) \quad (3.4)$$

Given the posterior probability, the expectation value of a function $f(\theta)$ will be

$$E[f(\theta)] = \int f(\theta)P(\theta|D)d\theta \propto \int f(\theta)P(D|\theta)P(\theta)d\theta \quad (3.5)$$

In a more general notation, we can consider a random variable X that comprises the model parameters θ and, through a *Monte Carlo integration*, we can approximate the expectation value of $f(X)$ by a sample mean, drawing n samples (X_1, \dots, X_n) from the posterior distribution $P(X|D)$

$$E[f(X)] \simeq \frac{1}{n} \sum_{t=1}^n f(X_t) \quad (3.6)$$

The samples can be drawn through a *Markov chain* that has the posterior distribution as its stationary distribution.

A Markov chain is defined as a sequence of random variables (X_0, X_1, X_2, \dots) such that, at each time $t \geq 0$, the next state X_{t+1} is sampled from $P(X_{t+1}|X_t)$. This means that the next state X_{t+1} depends only on the previous one and not on the rest of the chain. As t increases, the chain will converge to a stationary distribution $\phi(X)$ (that we want to coincide with the posterior $P(X|D)$) and after a *burn-in* period of, say m iterations, the points (X_{m+1}, \dots, X_n) will be dependent samples approximately from the stationary distribution $\phi(X)$:

$$E[f(X)] \simeq \frac{1}{n-m} \sum_{t=m+1}^n f(X_t) \quad (3.7)$$

In Fig. 3.2 we can visualise the chain convergence after the initial burn-in phase.

There are several MCMC sampling algorithms. In the next paragraphs, I will describe the *Metropolis-Hastings*, the most simple and used one, and an affine invariant sampling algorithm from Goodman & Weare (2010), the *Stretch Move*. We will also see how is possible to estimate the convergence rate of a chain using the *autocorrelation time*.

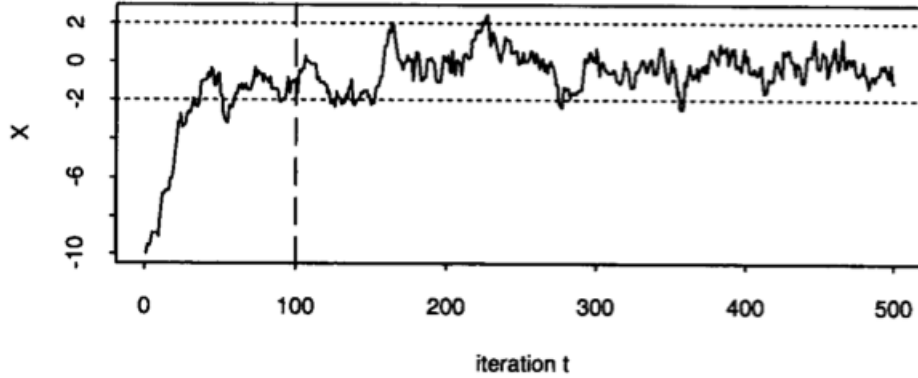


Figure 3.2 – After a certain number of iterations, the chain converges to its stationary distribution. The vertical line denotes the end of the burn-in phase (Gilks, Richardson & Spiegelhalter, 1996).

3.2.1 Metropolis-Hastings

The aim of every MCMC algorithm is to have the distribution of interest as the stationary distribution of the Markov chain. In our case we want that to be the posterior probability $P(X|D)$.

To see how we can construct such a chain, I first describe the most simple and widely used algorithm, the Metropolis-Hastings, first proposed by Metropolis et al. (1953) and then generalized by Hastings (1970).

At each step t , a candidate point Y is chosen for the next state X_{t+1} , sampling it from a *proposal* distribution $Q(.|X_t)$ that depends on the previous state X_t . The probability that Y is accepted as the next state is given by:

$$\alpha(X_t, Y) = \min \left(1, \frac{P(Y|D)Q(X_t|Y)}{P(X_t|D)Q(Y|X_t)} \right) \quad (3.8)$$

We then sample a random variable U from a uniform distribution $(0, 1)$, and compare it with α to decide if accept the proposed state:

$$\begin{aligned} \text{if } U \leq \alpha(X_t, Y) &\rightarrow X_{t+1} = Y \\ \text{if } U > \alpha(X_t, Y) &\rightarrow X_{t+1} = X_t \end{aligned}$$

This means that if Y is not accepted the chain doesn't move and the next state will be again X_t .

The chain will converge to its stationary distribution $P(X|D)$ regardless of the form of the proposal distribution $Q(.|X)$ but the rate of convergence

will depend on the relationship between the two distributions. Usually, a preliminary analysis is useful to choose the right proposal distribution which, for computational efficiency, should also be easy to sample and evaluate.

3.2.2 Stretch Move

The Stretch Move from Goodman & Weare (2010) is an algorithm which is based on the *affine invariance* property of an ensemble MCMC samplers.

An affine transformation is an invertible mapping $\mathbb{R}^n \rightarrow \mathbb{R}^n$ of the form $y = Ax + b$. If X has probability density $P(x)$, then $Y = AX + b$ has density:

$$P(Y) = P(y) = P(Ax + b) \propto P(x) \quad (3.10)$$

This property is particularly useful in case of high anisotropic distributions, for example the skewed probability density on \mathbb{R}^2 , shown in Fig. 3.3:

$$P(x) \propto \exp\left(\frac{-(x_1 - x_2)^2}{2\epsilon} - \frac{(x_1 + x_2)^2}{2}\right)$$

This probability would be difficult to sample with the algorithm described above because we would be forced to make perturbations of the same order in the two directions, and the chain would converge slowly. However, if we apply an affine invariant transformation we can scale the probability density in a form which is easier to sample, and that is independent of ϵ :

$$P(y) \propto \exp\left(\frac{-(y_1^2 - y_2^2)}{2}\right)$$

This means that the method is independent of the aspect ratio of the distribution.

Now to explain how the algorithm works, we can define an ensemble, and the complementary one, of K random variables, that we call *walkers*:

$$\begin{aligned} S &= \{X_k\} \\ S_{[k]} &= \{X_j, \forall j \neq k\} \end{aligned}$$

For every step t of the chain, one after the other every walker of the ensemble is updated using the position of the $k - 1$ walkers in the complementary ensemble:

$$X_{k,t} \rightarrow X_{k,t+1} \quad k = 1, \dots, K$$

To choose the proposed step Y for $X_{k,t}$, a walker X_j is drawn from $S_{[k]}$ and a random variable Z is drawn from the distribution:

$$g(z) \propto \begin{cases} 1/\sqrt{z} & \text{if } z \in [\frac{1}{a}, a] \\ 0 & \text{otherwise} \end{cases} \quad (3.12)$$

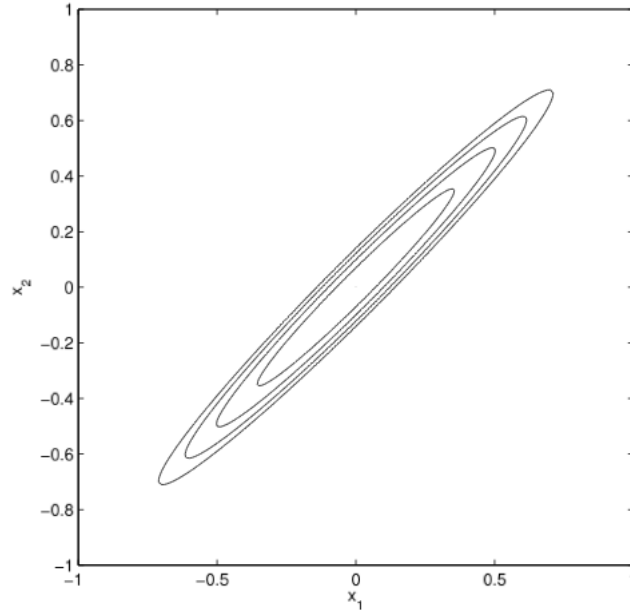


Figure 3.3 – *Example of a skewed probability density on \mathbb{R}^2 that would be difficult to sample using the Metropolis-Hastings algorithm (Goodman & Weare, 2010).*

where $a > 1$ is an adjustable parameter (that usually is set to $a = 2$).

Then the proposed next state Y is defined as:

$$Y = X_j + Z (X_{k,t} - X_j)$$

and it will be accepted with probability:

$$\alpha(X_{k,t}, Y) = \min \left(1, Z^{N-1} \frac{P(Y|D)}{P(X_{k,t}|D)} \right) \quad (3.13)$$

Then, as for the previous method, we sample a random variable U from a uniform distribution $(0, 1)$ and compare it with $\alpha(X_{k,t}, Y)$:

$$\begin{aligned} \text{if } U \leq \alpha(X_{k,t}, Y) &\rightarrow X_{k,t+1} = Y \\ \text{if } U > \alpha(X_{k,t}, Y) &\rightarrow X_{k,t+1} = X_{k,t} \end{aligned}$$

A visual representation of the Stretch Move is shown in Fig. 3.4.

This process needs to be repeated for every walker in the ensemble, one at a time, at each step t , but a parallel implementation is also possible to speed up the process.

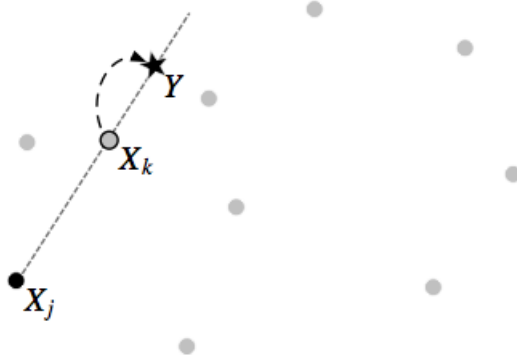


Figure 3.4 – Representation of a step of the Stretch Move. X_k is the current state, Y is the proposed next state and X_j is the current state of a randomly selected walker in the complementary ensemble. The grey dots are the other walkers in the complementary ensemble that don't take part in the move (Goodman & Weare, 2010).

In the *parallel* Stretch Move, the full ensemble S is divided in two subsets:

$$S^{(0)} = \{X_k, \forall k = 1, \dots, K/2\}$$

$$S^{(1)} = \{X_k, \forall k = K/2 + 1, \dots, K\}$$

All the walkers in $S^{(0)}$ are updated simultaneously drawing from $S^{(1)}$, and applying the normal Stretch Move. Then all the walkers in $S^{(1)}$ are updated simultaneously using the new values at step $t + 1$ of $S^{(0)}$.

In order to run MCMC for the weak lensing analysis, I used *emcee* (Foreman-Mackey et al., 2013), a Python implementation of the parallel Stretch Move by Goodman & Weare (2010). I used an ensemble of 100 walkers, a chain length of 1000 steps and a burn-in of 100 steps leading to a total of 90000 points in the parameters space

3.2.3 Autocorrelation time

The autocorrelation time can be used to estimate the number of steps required in the chain so that the samples drawn from the target posterior probability will be independent. It can be written as:

$$\tau_f = 1 + 2 \sum_{T=1}^{\infty} \frac{C_f(T)}{C_f(0)} \quad (3.16)$$

where $C_f(T)$ is the auto covariance function of a time series $X(t)$ and measures the covariance between samples at a time lag T :

$$C_f(T) = \lim_{t \rightarrow \infty} \text{cov} [f(X(t+T)), f(X(t))]$$

The shorter the autocorrelation time is, the fewer computations of the posterior will be needed to produce independent samples from the chain. As shown in Goodman & Weare (2010), the Stretch Move has a much shorter autocorrelation time, compared for example to the Metropolis-Hastings algorithm. Also, for the parallel version of the Stretch Move the autocorrelation time is the same as in the non parallel version, making it extremely powerful in terms of computational speed.

3.3 Aperture mass statistics

The aperture mass statistics (M_{ap}) is a statistical method for the detection of dark matter concentrations that allows us to generate signal-to-noise ratio maps from the ellipticities of faint galaxies. It was introduced by Schneider (1996), and it can be written as a filtered integral of the tangential shear γ_t :

$$M_{ap}(\boldsymbol{\theta}_c) = \int d^2\varphi \gamma_t(\boldsymbol{\varphi}; \boldsymbol{\theta}_c) Q(\varphi) \quad (3.17)$$

It can be interpreted as the filtered amount of the tangential shear around a point $\boldsymbol{\theta}_c$ on the sky, where $\gamma_t(\boldsymbol{\varphi}; \boldsymbol{\theta}_c)$ is the tangential shear at position $\boldsymbol{\varphi}$ relative to $\boldsymbol{\theta}_c$, and Q is a radially symmetric spatial filter function.

The signal-to-noise ratio of M_{ap} can be calculated through the *S-statistics* (Schirmer et al., 2006):

$$S(\theta_{out}; \boldsymbol{\theta}_c) = \sqrt{\frac{n}{\pi\sigma_\epsilon^2}} \frac{\int_c^\theta d^2\vartheta \gamma_t(\vartheta; \boldsymbol{\theta}_c) Q(\vartheta)}{\sqrt{\int_c^\theta d^2\vartheta Q^2(\vartheta)}} \quad (3.18)$$

where θ_{out} is the aperture radius, and ϑ is the distance inside this aperture from its centre $\boldsymbol{\theta}_c$.

To apply this formula to data, we need its discrete. We replace the tangential shear γ_t with the tangential ellipticity ϵ_t , which can be considered an unbiased estimator of γ_t in the weak lensing regime. So we get:

$$S(\boldsymbol{\theta}_c; \theta_{out}) = \frac{\sqrt{2} \sum_i \epsilon_{t,i} Q_i(x)}{\sigma_\epsilon \sqrt{\sum_i Q_i^2(x)}} \quad (3.19)$$

where $\epsilon_{t,i}$ is the tangential component of ϵ_i of the galaxy at $\boldsymbol{\theta}_i$:

$$\epsilon_t = -[\epsilon_1 \cos(2\phi) + \epsilon_2 \sin(2\phi)], \quad (3.20)$$

and x is the projected angular separation ϑ on the sky from the aperture centre $\boldsymbol{\theta}_c$, in units of the aperture radius θ_{out} :

$$x := \vartheta/\theta_{out} = |\boldsymbol{\theta}_i - \boldsymbol{\theta}_c|/\theta_{out} \quad (3.21)$$

The filter function Q that maximizes S for a given density profile of the lens can be derived using a variational principle (Schirmer et al., 2003), or the Cauchy-Schwarz inequality (Schneider, 1996). Schneider (1996) derived it for an isothermal sphere, while (Schirmer et al., 2006) constructed it considering an NFW density profile and, given its mathematical complexity, they introduced an approximating filter function that produces similarly good results:

$$Q(x) = \frac{x_c \tanh(x/x_c)}{x(1 + e^{a+bx} + e^{c+dx})} \quad (3.22)$$

with $a = 6$, $b = -150$, -47 , $d = 50$ and x_c is a dimensionless parameter that controls the sharpness of the filter (Du & Fan, 2014).

The aperture radius θ_{out} needs to be varied to find the value that maximizes S , then the position with the highest S value is chosen as the centre of the halo.

For the CFHTLS and NGVS data, I constructed a grid of side 1 Mpc for each cluster, centered on the *RedGold* optical centers, with a spacing of 0.001 deg . For the filter parameters I used $x_c = 0.15$ and $\theta_{out} = 6$ $arcmin$.

THE WEAK LENSING ANALYSIS OF CFHTLS AND NGVS GALAXY CLUSTERS

4.1 Aim of this work

The goal of my thesis work was to infer cluster masses using weak lensing measurements from the CFHTLS W1 and NVSG surveys. The cluster sample that I used was obtained with the optical cluster finder RedGOLD. In order to increase the shear signal, I stacked galaxy clusters according to their RedGOLD optical richness λ . In this way, I was able to calibrate the accuracy of RedGOLD richness as a mass-proxy, and to infer the mass-richness relation. I then compared lensing masses with X-ray masses, luminosity, and temperature.

In this chapter, I will describe:

- the observations
- the shear catalogs
- the photometric redshift catalog
- the optical and X-ray cluster catalogs
- how the RedGOLD algorithm works and how its richness parameter is defined
- how I calculated the shear profiles and the different models that I used to fit them
- the tests that I performed on my lensing analysis

- my results and the comparison with similar works in literature.

Throughout this work I assumed a standard Λ CDM model, with $\Omega_m = 0.3$, $\Omega_\Lambda = 0.7$ and $H_0 = 70 \text{ km s}^{-1} \text{ Mpc}^{-1}$.

Magnitudes are given in the AB system (Oke & Gunn, 1983; Sirianni et al., 2005).

4.2 Data

For this analysis, I used the shear and photometric data from the Canada-France-Hawaii Telescope Legacy Survey (CFHT-LS; Gwyn, 2012) Wide 1 (W1) field and from the Next Generation Virgo Cluster Survey (NGVS; Ferrarese et al., 2012). In this section, I will describe the two surveys, and the data reduction performed to obtain galaxy shape measurements and photometric redshifts.

4.2.1 CFHTLenS and NGVSLenS

The CFHT-LS and NGVS are multi-band optical surveys obtained with the CFHT optical multi-chip MegaPrime instrument (MegaCam¹; Boulade et al., 2003). The first consists of 171 pointings covering $\sim 154 \text{ deg}^2$, and the latter of 117 pointings covering 104 deg^2 , centered on the Virgo cluster.

The CFHT-LS has a complete coverage in the five bands $u^*g'r'i'z'$. All images used in this work were obtained under optimal seeing conditions with a seeing $< 0.8''$ in the primary lensing band i' (Erben et al., 2013). The 5σ point source limiting magnitudes in a $2.0''$ aperture in the five $u^*g'r'i'z'$ filters are ~ 25.2 , ~ 25.6 , ~ 24.9 , ~ 24.5 , ~ 23.5 mag, respectively (Erben et al., 2013).

The entire NGVS area was observed in the four bands $u^*g'i'z'$. 23 of the 117 pointings ($\sim 20 \text{ deg}^2$) are also covered in the deep r' -band (~ 23.6 mag). Again, the best seeing conditions were reserved to the i' -band which covers the entire field with a seeing $< 0.6''$. The 5σ point source limiting magnitudes in a $2.0''$ aperture in the five $u^*g'r'i'z'$ filters are ~ 25.6 , ~ 25.7 , ~ 24.7 , ~ 24.4 , ~ 23.6 mag, respectively (Raichoor et al., 2014).

Both the CFHTLenS and NGVSLenS data reductions that I used for this work were performed by Raichoor et al. (2014). They used an improved version of the THELI pipeline (Erben et al., 2005, 2009, 2013; Raichoor et al., 2014) on the preprocessed *Elixir*² data, available at the Canadian

¹<http://www.cfht.hawaii.edu/Instruments/Imaging/Megacam/>

²<http://www.cfht.hawaii.edu/Instruments/Elixir/>

Astronomical Data center (CADC³). The final products are co-added science images accompanied by weights, flag maps, sum frames, image masks and sky-subtracted individual chips that are then used as inputs of the shear and photometric pipelines. A detailed description of the THELI processing pipeline and a full systematic error analysis can be found in Erben et al. (2013) and Heymans et al. (2012).

The modification of the standard pipeline by Raichoor et al. (2014) consists in performing the zero-point calibration using the SDSS data, taking advantage of its internal photometric stability. The SDSS covers the entire NGVS field and 62 out of 72 pointings of the CFHT-LS W1 field ($\sim 60deg^2$). Raichoor et al. (2014) constructed the photometric catalogs as described in Hildebrandt et al. (2012), adopting a *global* PSF homogenization to measure unbiased colors. Multicolor catalogs were obtained from PSF-homogenized images using SExtractor (Bertin & Arnouts, 1996) in dual-image mode, with the un-convolved i' -band single-exposure as the detection image.

Galaxy shape measurements for the shear analysis were obtained applying the Bayesian *lensfit* algorithm of Miller et al. (2013) to single-exposure i' -band images with accurate PSF modeling. The code estimates the complex ellipticity of each galaxy:

$$\epsilon = \epsilon_1 + i\epsilon_2 \quad (4.1)$$

performing a fit to a PSF-convolved disc plus bulge galaxy model. The ellipticity components, ϵ_1 and ϵ_2 , are calculated from the mean likelihood of the model posterior probability, marginalized over model nuisance parameters of galaxy position, size, brightness and bulge fraction. The algorithm assigns a weight to each galaxy:

$$w_{\text{lens}} \propto (\sigma_e^2 + \sigma_{\text{pop}}^2)^{-1} \quad (4.2)$$

where σ_e^2 is the variance of the ellipticity likelihood surface and σ_{pop}^2 is the variance of the ellipticity distribution of the galaxy population.

The ellipticity estimated by *lensfit* is related to the true ellipticity (i.e. the sum of the shear and of the galaxy intrinsic ellipticity) by:

$$\epsilon_{\text{lens}} = (1 + m)[\gamma + \epsilon_{\text{int}}] + c \quad (4.3)$$

where m and c are calibration corrections. m is a multiplicative bias, calculated using simulated images, that is inversely proportional to the size and detection signal-to-noise ratio of the galaxy. c is an additive bias, estimated empirically from the data, that increases for the smallest brightest objects. The multiplicative bias needs to be applied as a weighted ensemble average correction, to avoid instabilities in case the term $(1 + m)$ tends to zero,

³ <http://www4.cadc-ccda.hia-ihp.nrc-cnrc.gc.ca/cadc/>

and to remove any correlation between the calibration correction and the intrinsic ellipticity (Miller et al., 2013). On a weighted average $\langle 1 + m \rangle$, this term corresponds to a 6% correction (Heymans et al., 2012). The additive bias is found to be significantly non-zero only for the second component of the ellipticity, ϵ_2 , and it's of order 10^{-4} . This correction can be applied on a galaxy-by-galaxy basis, since the subtraction of c is stable. The nature of this additive bias in the ϵ_2 component is not clear but could likely be attributed to the data processing (Heymans et al., 2012).

4.2.2 Photometric redshifts

The photometric redshifts that I used in this work were estimated by Raichoor et al. (2014), for the $\sim 60 \text{ deg}^2$ of the CFHTLenS covered by the SDSS and of the entire NGVSLenS. They were obtained using the Bayesian softwares *LePhare* (Arnouts et al., 1999; Arnouts et al., 2002; Ilbert et al., 2006) and BPZ (Benítez, 2000; Benítez et al., 2004; Coe et al., 2006). Raichoor et al. (2014) used the re-calibrated SED template set of Capak et al. (2004).

Both *LePhare* and BPZ are designed for high redshift studies, giving biased or low quality photo- z 's estimations for objects with $i' < 20$ mag which represent a non-negligible fraction of both samples. In order to improve the performance at low redshift, Hildebrandt et al. (2012) used an *ad hoc* modified prior for the CFHTLenS data. Raichoor et al. (2014) adopted a more systematic solution for the reprocessed CFHTLenS W1 field and for the NGVSLenS, building a new prior calibrated on observed data, using the SDSS Galaxy Main Sample spectroscopic survey (York et al., 2000; Strauss et al., 2002; Ahn et al., 2014) to include bright sources.

In order to analyze the accuracy of the photometric redshift estimates, Raichoor et al. (2014) used several spectroscopic surveys covering the CFHTLenS and NGVSLenS: the SDSS Galaxy Main Sample, two spectroscopic programs at the Multiple Mirror Telescope (MMT; Peng et al. 2016, in preparation) and at the Anglo-Australian Telescope (AAT; Zhang et al., 2015, 2016, in preparation), the Virgo Dwarf Globular Cluster Survey (Guhathakurta et al. 2016, in preparation), the DEEP2 Galaxy Redshift Survey over the Extended Groth Strip (DEEP2/EGS; Davis et al., 2003; Newman et al., 2013), the VIMOS Public Extragalactic Redshift Survey (VIPERS; Guzzo et al., 2014), and the F02 and F22 fields of the VIMOS VLT Deep Survey (VVDS; Le Fèvre et al., 2005, 2013).

As shown in Raichoor et al. (2014), when using all five filters, for $z_{\text{phot}} < 1$ and $i' < 23$ mag, they found a bias $\Delta z = \frac{z_{\text{phot}} - z_{\text{spec}}}{1 + z_{\text{spec}}} < 0.02$, scatter values in the range $0.02 < \sigma < 0.05$ and $< 5\%$ of outliers. When using four bands the quality of the measurements slightly decreases. In the range $0.3 < z_{\text{phot}} < 0.8$

and $i' > 21$ mag we obtain $-0.05 < bias < 0.02$, a scatter $\sigma \sim 0.06$ and an outliers rate of 10 – 15%, due to the lack of the r' -band to sample the 4000 Å break.

For my analysis, I used the photometric redshifts derived with BPZ, corresponding to z_{best} , the peak of the redshift posterior distribution (hereafter, z_{phot}).

4.3 Cluster catalogs

In this section, I will describe the optical and X-ray cluster catalogs, covering the CFHT-LS W1 and NGVS fields, that I used for my analysis. The optical catalogs were obtained using the RedGOLD cluster finding algorithm of Licitra et al. (2016a,b). The output from the code, for each cluster, are the center coordinates, the redshift, and the richness. In the following, I will explain how the algorithm works and how the richness parameter is defined. The X-ray catalogs were obtained by Gozaliasl et al. (2014) and Mehrtens et al. (2012).

4.3.1 The RedGOLD Optical Cluster Catalogs

4.3.1.1 RedGOLD algorithm

The RedGOLD algorithm (Licitra et al., 2016a,b) is based on a modified red-sequence technique, and it searches for passive and bright early-type galaxies (ETGs) overdensities. This choice relies on the observational evidence that the inner regions of galaxy clusters host a large population of ETGs, which are tightly distributed on a red-sequence on the color-magnitude diagram.

In order to distinguish between ETGs and dusty red star-forming galaxies, and to avoid contamination from the latter, the algorithm selects galaxies on the red sequence both in the rest-frame ($U - B$) and ($B - V$). It uses red sequence rest-frame zero point, slope and scatter from Mei et al. (2009), and with a ETG spectral classification from *LePhare*. In order to select an overdensity detection as a cluster candidate, the algorithm also imposes that the ETGs radial distribution follows an NFW (Navarro, Frenk & White, 1996) surface density profile.

RedGOLD centers the cluster detection on the ETG with the highest number of red companions, weighted on luminosity. This is motivated by the fact that the brightest cluster members lying near the X-ray centroid are better tracers of the cluster centers compared to using only the BCG (George et al., 2012). The redshift of the cluster is the median photometric redshift of the passive ETGs.

Each detection is characterized by two parameters, the significance σ_{det} and the richness λ , which quantifies the number of bright red ETGs inside the cluster, using an iterative algorithm.

RedGOLD is optimized to produce cluster catalogs with high completeness and purity. In Licitra et al. (2016a, ab), the *completeness* is defined as the ratio between detected structures corresponding to true clusters and the total number of true clusters, and the *purity* is defined as the number of

detections that correspond to real structures to the total number of detected objects. A *true cluster* is assumed to be a dark matter halo more massive than $10^{14}M_{\odot}$ (Evrard et al., 2008).

Details on the method and the performance of the algorithm when applied to numerical simulations can be found in Licitra et al. (2016a).

4.3.1.2 Richness definition

Rykoff et al. (2014) proposed redMaPPer, an optical cluster finder based on the red-sequence technique, and applied it to the Sloan Digital Sky Survey (SDSS; York et al., 2000). Their richness is computed using optimal filtering, as a sum of probabilities and depends on three filters based on colours, positions and luminosity, that consist of a linear red-sequence model in the colour-magnitude space, a projected NFW density profile and the Schechter (1976) luminosity function, respectively (Rozo et al., 2009a; Rozo & Rykoff, 2014; Rykoff et al., 2012, 2014, 2016).

The redMaPPer richness is defined as $\lambda_{\text{RM}} = \sum p_{\text{mem}}\theta_{\text{L}}\theta_{\text{R}}$, where p_{mem} is the probability that each galaxy in the vicinity of the cluster is a red-sequence member and $\theta_{\text{L}}, \theta_{\text{R}}$ are weights that depend on luminosity and radius. In this calculation, only galaxies brighter than $0.2L_*$ and within a scale radius R_{λ} are considered. The radius is richness dependent and it scales as $R_{\lambda} = 1.0(\lambda/100)^{0.2}h^{-1}Mpc$.

The RedGOLD richness is a simplified version of λ_{RM} . Licitra et al. (2016a,b) constrained the radial distribution of the red-sequence galaxies with an NFW profile and applied the same luminosity cut and the same scaling of the radius with richness as in Rykoff et al. (2014) but didn't apply a luminosity filter. Unlike the redMaPPer definition, RedGOLD richness is not a sum of probabilities. Those choices were made to minimize the scatter in the mass-richness relation.

In order to estimate the richness, RedGOLD divides the entire galaxy sample in overlapping redshift slices. Each slice is then divided in overlapping circular cells, with a fixed comoving radius of 500 *kpc*. The algorithm counts N_{gal} , the number of red ETGs inside each cell, brighter than $0.2L_*$, building the galaxy count distribution in each redshift slice. The background contribution is defined as N_{bkg} , the mode of this distribution, with standard deviation σ_{bkg} . The detection significance is then defined as $\sigma_{\text{det}} = (N_{\text{gal}} - N_{\text{bkg}})/\sigma_{\text{bkg}}$. Overdensities larger than $N_{\text{bkg}} + \sigma_{\text{det}} \times \sigma_{\text{bkg}}$ are selected as preliminary detections.

The algorithm then estimates the richness λ , counting N_{gal} inside a scale radius, initially set to 1 *Mpc*. The radius is iteratively scaled with richness as in Rykoff et al. (2014), until the difference in richness between two successive

iterations is less than N_{bkg} .

As shown in Licitra et al. (2016a), the difference $\frac{\lambda_{\text{RM}} - \lambda}{\lambda}$ is only of 5–15%, for redshifts $z < 0.3$, while it increases to 40–60% at $0.4 < z < 0.5$, where the redMaPPer richness is systematically higher than that estimated by RedGOLD. This difference might be due to the different depths of the CFHTLenS and SDSS surveys.

In Section 4.6, I will use this similarity to compare my results, obtained using RedGOLD richness as a mass proxy, with others in literature based on the redMaPPer cluster sample.

4.3.1.3 CFHT-LS W1 and NGVS cluster catalogs

For this work, I used the CFHT-LS W1 and NGVS cluster catalogs from Licitra et al. (2016a) and Licitra et al. (2016b), respectively. Those catalogs were obtained calibrating the σ_{det} and λ parameters to maximize the completeness and purity of clusters more massive than $\approx 10^{14} M_{\odot}$, the mass limit for which $\sim 90\%$ of dark matter halos at $z_{\text{phot}} < 1.5$ are virialized (Evrard et al., 2008).

Licitra et al. (2016a) demonstrated that when they considered only detections with $\sigma_{\text{det}} \geq 4$ and $\lambda \geq 10$ at $z_{\text{phot}} \leq 0.6$, and $\sigma_{\text{det}} \geq 4.5$ and $\lambda \geq 10$ at $z_{\text{phot}} \lesssim 1$, they obtained catalogs with a completeness of $\sim 100\%$ and $\sim 70\%$, respectively, and a purity of $\sim 80\%$.

Both in the CFHT-LS W1 and the NGVS, areas around bright stars and nearby galaxies were masked. Licitra et al. (2016a) found that in only $\sim 2\%$ of clusters (low richness structures at high redshift) $> 10\%$ of their bright potential members are masked. Therefore, the richness estimates are not significantly affected by masking.

For the NGVS, as explained above, the five band coverage was limited to only the $\sim 30\%$ of the survey. The lack of the r' -band in the remaining pointings, causes higher uncertainties on the determination of photometric redshifts for sources at $0.3 < z_{\text{phot}} < 0.8$ but the global accuracy on the photometric redshifts remains high even for this sample, as shown in Raichoor et al. (2014). Since there are some fields in which the quality of the r' -band is lower because of the lower depth and the lack of coverage of the intra-CCD regions, this makes also more difficult the detection of the less massive structures at intermediate and high redshifts and the determination of the clusters center and richness.

In order to quantify this effect in the richness estimation, Licitra et al. (2016b) compared the values recovered with a full band coverage λ_{r} with the ones obtained without the r' -band λ_{wr} , and measured $\Delta\lambda/\lambda_{\text{r}} \equiv (\lambda_{\text{r}} - \lambda_{\text{wr}})/\lambda_{\text{r}}$, in different redshift bins. Median values of $\Delta\lambda/\lambda_{\text{r}}$ and their standard

deviations are listed in Tab. 2 of Licitra et al. (2016b). At $z_{\text{phot}} < 0.5$ and $z_{\text{phot}} > 0.8$, the two estimates are in good agreement, with $\Delta\lambda/\lambda_r < 10\%$. This is due to the fact that the $(g - z)$ and $(i - z)$ colors straddle the 4000 Å break at $z_{\text{phot}} < 0.5$ and $z_{\text{phot}} > 0.8$, respectively. At $0.5 < z_{\text{phot}} < 0.6$, λ_{wr} is systematically underestimated by $\sim 40\%$ on average and, at $0.6 < z_{\text{phot}} < 0.8$, it's systematically overestimated by $\sim 20\%$ on average. The first systematic is due to the use of the $(g - z)$ color, that changes less steeply with redshift and has larger photometric errors, compared with $(r - i)$ and $(i - z)$ colors. The latter is caused by the use of the $(i - z)$ color only, without the additional cut in the $(r - z)$ or $(r - i)$ colors that allows us to reduce the contamination of dusty red galaxies on the red sequence (Licitra et al., 2016b).

For these reasons, for the NGVS, Licitra et al. (2016b) built two separate catalogs: the first for the $\sim 20 \text{ deg}^2$ covered by the r' -band and the second for the entire NGVS using only four bandpasses. In this last catalog, I corrected the λ_{wr} estimations using the average shifts given in Tab. 2 of Licitra et al. (2016b). As I will discuss later, since for this analysis I'm only selecting clusters at $z_{\text{phot}} < 0.5$, the level of completeness and purity remains the same, using four bands, as using the five bands catalog. Hereafter, I will refer to the NGVS catalog obtained on the area covered by the five bandpasses as NGVS5 and the catalog obtained with four bandpasses, after the λ correction, as NGVS4.

The CFHT-LS W1 published catalog includes 652 detections in an area of $\sim 60 \text{ deg}^2$. The NGVS published catalogs include 279 and 1505 detections, in the $\sim 20 \text{ deg}^2$ with the five band coverage and in the rest of the survey, respectively.

Hereafter, I will refer to these catalogs, optimized with the thresholds in richness and significance described above, as Licitra's *published* catalogs. The Licitra et al. (2016a,b) catalogs, without any threshold applied, will be referred as *complete* catalogs.

4.3.1.4 Weak lensing subsample selection

In order to optimize the weak lensing analysis, I selected a cluster subsample from the *published* catalogs.

The source galaxies in the complete sample have a mean redshift $z_{\text{phot}} \sim 1$. For this mean source redshift, the peak in the lensing efficiency is found at $z_{\text{phot}} \sim 0.3 - 0.4$ (Hamana et al., 2004), as can be seen in Figure 4.1. The lensing efficiency as been calculated as:

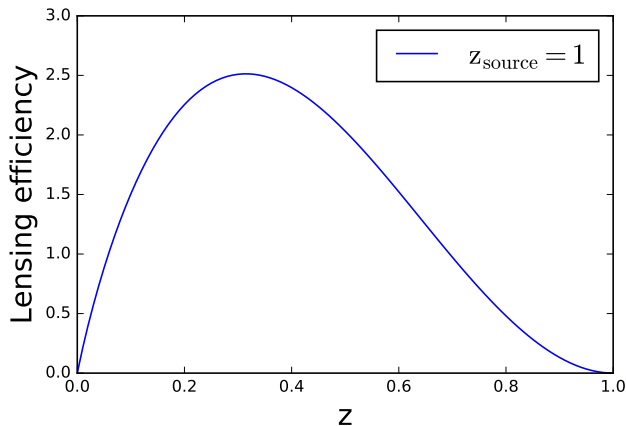


Figure 4.1 – *Lensing efficiency as a function of cluster redshift, for sources at $z = 1$. The peak is found at $\sim z = 0.3$*

$$g(z_{\text{lens}}) = \int_{D_M(z_{\text{lens}})}^{D_M(z_{\text{source}})} P(z) \left(1 - \frac{D_M(z_{\text{lens}})}{D_M(z)} \right) dD_M(z) \quad (4.4)$$

where D_M is the transverse comoving distance, and $P(z)$ is the distribution of sources, in this case assumed for simplicity as a step function equal to 1 if $z < z_{\text{source}}$, and zero otherwise.

Considering this, and that shear measurements from ground based telescopes are reliable for clusters with redshifts $0.2 < z_{\text{phot}} < 0.5$ (Kasliwal et al., 2008), I decided to select detections only in this redshift range.

I also discarded clusters with richness $\lambda < 10$ and $\lambda > 70$. In fact, as shown in Licitra et al. (2016a) at richness $\lambda < 10$, the purity decreases for a given significance threshold. For the significance threshold of $\sigma_{\text{det}} > 4$, applied to the *published* catalogs, $\lambda < 10$ implies a contamination of false detections larger than $\sim 20\%$. On the other hand, for $\lambda > 70$, there are very few detections and not enough clusters to obtain an average profile from a statistically significant sample.

The final selection for the weak lensing analysis includes 1323 clusters. Their richness and redshift distributions are shown in Fig. 4.2. Hereafter, I will refer to this cluster subsample, specifically selected from the *published* catalogs for the weak lensing analysis, as *selected* catalogs.

4.3.2 X-ray cluster catalog

In order to compare the weak lensing estimated masses with X-ray masses, temperatures and luminosities, I used Gozaliasl et al. (2014), Mehrtens et al.

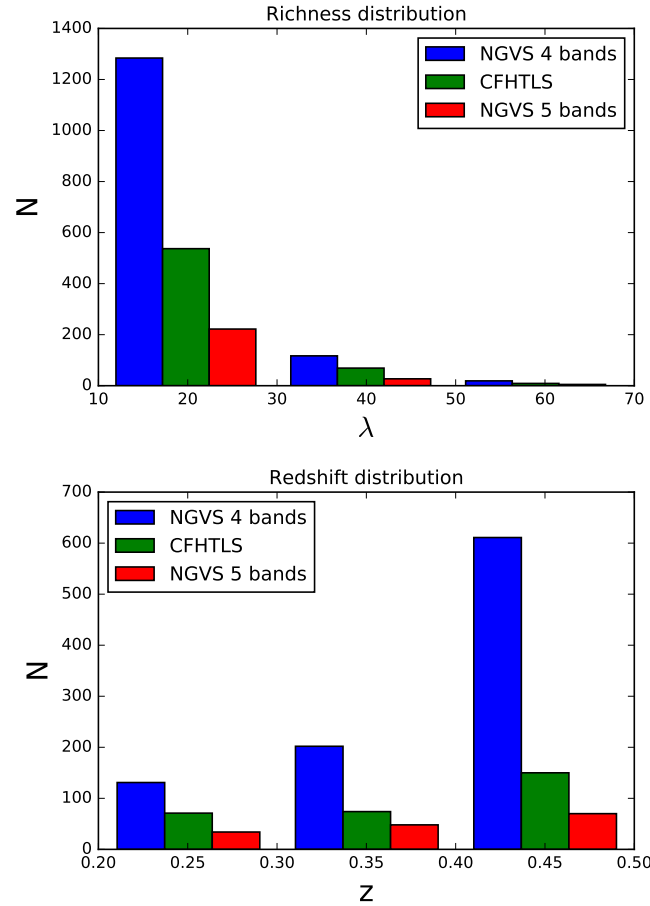


Figure 4.2 – The richness and redshift distributions of the RedGOLD CFHTLS W1, NGVS5, and NGVS4 1323 clusters from the selected catalogs (see text for the description of the catalogs). The richness is plotted in bins of $\Delta\lambda = 20$, and the redshift in bins of $\Delta z = 0.1$. In each bin, the bars corresponding to the three different samples are plotted next to each other.

(2012), and Piffaretti et al. (2011) X-ray catalogs.

Gozaliasl et al. (2014) analyzed the *XMM-Newton* observations in the $\sim 3 \text{ deg}^2$ overlapping the CFHT-LS W1 field, as a part of the XMM-LSS survey (Pierre et al., 2007). They presented a catalog of 129 X-ray groups, in a redshift range $0.04 < z_{\text{phot}} < 1.23$, characterized by a rest frame $0.1 - 2.4 \text{ keV}$ band luminosity range $10^{41} - 10^{44} \text{ ergs s}^{-1}$. They removed the contribution of AGN point sources from their flux estimates and applied a correction of $\sim 10\%$ for the removal of cool core flux based on the high resolution *Chandra* data on COSMOS as shown in Leauthaud et al. (2010). They used a two-color red-sequence finder to identify group members and calculate the mean group photometric redshift. They inferred cluster's M_{200} masses using the lensing $L_X - M$ relation of Leauthaud et al. (2010), with a systematic uncertainty of $\sim 20\%$.

Mehrtens et al. (2012) presented the first data release of the XMM Cluster Survey (XCS), a serendipitous search for galaxy clusters in the *XMM-Newton* Science Archive data. The catalog consists of 503 optically confirmed clusters, in a redshifts range $0.06 < z_{\text{phot}} < 1.46$. 402 of these clusters have measured X-ray temperatures in the range $0.4 < T_X < 14.7 \text{ keV}$. They derived photometric redshift with the red-sequence technique, using one color. They used a spherical β -profile model (Cavaliere & Fusco-Fermiano, 1976) to fit the surface brightness profile and derive the bolometric (0.05 - 100 keV band) luminosity in units of $10^{44} \text{ erg s}^{-1}$ within the radius R_{200} and R_{500} .

Piffaretti et al. (2011) presented the MCXC, which includes 1743 clusters and it's a compilation of the X-ray catalogs based on the ROSAT All Sky Survey (NORAS, REFLEX, BCS, SGP, NEP, MACS, CIZA) and the serendipitous cluster catalogs 160SD, 400SD, SHARC, WARPS, and EMSS. The MCMX catalog provides the $0.1 - 2.4 \text{ keV}$ band luminosity L_{500} , and the total mass M_{500} . These masses were estimated using the luminosity-mass relation calibrated from the $M - Y_X$ relation of Arnaud et al. (2007, 2010), adopting a non-self-similar slope (with $Y_X \equiv T_X M_{\text{gas}}$). Mass values were obtained fitting an NFW profile to the total mass profile calculated from the temperature profile, under the assumption of hydrostatic equilibrium.

I performed a match between these three catalogs and the RedGOLD detections imposing a maximum separation of 1 Mpc and a maximum difference in redshift of 0.1. I included detections from both the *published* and the *complete* catalogs to broaden the sample, and have more statistics to perform the scaling relation fits. Results obtained with the *complete* catalogs might be affected by contamination biases, since for those, I estimated the purity to decrease to $\sim 60\%$ (Fig. 8-9 of Licitra et al., 2016a).

Within all three fields, I recover 36(27) objects from the match of the

complete(published) catalog with Gozaliasl et al. (2014) (in this case all objects are from the CFHT-LS W1 field), 21(17) from objects from the match of the *complete(published)* catalog with Mehrrens et al. (2012), and 7 objects from the match of the *complete* catalog with Piffaretti et al. (2011). As shown in Licitra et al. (2016a), RedGOLD recovers 38 clusters, up to $z \sim 1$, in the 3 deg^2 of the CFHT-LS W1 field, covered by Gozaliasl et al. (2014) catalog. The clusters detected by RedGOLD that don't have an X-ray counterpart seem to be, from visual inspection, small galaxy groups. It is possible that these systems have an X-ray emission below the X-ray detection limit, or that they are not relaxed systems and don't have any X-ray emission at all.

In Section 4.6, I will show the results I obtained, using these catalogs to compare the lensing masses that I measured with X-ray masses and calculate the scaling relations between lensing masses and X-ray temperature and luminosity. I analyzed the three catalogs separately because of the different treatment of the emission from the central regions of the clusters leads to different mass estimates. In Chapter 5, I will discuss a comparison with other works in literature.

4.4 Weak lensing analysis

The aim of this work is to infer cluster masses by reconstructing the tangential shear radial profile $\gamma_t(R)$, averaging in concentric annuli around the halo center, and fitting it to a known density profile.

$\gamma_t(R)$ accounts for the distortion, due to the gravitational potential of the lens, of the shape of the background sources in the tangential direction with respect to the center of the lens and it's defined as:

$$\gamma_t = -Re [\gamma e^{-2i\phi}] \quad (4.5)$$

with $\gamma = \epsilon_1 + i\epsilon_2 = |\gamma|e^{2i\phi}$, where ϵ_1 and ϵ_2 are the ellipticity components of the galaxy and ϕ is the position angle of the galaxy respect to the center of the lens (Schneider, 2005).

As described in Wright & Brainerd (2000), the tangential shear profile $\gamma_t(R)$ is related to the surface density contrast by:

$$\Delta\Sigma(R) = \langle \gamma_t(R) \rangle \Sigma_c \quad (4.6)$$

Where R is the projected radius with respect to the center of the lens and:

$$\Sigma_c = \frac{c^2}{4\pi G} \frac{D_s}{D_1 D_{1s}} \quad (4.7)$$

is the critical surface density. Here c is the speed of light and D_s , D_1 , D_{1s} are the angular diameter distances from the observer to the source, from the observer to the lens, and from the lens to the source, respectively.

In order to infer cluster masses, I fitted the measured $\Delta\Sigma(R)$ profile, obtained as described in Section 4.4.1, to the shear profile theoretical model, described in Section 4.4.2.

4.4.1 Shear profile measurement

In this section, I will explain how I calculated the shear radial profiles of the stacked clusters of the *selected* catalogs.

Only the shear profiles of the most massive clusters in the sample ($M_{200} > 4 \times 10^{14} M_\odot$, for a signal-to-noise ratio $S/N > 3$; they represent the $\sim 2\%$ of the sample) can be reconstructed individually, while for lower masses the noise dominates the measurement. In order to increase the signal-to-noise ratio and measure average radial profiles for all the other detections, I stacked galaxy clusters in five richness bins, from $\lambda = 10$ to $\lambda = 70$, in steps of 10 (20 for the last bin) in richness.

I selected the background galaxy sample using the following criteria:

$$z_{\text{phot},s} > z_{\text{phot},l} + 3 \times \sigma_{z_{\text{phot}}} (i' - \text{mag}_s) \times (1 + z_{\text{phot},s}) \quad (4.8)$$

where $z_{\text{phot},s}$ is the source redshift, $z_{\text{phot},l}$ is the lens redshift, and $\sigma_{z_{\text{phot}}} (i' - \text{mag}_s)$ is the error on the photometric redshift as a function of the source i' -band magnitude. This function was obtained interpolating the values in Figure 9 of Raichoor et al. (2014), up to $i' \sim 24.7 \text{ mag}$. As I will show in Section 4.5, I tested different cuts in magnitude ($i' \sim 24.7, 24, 23.5, 23 \text{ mag}$), and found consistent results in all cases. We can conclude that the inclusion of faint sources in the background sample does not introduce a bias in the total cluster mass estimation.

Following Ford et al. (2015), I then sorted the background galaxies in 10 logarithmic radial bins from 0.09 Mpc from the center of the lens to 5 Mpc . In fact, at radii closer than 0.09 Mpc , I find a lack of background sources, due to low sky area, and at larger radii the scatter in the mass estimate can be $\geq 20\%$ because of the contribution of large scale structure (Becker & Kravtsov, 2011; Oguri & Hamana, 2011).

In each radial bin, I performed a weighted average of the lensing signal as follows:

$$\Delta\Sigma(R) = \frac{\sum_{i=1}^l \sum_{j=1}^s w_{ij} \Sigma_{c,ij} \gamma_{t,ij}}{\sum_{i=1}^l \sum_{j=1}^s w_{ij}} \quad (4.9)$$

where the sum is over every *lens-source* pair (i.e. i - j indices up to the l number of lenses and s number of sources). The weights $w_{ij} = \Sigma_{c,ij}^{-2} w_{\text{lens}}$ (Mandelbaum et al., 2005) quantify the quality of the shape measurements through the *lensfit* weights w_{lens} (defined in Section 4.2.1) and down-weight source galaxies that are close in redshift to the lens through $\Sigma_{c,ij}^{-2}$, which is evaluated for every *lens-source* pair using z_{phot} to calculate the angular diameter distances that appear in eq. 4.7.

The measured signal needs to be corrected applying the calibration corrections introduced in Section 4.2.1. As explained, the additive bias c only affects the second component of the ellipticity and the correction can be applied to single ellipticity measurements. Therefore, I simply calculated $\epsilon_{2,\text{corr}} = \epsilon_2 + c$, for each galaxy.

The multiplicative correction m needs to be applied as a weighted ensem-

ble average correction:

$$1 + K(R) \equiv \frac{\sum_{i=1}^l \sum_{j=1}^s w_{ij} [1 + m_{ij}]}{\sum_{i=1}^l \sum_{j=1}^s w_{ij}} \quad (4.10)$$

This is done to avoid possible instabilities in case the term $(1 + m)$ tends to zero. In this way, I also removed any correlation between the calibration correction and the intrinsic ellipticity (Miller et al., 2013). The calibrated signal is written as:

$$\Delta\Sigma_{\text{cal}}(R) = \frac{\Delta\Sigma(R)}{1 + K(R)} \quad (4.11)$$

In order to estimate the errors on $\Delta\Sigma(R)$, I created a set of 100 bootstrap realizations for each richness bin, selecting the same number of clusters for each stack but taking them with replacements. As already determined by Ford et al. (2015), increasing the number of realization from 100 to 1000 or 10000 does not change the estimated errors. I applied eq. 4.9 to obtain $\Delta\Sigma(R)$ for each bootstrap realization.

Following Ford et al. (2015), I then calculated the covariance matrix:

$$C(R_i, R_j) = \left[\frac{N}{N-1} \right]^2 \frac{1}{N} \sum_{k=1}^N [\Delta\Sigma_k(R_i) - \overline{\Delta\Sigma}(R_i)] \times [\Delta\Sigma_k(R_j) - \overline{\Delta\Sigma}(R_j)] \quad (4.12)$$

where R_i and R_j are the radial bins, N is the number of bootstrap samples and $\overline{\Delta\Sigma}(R_i)$ is the average over all bootstrap realizations.

For each radial bin, the shear was weighted using the *lensfit* weights as shown in eq. 4.9, so these error bars also include the error on the shape measurements of the source galaxies. I calculated the covariance matrix to take into account the correlation between radial bins and the contribution to the stacked signal of clusters with different masses inside the same richness bin.

4.4.2 Shear profile model

In order to fit the tangential shear profiles I used an analytic model for the cluster profile:

$$\Delta\Sigma(R) = p_{\text{cc}}[\Delta\Sigma_{\text{NFW}}(R) + \Delta\Sigma_{\text{nw}}(R)] + (1 - p_{\text{cc}})\Delta\Sigma_{\text{sm}}(R) + \Delta\Sigma_{\text{2halo}}(R) \quad (4.13)$$

$\Delta\Sigma_{\text{NFW}}$ is the surface density contrast calculated from an NFW density profile, assumed as the halo profile. $\Delta\Sigma_{\text{nw}}$, $\Delta\Sigma_{\text{sm}}$ and $\Delta\Sigma_{\text{2halo}}$ are correction terms that take into account, respectively, non-weak shear effects, cluster miscentering and the contribution to the signal from large scale structure. p_{cc} is a free parameter related to the miscentering term and represents the percentage of correctly centered clusters in each stack. I will describe in detail, in the following sections, each term and the free parameters of the model. This approach mainly follows the one adopted by Johnston et al. (2007) and Ford et al. (2015). However, I did not use the Ford et al. (2015) pipeline, but developed my own, and the data used (NGVSLenS+CFHTLenS), the cluster detections (much purer and complete), and the photometric redshift analysis are different. In particular, this work was performed in the context of the NGVS collaboration, and the cluster catalog used is much less contaminated than that used in Ford et al. (2015).

In addition to this model, hereafter *Basic Model*, I also considered two model extensions, discussed in Section 4.4.2.5, in order to study how the addition of new terms changes the final cluster profile.

All the averages in the equations below were performed using the same weighting as in Equation 4.9.

4.4.2.1 $\Delta\Sigma_{\text{NFW}}$ profile

For the halo profile, I assumed an NFW profile (Equation 1.5), and the Dutton & Macció (2014) mass-concentration relation:

$$\log c_{200} = a + b \log (M_{200}/[10^{12}h^{-1}M_{\odot}]) \quad (4.14)$$

with $a = 0.520 + (0.905 - 0.520) \exp(-0.617z^{1.21})$ and $b = -0.101 + 0.026z$. This reduces the dimensionality of the model to one parameter, r_{200} , from which I can calculate the halo mass using eq. 1.6.

I calculated the NFW surface density, integrating the tridimensional NFW density profile along the line of sight:

$$\Sigma_{\text{NFW}}(R) = 2 \int_0^{\infty} \rho_{\text{NFW}}(R, z) dz \quad (4.15)$$

Integrating again, I find $\bar{\Sigma}_{\text{NFW}}(R)$, the average surface density inside a radius R :

$$\bar{\Sigma}_{\text{NFW}}(< R) = \frac{2}{R^2} \int_0^R R' \Sigma_{\text{NFW}}(R') dR' \quad (4.16)$$

Finally, I can calculate the first term in eq. 4.13:

$$\Delta\Sigma_{\text{NFW}} = \bar{\Sigma}_{\text{NFW}}(< R) - \Sigma_{\text{NFW}}(R) \quad (4.17)$$

4.4.2.2 Miscentering Term

Since the NFW density profile is spherically symmetric, an error in the determination of the halo center would lead to underestimate the lens mass. In fact, the stacking of offset clusters smooths the differential surface mass density profile (George et al., 2012).

In order to obtain a model of the distribution of the offsets between the RedGOLD centers and the cluster true centers, I used both simulations and X-ray observations. Licitra et al. (2016a) applied RedGOLD to the lightcones of Henriques et al. (2012), and calculated the offsets between the centers estimated by the algorithm and the true centers from the simulations. I also matched the RedGOLD detections to X-ray detections in the same areas (Gozaliasl et al., 2014) to measure the average offset between RedGOLD and X-ray cluster centers. The matching procedure, and the number of recovered objects were discussed in Section 4.3.2.

In both cases, I found that the distribution of the offsets on the plane perpendicular to the line of sight can be modeled as a Rayleigh distribution with a mode of 23 *arcsec* and 13 *arcsec*, respectively (Figure 4.3, on the left; see also Johnston et al., 2007; George et al., 2012; Ford et al., 2015). In the analysis, I left the mode of this distribution as a free parameter in the fit. In Figure 4.3, on the right, I also show the offset distributions in *kpc*. A Rayleigh distribution is also consistent with the published center offset distribution predicted from cosmological simulations for X-ray detected clusters, including AGN feedback (Cui et al., 2016).

I assumed that this distribution represents the general offset distribution for the entire RedGOLD sample $P(R_{\text{off}})$ and modeled it following Johnston et al. (2007):

$$P(R_{\text{off}}) = \frac{R_{\text{off}}}{\sigma_{\text{off}}^2} \exp \left[-\frac{1}{2} \left(\frac{R_{\text{off}}}{\sigma_{\text{off}}} \right)^2 \right] \quad (4.18)$$

where R_{off} is the offset between the true and the estimated center, projected on the lens plane, and σ_{off} is the mode, or scale length, of the distribution. The surface density measured at the coordinates (R, θ) , with θ the azimuthal angle relative to the offset position R_{off} , is:

$$\Sigma_{\text{NFW}}(R, \theta | R_{\text{off}}) = \Sigma_{\text{NFW}} \left(\sqrt{R^2 + R_{\text{off}}^2 - 2RR_{\text{off}} \cos \theta} \right) \quad (4.19)$$

and the azimuthal averaged surface density around R_{off} is given by:

$$\Sigma_{\text{NFW}}(R | R_{\text{off}}) = \frac{1}{2\pi} \int_0^{2\pi} \Sigma_{\text{NFW}}(R, \theta | R_{\text{off}}) d\theta \quad (4.20)$$

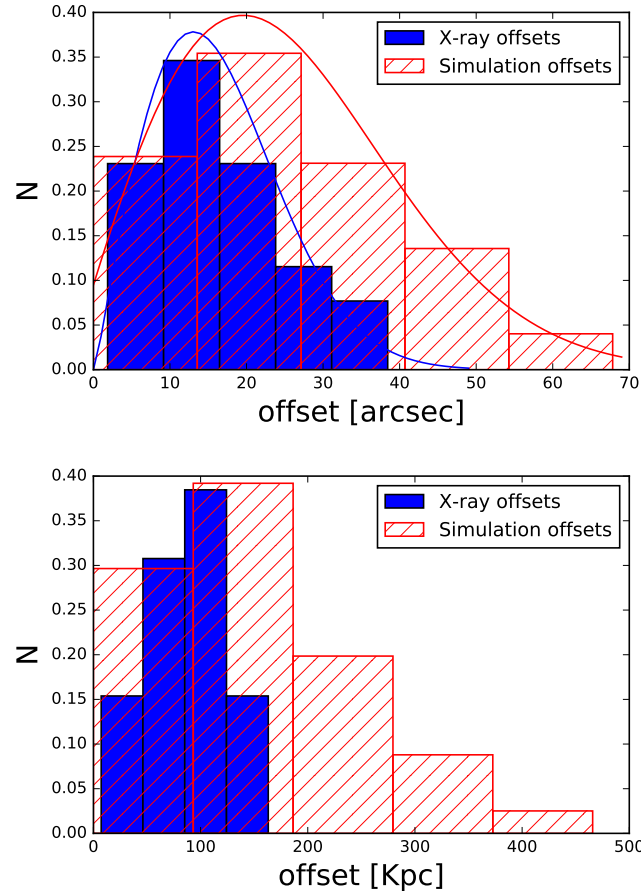


Figure 4.3 – On the top, the distribution of the offsets, in arcsec, between the RedGOLD and X-ray cluster centers (in blue), and between the RedGOLD and the Henriques et al. (2012) simulation centers (in red). The blue and red lines show the fitted Rayleigh distribution with mode of 13 arcsec and 23 arcsec, respectively. On the bottom, the offset distribution in kpc.

In order to model the effect of miscentering, I smoothed the $\Sigma_{\text{NFW}}(R|R_{\text{off}})$ profile convolving it with $P(R_{\text{off}})$:

$$\Sigma_{\text{sm}}(R) = \int_0^\infty \Sigma_{\text{NFW}}(R|R_{\text{off}})P(R_{\text{off}})dR_{\text{off}} \quad (4.21)$$

and obtained the stacked surface density profile $\Sigma_{\text{sm}}(R)$ around the offset positions of the ensemble of clusters with offset distribution $P(R_{\text{off}})$ (Yang et al., 2006; Johnston et al., 2007; George et al., 2012).

Finally, I can write the miscentering term as:

$$\Delta\Sigma_{\text{sm}}(R) = \bar{\Sigma}_{\text{sm}}(< R) - \Sigma_{\text{sm}}(R) \quad (4.22)$$

with $\bar{\Sigma}_{\text{sm}}(< R)$ being, as before, the average surface density within the radius R .

The miscentering term adds two free parameters to the model, σ_{off} and p_{cc} , which is the percentage of correctly centered clusters in the stack, already introduced in eq. 4.13.

4.4.2.3 Non-weak Shear Term

The non-weak shear correction arises from the fact that what we actually measure is the reduced shear:

$$g_t = \frac{\gamma_t}{1 - k} \quad (4.23)$$

where $k \equiv \Sigma_{\text{NFW}}/\Sigma_c$ is the convergence. Usually in the weak lensing regime $g_t \approx \gamma_t$, if $\gamma_t \ll 1$ and $k \ll 1$, but for relatively massive halos this assumption may no longer hold at the innermost radial bins in which the cluster profile is measured.

As described in Johnston et al. (2007), it is necessary to introduce the non-weak shear correction term, calculated in Mandelbaum et al. (2006). In non-weak regime, the tangential ellipticity component, ϵ_t is proportional to g_t , instead of γ_t . We can expand ϵ_t in power series as:

$$\epsilon_t = \sum_{n=0}^{\infty} A g_t^{2n+1} = A \left(\frac{\gamma_t}{1 - k} \right)^{2n+1} = A \left(\frac{\Delta\Sigma\Sigma_c^{-1}}{1 - \Sigma\Sigma_c^{-1}} \right)^{2n+1} \quad (4.24)$$

As shown in detail in appendix A of Mandelbaum et al. (2006), we can calculate the correction term from the expansion in power series to second order of ϵ_t , in powers of Σ_c . I obtained the following term, that I added in eq. 4.13:

$$\Delta\Sigma_{\text{nw}}(R) = \Delta\Sigma_{\text{NFW}}(R)\Sigma_{\text{NFW}}(R)\frac{\langle\Sigma_c^{-3}\rangle}{\langle\Sigma_c^{-2}\rangle} \quad (4.25)$$

4.4.2.4 Two-halo Term

On large scales, the lensing signal is dominated by nearby mass concentrations, halos, and filaments. Seljak (2000) developed an analytic halo model, in which all the matter in the Universe is hosted in virialized halos, described by a universal density profile. They computed analytically the power spectrum of dark matter and galaxies, and their cross-correlation based on the Press & Schechter (1974) model. They found that, ignoring the contribution from satellite galaxies, a cluster can be modeled by two contributions, the one-halo term and the two-halo term. The first represents the correlation between the central galaxy and the host dark matter halo and corresponds to $\Delta\Sigma_{\text{NFW}}(R)$. The second accounts for the correlation between the cluster central galaxy and the host dark matter halo of another cluster. On large scales, the two-halo power spectrum is proportional to the halo bias and the linear power spectrum, $P_{2\text{halo}} \propto b(M_{200,z})P_{\text{lin}}(k)$. In order to calculate the surface density associated to the two-halo term, we can integrate the galaxy-dark matter linear cross-correlation function $\xi_{\text{lin}}(r)$, obtained by the Fourier transform of the linear power spectrum.

Following Johnston et al. (2007) and Ford et al. (2015), we can write the two-halo term as:

$$\Delta\Sigma_{2\text{halo}}(R, b) = b(M_{200}, z)\Omega_{\text{m}}\sigma_8^2 D(z)^2 \Delta\Sigma_1(R) \quad (4.26)$$

where $b(M_{200}, z)$ is the bias factor, Ω_{m} is the matter density parameter, σ_8^2 is the amplitude of the power spectrum on scales of $8 h^{-1} \text{Mpc}$, $D(z)$ is the growth factor and:

$$\Delta\Sigma_1(R) = \bar{\Sigma}_1(< R) - \Sigma_1(R) \quad (4.27)$$

where

$$\Sigma_1(R, z) = (1+z)^3 \rho_{\text{c},0} \int_{-\infty}^{\infty} \xi_{\text{lin}} \left((1+z) \sqrt{R^2 + y^2} \right) dy \quad (4.28)$$

The factor $(1+z)$ arises from the conversion from physical units to comoving units.

For the bias factor, I used the analytic formula calculated by Seljak & Warren (2004), and for $P_{\text{lin}}(k)$, I used tabulated values from CAMB (Lewis, Challinor & Lasenby, 2000).

4.4.2.5 Model extensions

In order to take into account possible profile fitting biases, I introduced two modifications of the *Basic Model*.

As explained in Section 4.4.1, to enhance the shear signal, I stacked galaxy clusters in bins of richness. It has been proven that, when fitting the model profile to the measured stacked shear profile, the intrinsic scatter between the dark matter halo mass and the richness biases mass measurements (Becker et al., 2007; Rozo et al., 2009a). In order to take this into account, I assumed that the mass M_{200} has a log-normal distribution at fixed richness, with variance in $\ln M_{200}$, $\sigma_{\ln M_{200}|\lambda}$ (i.e. the intrinsic scatter). In the first extension to *Basic Model*, that I will call *Added Scatter Model*, I added $\sigma_{\ln M_{200}|\lambda}$ as a new free parameter. In addition, as shown by Gavazzi et al. (2007), the two contributions to the shear signal from the luminous and dark matter can be distinguished by fitting a two-component mass model, which take into account the contribution from the stellar mass of the halo central galaxy M_{BCG} .

In the second extension (hereafter *Two Component Model*), I added this contribution to the total halo mass in the *Basic Model*. In order to model the BCG signal, I followed Johnston et al. (2007) and added a point mass term to Equation 4.13:

$$\Delta\Sigma(R) = \frac{M_{\text{BCG}}}{\pi R^2} + p_{\text{cc}}[\Delta\Sigma_{\text{NFW}}(R) + \Delta\Sigma_{\text{nw}}(R)] + (1 - p_{\text{cc}})\Delta\Sigma_{\text{sm}}(R) + \Delta\Sigma_{\text{2halo}}(R) \quad (4.29)$$

The BCG mass, M_{BCG} , is either fixed at the value of the mean BCG stellar mass in each bin (hereafter M_{BCG}^*), or left as a free parameter in the fit. M_{BCG}^* were obtained by my collaborator Anand Raichoor, using the photometric and photometric redshift catalogs from Raichoor et al. (2014), and Bruzual & Charlot (2003) stellar population models with *LePhare*, in fixed redshift mode at the galaxy photometric redshift.

4.4.3 Fit the model to the measured shear profile

Here I will explain the method that I used to fit the measured shear profiles, obtained as described in Section 4.4.1, with the shear profile models of Section 4.4.2, for the *Basic Model*, the *Added Scatter Model* and the *Two Component Model*.

I performed the fit using Markov Chains Monte Carlo (MCMC; Metropolis et al., 1953). This method is particularly useful when the fitting model has a large number of parameters, the posterior distribution of the parameters is unknown, or the calculation is computationally expensive. MCMC

	Basic Model	Added Scatter Model	Two Component Model
$r_{200}[Mpc]$	(0, 2)	—	(0, 2)
$\sigma_{\text{off}}[arcmin]$	(0, 2)	(0, 2)	(0, 2)
pcc	(0, 1)	(0, 1)	(0, 1)
$\sigma_{\ln M \lambda}$	—	(0.1, 0.7)	—
$\log(M_{200}/M_{\odot})$	—	(11, 17)	—
$\log(M_{\text{BCG}}/M_{\odot})$	—	—	(9, 13) or fixed at $\log(M_{\text{BCG}}^*/M_{\odot})$

Table 4.1 – *MCMC uniform prior ranges for the different parameters of the three models. The lack of a numerical value indicates that the parameter is not included in the respective model.*

allow to efficiently sample the model likelihood by constructing a Markov chain that has the target posterior probability distribution as its stationary distribution. Each step of the chain is drawn from a model distribution and is accepted, or not, based on the criteria defined by the sampler algorithm.

In order to run MCMC, I used *emcee* (Foreman-Mackey et al., 2013), a Python implementation of the parallel Stretch Move by Goodman & Weare (2010). In order to choose the starting values of the chain, I first performed a minimization with the Python version of the Nelder-Mead algorithm, also known as downhill simplex (Nelder & Mead, 1965). I used flat priors (i.e. a uniform distribution within a given range) for all parameters. The priors, for the three different models, are shown in Tab. 4.1. All parameters are constrained to be positive and inside a range chosen according to their physical meaning. In order to choose the range for the intrinsic scatter, I referred to the values calculated by Licitra et al. (2016a). They found $\sigma_{\ln M|\lambda} = 0.39 \pm 0.07$ using the X-ray catalog of Gozaliasl et al. (2014) and $\sigma_{\ln M|\lambda} = 0.30 \pm 0.13$ from Mehtens et al. (2012).

MCMC produce a representative sampling of the likelihood distribution, from which I obtained the estimation of the error bars on the fitting parameters and of the confidence regions for each couple of parameters. I calculated the model likelihood using the bootstrap covariance matrix of eq. 4.12:

$$\ln \mathcal{L} = -\frac{1}{2} (\Delta \Sigma_{\text{data}} - \Delta \Sigma_{\text{model}})^T C^{-1} (\Delta \Sigma_{\text{data}} - \Delta \Sigma_{\text{model}}) \quad (4.30)$$

I used an ensemble of 100 walkers, a chain length of 1000 steps and a burn-in of 100 steps leading to a total of 90000 points in the parameters space.

In order to test the result of the chain, I checked the acceptance fraction

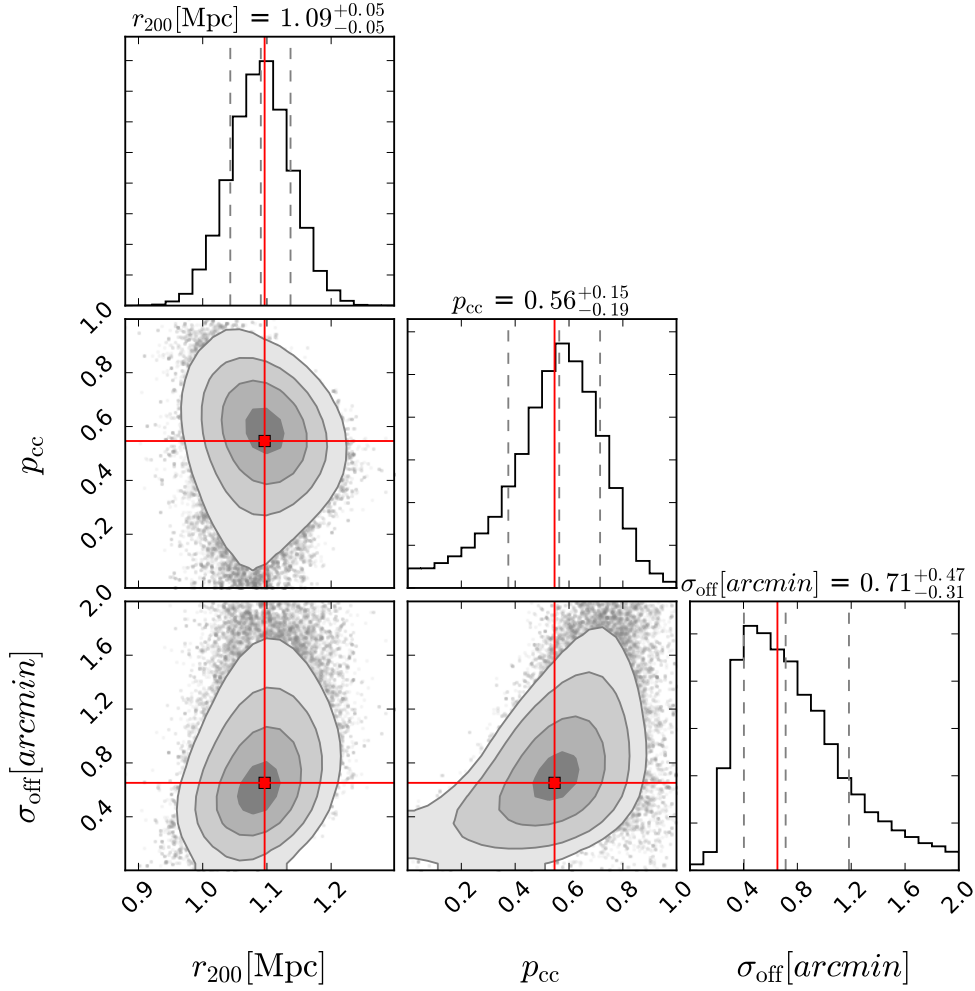


Figure 4.4 – Confidence levels on the fit parameters obtained with the MCMC analysis. On the diagonal, there are the 1-D histograms of each parameter. The 2-D histograms are also shown for each couple of parameters with confidence levels corresponding to 0.5σ , 1σ , 1.5σ , 2σ . The parameter values and errors are based on the 16th, 50th and 84th quantiles (shown as dashed lines in the 1-D histograms). The red squares and lines represents the values that correspond to the maximum likelihood. I obtained similar plots for each richness bin.

and the autocorrelation time to be sure of efficiently sample the posterior distribution and having enough independent samples.

Fig. 4.4 shows an example of error bars and the confidence regions of the parameters, obtained using the python package *corner* by Foreman-Mackey et al. (2016). This example corresponds to the third richness bin, fitted with the Two Component Model. On the diagonal are shown the one-dimensional histograms of the parameter values, representing the marginalized posterior probability distributions. Under the diagonal, the two-dimensional histograms for each couple of parameters and the confidence levels corresponding to 0.5σ , 1σ , 1.5σ and 2σ . The dashed lines in the 1-D histograms represent the 16th, 50th and 84th quantiles, while red squares and lines represents the values that correspond to the maximum likelihood. The 50th quantile and the maximum likelihood will match only in case the posteriori distribution is symmetrical.

4.5 Preliminary tests

In this section I will describe the tests that I performed before applying the lensing analysis described so far, to the real data. They consist in the validation of the code, an estimation of the completeness and purity of the selected background samples, a study of the effects of cluster redshift cut, richness binning, stacking, and centering.

4.5.1 Code validation

In order to validate my code, I applied my weak lensing analysis pipeline to real data. I used the entire CFHTLenS sample (W1, W2, W3, W4 fields), and the public cluster catalog of Milkeraitis et al. (2010), in order to compare my results with what found by Ford et al. (2015).

Ford et al. (2015) studied the weak lensing mass-richness relation using the CFHTLenS galaxy clusters, detected by the 3D-Matched-Filter (3D-MF) cluster finding algorithm of Milkeraitis et al. (2010), with masses ranging from small groups up to $\sim 10^{15} M_{\odot}$, and redshifts in the range $0.2 \lesssim z \lesssim 0.9$. They took into account non-weak shear effects, miscentring and nearby halos contribution, fixing the mass-concentration relation and the mass bias. They stacked clusters in richness and redshift bins, finding no evolution of the mass-richness relation in the redshift range considered.

The 3D-MF algorithm detects more than 18000 clusters in all the CFHTLenS area, assigning to each detection a significance parameter. Ford et al. (2015), defined the richness N_{200} of this cluster sample, starting from the detection significance. N_{200} is the number of galaxies within the radius r_{200} , and within $\Delta z = 0.08(1+z)$ (i.e. the 2σ scatter of photometric redshifts in the CFHTLenS) of the cluster redshift. Member galaxies are also selected to be brighter than $mag_i = -19.35$, that corresponds to the limiting apparent magnitude of the CFHTLenS, at the highest cluster redshift probed in their work, $z \sim 1$.

Using the N_{200} values supplied to me privately by Jes Ford, I stacked galaxy clusters in richness bins as in Ford et al. (2015) and applied my code to estimate the cluster masses in each stack.

The differences between our two analysis are:

- In order to select the background source sample for each cluster, Ford et al. (2015) used the entire redshift probability distribution $P(z)$. They imposed that the peak (i.e. z_{best} , corresponding to the z_{phot}) that I used, and at least 90% of this distribution have to be at higher redshift compared to the cluster.

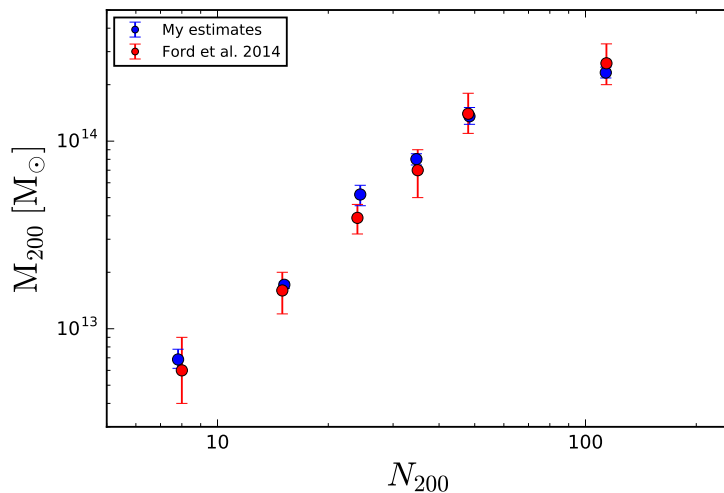


Figure 4.5 – Comparison of the mass-richness relation that I estimated (in blue) with that of Ford et al. (2015) (in red), obtained using the same sample and cluster catalog. For validation purposes, I used the richness N_{200} , as defined in Ford et al. (2015).

For my selection I used only z_{phot} and not the entire $P(z)$. I tested the use of the $P(z)$ for a small subsample of clusters without any evidence of significant improvement in the measured shear profiles. I don't expect then that this different selection choice will be relevant for the kind of analysis performed.

- Ford et al. (2015) used a composite-halo approach to fit the shear profiles. Instead of fitting a single average mass for each richness bin, they fit the normalization of the mass-richness relation, keeping the slope fixed. In this way, they were able to assign a mass to each cluster, in each bin, as a first approximation. They then performed a fit to the mass-richness relation, using the previously inferred cluster masses, leaving both normalization and slope as free parameters.

I instead simply fit to a single average mass, for each richness bin. Since Ford et al. (2015) fitted each richness bin individually, as I did, their choice of fitting directly the normalization of the mass-richness relation keeping the slope fixed should not make a difference in the final mass recovered with the two methods.

- Ford et al. (2015) used the downhill simplex method (Nelder & Mead, 1965) to perform the fits to the shear profiles. In order to calculate the errors they derived the χ^2 distribution of each parameter, leaving

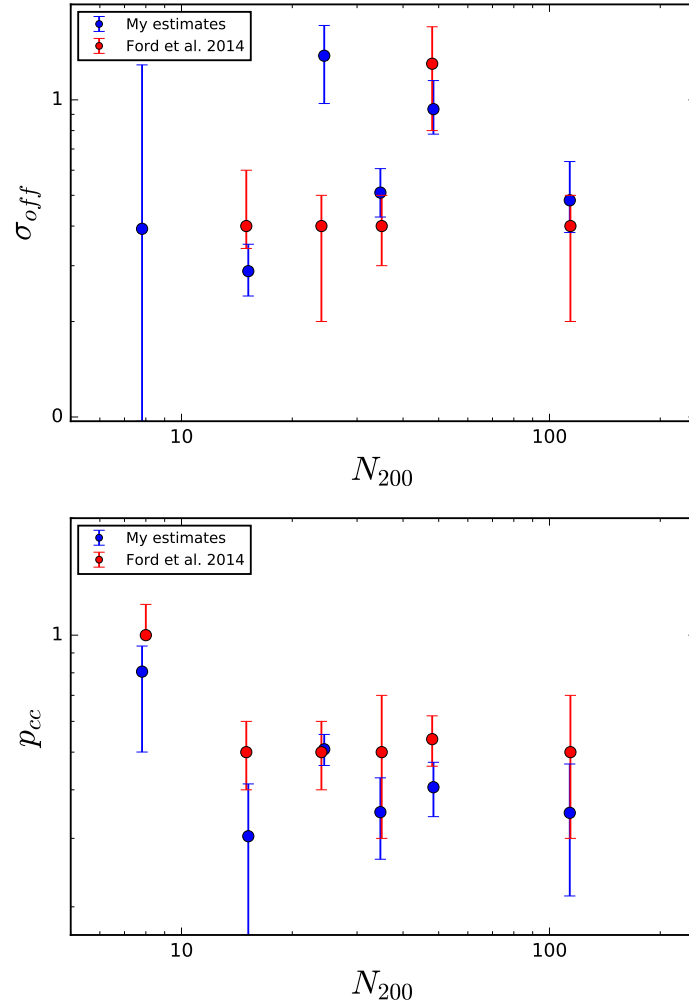


Figure 4.6 – Comparison of the miscentering parameters that I estimated (in blue) with those derived by Ford et al. (2015) (in red), obtained using the same sample and cluster catalog. The plot on the top shows σ_{off} , the mode of the offset distribution, modeled as a Reyleigh distribution, as a function of richness. The plot on the bottom shows, p_{cc} , the percentage of correctly centered clusters in the stack, as a function of richness.

free one parameter at a time and fixing all the others to the value corresponding to the minimum of the χ^2 .

I used MCMC to derive the errors and confidence regions for each couple of parameters. I used the downhill simplex method just to choose the starting values of the chains. I therefore expect the error bars that I calculated to be more accurate.

Figure 4.5 shows the comparison between the mass estimates from this work, in blue, and those from Ford et al. (2015), in red. The results are consistent within 1σ and the difference is of a few percent for all bins except two, in which it increases to 10 – 20%. The error bars on the red dots are larger than those on the blue dots. This could be due to the fact that the composite-halo approach used by Ford et al. (2015) introduces larger uncertainties in the fit, compared to the simpler approach used in this work. Also, Ford et al. (2015) didn't calculate the error bars in a rigorous way, as the sampling of the χ^2 distribution was done manually. The MCMC, on the other hand, have the advantage of producing an efficient sampling of the likelihood surface, giving more reliable confidence regions.

Figure 4.6 shows the comparison of the miscentering parameters, with my results in blue and those of Ford et al. (2015) in red. The results are still consistent within 1σ , for almost all the bins. We note that, due to the degeneracy of the two miscentering parameters, when σ_{off} is overestimated compared to Ford et al. (2015) results, the corresponding p_{cc} is underestimated, in the majority of the bins. This means that the miscentering correction is important to correctly model the cluster mass, but the value of the individual miscentering parameters is not well constrained by the data, since in each bin there could be different combinations of σ_{off} and p_{cc} that would lead to the same result.

4.5.2 Background selection

4.5.2.1 Selection criteria

Before deciding to use photometric redshift to select the background sources for the lensing analysis, I tested different kind of selection criteria.

I compared the photo-z used for this work, with spectroscopic redshifts from VIPERS (Guzzo et al., 2014) (assumed as the true redshifts) to identify the percentage of recovered background galaxies and the percentage of wrong selections (sources with redshift lower than the cluster redshift). I performed this comparison as a function of the cluster redshift, for three criteria:

- The selection used by Kettula et al. (2015), based on photo-z only:

$$z_{\text{phot},s} > z_{\text{phot},l} + 0.15$$

- The color criteria of Oguri et al. (2012).
- A combination of the first two.

As we can see from Figure 4.7, the third criteria (in black) is the one that gives the purest but less populated background sample. The photo-z selection (in red) and the color selection (in blue) both show less than 10% of contamination at $z < 0.5$ (the limit chose for the weak lensing analysis), and less than 3% at $z < 0.4$. In terms of completeness, the photo-z selection is much more efficient compared to the color selection, with a percentage of selected sources of 90 – 100% against 50 – 75%, up to $z < 0.5$.

I decided to use the photo-z selection since it's the best compromise between purity and background number density. In a previous version of my analysis, I used the same selection of Kettula et al. (2015), then I decided to refine the selection criteria using Equation 4.8. In next paragraph I will describe the tests that I performed to test this criterion, compared to the simpler redshift selection.

4.5.2.2 Magnitude limit

I selected the background sources applying a redshift cut that is magnitude dependent, using Equation 4.8. I will refer to this selection as $\sigma_{\text{photoz cut}}$. I tested this criterion comparing it with the results that I obtained using the simple redshift selection of Kettula et al. (2015), and the magnitude cuts $mag_i = 24.7, 24, 23.5, 23$.

In order to do so, I fitted the shear profiles using the *Basic Model*, and then I fitted the mass-richness relation to compare the normalization and slope obtained with the different kinds of selection. Since the brightest magnitude cuts significantly reduce the number density of background sources, I combined the two highest, less populated, richness bins (i.e. $40 < \lambda \leq 70$, for a total of 4 bins), to have enough signal to reconstruct the shear profile.

The results are shown in the top plot of Figure 4.8, and in Table 4.2, where $mag\ cut$ indicates the criteria used, n_{gal} is the number density of background sources per $arcmin^2$, a and b are the normalization and slope of the mass-richness relation. In Table 4.3, we find the difference between the mass-richness relation parameters calculated with each kind of selection, and the compatibility in σ . As we can see, all results are consistent within 1.5σ , 1σ , and 0.5σ (from the lighter to the darker shade of green, respectively). This means that the $\sigma_{\text{photoz cut}}$ can be considered as reliable as the brightest magnitude cut, $mag_i = 23$ (for which we expect more reliable photometric

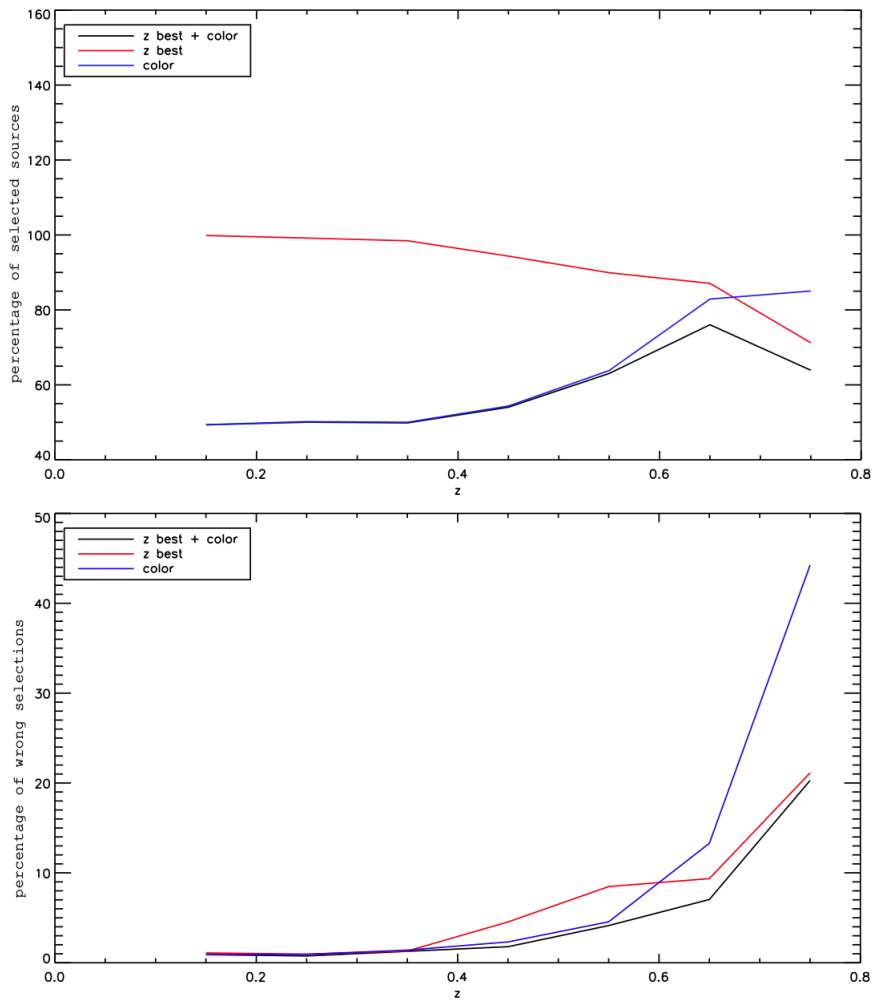


Figure 4.7 – On the top, the percentage of selected background sources as a function of the cluster redshift, for the three different criteria. On the bottom, the percentage of wrong selections as a function of the cluster redshift, for the three different criteria.

mag cut	n_{gal}	a	b
24.7	7.3 ± 1.5	14.43 ± 0.02	1.04 ± 0.07
24	4.7 ± 1.0	14.45 ± 0.04	1.19 ± 0.19
23.5	3.0 ± 0.8	14.47 ± 0.05	1.37 ± 0.24
23	1.7 ± 0.7	14.44 ± 0.04	1.09 ± 0.17
σ_{photoz}	5.2 ± 1.8	14.44 ± 0.03	1.09 ± 0.13

Table 4.2 – *Mass-richness relation parameters obtained with the different selection criteria (mag cut; see text for definition). n_{gal} is the number density of background sources. a and b are the normalization and slope of the mass-richness relation.*

mag cut	24.7	24	23.5	23	σ_{photoz}
24.7		$\Delta a = 0.01 \pm 0.05$ (0.5 σ) $\Delta b = 0.15 \pm 0.20$ (1 σ)	$\Delta a = 0.04 \pm 0.06$ (1 σ) $\Delta b = 0.34 \pm 0.25$ (1.5 σ)	$\Delta a = 0.01 \pm 0.05$ (0.5 σ) $\Delta b = 0.05 \pm 0.19$ (0.5 σ)	$\Delta a = 0.01 \pm 0.03$ (0.5 σ) $\Delta b = 0.05 \pm 0.15$ (0.5 σ)
24			$\Delta a = 0.02 \pm 0.07$ (0.5 σ) $\Delta b = 0.18 \pm 0.31$ (1 σ)	$\Delta a = 0.00 \pm 0.06$ (0.5 σ) $\Delta b = 0.10 \pm 0.26$ (0.5 σ)	$\Delta a = 0.00 \pm 0.05$ (0.5 σ) $\Delta b = 0.10 \pm 0.23$ (0.5 σ)
23.5				$\Delta a = 0.03 \pm 0.07$ (0.5 σ) $\Delta b = 0.28 \pm 0.30$ (1 σ)	$\Delta a = 0.03 \pm 0.06$ (0.5 σ) $\Delta b = 0.29 \pm 0.28$ (1 σ)
23					$\Delta a = 0.00 \pm 0.05$ (0.5 σ) $\Delta b = 0.00 \pm 0.22$ (0.5 σ)
σ_{photoz}					

Table 4.3 – *Difference between the mass-richness relation parameters (and compatibility within $n\sigma$) obtained with the different selection criteria (see text for definition). The different shades of green indicates that the results are consistent within 1.5 σ , 1 σ , and 0.5 σ , from lighter to darker respectively.*

redshift estimation, and therefore less contamination from foreground source or cluster member galaxies in background sample) and, at the same time, it preserves a higher n_{gal} .

The number density of background sources obtained with the σ_{photoz} cut is enough to split the highest richness bin in two bins (i.e. $40 < \lambda \leq 50$, and $50 < \lambda \leq 70$, for a total of 5 bins), as in the final analysis that I performed. I then compared the mass-richness relations obtained with σ_{photoz} cut, using 4 bins and 5 bins. The results are shown in the bottom plot of Figure 4.8. The difference between the normalization and slopes in the two cases is $\Delta a = 0.01 \pm 0.03$ and $\Delta b = 0.04 \pm 0.15$. The results are consistent within 0.5σ .

4.5.3 Cluster redshift cut

As said before, shear measurements from ground based telescopes are reliable for clusters with redshifts $0.2 < z_{phot} < 0.5$ (Kasliwal et al., 2008), and for this reason, I restricted my analysis to this redshift range.

In order to test the validity of this assumption, I fitted individually the most massive clusters in the sample, with $\lambda > 50$ and an expected $M_{200} > 10^{14}M_{\odot}$.

The results are shown in Figure 4.9. As we can see, the clusters with $z > 0.5$ (in blue) show a higher scatter, and some underestimated masses, compared to the clusters sample at $z < 0.5$ (in red).

This can also be explained looking at Figure 4.10 that shows the number density of background sources as a function of redshift for all the clusters in the sample, and the mean values in redshift bins (red). For redshift higher than 0.5, the mean number of sources is below 2 arcmin^{-2} , which is not enough to properly recover the shear signal.

In Figure 4.11, we can see the redshift-richness plane, color coded by the mean number of background sources. The dashed black line shows the region selected for the study of individual cluster profiles, which corresponds to $z < 0.5$, and $\lambda > 50$. The mean background count in this region is $n_{gal} \sim 6 \text{ arcmin}^{-2}$.

This test confirms the greater reliability of the shear measurements of the cluster sample selected for this work, with $z < 0.5$.

4.5.4 Richness binning

In order to test the stability of the mass-richness relation, I performed the fit using different λ binnings. In Table 4.4, I show the range in λ , the number of clusters, and the mean λ , for each bin.

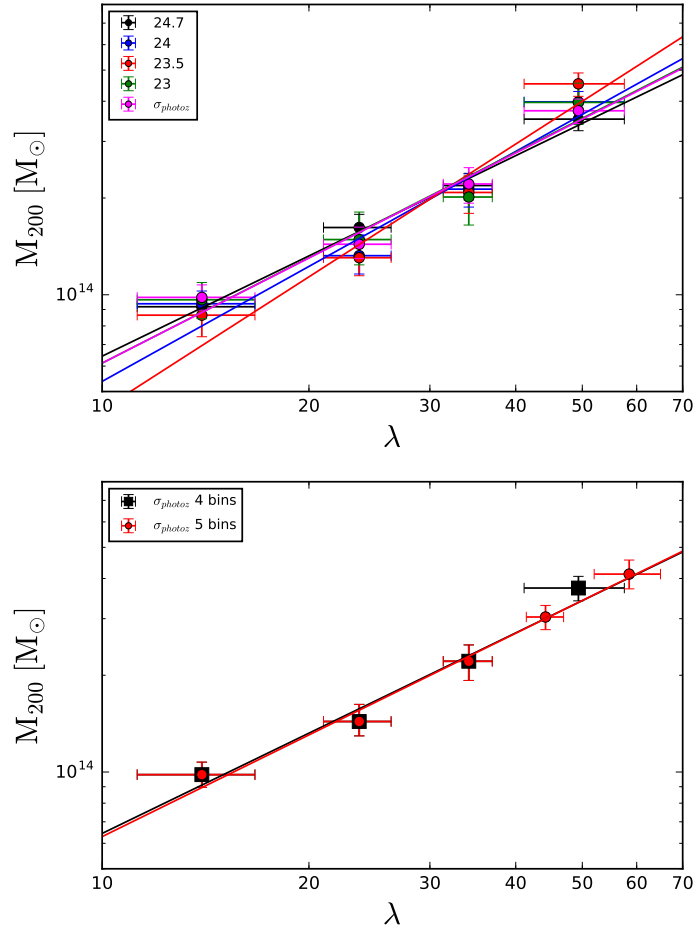


Figure 4.8 – *On the top, the mass-richness relations obtained using the different selection criteria (see text for definition). On the bottom the comparison between the mass-richness relations obtained with σ_{photoz} cut, using 4 bins and 5 bins (as in the final analysis that I performed).*

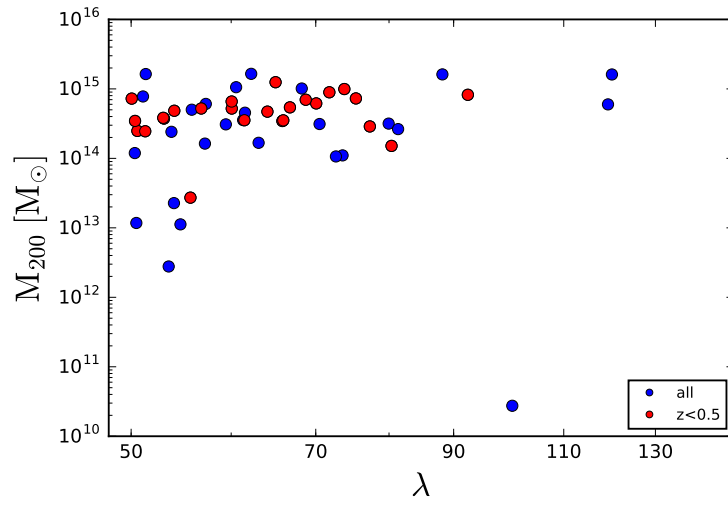


Figure 4.9 – Masses inferred fitting individual clusters with $\lambda > 50$. In red, clusters with $z < 0.5$, and in blue, all clusters. The blue points show a greater scatter and some underestimated masses.

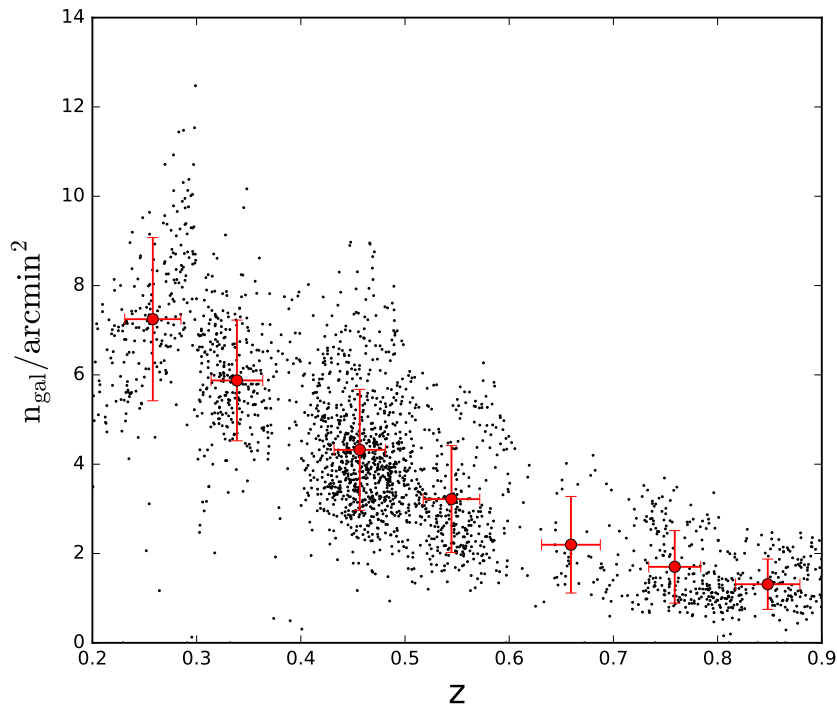


Figure 4.10 – Number density of background sources as a function of redshift for all the clusters in the sample (in black). The mean values in redshift bins are shown in red.

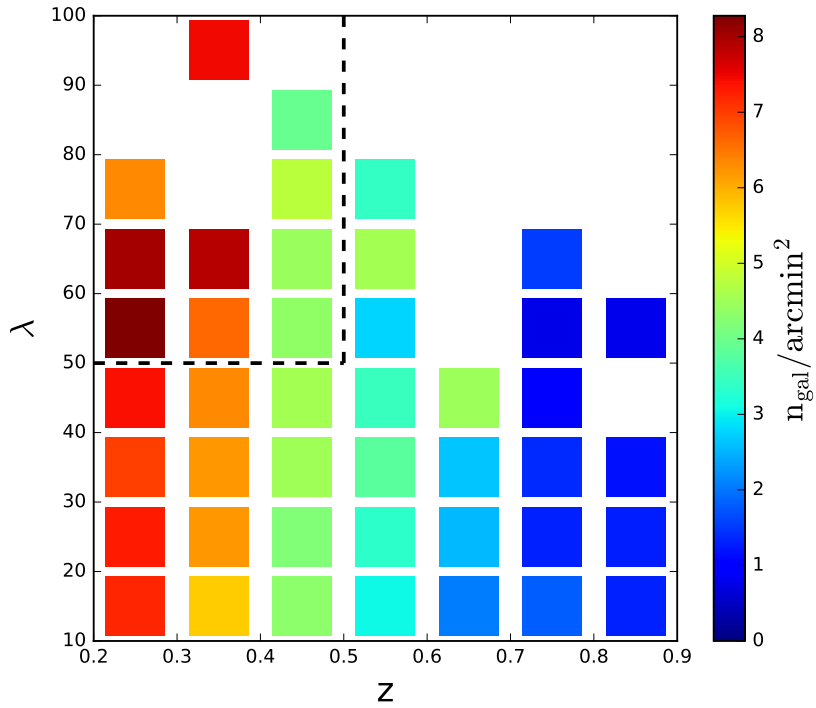


Figure 4.11 – Mean number density of background sources as a function of redshift and richness. The region enclosed in the dashed line is the sample selected for individual cluster profile studies, which is characterized by $n_{gal} \sim 6 \text{ arcmin}^{-2}$.

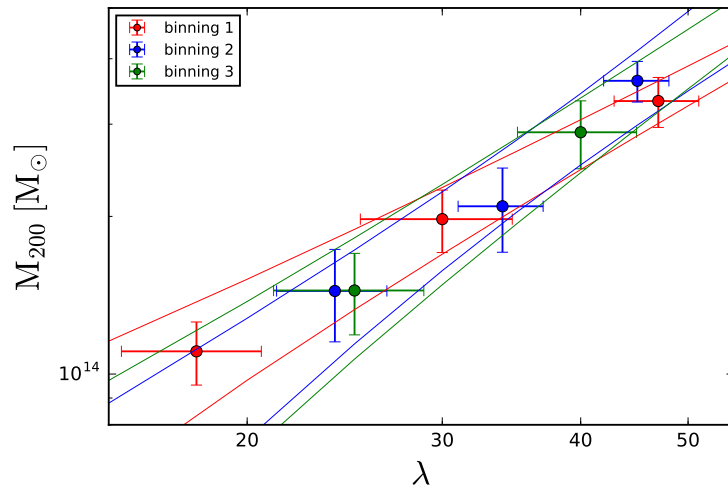


Figure 4.12 – Mass-richness relations obtained fitting different λ bins. The difference in normalization is $< 1\%$, and the difference in slope is $5 - 30\%$.

Binning	λ range	N	$\langle \lambda \rangle$
1	$15 < \lambda \leq 25$	91	18.5
	$25 < \lambda \leq 40$	45	30.7
	$40 < \lambda \leq 55$	12	47.0
2	$20 < \lambda \leq 30$	48	24.0
	$30 < \lambda \leq 40$	23	34.7
	$40 < \lambda \leq 50$	10	45.7
3	$20 < \lambda \leq 35$	58	25.3
	$35 < \lambda \leq 50$	23	40.8

Table 4.4 – Range in λ , the number of clusters, and the mean λ , for each bin in the different λ binnings

In Figure 4.12, I show the fitted mass-richness relations for the different binnings, and the 1σ confidence regions. I found that the relations are consistent within the errors. The difference in normalization is $< 1\%$, and the difference in slope is $5 - 30\%$. The binning affects mostly the size of the λ error bars and, therefore, the slope of the fitted relation.

This test shows that is important to bin clusters in richness bins as narrow as possible, and still preserve a significant signal-to-noise ratio in each stack of clusters.

4.5.5 Stacking and shear components

Stacking clusters is useful to increase the lensing signal-to-noise ratio and to make the coherent shear signal emerge from the noise of the background galaxies intrinsic ellipticity. As we saw, the shear aligns along the cluster potential lines. This means that for a spherically symmetric lens, we should observe only the tangential component of the shear.

In order to visualize this effect, in Figure 4.13, I show the shear field maps of the stacking of 50, 100, 150 clusters. We can clearly observe the expected progressive alignment of the shear bars around the center of the lens.

The cross component of the shear should be consistent with zero. This is observable in the stacked shear profiles of Figure 4.14, measured using the weak lensing *selected* CFHT-LS W1 + NGVS5 + NGVS4. In red, we find

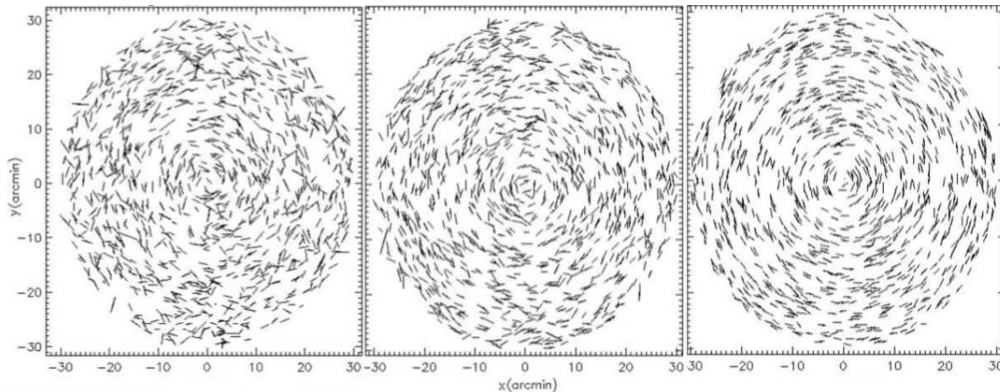


Figure 4.13 – *Shear field maps for the stacking of 50, 100, 150 clusters. Increasing progressively the number of stacked clusters, the shear signal emerges from the noise of the intrinsic ellipticity, and the shear bars align tangentially to the center of the stack.*

the tangential component (used to fit the profiles to the model), and in blue, the cross component that behaves as expected, within the error bars.

4.5.6 Centering

The error in the determination of the true cluster center is the systematic that can bias the most the mass estimation, if not correctly taken into account. From the fit to the stacked shear profiles, I found that miscentering can bias the mass low by 10 – 40%.

As we can see in Figure 4.15, this is true also for individual clusters. Masses estimated without taking into account miscentering (blue circles) are systematically underestimated, compared to the masses inferred with the miscetering correction (blue dots). In a few cases, the masses are underestimated of different orders of magnitude.

This shows again the importance of the cluster center selection, and of the correct modeling of miscentering.

In principle, cluster centers could be detected through the weak lensing signal, applying the aperture mass statistics, previously described. In order to test the reliability of weak lensing centers, I performed this analysis to simulated shear maps, to simulated clusters, and to observed RedGold clusters.

$\Delta\Sigma$ profiles

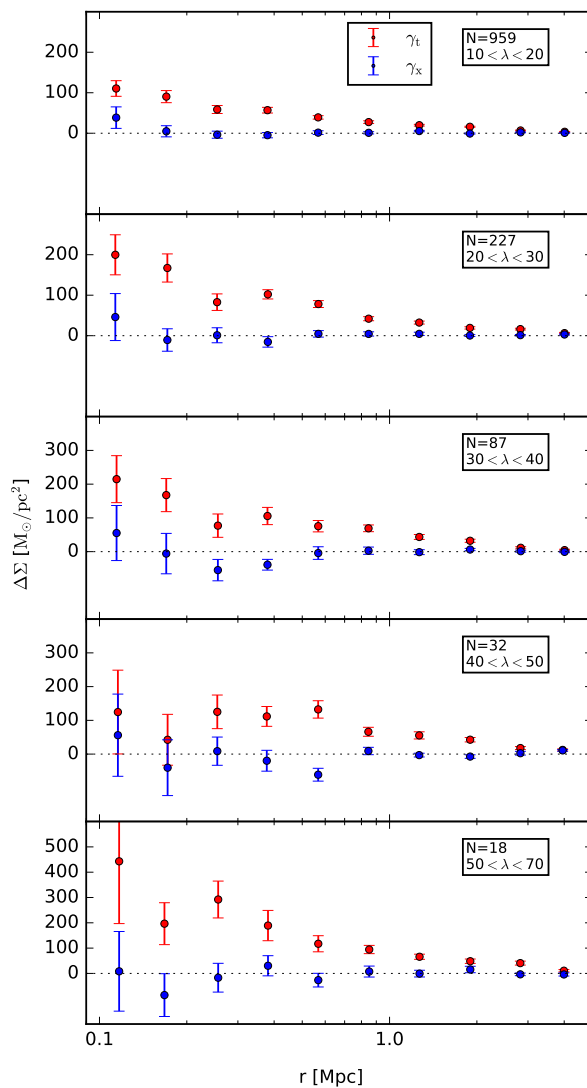


Figure 4.14 – *Shear profiles measured with the weak lensing selected CFHT-LS W1 + NGVS5 + NGVS4. In red the tangential shear component, and in blue the cross shear component. The cross component is consistent with zero, as expected from theory.*

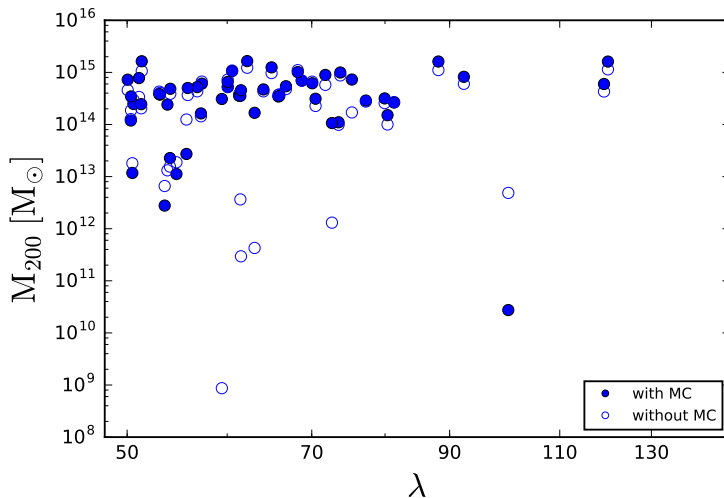


Figure 4.15 – *Masses of individual clusters obtained with the miscentering correction (blue dots), and without (blue circles). Masses are systematically underestimated without the miscentering correction.*

4.5.6.1 Simulated shear maps

I use a simple simulation of a background field of lensed source galaxies, provided by my collaborator Thomas Erben. The lens is a Singular Isothermal Sphere (SIS), with a velocity dispersion of 816 Km/s , located at $x = 677 \text{ pixel}$ and $y = 744 \text{ pixel}$, in an area that corresponds to 64 arcmin^2 , using a pixel scale of $0.238''$. The cosmology used for the simulation is an Einstein de Sitter universe (i.e. $\Omega_m = 1$ and $\Omega_\Lambda = 0$). The redshift of the lens is $z_1 = 0.3$, and the redshift of all the sources is $z_s = 1$. The number density of the sources is 25 arcmin^{-2} . I used two versions of this simulated shear field, one in which the galaxies don't have intrinsic ellipticities, and one more realistic in which this noise contribution is present.

In Figure 4.16, I show the lensing S/N ratio maps, obtained with aperture mass statistics and the shear field map, for the two versions on the simulation. The shear field maps were obtained averaging the ellipticity components in a grid of cells with side of 100 pixel .

The center is correctly identified in both cases, in the dark red region. The maps of the version without intrinsic ellipticity (on the top) are more regular, and show a much higher and unrealistic S/N ratio, compared to the version with intrinsic ellipticity (on the bottom). The maximum S/N ratio of the more realistic version is ~ 5 . This is typically considered a high lensing signal, and can be found for observed clusters with $M_{200} \gtrsim 5 \times 10^{14} M_\odot$.

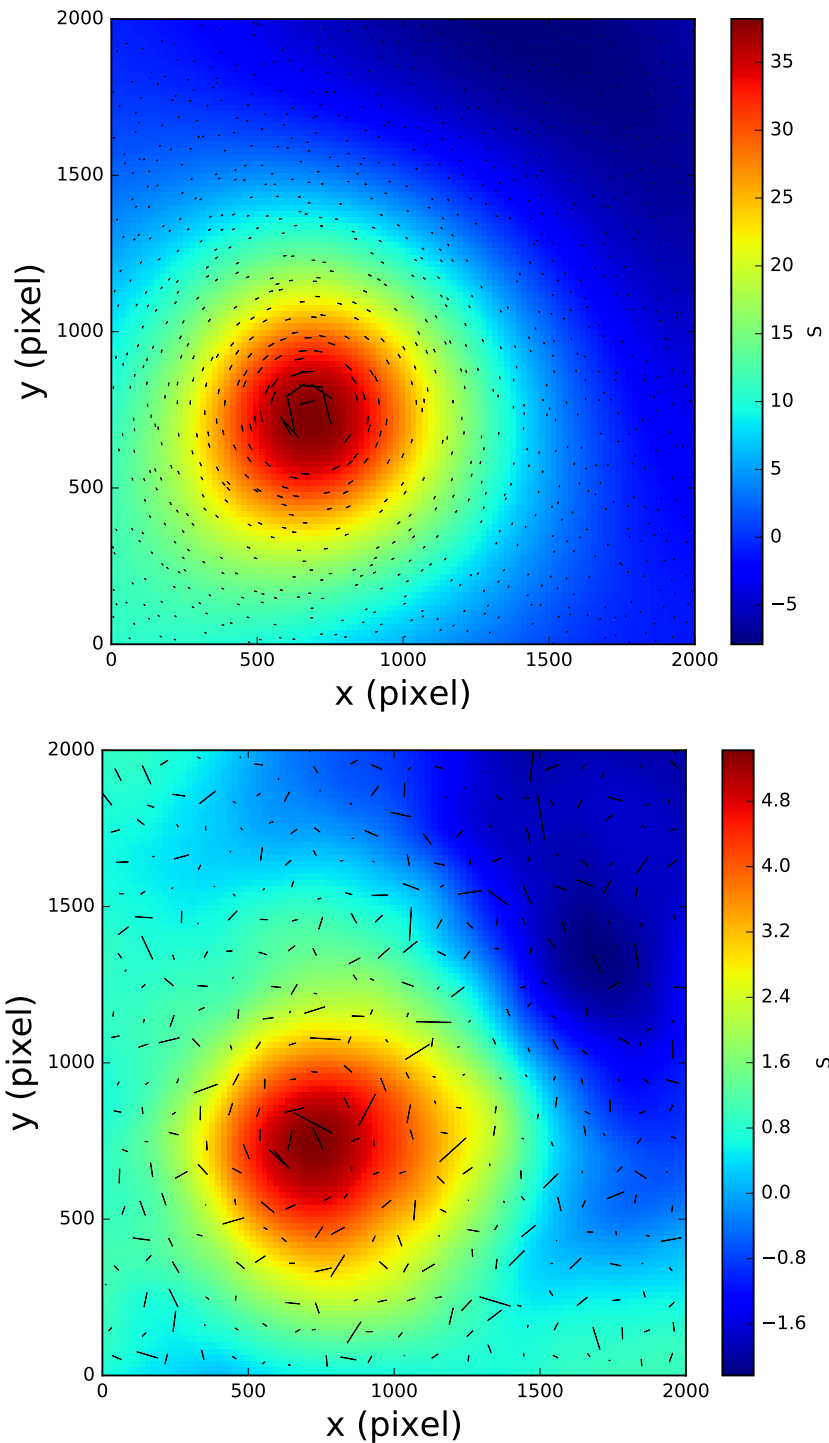


Figure 4.16 – On the top, the lensing S/N ratio map of the simulation without intrinsic ellipticity. On the bottom, the lensing S/N ratio map of the simulation with intrinsic ellipticity. The center (in dark red) is correctly recovered in both cases. We can notice that the contours and the orientation of the shear bars are less regular in the case with intrinsic ellipticity, as expected.

This means that it is possible to identify the center of observed massive clusters, using the lensing signal.

4.5.6.2 Simulated clusters

I used a simulated cluster Subaru observation in the r -band, performed by my collaborator Massimo Meneghetti (Meneghetti et al., 2016). The lens redshift is $z = 0.5$, and the cluster center coincides with the center of the field of view, which is $30' \times 30'$. The cluster image was processed with the public KSB pipeline, the KSBf90⁴. There are no substructures in the cluster.

In Figure 4.17, we find the image of the convergence of the simulated clusters (on top), and its S/N ratio map with the shear field map superimposed (on the bottom). As we can see, the center is correctly identified with the center of the field of view, in dark red. The color map and the shear field map are not perfectly circular but slightly elongated diagonally. They correctly reproduce what observed in the convergence map on the top.

4.5.6.3 Weak lensing analysis of the observed RedGOLD clusters

The tests that I performed have shown that the centering based on the weak lensing signal worked well for the simulations above. In order to test its performance on observed data, I applied the same analysis to the most massive clusters in the RedGOLD sample, with $\lambda > 50$, and compared the results with optical images. In Figure 4.18 and 4.19, I show the optical images (on the left), and the S/N ratio maps superimposed to the negative of the optical images (on the right). The white circles have a radius of $0.5r_{200}$ and r_{200} . The red squares sign the position of the cluster member galaxies and the black square is the center identified by RedGOLD. The S/N ratio maps were calculated inside r_{200} .

In Figure 4.18, the cluster centers identified by RedGOLD and those calculated using the weak lensing signal are in good agreement within a few arc seconds. The maximum of the lensing S/N ratio is between 3 and 4, as expected for observed clusters with $M_{200} \sim 10^{14}M_{\odot}$. The contours of the color maps are much more irregular compared to those obtained applying the centering algorithm to the simulations previously described. This is due to the fact that in observed images we find additional sources of noise (other than the intrinsic ellipticity) that are not present in the simulations, and a much lower background source density. In all maps, beside the cluster center in dark red, we can observe some orange and yellow regions that correspond to secondary lensing peaks. These peaks can represent real structures, as

⁴<http://www.roe.ac.uk/~heymans/KSBf90/Home.html>

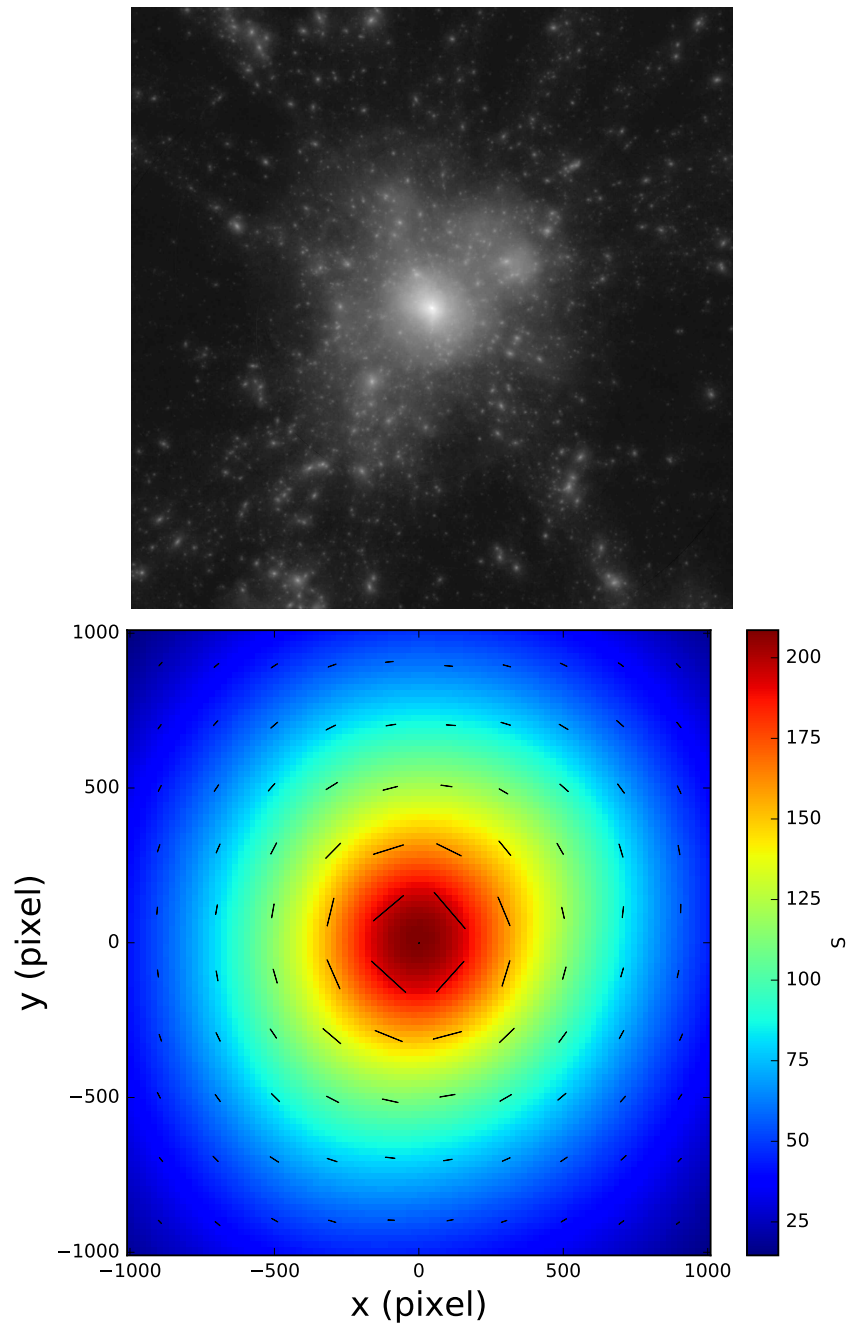


Figure 4.17 – *On the top, the convergence map of the simulated cluster. On the bottom, the S/N ratio map and the shear field map of the simulated cluster. The simulation comes from Meneghetti et al. (2016). We notice that the cluster center is correctly identified, and the color contours reproduce the diagonally elongated shape that we can see in the image on the top.*

for the cluster in the middle, in which the color map follows the diagonal distribution of the member galaxies (in red on the optical image on the left). In most of the cases though, the secondary peaks are due to noise that can simulate the lensing signal.

In Figure 4.19, I show some cases in which there is disagreement between the RedGOLD centers and the lensing centers, or in which other systematics make more difficult the center determination. In the images on the top, we can see that the member galaxy distribution is not well represented by the lensing map. The high S/N ratio region is smaller than what we would expect from the optical image, and the center is lower. The images in the middle present a masked region on the left due to a bright star. This could explain the asymmetry observed in the distribution of the cluster members that affects also the lensing map. In the images on the bottom, we can see a case in which RedGOLD fails to identify the cluster center. The cluster members distribution is clearly asymmetric and shows a higher density on the top right part of the image. The lensing map correctly identify the cluster center on the right, but shows a not negligible secondary peak on the left. The mean offset found in these case between the two center estimates is ~ 100 *arcsec*.

This analysis showed that, for observed data, the centering based on weak lensing cannot be used systematically since it is reliably applicable only on very massive clusters. This test showed also that aperture mass statistics gives reliable contours and S/N ratio in low noise situations, such as simulations or stacking of many observed clusters. Even though RedGOLD misidentifies the cluster center in some cases, the miscentering correction applied to the fit of stacked shear profiles is enough to account for this systematic.

4.5.7 Joint fit

In order to check that fitting the profile of each richness bin individually doesn't introduce a bias in the determination of the mass-richness relation parameters, I tested a *joint fit*. This method consists in the fit of the profiles associated to all richness bin simultaneously. In this case, the fitting parameters will be directly the normalization and slope of the mass-richness relation, and the likelihood of the model will be the sum of the likelihoods of all shear profiles.

Also for the *joint fit*, I tested different models:

Model 1) It has four parameters: $\log M_0$, α , p_{cc} , and σ_{off} , which are the normalization and slope of the mass-richness relation, and the miscentering

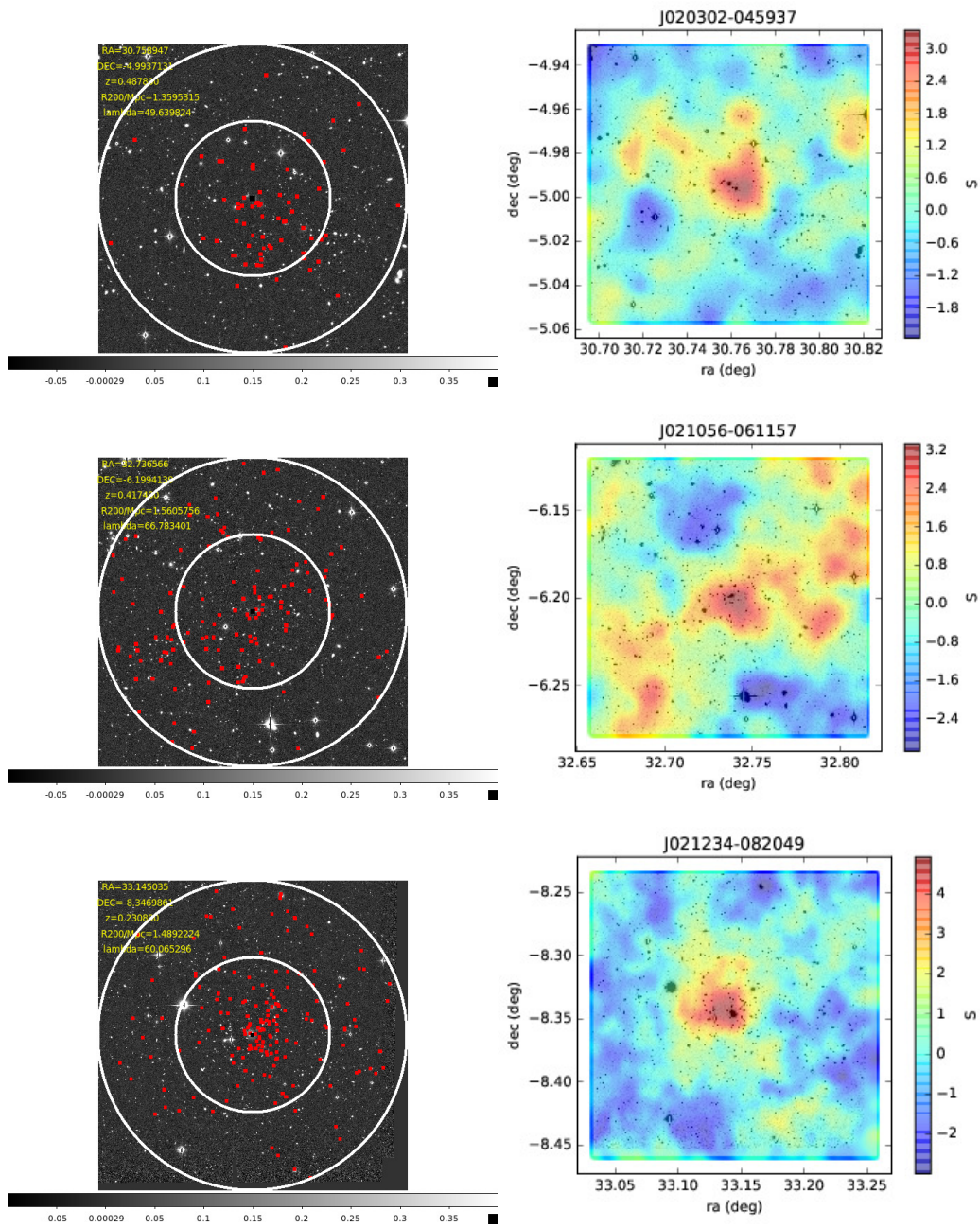


Figure 4.18 – On the left, the optical images of some of the most massive RedGOLD clusters. The white circles have a radius of $0.5r_{200}$ and r_{200} . The red squares sign the position of the cluster member galaxies and the black square is the center identified by RedGOLD. On the right, lensing S/N map inside r_{200} , superimposed on the negative of the optical image. There is good agreement between the centers estimated with the two different methods.

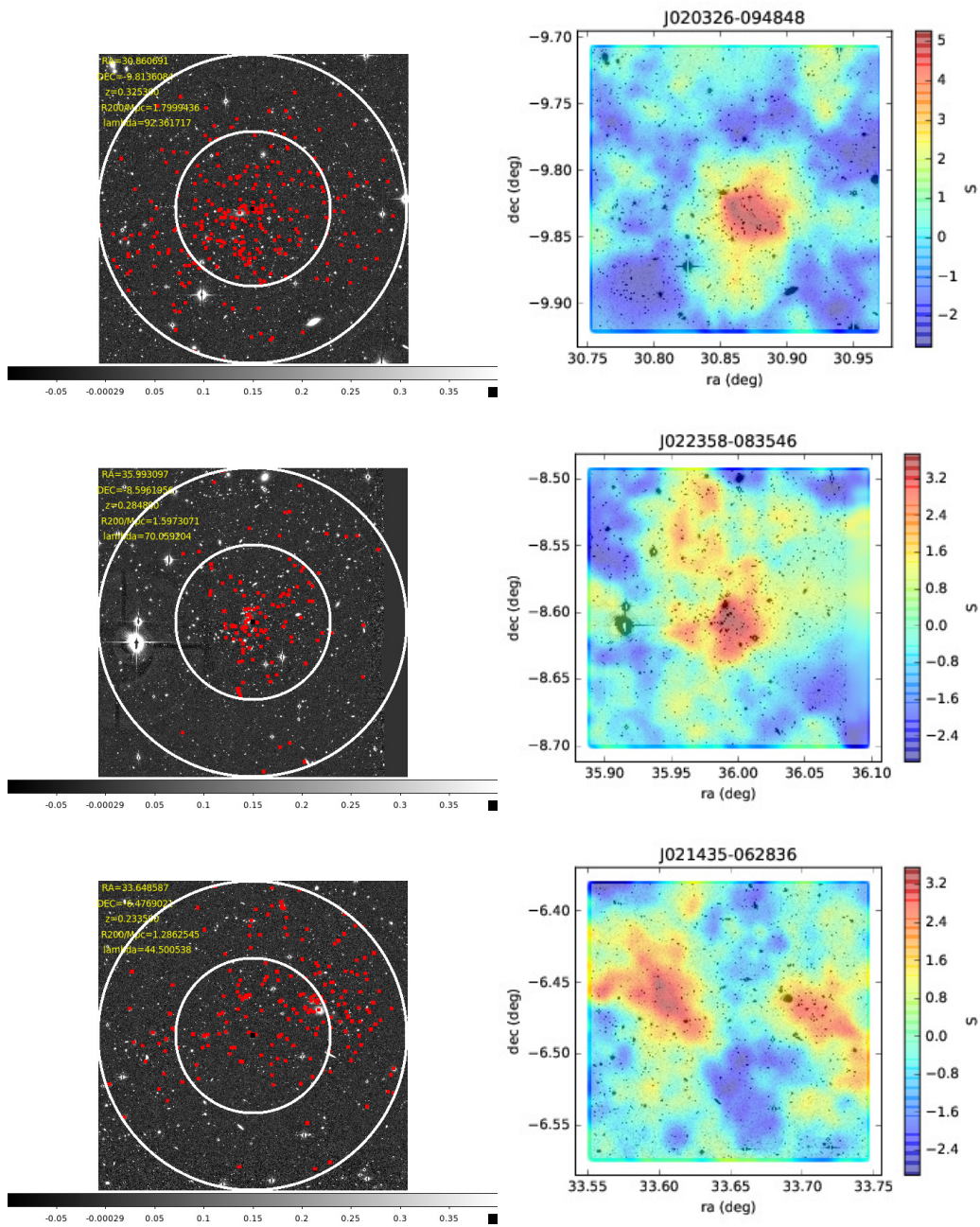


Figure 4.19 – Same as in Figure 4.18 but in this case the estimated centers don't agree. The mean offset is ~ 100 arcsec.

parameters. The BCG mass is fixed at the stellar mass calculated by my collaborator Anand Raichoor using *lePhare* (hereafter M_{BCG_*}).

Model 2) It has five parameters: $\log M_0$, α , p_{cc} , σ_{off} , and $\sigma_{M|\lambda}$, which are the parameters of Model 1 plus the intrinsic scatter of the mass-richness relation. The BCG mass is fixed at M_{BCG_*} .

Model 3) It has five parameters: $\log M_0$, α , p_{cc} , σ_{off} , and $aMbcg$, which are the parameters of Model 1 plus a constant that multiplies M_{BCG_*} so that, if we define the true BCG mass as M_{BCG} , we have $M_{\text{BCG}} = aMbcg \times M_{\text{BCG}_*}$.

Model 4) It has five parameters: $\log M_0$, α , p_{cc} , σ_{off} , and aCM , which are the parameters of Model 1 plus the amplitude of the mass-concentration relation used (i.e. Dutton & Macció, 2014). The BCG mass is fixed at M_{BCG_*} .

Model 5) has seven parameters: $\log M_0$, α , p_{cc} , σ_{off} , $\sigma_{M|\lambda}$, $aMbcg$, and aCM .

In Table 4.5 we find the priors on the parameters. In Table 4.6, we find the results of the MCMC for the different models.

Model	$\log M_0$	α	p_{cc}	σ_{off}	$\sigma_{M \lambda}$	aMbcg	aCM
1	(11,16)	(-2, 2)	(0, 1)	(0, 2)	–	–	–
2	(11,16)	(-2, 2)	(0, 1)	(0, 2)	(0.1, 0.7)	–	–
3	(11,16)	(-2, 2)	(0, 1)	(0, 2)	–	(0, 10)	–
4	(11,16)	(-2, 2)	(0, 1)	(0, 2)	–	–	(0, 10)
5	(11,16)	(-2, 2)	(0, 1)	(0, 2)	(0.1, 0.7)	(0, 10)	(0, 10)

Table 4.5 – *MCMC uniform prior ranges for the different parameters of the five models of the joint fit. The lack of a numerical value indicates that the parameter is not included in the respective model.*

I found that the results from the different models are consistent with each other within 1σ or 2σ . The normalization and slope of the mass-richness relation are well constrained in all models. $aMbcg$ is not constrained, as the BCG mass is not constrained even in the *Two Component Model*, with the version of the fit I used for my final analysis. aCM is constrained but it is slightly degenerate with the miscentering parameters. σ_{off} in particular is less well constrained in the models that include aCM . Moreover, for these

Model	$\log M_0$	α	p_{cc}	σ_{off}	$\sigma_{M \lambda}$	aMbcg	aCM
1	$14.49^{+0.03}_{-0.03}$	$1.28^{+0.06}_{-0.06}$	$0.65^{+0.05}_{-0.05}$	$0.86^{+0.45}_{-0.33}$	–	–	–
2	$14.49^{+0.05}_{-0.05}$	$1.27^{+0.15}_{-0.13}$	$0.65^{+0.04}_{-0.06}$	$1.00^{+0.49}_{-0.43}$	$0.12^{+0.05}_{-0.01}$	–	–
3	$14.48^{+0.03}_{-0.03}$	$1.28^{+0.06}_{-0.06}$	$0.65^{+0.05}_{-0.06}$	$0.82^{+0.46}_{-0.35}$	–	$3.69^{+4.10}_{-2.79}$	–
4	$14.41^{+0.02}_{-0.02}$	$1.19^{+0.06}_{-0.06}$	$0.83^{+0.10}_{-0.18}$	$0.56^{+0.75}_{-0.40}$	–	–	$0.65^{+0.07}_{-0.06}$
5	$14.40^{+0.04}_{-0.06}$	$1.17^{+0.14}_{-0.12}$	$0.83^{+0.11}_{-0.16}$	$0.56^{+0.69}_{-0.40}$	$0.13^{+0.07}_{-0.02}$	$2.25^{+4.23}_{-1.26}$	$0.64^{+0.08}_{-0.06}$

Table 4.6 – *Parameters derived for the five models of the joint fit. The results are consistent with each other within 1σ or 2σ .*

models the normalization and slope of the mass-richness relation have lower values compared to the models without *aCM*. $\sigma_{M|\lambda}$ seems to be constrained but it has a much smaller value compared to what expected from Licitra et al. (2016a,b).

When comparing the results from the *joint fit* with what obtained fitting each richness bin individually and then inferring the mass-richness relation as a different step, I find consistent results ($< 1 - 2\sigma$), confirming the validity of both approaches.

4.6 Results

In this section I will show the results that I obtained applying the method described so far, and tested on different data and simulations.

I will describe the mass estimation procedure for the different models and the fit of the mass-richness relation and of the lensing mass versus X-ray mass proxies scaling relations.

4.6.1 Mass estimation

After calculating the shear profiles as described in Section 4.4.1, I fit them with the shear profile models of Section 4.4.2, for the *Basic Model*, the *Added Scatter Model*, and the *Two Component Model*, as explained in Section 4.4.3.

Here I summarize the characteristics of the three models:

Basic Model) It consists of a basic halo model, with an NFW surface density contrast and correction terms that take into account cluster miscentering, non-weak shear and the two halo term. It has three free parameters: the radius r_{200} , from which we calculate the mass M_{200} from Equation 1.6, and the miscentering parameters p_{cc} , and σ_{off} .

Added Scatter Model) It is based on the *Basic Model* but takes into account also the intrinsic scatter in the mass-richness relation. It has four free parameters: $\log M_{200}$, p_{cc} , σ_{off} , and $\sigma_{M|\lambda}$. For each bin, we use the mass-richness relation calculated from the *Basic Model* to infer the mean mass of the stacked clusters, as a first approximation. We then randomly scatter the mass using a gaussian distribution with mean $\langle \ln M_{200} \rangle$ and width $\sigma_{\ln M_{200}|\lambda}$.

Two Component Model) It is based on the *Basic Model* but takes into account also the contribution from the BCG mass. When we set free the BCG mass, this model has four free parameters: r_{200} , p_{cc} , σ_{off} , and $\log M_{BCG}$. When we fix the BCG mass to the mean stellar mass for each richness bin, $M_{BCG} = M_{BCG}^*$, the free parameters reduce to three.

I performed this analysis on the CFHTLS-W1, NGVS5 and NGVS4 samples individually, then on the CFHTLS-W1 and the NGVS5 samples combined and, finally, on the three samples together. This was done to check the improvement obtained in the shear profiles, stacking a progressively greater number of clusters. With this procedure I also checked that the addition of the four bands catalog didn't introduce a bias in the shear profiles and mass estimates.

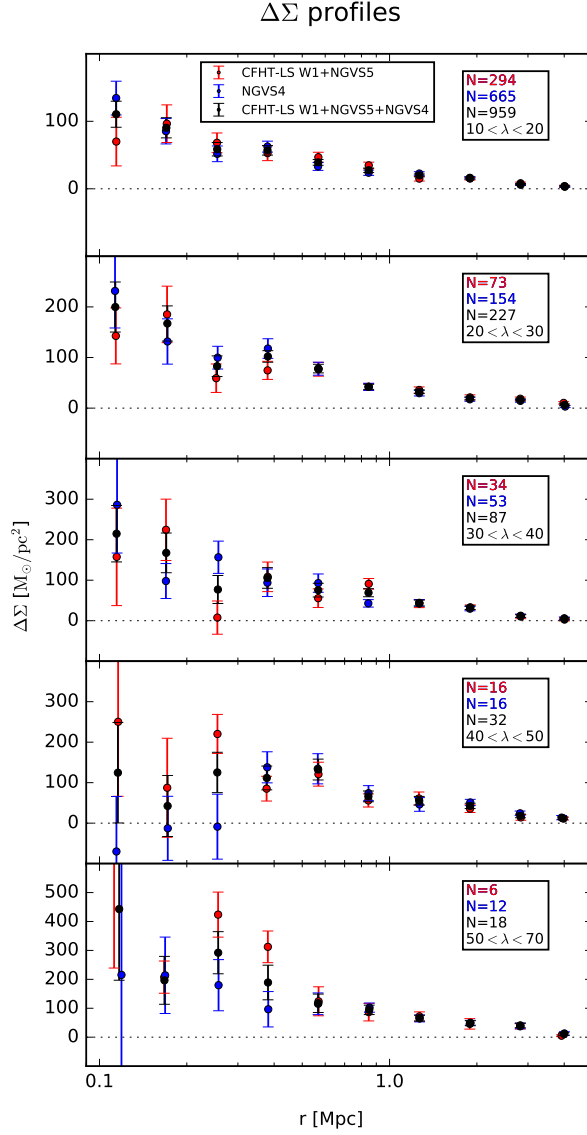


Figure 4.20 – Shear profiles measured with the weak lensing selected CFHT-LS W1 + NGVS5, in red, with weak lensing selected NGVS4, in blue, and with the weak lensing selected CFHT-LS W1 + NGVS5 + NGVS4, in black. We notice that the addition of the four bands sample does not significantly change the profiles. The profiles measured using the three different samples are compatible within 1σ and the profiles obtained using CFHT-LS W1 + NGVS5 + NGVS4 have smaller error bars.

	NGVS4			CFHT-LS W1 + NGVS5			ALL		
	N cluster	n_{gal}	$\langle n_{gal} \rangle$	N cluster	n_{gal}	$\langle n_{gal} \rangle$	N cluster	n_{gal}	$\langle n_{gal} \rangle$
bin 1	665	3359	5	294	1801	6	959	5184	5
bin 2	154	787	5	73	463	6	227	1263	5
bin 3	53	257	5	34	233	7	87	499	5
bin 4	16	88	5	16	102	6	32	190	5
bin 5	12	79	6	6	38	6	18	118	6

Table 4.7 – Total number of clusters, total number density of background sources, mean number density of background sources, for each richness bin and for the three samples considered.

The profiles measured using the CFHT-LS W1 + NGVS5 sample, the NGVS4 sample, and the complete sample are shown in Figure 4.20. They are consistent within 1σ and the error bars are smaller in the last case. We can conclude that the richness shifts applied to NGVS4 seem not to bias the results, when this sample is added to the other two, covered by five bands. As shown in Table 4.7, increasing the sample size, and therefore the number density of background sources, we notice a progressive improvement in the profiles which are recovered with a lower noise level.

The profiles obtained using the *Basic Model* and the complete sample (CFHT-LS W1 + NGVS5 + NGVS4) are shown in green in Fig. 4.21. The error bars on the shear profiles are the square root of the diagonal elements of the covariance matrix.

Since the miscentering correction is the one that most affects the mass estimation, in Figure 4.21, on the left, I show the fitted profiles (green lines), and the profiles that we would obtain with and without the miscentering term. The red lines represent the profiles we would obtain in the case in which all the clusters in the stack were perfectly centered ($p_{cc} = 1$), and the blue lines show the opposite case ($p_{cc} = 0$). An incorrect modeling of this effect leads to biased mass values (i.e. mass underestimation between 10 – 40%, Ford et al., 2015).

In Figure 4.21, on the right, I show the lensing signal-to-noise ratio maps. I calculated these maps using aperture mass statistics (Schneider, 1996; Schirmer et al., 2006; Du & Fan, 2014). For each richness bin, I created a grid with a side of 1 Mpc and binning of 0.001 deg , centered on the stacked clusters. In each cell, I evaluated the amount of tangential shear, filtered by a function that maximizes the signal-to-noise ratio of an NFW profile, inside

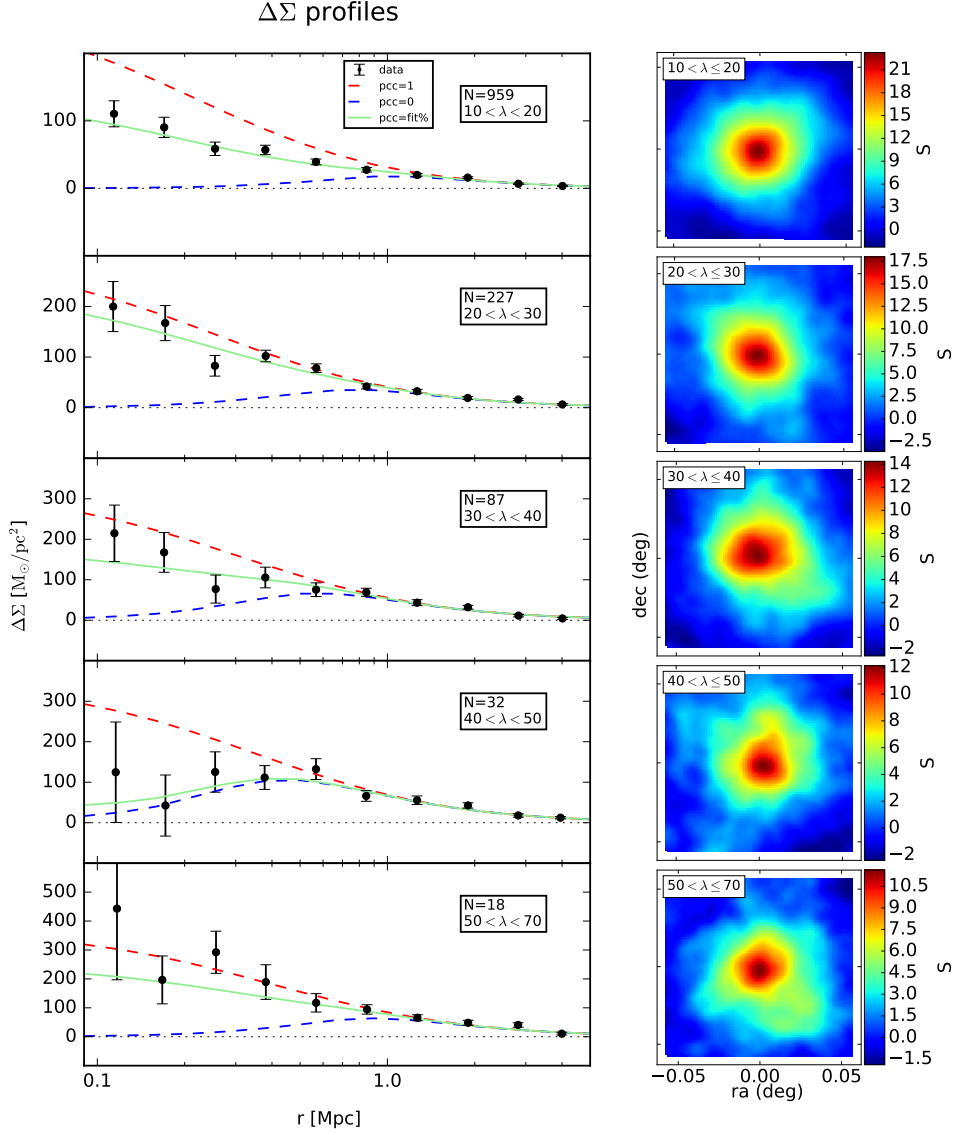


Figure 4.21 – On the left: shear profiles measured with the complete sample (CFHT-LS W1 + NGVS5 + NGVS4). The fits were obtained using the Basic Model. I show the shear profile measurement (black), the fit results (green), the ideal profiles that we would obtain in the case in which all the clusters in the stack were perfectly centered (red) and when they would have been all miscentered (blue). The dotted lines show $\Delta\Sigma(R) = 0$. I get similar results using the Added Scatter Model and the Two Component Model. On the right: lensing signal-to-noise ratio maps in each richness bin for the complete sample. I applied aperture mass statistics.

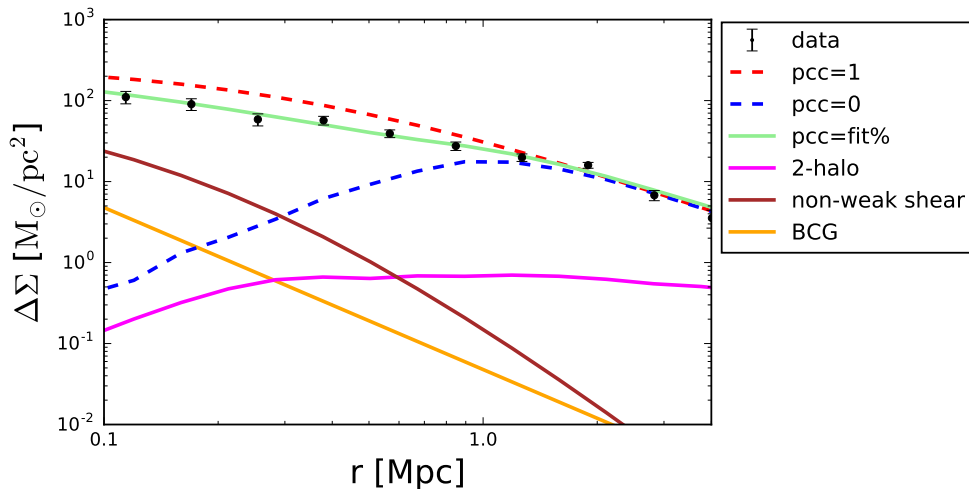


Figure 4.22 – Contribution of the different terms of Equation 4.29 to the shear profile, calculated from the first richness bin.

a circular aperture, following Schirmer et al. (2006). For stacked clusters, a $S/N \sim 10$ is considered sufficient to recover the fitting parameters (Oguri & Takada, 2011). All richness bins have $S/N \geq 10$. The highest richness bin shows the lowest S/N , being less populated than the others.

I show the results of the fits in Table 4.8, for the three models. The values of the radius, of the mass, and of the miscentering parameters, for each richness bin, are consistent within 1σ for the three models. I found that the intrinsic scatter and BCG mass are not constrained by the data. The main effect of the addition of $\sigma_{M|\lambda}$ to the fit is to introduce more uncertainties and to increase the error on the estimated parameters. The inclusion of M_{BCG} in the model (either set as a free parameter or fixed to M_{BCG}^*) has no impact on the estimated parameters, that are therefore the same as those obtained using the *Basic Model*. We can conclude that the contribution of the BCG mass is not significant in the radial range that I used to fit the shear profiles. This is confirmed looking at Figure 4.22, where the contribution from the different terms is shown for the first richness bin. The green, red, and blue lines have the same meaning as In Figure 4.21, while the magenta line represents the contribution from the 2-halo term, the brown line is the non-weak shear term, and the orange line is the BCG point mass signal. As expected the non-weak shear term and the BCG signal increase in the inner part of the radial profile, while the 2-halo term is more important for the outer part.

λ range	N	λ	z	Model	r_{200} Mpc	M_{200} $10^{13}M_{\odot}$	σ_{off} arcmin	p_{cc}	$\sigma_{\ln M \lambda}$	$M_{\text{BCG}} (M_{\text{BCG}}^*)$ $10^{11}M_{\odot}$
$10 < \lambda \leq 20$	959	14 ± 3	0.40	Basic	$0.83_{-0.03}^{+0.03}$	10_{-1}^{+1}	$1.5_{-0.3}^{+0.3}$	$0.5_{-0.1}^{+0.1}$	–	–
				Added Scatter	$0.86_{-0.13}^{+0.13}$	11_{-5}^{+5}	$1.5_{-0.3}^{+0.3}$	$0.5_{-0.1}^{+0.1}$	$0.4_{-0.2}^{+0.2}$	–
				Two Component	$0.83_{-0.03}^{+0.02}$	10_{-1}^{+1}	$1.5_{-0.3}^{+0.3}$	$0.5_{-0.1}^{+0.1}$	–	$1_{-3}^{+3} (1.53_{-0.02}^{+0.02})$
$20 < \lambda \leq 30$	227	24 ± 3	0.39	Basic	$0.94_{-0.04}^{+0.03}$	14_{-2}^{+1}	$1.0_{-0.7}^{+0.7}$	$0.7_{-0.1}^{+0.2}$	–	–
				Added Scatter	$0.94_{-0.08}^{+0.08}$	14_{-3}^{+4}	$0.9_{-0.8}^{+0.7}$	$0.8_{-0.1}^{+0.2}$	$0.4_{-0.2}^{+0.2}$	–
				Two Component	$0.94_{-0.04}^{+0.03}$	14_{-2}^{+1}	$1.0_{-0.7}^{+0.7}$	$0.7_{-0.1}^{+0.2}$	–	$1_{-3}^{+3} (1.7_{-0.1}^{+0.1})$
$30 < \lambda \leq 40$	87	34 ± 3	0.39	Basic	$1.09_{-0.05}^{+0.05}$	22_{-3}^{+3}	$0.7_{-0.5}^{+0.3}$	$0.6_{-0.1}^{+0.2}$	–	–
				Added Scatter	$1.12_{-0.13}^{+0.11}$	24_{-9}^{+7}	$0.7_{-0.4}^{+0.3}$	$0.6_{-0.2}^{+0.2}$	$0.4_{-0.2}^{+0.2}$	–
				Two Component	$1.09_{-0.05}^{+0.05}$	22_{-3}^{+3}	$0.7_{-0.5}^{+0.3}$	$0.6_{-0.2}^{+0.2}$	–	$1_{-3}^{+3} (1.8_{-0.1}^{+0.1})$
$40 < \lambda \leq 50$	32	44 ± 3	0.39	Basic	$1.21_{-0.03}^{+0.04}$	30_{-3}^{+3}	$0.5_{-0.1}^{+0.1}$	$0.1_{-0.1}^{+0.1}$	–	–
				Added Scatter	$1.18_{-0.11}^{+0.10}$	28_{-8}^{+7}	$0.5_{-0.1}^{+0.1}$	$0.1_{-0.1}^{+0.1}$	$0.4_{-0.2}^{+0.2}$	–
				Two Component	$1.21_{-0.03}^{+0.04}$	30_{-3}^{+3}	$0.5_{-0.1}^{+0.1}$	$0.1_{-0.1}^{+0.1}$	–	$1_{-3}^{+3} (1.9_{-0.2}^{+0.2})$
$50 < \lambda \leq 70$	18	59 ± 6	0.38	Basic	$1.35_{-0.05}^{+0.04}$	41_{-4}^{+4}	$1.1_{-0.6}^{+0.8}$	$0.7_{-0.2}^{+0.2}$	–	–
				Added Scatter	$1.35_{-0.27}^{+0.26}$	41_{-2}^{+2}	$0.9_{-0.7}^{+0.7}$	$0.7_{-0.2}^{+0.3}$	$0.4_{-0.2}^{+0.2}$	–
				Two Component	$1.35_{-0.05}^{+0.04}$	41_{-5}^{+4}	$1.1_{-0.6}^{+0.8}$	$0.7_{-0.2}^{+0.2}$	–	$1_{-4}^{+4} (2.0_{-0.2}^{+0.2})$

Table 4.8 – *Parameters derived from the fit of the Basic Model, the Added Scatter Model, and the Two Component Model shear profiles to the measurements. λ is the cluster optical richness derived with RedGOLD and the first column gives the richness range; N is the number of stacked clusters in each bin; z is the mean redshift; r_{200} is the mean radius in Mpc; M_{200} is the mean mass in units of $10^{13}M_{\odot}$; σ_{off} is the scale length of the offset distribution in arcmin; p_{cc} is the percentage of correctly centered clusters in the stack; $\sigma_{\ln M|\lambda}$ is the intrinsic scatter in the mass-richness relation; $M_{\text{BCG}} (M_{\text{BCG}}^*)$ is the mean BCG mass in units of $10^{11}M_{\odot}$, left as a free parameter in the fit, and fixed at the stellar mass value recovered with LePhare, respectively.*

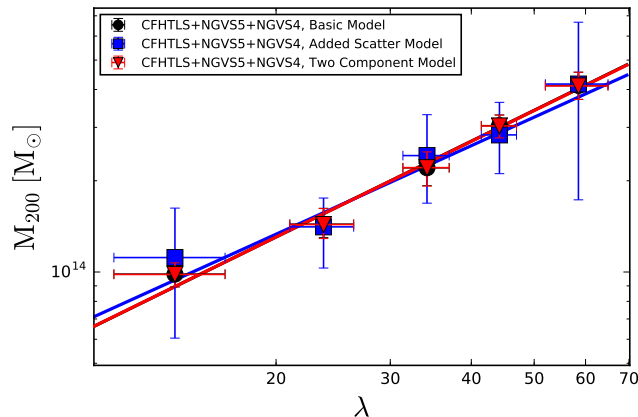


Figure 4.23 – The weak lensing mass-richness relations obtained with the complete sample *CFHT-LS W1 + NGVS5 + NGVS4*, using the *Basic Model* (black line and black dots), the *Added Scatter Model* (blue line and blue squares), and the *Two Component Model* (red line and red triangles). See text for the description of the models.

4.6.2 Mass-richness relation

Using the mass measured for each richness bin, I performed a fit to a power law to infer the mass-richness relation for all three models, using the python orthogonal distance regression routine (ODR; Boggs & Rogers, 1990) to take into account the errors in both $\log \lambda$ and $\log M_{200}$:

$$\log M_{200} = \log M_0 + \alpha \log \lambda / \lambda_0 \quad (4.31)$$

with a pivot richness $\lambda_0 = 40$.

In Table 4.9 and in Figure 4.23, I show the results obtained fitting the three models. The slope and the normalization values are all consistent within 1σ , for the three models. We notice that the uncertainties in the fit of the *Added Scatter Model* are larger, due to the inclusion of the intrinsic scatter as a free parameter.

In order to take into account the intrinsic scatter between richness and mass also in the *Basic Model* and in the *Two Component Model*, and compare the results with those obtained when using the *Added Scatter Model*, I applied an a posteriori correction as in Ford et al. (2015). Using the mass-richness relation inferred from the *Basic Model* and the *Two Component Model*, I calculated the mass of all the clusters in the sample, then I scattered those masses assuming a log-normal distribution centered on $\log M_{200}$ and with a width $\sigma_{\ln M|\lambda} = 0.39$, based on the value measured by Licitra et al. (2016a). I

Model	$\log M_0$	α	$\langle \text{diff} \rangle_G$	$\langle \text{diff} \rangle_M$	$\langle \text{diff} \rangle_P$	$\langle M_L/M_X \rangle_G$	$\langle M_L/M_X \rangle_M$	$\langle M_L/M_X \rangle_P$
Basic	14.43 ± 0.01	1.05 ± 0.07	0.06 ± 0.19	-0.07 ± 0.99	0.42 ± 0.22	1.06 ± 0.19	0.93 ± 0.99	1.42 ± 0.22
Basic + ISC	14.47 ± 0.02	1.05 ± 0.09	0.17 ± 0.20	0.01 ± 1.07	0.56 ± 0.24	1.17 ± 0.20	1.01 ± 1.07	1.56 ± 0.24
Added Scatter	14.42 ± 0.03	0.97 ± 0.14	0.12 ± 0.21	-0.07 ± 1.06	0.35 ± 0.24	1.12 ± 0.21	0.93 ± 1.06	1.35 ± 0.24
Two Component	14.43 ± 0.01	1.05 ± 0.07	0.06 ± 0.19	-0.07 ± 0.99	0.42 ± 0.22	1.06 ± 0.19	0.93 ± 0.99	1.42 ± 0.22
Two Component + ISC	14.46 ± 0.02	1.04 ± 0.09	0.15 ± 0.20	-0.00 ± 1.06	0.52 ± 0.24	1.15 ± 0.20	1.00 ± 1.06	1.52 ± 0.24

Table 4.9 – *Results of the fit of the mass-richness relation: $\log M_{200} = \log M_0 + \alpha \log \lambda/\lambda_0$, with a pivot $\lambda_0 = 40$, obtained using the three models. For the Basic Model and for the Two Component Model, I also show the results after applying the a posteriori intrinsic scatter correction (ISC). The last six columns show the normalized average difference between lensing and X-ray masses, $\langle \text{diff} \rangle = (M_L - M_X)/M_X$, and the average ratio of the two, $\langle M_L/M_X \rangle$, using the X-ray detections of Gozaliasl et al. (2014) (G), Mehrrens et al. (2012) (M), and Piffaretti et al. (2011) (P).*

repeated this procedure creating 1000 bootstrap realizations, choosing masses randomly with replacements from the entire sample. I calculated the new mean mass values in each richness bin and averaged them over all bootstrap realizations. I then repeated the fit to infer the new mass-richness relation. This procedure is illustrated in Fig. 4.24, where I show the results from the fit to the *Two Component Model* (in black), the scattered masses (in light red), and the new mean masses and mass-richness relation (in red). Due to the shape of the halo mass function, the net effect of the intrinsic scatter correction is to lead to a slightly higher normalization value of the mass-richness relation. The difference in normalization for the *Basic Model* and the *Two Component Model*, and their scattered versions is less than 1%.

Having verified the impact of each model term on the final results, I consider as the *Final Model* the model that takes into account all the parameters considered so far, the *Two Component Model* with the a posteriori intrinsic scatter correction. Hereafter I will quote as the final mass-richness relation the one calculated from the *Final Model*: $\log M_0 = 14.46 \pm 0.02$ and $\alpha = 1.04 \pm 0.09$.

As shown in Section 4.5, I checked that the richness binning choice does not affect significantly the recovered mass-richness relation. I verified that fitting each richness bin individually, and then fitting the mass-richness relation as a second step, does not significantly change my results. Moreover, the addition of a scatter of 0.14 dex (as in Simet et al., 2016) in the concentration-mass relation, does not change the fitted parameters and the derived mass-richness relation, as can be seen in Figure 4.25.

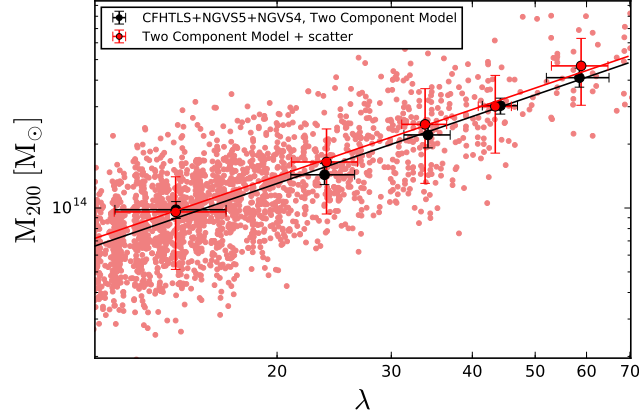


Figure 4.24 – *Effect of the a posteriori intrinsic scatter correction. Using the mass-richness relation inferred from Two Component Model (in black), I calculated cluster masses for the selected sample. I scattered those masses assuming a log-normal distribution centered on $\log M_{200}$ and with a width $\sigma_{\ln M|\lambda} = 0.39$, based on the value measured by Licitra et al. (2016a) (in light red). I repeated this procedure creating 1000 bootstrap realizations and calculated the new mean mass values in each richness bin, averaging over all realizations. I then repeated the fit to infer the new mass-richness relation (in red), which is shifted towards larger masses.*

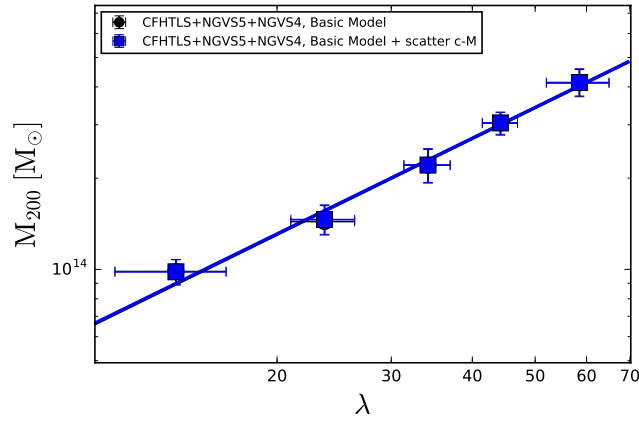


Figure 4.25 – *Comparison of the mass-richness relations derived with (blue) and without scatter (black) in the concentration-mass relation. The value of the scatter was fixed to 0.14 dex as in Simet et al. (2016).*

4.6.3 Weak lensing mass vs X-ray mass proxies relations

In order to compare the lensing masses that I calculated with X-ray mass proxies, I used the X-ray catalogs described in Section 4.3.2. As said before, Gozaliasl et al. (2014) M_{200} masses were estimated using the lensing $M_X - L$ relation of Leauthaud et al. (2010). I estimated Mehrrens et al. (2012) M_{200} masses from the r_{200} values given in their catalog, using eq. 1.6. Piffaretti et al. (2011) masses were estimated using the luminosity-mass relation calibrated from the $M - Y_X$ relation of Arnaud et al. (2007, 2010), assuming hydrostatic equilibrium. The masses M_{200}^{lens} were calculated using the mass-richness relation from the *Final Model*.

In Figure 4.26, I show the normalized difference between the lensing masses and the X-ray masses $(M_{200}^{lens} - M_{200}^X) / M_{200}^X$ as a function of M_{200}^X , for Gozaliasl et al. (2014) catalog (top), Mehrrens et al. (2012) catalog (middle), and Piffaretti et al. (2011) (bottom). The ratio is measured with respect to M_{200}^X since this sample is X-ray selected (i.e. I selected the clusters in the X-ray catalog, and then compare their X-ray and lensing mass estimate).

In the last six columns of Table 4.9, I show the mean normalized difference and the mean ratio between lensing and X-ray masses, for the three models, obtained with Gozaliasl et al. (2014), Mehrrens et al. (2012), and Piffaretti et al. (2011) catalogs. For all models, the mean differences obtained using M_{200}^X from Piffaretti et al. (2011) ($\sim 0.4 - 0.6$) are higher than those obtained using Gozaliasl et al. (2014) ($\sim 0.1 - 0.2$) and Mehrrens et al. (2012) ($\sim -0.1 - 0.0$). However, uncertainties on the individual measurements are larger and the scatter in the difference is about an order of magnitude higher for the Mehrrens et al. (2012) sample, as can be seen in Figure 4.26. Piffaretti et al. (2011) did not give an estimate of the error on the mass in their catalog.

Using Gozaliasl et al. (2014) catalog and the lensing masses estimated from the mass-richness relation derived from the *Final Model*, applied on the *complete* catalogs, I found a mean normalized difference of 0.15 ± 0.20 ($\frac{M_{200}^{lens}}{M_{200}^X} = 1.15 \pm 0.20$), considering the whole mass range. If we consider two different mass ranges, we find a mean normalized difference of 0.17 ± 0.24 for $M_{200}^X < 10^{14} M_\odot$, and a mean normalized difference of 0.14 ± 0.18 for $M_{200}^X \geq 10^{14} M_\odot$.

With Piffaretti et al. (2011) catalog I found a mean normalized difference of 0.52 ± 0.24 ($\frac{M_{200}^{lens}}{M_{200}^X} = 1.52 \pm 0.24$).

Matching the lensing masses with those of Gozaliasl et al. (2014) and Piffaretti et al. (2011), based on core-excised X-ray luminosities and temperatures, I found a much lower scatter compared with Mehrrens et al. (2012) masses, calculated without core excision. This indicates that core-excised X-

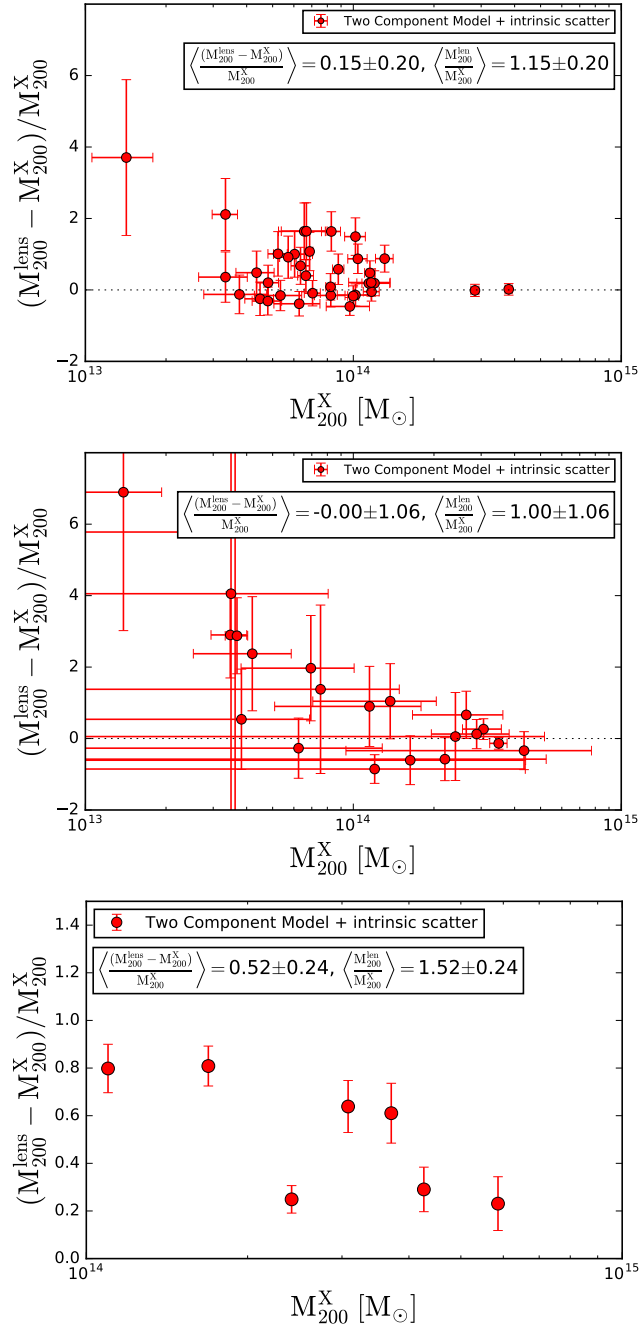


Figure 4.26 – Comparison of lensing masses and X-ray masses calculated from the fitted mass-richness relations obtained using the Final Model (i.e. the Two Component Model with the a posteriori intrinsic scatter correction). Using Gozaliasi et al. (2014) catalog (top), I obtained a mean normalized difference of 0.15 ± 0.20 and a mean ratio of 1.15 ± 0.20 , using Mehrrens et al. (2012) catalog (middle), I found -0.00 ± 1.06 and 1.00 ± 1.06 , while using Piffaretti et al. (2011) I found 0.52 ± 0.24 and 1.52 ± 0.24 , respectively.

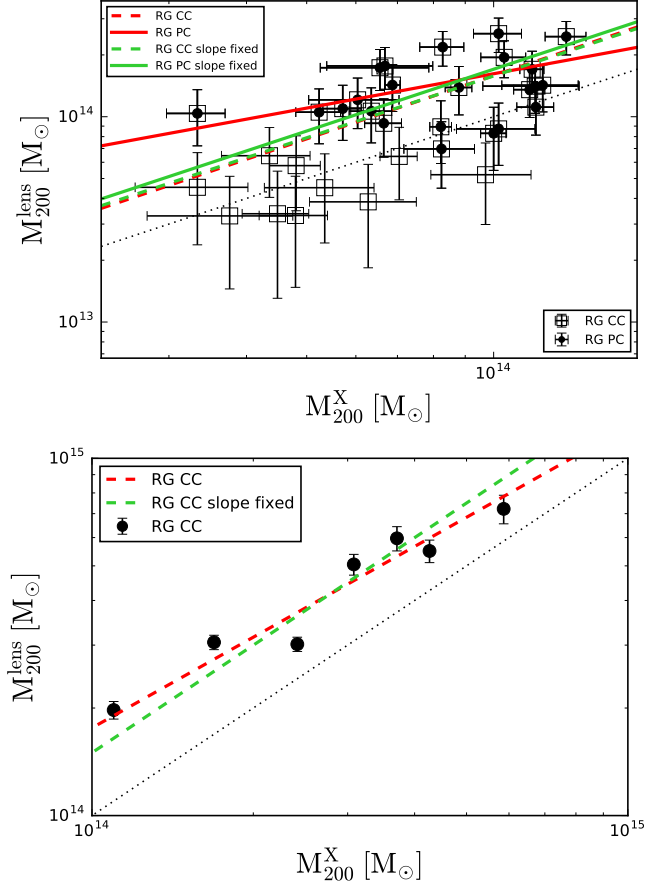


Figure 4.27 – I compare the weak lensing derived masses with the masses from Gozaliasl et al. (2014) (top) and Piffaretti et al. (2011) (bottom) X-ray catalogs. The weak lensing masses have been derived from the fit of the mass-richness relation using the Final Model with the a posteriori intrinsic scatter correction. The black dots are the RedGOLD detections from the published catalogs (RG PC) and the black squares are the detections from the complete catalogs (RG CC). The red lines show the fits obtained with the slope as a free parameter, and the green lines those obtained with the slope fixed at unity. In both cases, solid lines refer to the published catalogs, and the dashed lines, to the complete catalogs. The black dotted line is the diagonal. See Section 4.3.1 for the catalog definitions.

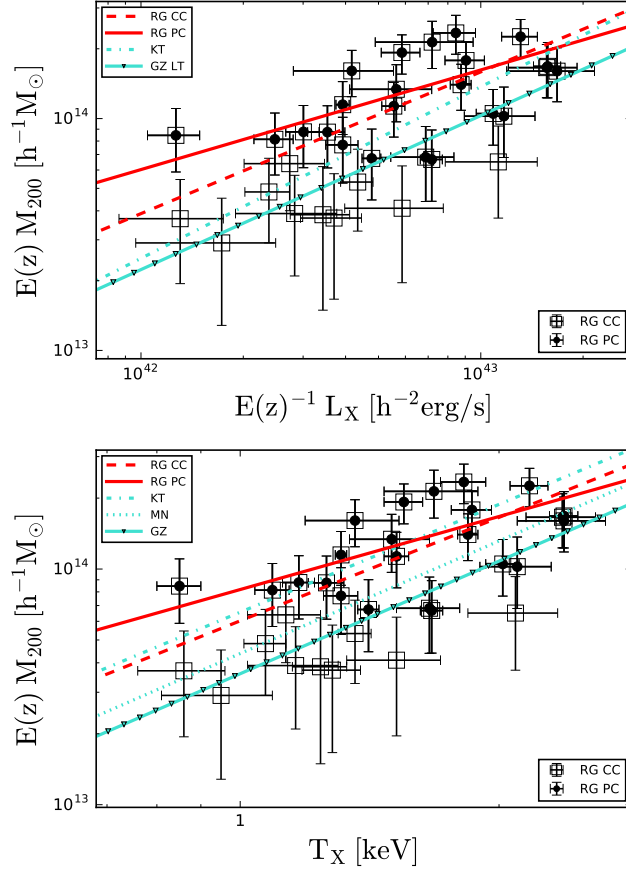


Figure 4.28 – I compare the weak lensing derived masses with X-ray mass proxies. On top, I show the mass-luminosity relation, and on the bottom, the mass-temperature relation, compared with others in literature. The black dots, the black squares, and the red lines have the same meaning as in Fig. 4.27. The different cyan lines show the relations obtained using the X-ray masses from Gozaliasl et al. (2014) catalog (GZ), calculated with the M-L relation of Leauthaud et al. (2010) (LT), the relations inferred by Kettula et al. (2015) (KT), and by Mantz et al. (2016) (MN) (see the legend for the line styles).

ray measurements better correlate with the total cluster mass (Pratt et al., 2009). For this reason, I decided to exclude Mehrtens et al. (2012) catalog from the rest of the analysis.

In the following analysis, I excluded the two clusters with mass $M_{200}^X < 2 \times 10^{13} M_\odot$ from the matched sample with Gozaliasl et al. (2014), because both the lensing catalog and the X-ray catalog are incomplete at these low masses. I also did not consider the two highest mass matches ($M_{200}^X > 2 \times 10^{14} M_\odot$), because the catalog used is incomplete at this masses, given the low area coverage. All four excluded clusters were matches with the Licitra’s *published* catalog.

In Fig. 4.27, I plot the $M_{200}^X - M_{200}^{lens}$ relation, obtained with Gozaliasl et al. (2014) and Piffaretti et al. (2011) catalogs, and in Fig. 4.28, the $L_X - M_{200}^{lens}$ and the $T_X - M_{200}^{lens}$ relations, obtained with Gozaliasl et al. (2014) catalog. In those plots, the black dots represent matches with the RedGOLD cluster detections in Licitra’s *published* catalogs, while the black squares represent all those with the *complete* catalogs (see Section 4.3.1).

In Fig. 4.27, I show the relation between X-ray and lensing masses:

$$\log(M_{200}^{lens}) = a + b \log(M_{200}^X) \quad (4.32a)$$

The black dotted line is the diagonal, the solid lines are the fit to the *published* catalogs, and the dashed lines are the fit to the *complete* catalogs. The red lines were obtained with the slope as a free parameter of the fit, and the green lines with the slope fixed at unity. For the *published* catalogs, the threshold in richness and σ_{det} is meant to select clusters with $M_{200} > 10^{14} M_\odot$ with a completeness $\sim 80\%$. Part of these detections have X-ray masses lower than the selection threshold of $M_{200} > 10^{14} M_\odot$, in fact their X-ray masses are in the range $2 \times 10^{13} M_\odot < M_{200}^X < 10^{14} M_\odot$. I expect to have a contamination of clusters with these lower masses and a lower completeness ($< 80\%$) in this mass range ($M_{200}^X < 10^{14} M_\odot$), as shown in Licitra et al. (2016a).

Using Gozaliasl et al. (2014) catalog, when fixing the slope at unity, I obtained $a = 0.20 \pm 0.03$ ($a = 0.23 \pm 0.03$), and a scatter of $\sigma_M = 0.20$ dex ($\sigma_M = 0.17$ dex), for the *complete(published)* catalogs. In this case, the difference in a for the two samples is negligible, $\sim 0.03 \pm 0.06$ dex. When leaving the slope as a free parameter, I found $a = -0.13 \pm 2.96$ and $b = 1.02 \pm 0.21$, with a scatter of $\sigma_M = 0.20$ dex ($a = 6.42 \pm 3.17$ and $b = 0.56 \pm 0.23$, with a scatter of $\sigma_M = 0.15$ dex) for the *complete(published)* catalogs. The incompleteness when using the *published* catalogs appears to bias the fit slope, which becomes much shallower than the diagonal.

Using Piffaretti et al. (2011) catalog, I found $a = 0.18 \pm 0.03$ with a scatter of $\sigma_M = 0.07$ dex, fixing the slope at unity, and $a = 2.44 \pm 1.46$ and

$b = 0.84 \pm 0.10$, with a scatter of $\sigma_M = 0.05$ dex, leaving the slope as a free parameter.

As explained in Section 4.3.2, Gozaliasl et al. (2014) masses were calculated from the lensing mass - X-ray luminosity relation of Leauthaud et al. (2010), after the excision of the AGN contribution and the correction for cool core flux removal. Therefore it is not accurate to define these masses as proper X-ray masses, as those of Mehrrens et al. (2012) and Piffaretti et al. (2011). Leauthaud et al. (2010) calculated their scaling relation stacking clusters according to their L_X , while I used the optical richness. The difference between the lensing masses that I estimated from the *Final Model*, and those of Gozaliasl et al. (2014) calibrated by Leauthaud et al. (2010), is not straightforward to interpret since includes different contributions (i.e. samples selected in different ways, different data, and shear calibration). Interpreting this difference precisely implies degeneracies on each contribution.

On the other hand, there are only 7 clusters matching between Piffaretti et al. (2011) catalog, and the sample that I used, in mass range in which the RedGOLD catalog has a lower completeness, given the low area coverage.

For the above reasons, I cannot use these two catalogs to interpret in a rigorous way the difference and the relation between lensing and X-ray masses.

In Fig. 4.28, I show the mass-luminosity and mass-temperature relations, derived from Gozaliasl et al. (2014) catalog. I applied a logarithmic linear fit, in the form:

$$\log \left(\frac{M_{200}E(z)}{M_0} \right) = a + b \log \left(\frac{L_X}{L_0 E(z)} \right) \quad (4.33a)$$

$$\log \left(\frac{M_{200}E(z)}{M_0} \right) = a + b \log \left(\frac{T_X}{T_0} \right) \quad (4.33b)$$

where $E(z) = H(z)/H_0$, $M_0 = 8 \times 10^{13} h^{-1} M_\odot$ for the $M_{200} - L_X$, $M_0 = 6 \times 10^{13} h^{-1} M_\odot$ for the $M_{200} - T_X$, $L_0 = 5.6 \times 10^{42} h^{-2} \text{erg/s}$, and $T_0 = 1.5 \text{ keV}$.

For the mass-luminosity relation, I found $a = 0.10 \pm 0.03$ and $b = 0.61 \pm 0.12$, with a scatter $\sigma_{\log M_{200}|L_X} = 0.20$ dex ($a = 0.16 \pm 0.03$ and $b = 0.43 \pm 0.12$, with a scatter $\sigma_{\log M_{200}|L_X} = 0.15$ dex) for the *complete(published)* catalogs. For the mass-temperature relation, I found $a = 0.23 \pm 0.03$ and $b = 1.46 \pm 0.28$, with a scatter $\sigma_{\log M_{200}|T_X} = 0.20$ dex ($a = 0.28 \pm 0.03$ and $b = 1.03 \pm 0.30$, with a scatter $\sigma_{\log M_{200}|T_X} = 0.15$ dex), for the *complete(published)* catalogs). The relations obtained with the *published* catalogs show again shallower slopes.

I summarize the results in Tab.4.10.

Relation	Sample	a	b	scatter
$M_L - M_X$	CC	-0.13 ± 2.96	1.02 ± 0.21	0.20
	PC	6.42 ± 3.17	0.56 ± 0.23	0.15
	CC (P)	2.44 ± 1.46	0.84 ± 0.10	0.05
$M_L - M_X$	CC	0.20 ± 0.03	fixed at 1	0.20
	PC	0.23 ± 0.03	fixed at 1	0.17
	CC (P)	0.18 ± 0.03	fixed at 1	0.07
$M_L - T_X$	CC	0.23 ± 0.03	1.46 ± 0.28	0.20
	PC	0.28 ± 0.03	1.03 ± 0.30	0.15
$M_L - L_X$	CC	0.10 ± 0.03	0.61 ± 0.12	0.20
	PC	0.16 ± 0.03	0.43 ± 0.12	0.15

Table 4.10 – *Results of the fit of the weak lensing mass versus X-ray mass and mass proxy relations: $\log M_L = a + b \log M_X$; $\log (M_{200}E(z)/M_0) = a + b \log (L_X/L_0E(z))$; $\log (M_{200}E(z)/M_0) = a + b \log (T_X/T_0)$. "CC" refers to the complete catalogs and "PC" to the published catalogs. All results were obtained using Gozaliasl et al. (2014) catalog, except for those marked with P, derived from Piffaretti et al. (2011) catalog (See text for the catalogs definitions and for the values of the pivot mass, luminosity and temperature used in the fit of the scaling relations).*

Relation	Comparison	Sample	Δa	Δb	a compatibility	b compatibility
$M_L - T_X$	Kettula et al. (2015)	CC	0.08 ± 0.14	0.06 ± 0.33	1σ	1σ
		PC	0.25 ± 0.15	0.49 ± 0.34	2σ	1.5σ
	Mantz et al. (2016)	CC	0.27 ± 0.28	0.06 ± 0.13	1σ	1σ
		PC	0.22 ± 0.54	0.34 ± 0.28	1σ	1.5σ
$M_L - L_X$	Kettula et al. (2015)	CC	0.06 ± 0.15	0.13 ± 0.15	1σ	1σ
		PC	0.24 ± 0.15	0.31 ± 0.15	1.5σ	2σ
	Leauthaud et al. (2010)	CC	0.22 ± 0.08	0.05 ± 0.18	2.5σ	1σ
		PC	0.33 ± 0.09	0.23 ± 0.19	4σ	1.5σ

Table 4.11 – Comparison of the mass-temperature and mass-luminosity relations with others in literature. "CC" refers to the results obtained using the complete catalogs and "PC" using the published catalogs (See text for the catalogs definitions). Δa is the difference in normalization, and Δb the difference in slope, between my results and those obtained by Kettula et al. (2015), Mantz et al. (2016) and Leauthaud et al. (2010). The last two columns show that the relations that I inferred are consistent, in normalization and slope, within $\lesssim 1 \sigma$ with the others in literature ($\lesssim 2.5 \sigma$ in normalization with Leauthaud et al. (2010)), when using the complete catalogs.

DISCUSSION

In this Chapter, I will discuss my results in the context of similar recent studies. I will compare the mass-richness relation that I inferred, and lensing mass versus X-ray mass proxies relations, with others in literature.

5.0.4 Comparison with previously derived mass-richness relations

As stated in Section 4.3.1 and shown in Licitra et al. (2016a,b), the richness estimator used in this work, λ , is defined in a similar way as the richness from redMaPPer (Rykoff et al., 2014). This allows me to compare the results of this analysis with other works that used the redMaPPer cluster sample.

Simet et al. (2016) performed a stacking analysis of the redMaPPer cluster sample, using shear measurements from the SDSS. Their sample is much larger than the one considered in this work, consisting of 5,570 clusters, with a redshift range $0.1 < z < 0.3$, and a richness range $20 \leq \lambda_{\text{RM}} \leq 140$. With these data, they were able to characterize the different systematic errors arising in their analysis with great accuracy. For the mass-richness relation, they obtained the normalization $\log(M_0 [h^{-1}M_\odot]) = 14.34 \pm 0.04$ (the error includes both statistical and systematic error) and the slope $\alpha = 1.33_{-0.1}^{+0.9}$.

To compare my results to theirs, I used masses in units of $h^{-1}M_\odot$ and I repeated the fits. Using the *Final model*, I obtained $\log M_0 = 14.31 \pm 0.02$ and $\alpha = 1.04 \pm 0.09$ (the errors are only statistical). The normalization I found is consistent within 1σ and the slope is consistent within $\sim 2\sigma$ with Simet et al.'s. Comparing the masses at the pivot richness, $\lambda_0 = 40$, I obtained $2.04 \times 10^{14} h^{-1} M_\odot \pm 0.02$ compared to Simet et al.'s $2.21 \times 10^{14} h^{-1} M_\odot \pm 0.15$.

In another recent work, Farahi et al. (2016) inferred the mass-richness

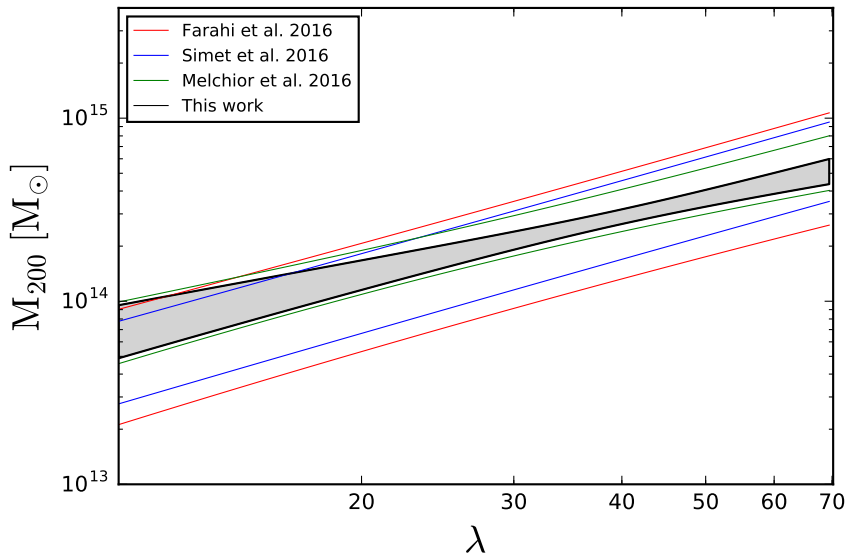


Figure 5.1 – Comparison of the mass-richness relation derived from the Two Component Model, with the a posteriori intrinsic scatter correction, with others in literature. All relations are consistent within 1σ (the grey area, and the area between the colored lines represent the 1σ confidence regions).

relation using the same sample of SDSS redMaPPer clusters ($0.1 < z < 0.3$ and $\lambda_{\text{RM}} > 20$), performing a stacking analysis and estimating the velocity dispersion of the dark matter halos from satellite-central galaxy pairs measurements. For the mass-richness relation, they found a normalization of 14.19 ± 0.1 and a slope of 1.31 ± 0.19 (the error includes both statistical and systematic error), using a pivot $\lambda_0 = 30$. Repeating the fit using their pivot richness, I obtained $\log M_0 = 14.18 \pm 0.02$ and $\alpha = 1.04 \pm 0.09$, consistent within less than 1σ in normalization and 1.5σ in slope, with their results. At the pivot richness $\lambda_0 = 30$ I found a mass of $1.51 \times 10^{14} M_\odot \pm 0.02$, consistent with their value of $1.56 \times 10^{14} M_\odot \pm 0.35$.

Melchior et al. (2016) calibrated the mass-richness relation and its evolution with redshift up to $z < 0.8$, using 8000 RedMaPPer clusters in the Dark Energy Survey Science Verification (DES; Dark Energy Survey Collaboration, 2016) with $5 \leq \lambda_{\text{RM}} \leq 180$. They found a normalization $M_0 = 2.35 \pm 0.34 \times 10^{14} M_\odot$ and a slope 1.12 ± 0.26 , using the pivot richness $\lambda_0 = 30$ and a mean redshift $z = 0.5$. Their errors include both statistical and systematic errors. Once again these results are consistent with what found in this analysis, within less than 1σ , even if this sample has a larger average redshift, where we expect the two richness definitions to be less sim-

ilar. As discussed in Section 4.3.1, the difference $\frac{\lambda_{\text{RM}} - \lambda}{\lambda}$ ranges from 5 – 15% at redshift $z < 0.3$ and it increases to 40 – 60% at $0.4 < z < 0.5$.

The normalization that I found is in perfect agreement with all the works cited above ($< 1\sigma$). On the other hand, there is a slight tension between slope that I obtained and those of Simet et al. (2016) and Farahi et al. (2016) ($1.5 - 2\sigma$), but not with Melchior et al. (2016) ($< 1\sigma$). The slope I obtained is also consistent with the first mass-richness relation inferred using the redMaPPer cluster sample from Rykoff et al. (2012), and with Saro et al. (2015) richness-mass relation, inferred cross-matching the SPT-SZ survey with the DES redMaPPer cluster sample. They found a value of 1.08 (the error is not given), and 0.91 ± 0.18 , respectively. Saro et al. (2015) value has been converted from the slope of the richness-mass relation to the slope of the mass-richness relation by Simet et al. (2015).

Figure 5.1, shows the comparison of the cited mass-richness relations. The 1σ region of the mass-richness relation from this work (in grey) is smaller compared to others because it accounts only for statistical errors. All relations are consistent within $1 - 2\sigma$.

A possible explanation of the slope discrepancy between what I found using the RedGOLD cluster sample, and the results obtained by Simet et al. (2016) and Farahi et al. (2016), using the SDSS redMaPPer sample, could be due to the different mean redshift of the stacked clusters. In fact, as said before, though the median difference between RedGOLD and redMaPPer richness is $\sim 5 - 15\%$ at $z < 0.3$, it increases up to $\sim 60\%$ for higher redshift, as can be seen in Figure 5.2, taken from Licitra et al. (2016a).

Licitra et al. (2016a) explained the observed trend considering that, due to the different depths of the CFHTLS and SDSS surveys ($i' \sim 24.7$ and $i' \sim 21.3$, respectively), redMaPPer richness is calculated with an extrapolation technique to reach the required limit in L_* for the ETG selection. As a result, for $z > 0.45$ redMaPPer richness is higher compared to RedGOLD richness by a factor ~ 2 . In other words, for a given mass, redMaPPer richness is higher compared to RedGOLD richness, and for a given richness redMaPPer mass is lower than RedGOLD mass. Figure 5.2 shows that, with increasing redshift, richness values $\lambda < 40$ are more affected by this bias. This implies that, compared to RedGOLD, redMaPPer assigns on average lower masses in the richness range $10 < \lambda \leq 40$, explaining the steeper slope found by Simet et al. (2016) and Farahi et al. (2016). On the other hand, Melchior et al. (2016) and Saro et al. (2015) used the DES redMaPPer sample. Licitra et al. (2016a) did not compare their richness estimates with this sample, but it is reasonable to assume that, since DES depth ($i' \sim 24$) is closer to that of the CFHTLS, the richness discrepancy shouldn't be very important in this case. This would explain the agreement in the slope values found comparing

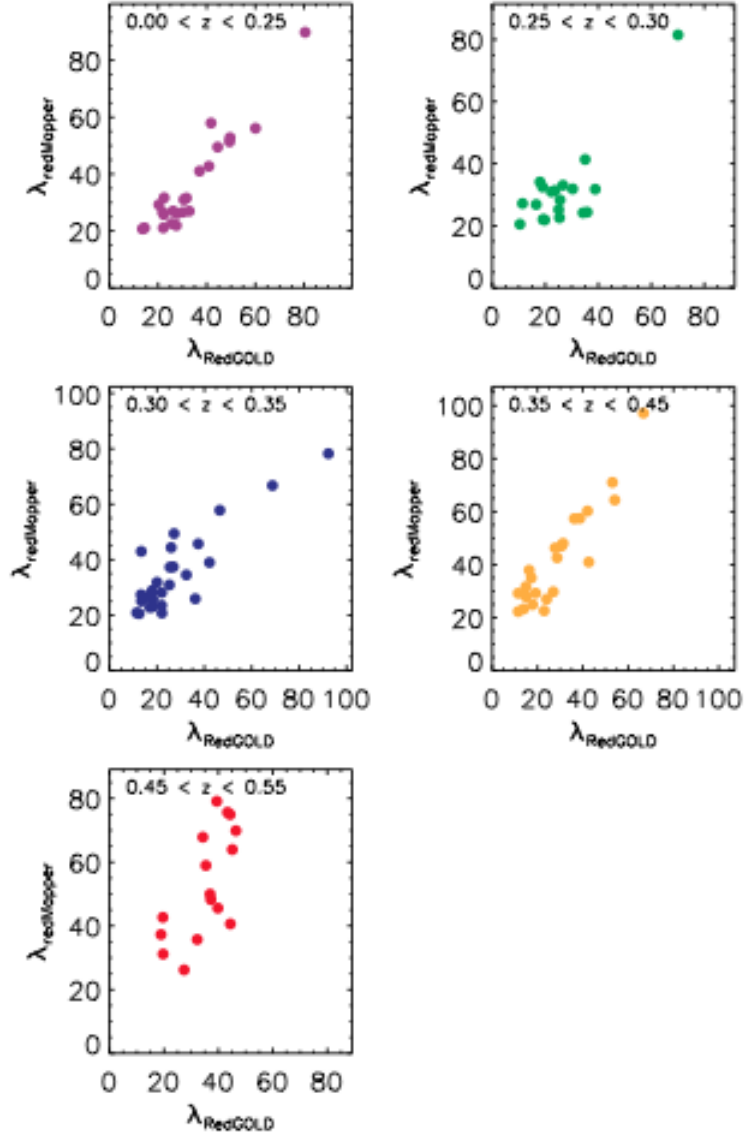


Figure 5.2 – Comparison of RedGOLD and redMaPPer richnesses as a function of redshift. The difference is $\sim 5 - 15\%$ at $z < 0.3$, and it increases up to $\sim 60\%$ for higher redshift. Figure taken from Licitra et al. (2016a).

my results to those of Melchior et al. (2016) and Saro et al. (2015).

van Uitert et al. (2016) also found an increase of the normalization of the mass-richness relation with redshift. This is counter intuitive because, since M_{200} masses are defined with respect to the critical density of the universe, they are expected to increase of lower redshifts, as the critical density decreases while cluster densities do not significantly change given that clusters are virialized. They then explain the observed trend by the evolution of the fraction of quenched galaxy, which increases at lower redshift increasing also the richness of the clusters (calculated as the number of red galaxies in a given radius). This could explain why SDSS redMaPPer richness values are systematically higher than those of RedGOLD, and my results are more in agreement with what found using the DES redMaPPer cluster sample, which extend to higher redshifts (i.e. DES clusters have a mean redshift of $z = 0.5$)

Moreover, assuming that the difference in richness between the different samples is negligible, the method used to derive lensing masses could play a role in explaining the observed results. As shown in Section 4.5, when performing the *joint fit* of the shear profiles, as in Simet et al. (2016), I obtained higher slope values, closer to the Simet et al. (2016) slope, even if always consistent within $1-2\sigma$ with the results of the *Final Model*. This could be explained considering that in the *joint fit*, we are imposing that there is a log-log linear relation between mass and richness, and this could cause a bias in the recovered parameters of the mass-richness relation. Fitting each bin individually, we allow the miscentering parameters to vary in each bin, and we don't make any assumption on the relation between the mean richness of the stack and the corresponding mass, other than for a narrow richness bin we expect to be selecting similar cluster masses, within the intrinsic scatter. In any case, the mass-richness relation parameters obtained with this technique are all consistent with what found with the *Final Model*, within $1 - 2\sigma$.

5.0.5 Comparison with previously derived X-ray scaling relations

In Fig. 4.28, I compare the lensing mass versus X-ray mass proxies relations, with other works in literature.

In the $L_X - M_{200}^{lens}$ plot, I compare my results with those from Kettula et al. (2015) and Leauthaud et al. (2010). As stated before, the fit to the *published* catalogs (solid red line) shows a shallower slope because of the selection in mass, which, while optimizes purity, leads to a bias in slope due to the lack of clusters detected at masses $M_{200} < 10^{14} M_\odot$.

Because of the large uncertainties, the fit to both the *complete* and *pub-*

lished catalogs (dashed red line) are consistent within $< 1\sigma$ and $< 2\sigma$, respectively, in normalization and slope with results from Kettula et al. (2015), even if the normalizations I found are higher.

With respect to the $E(z)M_{200}$ derived from Leauthaud et al. (2010) (and, as a consequence, from Gozaliasl et al. (2014), since they used Leauthaud et al. (2010) to derive their mass relations), my results are consistent within $< 2.5\sigma$ in normalization and within $< 1\sigma$ slope for the *complete* catalogs. For the *published* catalogs, normalization difference is $\sim 3.7\sigma$, while the slopes are consistent within $< 1.5\sigma$.

Both Kettula et al. (2015) and Leauthaud et al. (2010) didn't apply the miscentering correction but, while the first performed their lensing analysis on single clusters, the latter stacked their low mass clusters in very poorly populated bins. This procedure could have introduced a bias that lead to more smoothed profiles and thus to lower mass estimates and to a lower normalization of the scaling relation.

In the $T_X - M_{200}^{lens}$ plot, I compare my results with Kettula et al. (2015) and Mantz et al. (2016). Since their masses are derived at the overdensity $\Delta = 500$, I converted their M_{500} values to M_{200} , using $M_{200} = 1.35M_{500}$ from Rines et al. (2016), derived considering that the mass-concentration relation weakly depends on mass (Bullock et al., 2001) and assuming an NFW profile with a fixed concentration $c = 5$. I found that the normalization and slope of the fit to the *complete(published)* catalogs are consistent with Kettula et al. (2015) results within $< 1\sigma$ ($\lesssim 2\sigma$), and with Mantz et al. (2016) results within $< 1\sigma$ ($< 1.5\sigma$) in normalization and slope.

In Tab. 4.11, I show the differences in normalization, Δa , and in slope, Δb , between my results and those used for comparison for the mass-luminosity, and the mass-temperature relations.

Given that my results based on the RedGOLD *complete* catalogs are consistent with other results in the literature, we can conclude that the thresholds that were applied in the RedGOLD *published* catalog introduces systematics in the fit of the cluster lower mass end.

Assuming a cosmological model, and the predictions of spherical collapse in the absence of additional heating or cooling, we can calculate the theoretical slope of these scaling relations. In fact, galaxy clusters form from the amplification of the initial density fluctuations in the large-scale matter distribution, that can be described by a Gaussian random field, characterized by a power spectrum with a smoothly changing power law index, over relevant length scales. Galaxy clusters therefore reflect this behavior, in the sense that the evolution of their characterizing parameters shows self-similarity in scale and time. From the point of view of purely gravitational interactions, Navarro, Frenk & White (1996) showed how dark matter halos

on different scales can be described by a universal profile, dependent on two parameters, the NFW profile. This average profile is then scattered by the different statistical realizations of mass distributions in the protoclusters and by merger events that produce deviations from equilibrium. This scenario is then complicated by the addition of the baryons to the dark matter only approximation, through hydrodynamical processes, such as radiative cooling, feedback from star formation, AGN activity. As a first approximation though, self-similar scaling relation between cluster parameters can be derived in a purely gravitational picture (e.g. Böhringer et al., 2011). In particular X-ray self-similar scaling relations are:

$$M \propto T_X^{1.5}; M \propto L_X; M \propto L_{bol}^{0.75}; L_{bol} \propto T^2 \quad (5.1)$$

Comparing these predictions with observations, different slope values have been found (Böhringer et al., 2011):

$$M \propto T_X^{1.5}; M \propto L_X^{0.62}; M \propto L_{bol}^{0.52}; L_{bol} \propto T^{2.9} \quad (5.2)$$

This result can be explained considering that the ICM gas mass fraction is not constant as a function of cluster mass, but decreases for lower masses:

$$f_{gas} \propto M_{tot}^{0.3} \quad (5.3)$$

this is due to an increase of the specific energy of the ICM introduced by star formation and AGN feedback, that were neglected in the calculation of the self-similar scaling relations (Böhringer et al., 2011). Feedback regulates the amount of baryons that condense into stars and cold gas clouds. Implementing cooling in simulations leads to a larger fraction of condensed baryons in cool clusters, causing a decrease of their mass-to-light ratio (Voit, 2005). Also radiative cooling is an important process to consider since, the ICM radiating thermal energy loses its low-entropy gas, raising the mean entropy of the remaining gas, and therefore its temperature. On the other hand the lower gas density implies a lower luminosity (Voit, 2005). This means the observed deviations from self-similar prediction can be interpreted as an effect of hydrodynamical processing acting.

The slope values that I found for the mass-temperature and the mass-luminosity relations confirm this picture.

Simulations predict that mass measurements from lensing and X-ray proxies are systematically lower of $\sim 5 - 10\%$ and $\sim 25 - 35\%$, respectively, than the cluster total mass, with $\langle M_X^{sim}/M_L^{sim} \rangle \sim 0.7 - 0.8$ (Meneghetti et al., 2010; Rasia et al., 2012).

When I compared the weak lensing mass measurements to Gozaliasl et al. (2014) cluster masses, derived from X-ray luminosity based lensing measurements (Figure 4.26 (top) and Tab. 4.9) for *Final Model*, I obtained a difference of $\sim 15\%$.

As mentioned before in Section 4.6.3, and from Tab. 4.9 and Fig. 4.26, the mean residuals and ratio values obtained using Mehrtens et al. (2012) catalog are lower, with $\langle M_L/M_X \rangle \sim -0.1 - 0.0$, which means that non core-excised temperature lead to overestimated X-ray masses, as expected (Pratt et al., 2009). This is also confirmed in Mehrtens et al. (2012), since some of the clusters their catalog are contaminated by low signal-to-noise line-of-sight or embedded point sources (AGN and cool core). Analyzing one cluster that was observed also with Chandra, that is significantly more sensitive to point sources, they found a contamination in the flux of 15%. The correction to this contamination lead to a decrease of the luminosity of 33%. This means that Mehrtens et al. (2012) masses could actually be overestimated.

On the other hand, in my analysis I have assumed that dark matter halos can be fitted with a spherically symmetric NFW profile. From the LCDM predictions we expect halos to actually be triaxial. Optical cluster finder selection function is biased towards line-of-sight elongated objects, which are easier to detect, since the contrast with the background is maximized. Bartelmann (1995); Hamana et al. (2004); Oguri et al. (2005) have shown that such an orientation enhances significantly the lensing signal, which leads to overestimated cluster masses by up to 50%. Corless & King (2007) though showed that, according to the triaxial halo orientation, there can be an equivalent mass underestimation. Since I calculated stacked masses, this effect should be reduced to a few percent bias by the superposition of randomly oriented and elongated objects (2 – 4%, Simet et al., 2016).

Previously published XMM-Newton X-ray to lensing mass ratios show values of $\langle M_X/M_L \rangle \sim 0.91 - 0.99$ (Zhang et al., 2008) and $\sim 0.72 - 0.96$ (Simet et al. (2015), using observations from Piffaretti et al., 2011; Hajian et al., 2013). Given that I measured the bias on the lensing mass given an X-ray selection, I cannot compare my measurements directly with those, obtained by the measure of the bias in the X-ray mass given the lensing mass. However, the trend is similar and consistent with simulation. Our uncertainty on $\langle M_L/M_X \rangle$ ($\sigma_{\langle M_L/M_X \rangle} \sim 15 - 20\%$) is also similar to those cited in these works ($\sigma_{\langle M_X/M_L \rangle} \sim 3 - 20\%$).

It is also known that XMM-Newton and Chandra have different instrument calibrations that lead to different temperature estimations, with Chandra X-ray temperatures being higher, and leading to higher cluster mass estimation (Israel et al., 2014; von der Linden et al., 2014; Schellenberger et al., 2015). Applying the correction from Schellenberger et

al. (2015), to convert *XMM-Newton* masses to *Chandra* masses, I found $\langle M_X/M_L \rangle_{\text{Chandra}} = 0.99 \pm 0.17$, using the lensing masses from the *Final Model*.

I remind the reader though that even if these results are consistent with previous work, the scaling relations, normalized difference and ratios that I obtained between the lensing masses from the *Final Model*, and those of Gozaliasl et al. (2014), depend in a not straightforward way on the X-ray and optical sample selections, on the data used, and on the analyses that were performed which include different biases. It is therefore not possible to interpret precisely the relation between lensing and X-ray masses, with the available catalogs.

CONCLUSIONS AND PERSPECTIVES

6.1 Summary and conclusions

The aim of my thesis work is to infer galaxy cluster masses using weak lensing measurements, through the reconstruction of their stacked shear profiles, and to calibrate the precision of the RedGOLD optical richness as a mass proxy.

In order to do so, I wrote and optimized a weak lensing analysis pipeline that, starting from an input cluster catalog and shear catalog of background sources, returns as output the lensing cluster masses in richness bins, and the mass-richness relation.

The input catalogs are:

- The CFHT-L1 W1 and NGVS cluster catalogs obtained with the RedGOLD (Licitra et al., 2016a) optical cluster finder algorithm. As explained in Chapter 4 and Section 4.3.1, this algorithm is based on a revised red-sequence technique. It searches for ETGs overdensities and identifies the cluster center with the ETG with the highest number of red companions, weighted on luminosity. Other than the center coordinates, RedGOLD assigns to each cluster detection a redshift, a significance parameter, and a richness. The algorithm is optimized to detect massive galaxy clusters ($M_{200} > 10^{14}M_{\odot}$), and to produce optical cluster catalogs with high completeness and purity.

For this work, I used the RedGOLD catalogs obtained by Licitra et al. (2016a,b) from the CFHT-LS W1 and NGVS surveys, and binned the detected clusters according to their richness λ . When applied to the $\sim 60deg^2$ of the CFHTLS W1 field, RedGOLD found 652 detections, and when applied to the $\sim 20deg^2$ ($\sim 104deg^2$) of the NGVS covered by

five and four bands, found 279 and 1704 clusters respectively. I used a subsample of 1323 published clusters, selected with a threshold in significance of $\sigma_{\text{det}} \geq 4$ and in richness $\lambda \geq 10$, at redshift $0.2 \leq z \leq 0.5$, for which the published catalogs are $\sim 100\%$ complete and $\sim 80\%$ pure Licitra et al. (2016a)

- The photometric redshifts catalogs that I used in this work, and that were used by Licitra et al. (2016a,b), for both the $\sim 60 \text{ deg}^2$ of the CFHTLenS covered by the SDSS and for the entire NGVSLenS, were obtained by Raichoor et al. (2014). They used the Bayesian softwares *LePhare* and BPZ, improving the performance at low redshift building a new prior calibrated on observed data, using the SDSS Galaxy Main Sample spectroscopic survey. Comparing their results with spectroscopic redshift, Raichoor et al. (2014) found a bias $-0.05 < \Delta z < 0.02$, scatter values in the range $0.02 < \sigma < 0.06$, and 5 – 15% of outliers, for $i' < 23$ mag.
- Both the CFHTLenS and NGVSLenS shear catalogs data that I used for this work were obtained by my collaborator Ludovic van Waerbeke using the data reduction performed by Raichoor et al. (2014).

Galaxy shape measurements for the shear analysis were obtained applying the Bayesian *lensfit* algorithm. The code estimates the ellipticity components of each background galaxy and the associated multiplicative and additive biases that need to be applied as explained in Chapter 4 and Section 4.2.1.

Given these ingredients, the first step in my lensing analysis pipeline consists in the selection of the background galaxy samples inside a circular area of 5 Mpc , around each cluster in the reference cluster catalog. In order to separate the background sources from the foreground galaxies and cluster members, I tested different kind of selections. As shown in Chapter 4 and Section 4.5, from the comparison with a matching spectroscopic sample, the most efficient selection resulted to be the one based on photometric redshift instead of colors, along with a cut in the i -band magnitude. The tests that I performed prove that from different cuts in magnitude we can obtain consistent results, with some adjustment in the richness binning for the highest cluster masses.

The second step consists in the binning of the clusters according to their richness, and in the stack of their background samples. In this phase, the stacked radial shear profiles are calculated by averaging the tangential shear in logarithmic radial bins around the center of the stacked samples. As

described in Chapter 4 and Section 4.4.1, I applied lens-source pairs weights that depend on the lensing efficiency and on the quality of background galaxy shape measurements, and the *lensfit* calibration corrections. In order to obtain the error bars on each point of the radial shear profiles, I calculated the bootstrap covariance matrices, taking clusters with replacements in each richness bin. In order to check the signal-to-noise ratio of each richness bin, I calculated S/N maps using aperture mass statistics.

In the last step, once I obtained the shear profiles for each stack of clusters, I fitted them using MCMC as described in Chapter 4 and Section 4.4.3.

I extensively tested my code and checked whether the choices made introduced a bias in the results, as described in Chapter 4 and Section 4.5.

- I validated my code comparing my results with those of Ford et al. (2015), obtained in an independent way, using the entire CFTHLS W1, W2, W3, W4, and the public cluster catalog of Milkeraitis et al. (2010).
- I tested different kinds of background selection and magnitude cuts.
- I checked the goodness of restricting my analysis to the sample of clusters in the redshift range $0.2 < z_{\text{phot}} < 0.5$ (Kasliwal et al., 2008), individually fitting massive clusters ($\lambda > 50$), and I found a lower scatter when applying this selection.
- I tested different binnings in richness and found a difference in normalization $< 1\%$, and a difference in slope of $5 - 30\%$, in the mass-richness relations obtained.
- I checked the progressive improvements in the signal-to-noise ratio of the tangential shear profiles, increasing the number of stacked clusters and, at the same time, I checked the consistency with zero of the cross shear profile, as expected from theory.
- I tested the importance of the miscentering correction, individually fitting massive clusters ($\lambda > 50$), and found a mass underestimation of $10 - 40\%$, when the correction is not taken into account.
- I tested the use of aperture mass statistics for the identification of cluster centers, using simulated shear maps, simulated clusters, and observed RedGOLD clusters. I found that, while on simulation the method works well, on observed clusters there is often ambiguity on the detected center, due to the fact that noise simulates shear peaks.
- I tested a *joint fit* (i.e. the fit of all richness bins simultaneously) and found consistent results with the method I used for my analysis.

As explained in detail in Chapter 4 and Section 4.4.2, I used three analytic models in order to fit the tangential shear profiles:

Basic Model) It consists of a basic halo model, with an NFW surface density contrast and correction terms that take into account cluster miscentering, non-weak shear and the two halo term. It has three free parameters: the radius r_{200} , from which we calculate the mass M_{200} from Equation 1.6, and the miscentering parameters p_{cc} , and σ_{off} .

Added Scatter Model) It is based on the *Basic Model* but takes into account also the intrinsic scatter in the mass-richness relation. It has four free parameters: $\log M_{200}$, p_{cc} , σ_{off} , and $\sigma_{M|\lambda}$. For each bin, we use the mass-richness relation calculated from the *Basic Model* to infer the mean mass of the stacked clusters, as a first approximation. We then randomly scatter the mass using a gaussian distribution with mean $\langle \ln M_{200} \rangle$ and width $\sigma_{\ln M_{200}|\lambda}$.

Two Component Model) It is based on the *Basic Model* but takes into account also the contribution from the BCG mass. When we set free the BCG mass, this model has four free parameters: r_{200} , p_{cc} , σ_{off} , and $\log M_{BCG}$. When we fix the BCG mass to the mean stellar mass for each richness bin, $M_{BCG} = M_{BCG}^*$, the free parameters reduce to three.

From the fit results, I found that the intrinsic scatter and BCG mass are not constrained by the data. The main effect of the addition of $\sigma_{M|\lambda}$ to the fit is to introduce more uncertainties and to increase the error on the estimated parameters. The inclusion of M_{BCG} in fit has no impact on the estimated parameters, that are therefore the same as those obtained using the *Basic Model*. For these reasons, I decided to discard the *Added Scatter Model*, and to apply an a posteriori intrinsic scatter correction to the *Basic Model* and to the *Two Component Model*. This correction has the effect of increasing the normalization of the mass-richness relation by less than 1%.

Since it is the most complete and reliable between the three models described, I chose to use *Two Component Model* with the intrinsic scatter correction (*Final Model*), in the remaining of my analysis, and obtained the mass-richness relation.

Once I obtained a mass for each cluster in the sample, using the mass-richness relation that I inferred, I compared these results with X-ray masses, temperatures and luminosities, using Gozaliasl et al. (2014), Mehtens et al. (2012), and Piffaretti et al. (2011) X-ray catalogs.

I performed a match between these three catalogs and the RedGOLD detections imposing a maximum separation of 1 *Mpc* and a maximum difference in redshift of 0.1. Within all three fields, I recovered 36 objects from

the match with Gozaliasl et al. (2014), 21 from Mehrtens et al. (2012), and 7 from Piffaretti et al. (2011). I analyzed the three catalogs separately because the different treatment of the emission from the central regions of the clusters leads to different mass estimates.

Summarizing, the main results of this work are:

- I implemented and optimized my own weak lensing pipeline that analyzes shear profiles and calculates weak lensing masses of individual or stacked clusters.
- I tested different profile models and different fitting techniques, obtaining results in good agreement with each other. In particular, the miscentering correction resulted to be the one that most affects the halo mass measurements, while including or not the BCG mass doesn't make a difference in the recovered parameters. The intrinsic scatter in the mass-richness relation is generally not constrained by the data. The amplitude of the mass-concentration relation, set as a free parameter, is slightly degenerate with the miscentering parameters and can lead to an underestimation of the parameters of the mass-richness relation.
- I calibrated RedGOLD optical richness, using weak lensing masses, fitting the mass-richness relation $\log M_{200} = \log M_0 + \alpha \log \lambda/\lambda_0$. For the *Final Model*, I obtained $\log M_0 = 14.46 \pm 0.02$ and $\alpha = 1.04 \pm 0.09$, with a pivot richness $\lambda_0 = 40$.

Even if the cluster sample used in this analysis is one order of magnitude smaller than the SDSS and DES redMaPPer cluster samples used in Simet et al. (2016), Farahi et al. (2016) and Melchior et al. (2016), my results are consistent with theirs within $1 - 2\sigma$. This confirms that RedGOLD cluster selection is not biased towards a different cluster selection when compared to the SDSS and DES redMaPPer cluster samples, as expected.

- Using the mass-richness relation that I measured, I inferred scaling relations between lensing masses and X-ray proxies. For the $M_{200}^{lens} - M_{200}^X$ relation, fixing the slope at unity, I obtained $\log M_{200}^{lens} = (0.20 \pm 0.03) \log M_{200}^X$, using Gozaliasl et al. (2014) catalog. With Piffaretti et al. (2011) catalog, I found $a = 0.18 \pm 0.03$, fixing the slope at unity, and $a = 2.44 \pm 1.46$ and $b = 0.84 \pm 0.10$, leaving the slope as a free parameter.

For the lensing mass vs X-ray luminosity relation $\log \left(\frac{M_{200} E(z)}{M_0} \right) = a + b \log \left(\frac{L_X}{L_0 E(z)} \right)$, I found $a = 0.10 \pm 0.03$ and $b = 0.61 \pm 0.12$, with

$M_0 = 8 \times 10^{13} h^{-1} M_\odot$ and $L_0 = 5.6 \times 10^{42} h^{-2} \text{erg/s}$.

For the lensing mass vs X-ray temperature relation $\log\left(\frac{M_{200E}(z)}{M_0}\right) = a + b \log\left(\frac{T_X}{T_0}\right)$, I obtained $a = 0.23 \pm 0.03$ and $b = 1.46 \pm 0.28$, with $M_0 = 6 \times 10^{13} h^{-1} M_\odot$ and $T_0 = 1.5 \text{KeV}$.

These results are consistent with those of Kettula et al. (2015) and Mantz et al. (2016), within $< 1\sigma$. The normalization is consistent within $< 2.5\sigma$, and the slope within 1σ , with the results of Leauthaud et al. (2010) (and therefore with Gozaliasl et al., 2014).

- I found a scatter of 0.20 dex, for all three relations, consistent with redMaPPer scatters, confirming the Licitra et al. (2016a,b) results that the RedGOLD optical richness is an efficient mass proxy. This is very promising since the mass range used in this work is lower than that probed by redMaPPer, and the scatter does not increase as expected to these lower mass ranges.

6.2 Current projects

My first author refereed paper describing my thesis work was submitted to the Astrophysical Journal and I'm in the process of answering the referee report. The submitted paper is reproduced in the Appendix.

In the future, I will focus on projects that are complementary to what I've done so far.

This analysis showed that, with the data used, it's not possible to constrain the BCG mass and neither a constant that multiplies the BCG stellar mass, inferred with a tool external to the lensing pipeline. In order to calculate a scaling relation between lensing mass and BCG mass, in my next project, I will repeat the weak lensing analysis described but, this time, binning clusters according to their BCG stellar mass.

I will use different parameters and criteria to select the cluster members, and to identify the BCG:

- I will select galaxies inside a radius of 50 or 500 *kpc*.
- I will select members based on a simple cut in photometric redshift:

$$|z_{members}| < z_{cluster} + 0.15$$

or using the velocity dispersions:

$$|z_{members}| < \sqrt{(0.03(1 + z_{cluster}))^2 + \left(\frac{\sigma_{DM}(1 + z_{cluster})}{v_c}\right)^2}$$

where v_c is the speed of light and σ_{DM} is the virial relation of Evrard et al. (2008):

$$\sigma_{DM} = (1082.9 \pm 4.0 \text{ km s}^{-1}) \left[\frac{h(z)M_{200}}{10^{15}M_{\odot}} \right]^{0.3361 \pm 0.0026}$$

- I will select the BCG within the cluster members choosing the most massive galaxy, or the most luminous in magnitude b rest frame.

This work will allow me to study how a different kind of BCG selection, and therefore a different cluster center, will affect the estimated lensing masses. It will also allow me to calculate the stellar-to-halo mass ratio for cluster central galaxies, and again, compare the results for different selection criteria. At the same time, having information on the b rest frame luminosity of central galaxies and of the entire cluster, I will be able to infer an optical mass-luminosity relation.

At the same time, I will use galaxy-galaxy lensing to infer the stellar-to-halo mass relation of satellite galaxies. The concept behind this analysis is the same compared to my thesis work, since it consists in stacking galaxies instead of clusters, according to their BCG stellar mass, and then calculate and fit the shear radial profiles with an analytical model of the kind:

$$\Delta\Sigma = \Delta\Sigma_{star} + \Delta\Sigma_{sat} + f_{sat}\Delta\Sigma_{host} + \Delta\Sigma_{2halo} \quad (6.1)$$

A very preliminary result can be found in Figure 6.1, where we can see in red, the results obtained from stacked cluster lensing, in blue those derived from individual cluster mass fits, and in green what found whit galaxy-galaxy lensing.

On the other hand, I would like to study in more detail the miscentering problem to see how different center choices would affect the shear profiles and the mass measurements of stacked or individual massive clusters.

As shown in Chapter 4 and Section 4.5.6, aperture mass statistics can be used to create a lensing signal-to-noise ratio map from the background source sample, and to identify the center of the cluster with the peak of the lensing signal. This technique gives optimal results when applied to simulations of low noise shear fields or of very massive clusters. The situation is different when we obtain maps from observed clusters. Comparing lensing

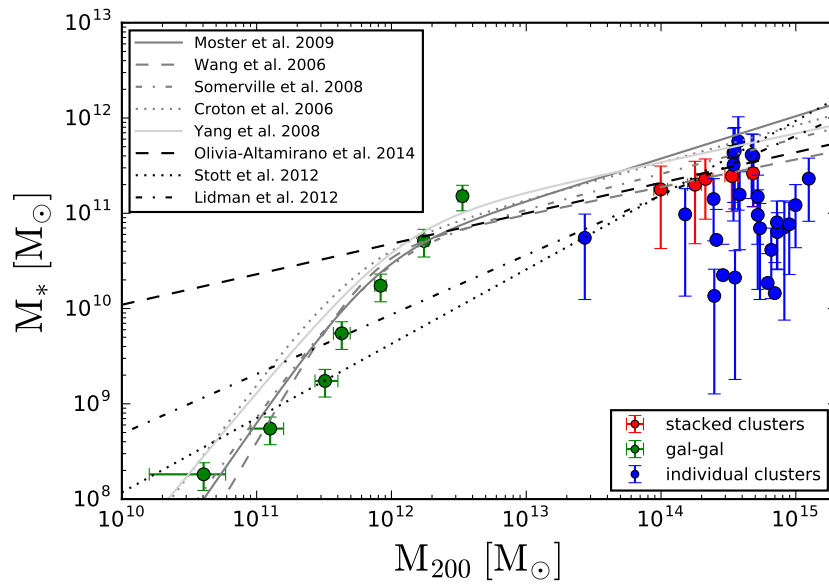


Figure 6.1 – Halo masses inferred from lensing versus stellar masses calculated through SED fitting. The green symbols correspond to galaxy-galaxy lensing, the red dots to cluster lensing, and the blue dots to individual massive cluster measurements. The gray lines are results from previous observations and simulations.

center estimated in this way with RedGOLD centers, I found results often in disagreement.

While RedGOLD centers are based on optical data and should correspond with the position of the BCG, the peak of the lensing signal should correspond to the center of the halo. In principle then, a difference in the two center estimates can be justified considering that the BCG could be offset with respect to the dark matter halo center, but it could also be due to fails of the centering method.

Visually inspecting the images of the most massive clusters in the sample, I found that in some cases RedGOLD failed to identify the center with a galaxy in the most densely populated region, while the lensing center seemed to be more accurate. In other cases though, the lensing center was completely wrong and what was detected as the cluster center was actually a noise peak.

I would like to expand the work of George et al. (2012) and include in the comparison also centers based on the peak of the weak lensing signal and on the hybrid approach between galaxy centers and centroids (used for example in RedGOLD), not considered in the cited work. Also I will test the use of a different filter for the calculation of the lensing signal-to-noise ratio maps. For example, Maturi et al. (2005) developed an optimal filter that takes into account the noise associated to the large scale structure, to better isolate the shear signal of the cluster. This method has proven to be more efficient in detecting galaxy clusters and shear peaks (Maturi et al., 2005), and should be then in principal a better instrument to study cluster centers. In Figure 6.2, we can see a comparison of the simple filter developed by Schneider (1996), and the more refined optimal filter of Maturi et al. (2005), considering only poisson noise or also the contribution from the large scale structure.

In order to calculate this other source of noise Maturi et al. (2005) scaled the filter obtained consider a simple NFW profile (i.e. what I used for the aperture mass analysis) with the effective convergence power spectrum, that in the Limber approximation can be written as:

$$P_k = \frac{9H_0^2\Omega_m^2}{4c^2} \int_0^{D_{C,H}} dD_C \frac{\overline{W}^2(D_C)}{a^2(D_C)} P_\delta \left(\frac{k}{D_M(D_C)}, D_C \right) \quad (6.2)$$

where D_C and D_M are the comoving line-of-sight distance and the transverse comoving distance defined in Chapter 1, $\overline{W}^2(D_C)$ is a function that depends on the redshift distribution of the background sources, and P_δ is the power spectrum of the three-dimensional matter density fluctuations.

The effective convergence power spectrum for sources at redshift $z = 1$ is shown in Figure 6.3. The non linear matter power spectrum has been calcu-

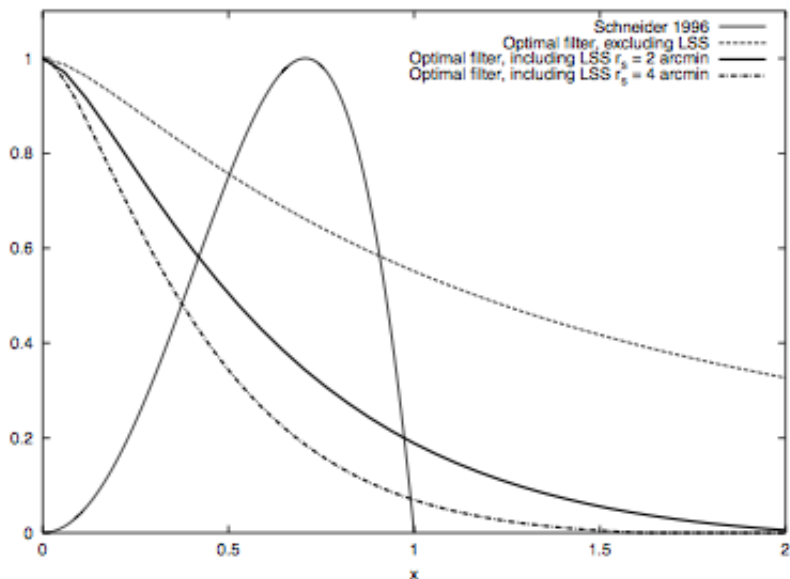


Figure 6.2 – Comparison of the filter of Schneider (1996), with the filter of Maturi et al. (2005), with and without considering the large scale structure contribution.

lated using the Python package Cosmicpy¹, following Smith et al. (2003).

In Figure 6.4, I show a preliminary comparison of the centers of a RedGOLD cluster obtained using aperture mass statistics (cyan dot) and Maturi et al. (2005) optimal filter (magenta dot). The latter is closer to the optical center estimated by RedGOLD (green dot), suggesting a promising improving of this future analysis.

Moreover, for these new projects I will use the new self calibrating version of the *lensfit* algorithm, and refined photometric redshift estimations on the CFHTLS W1 and on entire NGVS. With these new data, I will also be able to check whether the improvements in the shear estimates affect the mass measurements in a meaningful way.

6.3 Future perspectives

In weak lensing mass measurements, the selection of the background sample is of great importance. In this context, the main challenge to reach the accuracy of $\sim 1\%$ we would like to get from future large scale optical, near-infrared surveys such as *Euclid* and LSST, comes from the photometric

¹<http://cosmicpy.github.io/>

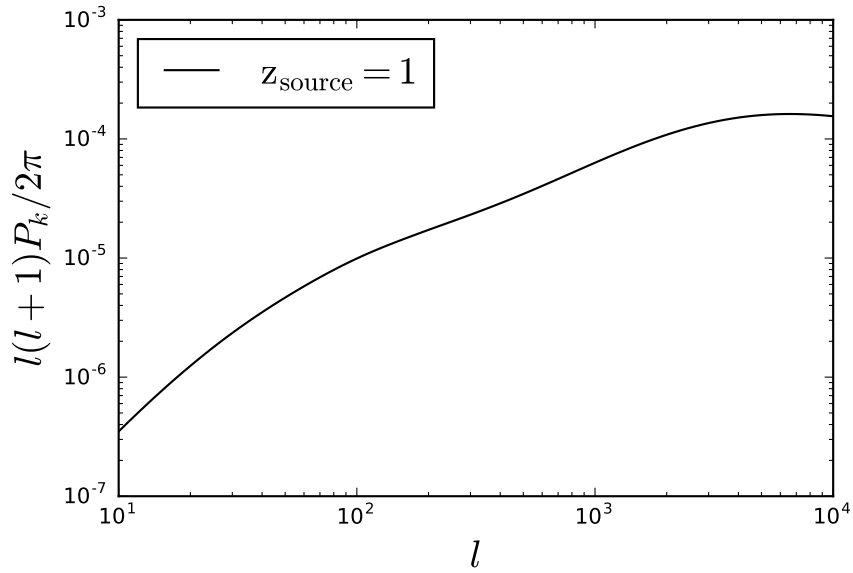


Figure 6.3 – *Effective convergence power spectrum for sources at $z = 1$.*

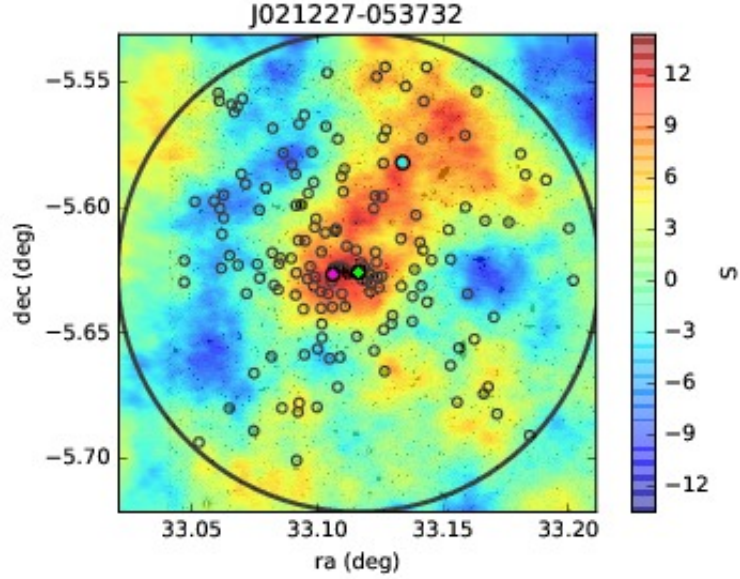


Figure 6.4 – *Lensing signal-to-noise ratio map obtained using Maturi et al. (2005) optimal filter. The green dot is the center estimated with RedGOLD, the magenta one with the optimal filter, and the cyan one with aperture mass statistics.*

redshift estimation.

The redshift of source galaxies, or their redshift distribution $P(z)$, is also required to appropriately weight the shear estimator. The weak lensing signal is proportional to the surface mass density of the lens and to the geometry of the system formed by observer, lens and source. The efficiency of the lensing signal for a given lens-source pair is $\propto D_l/(D_{ls}/D_s)$ (Hoekstra et al., 2015), the angular diameter distance from the observer to the lens, from the lens to the source and from the observer to the lens, respectively.

The knowledge of the spectroscopic redshift of each lens and source galaxy would allow us to estimate these quantities, and consequently the shear signal, in an unbiased way. Unfortunately, current or near-future instruments will not be able to provide a spectroscopic follow-up of faint galaxies of the next generation large scale surveys such as Euclid and LSST. We will then need to rely on photometric redshifts that, to meet the requirements on systematic errors, will need to be measured with an accuracy of $\sim (0.002)(1+z)$ (Newman et al., 2015).

Different techniques have been developed to infer photometric redshifts, from likelihood maximization to Bayesian and neural network based methods. Every photometric redshift algorithm needs to rely on spectroscopic informations for the purpose of training and calibration. The goal of the first is the minimization of the difference between the estimated redshift and the true one, and the aim of the latter is to constrain and control the biases involved in the measurement. The application of different training and calibration techniques, and the use of different spectroscopic samples impact the estimated photometric redshifts and the associated errors. It is therefore important to study how the choice of a method and the relative uncertainties propagate in the quantities estimated through weak lensing analysis, such as the cosmological parameters, the power spectrum, galaxy and cluster masses.

Calibration methods can be divided in two categories: direct and indirect. Direct methods, such as template based and machine learning algorithms, consists in the calibration of a mapping from the flux in photometric bands to a galaxy redshifts. Indirect calibration can be obtained trough cross correlation methods (Johnson et al., 2017).

Hildebrandt et al. (2016) compared the results of three different kind of photometric redshift calibrations on the cosmological parameters estimation through the tomographic weak lensing analysis of the KiDS-450 data. The first is a weighted direct calibration, it consists in the use of the distribution of spectroscopic redshifts of object selected in the same way as the photometric sample that we want to analyze. In order to account for the fact that spectroscopic catalogs are never complete and representative samples of the photometric counterpart, they implemented a weighting system based on

the volume density of objects in the magnitude space of both catalogs. The second is an indirect method based on the angular cross-correlation function between the photometric and spectroscopic samples. Unlike direct methods, this one has the advantage of not requiring the spectroscopic sample to be complete in the color and magnitude space but only to span the full redshift range of the photometric sample. The third is the recalibration of the photometric $P(z)$ through its integration over the spectroscopic redshift range for each spectroscopic training object.

They then compared the sensitivity of the cosmological parameters constraints to the calibration method used. In Chapter 2, Figure 2.16 from Hildebrandt et al. (2016), we find the confidence contours in the $\Omega_m - \sigma_8$ plane obtained through the photometric redshift distributions inferred with the three methods described, and through the original $P(z)$ calculated by BPZ.

All cases give consistent results but the first two methods provide a better fit to the data. The direct calibration technique has uncertainties that are subdominant compared to the measurements errors, while the indirect one has much larger constraints. In this case the uncertainties dominate the error budget due to the small areal coverage of the used spectroscopic sample.

In my future work, I would like to apply a similar kind of analysis to the weak lensing mass estimates of galaxy clusters, in order to study how the use of the photometric redshift distribution derived with a method over another influences this kind of measurements. The photometric redshift calibration would have an impact also on cluster centering techniques.

Euclid will provide imaging data in a very broad *RIZ* band and in the broad *Y, J, H* bands. It will be complemented with optical ground based data in the *g, r, i, z* bands. In addition, the mission will use near-IR slit less spectroscopy that will identify mainly $H\alpha$ emitters up to $z \sim 2$. In the redshift range $0.9 < z < 1.8$, we expect to find a total of 30-72 million of sources in the 15000 deg^2 covered by *Euclid* (Pozzetti et al., 2016). On the other hand, LSST will cover over 20000 deg^2 in the *ugrizy* bands. These observations, in conjunction with spectroscopic follow up of areas covered by the space survey will allow us to step forward in constraining the photometric redshift bias. In particular, given the availability of larger and deeper spectroscopic samples, indirect calibration methods such as cross-correlation will be substantially improved.

In preparation for the *Euclid* survey, it would be interesting to test this kind of analysis on realistic simulations and study how the available filters and the wide coverage can be used to constrain calibration uncertainties.

Moreover, the VISTA Kilo-Degree Infrared Galaxy survey (VIKINGS; Edge et al., 2013) will complement KiDS in five near-infrared bands, bringing

the total number of bands up to 9 (*ugriZYJHK*). This will lead to better and deeper photometric redshifts estimations and will allow us to perform a direct comparison with the standard four bands KiDS data.

APPENDIX

A

SUBMITTED PAPER

Next Generation Virgo Cluster Survey. XXI. The weak lensing masses of the CFHTLS and NGVS RedGOLD galaxy clusters and calibration of the optical richness

Carolina Parroni^{1,2}, Simona Mei^{1,2,3}, Thomas Erben⁴, Ludovic Van Waerbeke⁵,
Anand Raichoor⁶, Jes Ford⁷, Rossella Licitra^{1,2}, Massimo Meneghetti⁸,
Hendrik Hildebrandt⁴, Lance Miller⁹, Patrick Côté¹⁰, Giovanni Covone¹¹,
Jean-Charles Cuillandre¹², Pierre-Alain Duc^{13,14}, Laura Ferrarese¹⁰, S.D.J. Gwyn¹⁰,
Thomas H. Puzia¹⁵

Abstract

We measured stacked weak lensing cluster masses for a sample of 1325 galaxy clusters detected by the RedGOLD algorithm in the Canada-France-Hawaii Telescope Legacy Survey W1 and the Next Generation Virgo Cluster Survey at $0.2 < z < 0.5$, in the optical richness range $10 < \lambda < 70$. After a selection of our best richness subsample ($20 < \lambda < 50$), this is the most comprehensive lensing study of a $\sim 100\%$ complete and $\sim 90\%$ pure optical cluster catalogue in this redshift range, with a total of 346 clusters in $\sim 164 \text{ deg}^2$. We test three different mass models, and our best model includes a basic halo model, with a Navarro Frenk and White profile, and correction terms that take into account cluster miscentering, non-weak shear, the two-halo term, the contribution of the Brightest Cluster Galaxy, and an a posteriori correction for the intrinsic scatter in the mass-richness relation. With this model, we obtain a mass-richness relation of $\log M_{200}/M_{\odot} = (14.48 \pm 0.04) + (1.14 \pm 0.23) \log(\lambda/40)$ (statistical uncertainties). This result is consistent with other published lensing mass-richness relations. When compared to X-ray masses and mass proxies, we find that on average weak lensing masses are $\sim 10\%$ higher than those derived in the X-ray in the range $2 \times 10^{13} M_{\odot} < E(z)M_{200}^X < 2 \times 10^{14} M_{\odot}$, in agreement with most previous results and simulations. We also give the coefficients of the scaling relations between the lensing mass and X-ray mass proxies, L_X and T_X , and compare them with previous results.

Subject headings:

¹LERMA, Observatoire de Paris, PSL Research University, CNRS, Sorbonne Universités, UPMC Univ. Paris 06, F-75014 Paris, France

²University of Paris Denis Diderot, University of Paris Sorbonne Cité (PSC), 75205 Paris Cedex 13, France

³Jet Propulsion Laboratory, Cahill Center for Astronomy & Astrophysics, California Institute of Technology, 4800 Oak Grove Drive, Pasadena, California, USA

⁴Argelander-Institut für Astronomie, University of Bonn, Auf dem Hügel 71, D-53121 Bonn, Germany

⁵Department of Physics and Astronomy, University of British Columbia, 6224 Agricultural Road, Vancouver, B.C., V6T 1Z1, Canada

⁶Institute of Physics, Laboratory of Astrophysics, Ecole Polytechnique Fédérale de Lausanne (EPFL), Observatoire

de Sauvigny, 1290 Versoix, Switzerland

⁷eScience Institute, University of Washington, Campus Box 351570, Seattle, WA 98195

⁸INAF - Osservatorio Astronomico di Bologna, Bologna, Italy & INFN, Sezione di Bologna, Bologna, Italy

⁹Department of Physics, University of Oxford, Denys Wilkinson Building, Keble Road, Oxford OX1 3RH, U.K

¹⁰National Research Council of Canada, Herzberg Astronomy and Astrophysics Program, 5071 West Saanich Road, Victoria, BC, V9E 2E7, Canada

¹¹INAF Osservatorio Astronomico di Capodimonte, Dipartimento di Fisica, University of Naples Federico II, INFN, Via Cinthia, I-80126 Napoli, Italy

¹²CEA/IRFU/SAP, Laboratoire AIM Paris-Saclay, CNRS/INSU, Université Paris Diderot, Observatoire de

1. INTRODUCTION

Galaxy clusters are the largest and most massive gravitationally bound systems in the Universe and their number and distribution permit us to probe the predictions of cosmological models. They are the densest environments where we can study galaxy formation and evolution, and their interaction with the intra-cluster medium (Voit 2005). For both these goals, an accurate estimate of the cluster mass is essential.

The cluster mass cannot be measured directly and is inferred using several mass proxies. Galaxy clusters emit radiation at different wavelengths and their mass can be estimated using different tracers. Different mass proxies usually lead to mass estimations that are affected by different systematics.

From X-ray observations of the cluster gas, we can derive the gas temperature, which is related to its total mass (Sarazin 1988), under the assumption of hydrostatic equilibrium. X-ray mass measurements are less subjected to projection and triaxiality effects but the mass proxies are not reliable in systems undergoing mergers or in the central regions of clusters with strong AGN feedback (Allen, Evrard & Mantz 2011).

The intracluster medium (ICM) can also be detected in the millimeter by the thermal Sunyaev-Zel'dovich effect (S-Z effect; Sunyaev & Zeldovich 1972) and the S-Z flux is related to the total cluster mass. Unlike optical and X-ray surface brightness, the integrated S-Z flux is independent of distance, allowing for almost constant mass limit measurements at high redshifts. For the same reason, though, the method is also subjected to projection effects due to the overlap of all the groups and clusters along the line of sight (Voit 2005).

In the optical and infrared bandpasses, we observe the starlight from cluster galaxies. If a clus-

ter is in dynamical equilibrium, the velocity distribution of its galaxies is expected to be Gaussian and the velocity dispersion can be directly linked to its mass through the virial theorem. An advantage of this method is that, unlike X-ray and S-Z mass measurements, it is not affected by forms of non-thermal pressure such as magnetic fields, turbulence and cosmic ray pressure. As a downside, it is sensitive to triaxiality and projection effects, the precision of the measurements is limited by the finite number of galaxies, and the assumption of dynamical and virial equilibrium is not always correct (Allen, Evrard & Mantz 2011).

Also, considering that light traces mass, the total optical or infrared luminosity of a cluster is another indicator of its mass. Abell (1958) defined a *richness* class to categorize clusters based on the number of member galaxies brighter than a given magnitude limit. The luminosity distribution function of cluster galaxies, is also well described by the Schechter (1976) profile and the observation of the high luminosity tip of this distribution allows us to better constrain cluster masses. Postman et al. (1996), for example, defined the richness parameter as the number of cluster galaxies brighter than the characteristic luminosity of the Schechter (1976) profile, L_* . Different definitions are possible and intrinsically related to the technique used to optically detect galaxy clusters.

Rykoff et al. (2014) built an optical cluster finder based on the red-sequence finding technique, redMaPPer, and applied it to the Sloan Digital Sky Survey (SDSS; York et al. 2000). Their richness is computed using optimal filtering, as a sum of probabilities and depends on three filters based on colors, positions and luminosity (Rozo et al. 2009; Rozo & Rykoff 2014; Rykoff et al. 2012, 2014, 2016).

In Licitra et al. (2016a,b), we introduced a simplified definition of cluster richness based on the redMaPPer richness measurement, within our detection and cluster selection algorithm RedGOLD. RedGOLD is based on a revised red-sequence technique.

RedGOLD richness quantifies the number of red, passive early type galaxies (ETGs) brighter than $0.2L_*$, inside a scale radius, subtracting the scaled background. When compared to X-ray mass proxies, the RedGOLD richness leads to scatters in the X-ray temperature-richness relation

Paris, PSL Research University, F-91191 Gif-sur-Yvette Cedex, France

¹³AIM Paris-Saclay Service d'astrophysique, CEA-Saclay, 91191 Gif sur Yvette, France

¹⁴Université de Strasbourg, CNRS, Observatoire astronomique de Strasbourg, UMR 7550, F-67000 Strasbourg, France

¹⁵Institute of Astrophysics, Pontificia Universidad Católica de Chile, Av. Vicuña Mackenna 4860, 7820436 Macul, Santiago, Chile

similar to those obtained with redMaPPer (Rozo & Rykoff 2014), which is very promising since RedGOLD was applied to a lower richness threshold (i.e. lower cluster mass).

The total cluster mass can also be derived by its strong and weak gravitational lensing of background sources. In the weak lensing regime, the gravitational potential of clusters of galaxies produces small distortions in the observed shape of the background field galaxies, creating the so-called shear field, which is proportional to the cluster mass.

Because the shear is small relative to the intrinsic ellipticity of the galaxies (due to their random shape and orientation), a statistical approach is required to measure it and the signal is averaged over a large number of background sources to increase the signal-to-noise ratio (Schneider 2005). Gravitational lensing does not require any assumption on the dynamical state of the cluster and it is sensitive to the projected mass along the line of sight, representing a more reliable tool to determine total cluster masses (Meneghetti et al. 2010; Allen, Evrard & Mantz 2011; Rasia et al. 2012).

In the future, as shown in Ascaso et al. (2016), optical and near-infrared (NIR) cluster surveys, such as Euclid¹ (Laureijs et al. 2011), LSST² and J-PAS (Benítez et al. 2014), will reach deeper than X-ray and S-Z surveys, such as e-Rosita (Merloni et al. 2012), SPTpol (Carlstrom et al. 2011) and ACTpol (Marriage et al. 2011). It is then important to understand the reliability of optical and NIR mass proxies, since they will be the only mass proxy available for these new detections.

Several works in the literature have proven that the optical richness shows a good correlation with the cluster total masses derived from weak lensing (Johnston et al. 2007; Covone et al. 2014; Ford et al. 2015; van Uitert et al. 2015; Simet et al. 2016; Melchior et al. 2016). The typical scatter found in the cluster virial mass at a given richness is of $\sim 10 - 25\%$ including statistical and systematic errors, in the mass range $6 \times 10^{12} M_{\odot} \lesssim M \lesssim 10^{15} M_{\odot}$ and in the redshift range $0.1 \lesssim z \lesssim 0.9$.

The aim of this work is to calibrate and evaluate the precision of the RedGOLD richness as a mass proxy, and to compare it to stacked weak

lensing masses. We then compare our lensing calibrated masses to X-ray mass proxies. Our approach mainly follows the one adopted by Johnston et al. (2007) and Ford et al. (2015), and we compare our results to Simet et al. (2016), Farahi et al. (2016) and Melchior et al. (2016).

The paper is organized as follows: in Section 2, we describe the shear data set and the photometric redshifts catalog; in Section 3, we briefly present the RedGOLD detection algorithm and the cluster catalogs; in Section 4, we describe the weak lensing equations and the method; in Section 5, we present the results; in Section 6, we discuss our findings in comparison with other recent works; in Section 7, we present our conclusions.

Throughout this work we assume a standard Λ CDM model, with $\Omega_m = 0.3$, $\Omega_{\Lambda} = 0.7$ and $H_0 = 70 \text{ km s}^{-1} \text{ Mpc}^{-1}$.

Magnitudes are given in the AB system (Oke & Gunn 1983; Sirianni et al. 2005).

2. DATA

For our analysis, we use our own data reduction (Raichoor et al. 2014) of the Canada-France-Hawaii Telescope Legacy Survey (CFHT-LS; Gwyn 2012) Wide 1 (W1) field and of the Next Generation Virgo Cluster Survey (NGVS; Ferrarese et al. 2012). We describe below these two datasets.

2.1. CFHTLenS and NGVSLenS

The CFHT-LS is a multi-color optical survey conducted between 2003 and 2008 using the CFHT optical multi-chip MegaPrime instrument (MegaCam³; Boulade et al. 2003). The survey consists of 171 pointings covering $\sim 154 \text{ deg}^2$ in four wide fields ranging from 25 to 72 deg^2 , with complete color coverage in the five filters $u^*g'r'i'z'$. All the pointings selected for this analysis were obtained under optimal seeing conditions with a seeing $< 0.8''$ in the primary lensing band i' (Erben et al. 2013). The 5σ point source limiting magnitudes in a $2.0''$ aperture in the five $u^*g'r'i'z'$ filters are ~ 25.2 , ~ 25.6 , ~ 24.9 , ~ 24.5 , ~ 23.5 mag, respectively (Erben et al. 2013).

¹<http://euclid-ec.org>

²<http://www.lsst.org>

³<http://www.cfht.hawaii.edu/Instruments/Imaging/MegaCam/>

The NGVS (Ferrarese et al. 2012) is a multi-color optical imaging survey of the Virgo Cluster, also obtained with the CFHT MegaCam instrument. This survey covers 104 deg^2 with 117 pointings in the four filters $u^*g'i'z'$. 34 of these pointings are also covered in the r' band. As for the CFHT-LS, the optimal seeing conditions were reserved to the i' -band which covers the entire survey with a seeing $< 0.6''$. The 5σ point source limiting magnitudes in a $2.0''$ aperture in the five $u^*g'r'i'z'$ filters are ~ 25.6 , ~ 25.7 , ~ 24.7 , ~ 24.4 , ~ 23.6 mag, respectively (Raichoor et al. 2014).

Both our CFHTLenS and NGVSLenS photometry and photometric redshift catalogs were derived using the dedicated data processing described in Raichoor et al. (2014). The preprocessed *Elixir*⁴ data, available at the Canadian Astronomical Data Centre (CADC⁵) were processed with an improved version of the THELI pipeline (Erben et al. 2005, 2009, 2013; Raichoor et al. 2014) to obtain co-added science images accompanied by weights, flag maps, sum frames, image masks and sky-subtracted individual chips that are at the base of the shear and photometric analysis. We refer the reader to Erben et al. (2013) and Heymans et al. (2012) for a detailed description of the different THELI processing steps and a full systematic error analysis. Raichoor et al. (2014) modified the standard pipeline performing the zero-point calibration using the SDSS data, taking advantage of its internal photometric stability. The SDSS covers the entire NGVS field and 62 out of 72 pointings of the CFHT-LS W1 field ($\sim 60 \text{ deg}^2$). Raichoor et al. (2014) constructed the photometric catalogs as described in Hildebrandt et al. (2012), adopting a *global* PSF homogenization to measure unbiased colors. Multicolor catalogs were obtained from PSF-homogenized images using SExtractor (Bertin & Arnouts 1996) in dual-image mode, with the un-convolved i' -band single-exposure as the detection image.

We restrict our analysis to the entire NGVS and the $\sim 60 \text{ deg}^2$ of the W1 field that were reprocessed by Raichoor et al. (2014), to have an homogeneously processed photometric catalog on a total of $\sim 164 \text{ deg}^2$.

For the shear analysis, as described in Miller

et al. (2013), shape measurements were obtained applying the Bayesian *lensfit* algorithm to single-exposure i' -band images with accurate PSF modeling, fitting PSF-convolved disc plus bulge galaxy models. The ellipticity of each galaxy is estimated from the mean likelihood of the model posterior probability, marginalized over model nuisance parameters of galaxy position, size, brightness and bulge fraction. The code assigns to each galaxy an inverse variance weight $w_{\text{lens}} \propto (\sigma_e^2 + \sigma_{\text{pop}}^2)^{-1}$, where σ_e^2 is the variance of the ellipticity likelihood surface and σ_{pop}^2 is the variance of the ellipticity distribution of the galaxy population. Calibration corrections consist in a multiplicative bias m , calculated using simulated images, and an additive bias c , estimated empirically from the data. As discussed in Miller et al. (2013), the former increases as the size and the signal-to-noise ratio of a galaxy detection decrease, while the latter increases as the signal-to-noise ratio of a galaxy detection increases and the size decreases.

2.2. Photometric Redshifts

The photometric redshift catalogs of the $\sim 60 \text{ deg}^2$ of the CFHTLenS covered by the SDSS and of the entire NGVSLenS were obtained using the Bayesian softwares *LePhare* (Arnouts et al. 1999; Arnouts et al. 2002; Ilbert et al. 2006) and BPZ (Benítez 2000; Benítez et al. 2004; Coe et al. 2006), as described in Raichoor et al. (2014). We used the re-calibrated SED template set of Capak et al. (2004).

Both *LePhare* and BPZ are designed for high redshift studies, giving biased or low quality photo- z 's estimations for objects with $i' < 20$ mag which represent a non-negligible fraction of both samples. In order to improve the performance at low redshift, Hildebrandt et al. (2012) used an *ad hoc* modified prior for the CFHTLenS data. Raichoor et al. (2014) adopted a more systematic solution for our reprocessed CFHTLenS W1 field and for the NGVSLenS, building a new prior calibrated on observed data, using the SDSS Galaxy Main Sample spectroscopic survey (York et al. 2000; Strauss et al. 2002; Ahn et al. 2014) to include bright sources.

To analyze the accuracy of the photometric redshift estimates, Raichoor et al. (2014) used several spectroscopic surveys covering the CFHTLenS and NGVSLenS: the SDSS Galaxy Main Sam-

⁴<http://www.cfht.hawaii.edu/Instruments/Elixir/>

⁵<http://www4.cadc-ccda.hia-ihp.nrc-cnrc.gc.ca/cadc/>

ple, two spectroscopic programs at the Multiple Mirror Telescope (MMT; Peng et al. 2016, in preparation) and at the Anglo-Australian Telescope (AAT; Zhang et al. 2015, 2016, in preparation), the Virgo Dwarf Globular Cluster Survey (Guhathakurta et al. 2016, in preparation), the DEEP2 Galaxy Redshift Survey over the Extended Groth Strip (DEEP2/EGS; Davis et al. 2003; Newman et al. 2013), the VIMOS Public Extragalactic Redshift Survey (VIPERS; Guzzo et al. 2014), and the F02 and F22 fields of the VIMOS VLT Deep Survey (VVDS; Le Fèvre et al. 2005, 2013).

As shown in Raichoor et al. (2014), when using all five filters, for $z_{\text{phot}} < 1$ and $i' < 23$ mag we found a bias $\Delta z = \frac{z_{\text{phot}} - z_{\text{spec}}}{1 + z_{\text{spec}}} < 0.02$, scatter values in the range $0.02 < \sigma < 0.05$ and $< 5\%$ of outliers. When using four bands the quality of the measurements slightly decreases, due to the lack of the r' -band to sample the 4000 Å break. In the range $0.3 < z_{\text{phot}} < 0.8$ and $i' > 21$ mag we obtained $-0.05 < \text{bias} < 0.02$, a scatter $\sigma \sim 0.06$ and an outliers rate of 10 – 15%.

In this analysis, we use the photometric redshifts derived with BPZ, corresponding to z_{best} , the peak of the redshift posterior distribution (hereafter, z_{phot}).

3. CLUSTER CATALOGS

3.1. The RedGOLD Optical Cluster Catalogs

3.1.1. The RedGOLD Algorithm

The RedGOLD algorithm (Licitra et al. 2016a,b) is based on a modified red-sequence search algorithm. Since the inner regions of galaxy clusters host a large population of passive and bright early-type galaxies (ETGs), RedGOLD searches for passive ETG overdensities. To avoid the selection of dusty red star-forming galaxies, the algorithm selects galaxies on the red sequence both in the rest-frame ($U - B$) and ($B - V$), using red sequence rest-frame zero point, slope and scatter from Mei et al. (2009), and with a ETG spectral classification from *LePhare*. In order to select an overdensity detection as a cluster candidate, the algorithm also imposes that the ETG radial distribution follows an NFW (Navarro, Frenk & White 1996) surface density profile.

RedGOLD centers the cluster detection on the ETG with the highest number of red companions, weighted on luminosity. This is motivated by the fact that the brightest cluster members lying near the X-ray centroid are better tracers of the cluster centers compared to using only the BCG (George et al. 2012). The redshift of the cluster is the median photometric redshift of the passive ETGs.

Each detection is characterized by two parameters, the significance σ_{det} and the richness λ , which quantifies the number of bright red ETGs inside the cluster, using an iterative algorithm.

The entire galaxy sample is divided in overlapping photometric redshift slices. Each slice is then divided in overlapping circular cells, with a fixed comoving radius of 500 *kpc*. The algorithm counts N_{gal} , the number of red ETGs inside each cell, brighter than $0.2L_*$, building the galaxy count distribution in each redshift slice. The background contribution is defined as N_{bkg} , the mode of this distribution, with standard deviation σ_{bkg} . The detection significance is then defined as $\sigma_{\text{det}} = (N_{\text{gal}} - N_{\text{bkg}})/\sigma_{\text{bkg}}$. Overdensities larger than $N_{\text{bkg}} + \sigma_{\text{det}} \times \sigma_{\text{bkg}}$ are selected as preliminary detections. The uncertainties on the cluster photometric redshift range between 0.001 and 0.005, with an average of 0.003 ± 0.002 . In this paper we assume that these uncertainties are negligible for our analysis (see also Simet et al. 2016).

The algorithm then estimates the richness λ , counting N_{gal} inside a scale radius, initially set to 1 *Mpc*. The radius is iteratively scaled with richness as in Rykoff et al. (2014), until the difference in richness between two successive iterations is less than N_{bkg} .

RedGOLD is optimized to produce cluster catalogs with high completeness and purity. In Licitra et al. (2016a,b), the *completeness* is defined as the ratio between detected structures corresponding to true clusters and the total number of true clusters, and the *purity* is defined as the number of detections that correspond to real structures to the total number of detected objects. Following the definition of a *true cluster* in the literature (e.g, Finoguenov et al. 2003; Lin et al. 2004; Evrard et al. 2008; Finoguenov et al. 2009; McGee et al. 2009; Mead et al. 2010; George et al. 2011; Chiang et al. 2013; Gillis et al. 2013; Shankar et al. 2013), we define a *true cluster* as a dark matter

halo more massive than $10^{14} M_{\odot}$. In fact, numerical simulations show that 90% of the dark matter haloes more massive than $10^{14} M_{\odot}$ are a very regular virialized cluster population up to redshift $z \sim 1.5$ (e.g., Evrard et al. 2008; Chiang et al. 2013). In order to validate the performance of our algorithm to find clusters with a total mass larger than $10^{14} M_{\odot}$ and measure our obtained sample completeness and purity, we have applied RedGOLD to simulations and observations. We then have compared our RedGOLD optical detection with X-ray detected cluster masses. For details on the method and the performance of the algorithm when applied to numerical simulations we refer the reader to Licitra et al. (2016a).

3.1.2. The RedGOLD CFHT-LS W1 and NGVS Cluster Catalogs

We use the CFHT-LS W1 and NGVS cluster catalogs from Licitra et al. (2016a) and Licitra et al. (2016b), respectively. For both surveys, when using five bandpasses, in the published catalogs, we selected clusters more massive than $\approx 10^{14} M_{\odot}$, the mass limit for which $\sim 90\%$ of dark matter halos at $z_{\text{phot}} < 1.5$ are virialized (Evrard et al. 2008). In Licitra et al. (2016a,b), we calibrated the σ_{det} and λ parameters to maximize the completeness and purity of the catalog of these type of objects. Licitra et al. (2016a) demonstrated that when we considered only detections with $\sigma_{\text{det}} \geq 4$ and $\lambda \geq 10$ at $z_{\text{phot}} \leq 0.6$, and $\sigma_{\text{det}} \geq 4.5$ and $\lambda \geq 10$ at $z_{\text{phot}} \lesssim 1$, we obtain catalogs with a completeness of $\sim 100\%$ and $\sim 70\%$, respectively, and a purity of $\sim 80\%$.

Both in the CFHT-LS W1 and the NGVS, we masked areas around bright stars and nearby galaxies. We found that in only $\sim 2\%$ of the cluster candidates (low richness structures at high redshift) more than 10% of their bright potential members are masked (Licitra et al. 2016a). Therefore our richness estimates are not significantly affected by masking.

For the NGVS, as explained above, the five band coverage was limited to only the $\sim 30\%$ of the survey. The lack of the r' -band in the remaining pointings, causes higher uncertainties on the determination of photometric redshifts for sources at $0.3 < z_{\text{phot}} < 0.8$ but the global accuracy on the photometric redshifts remains high even for this sample, as shown in Raichoor et al. (2014).

Since there are some fields in which the quality of the r' -band is lower because of the lower depth and the lack of coverage of the intra-CCD regions, this makes also more difficult the detection of the less massive structures at intermediate and high redshifts and the determination of the clusters center and richness.

To quantify this effect in the richness estimation, Licitra et al. (2016b) compared the values recovered with a full band coverage λ_r with the ones obtained without the r' -band λ_{wr} , and measured $\Delta\lambda/\lambda_r \equiv (\lambda_r - \lambda_{\text{wr}})/\lambda_r$, in different redshift bins. Median values of $\Delta\lambda/\lambda_r$ and their standard deviations are listed in Table 2 of Licitra et al. (2016b). At $z_{\text{phot}} < 0.5$ and $z_{\text{phot}} > 0.8$, the two estimates are in good agreement, with $\Delta\lambda/\lambda_r < 10\%$. This is due to the fact that the $(g-z)$ and $(i-z)$ colors straddle the 4000 Å break at $z_{\text{phot}} < 0.5$ and $z_{\text{phot}} > 0.8$, respectively. At $0.5 < z_{\text{phot}} < 0.6$, λ_{wr} is systematically underestimated of $\sim 40\%$ on average and, at $0.6 < z_{\text{phot}} < 0.8$, it's systematically overestimated of $\sim 20\%$ on average. The first systematic is due to the use of the $(g-z)$ color, that changes less steeply with redshift and has larger photometric errors, compared with $(r-i)$ and $(i-z)$ colors. The latter is caused by the use of the $(i-z)$ color only, without the additional cut in the $(r-z)$ or $(r-i)$ colors that allows us to reduce the contamination of dusty red galaxies on the red sequence (Licitra et al. 2016b).

To take this into account, we correct the λ_{wr} estimations using the average shifts given in Table 2 of Licitra et al. (2016b). As we will discuss later, since for this analysis we are only selecting clusters at $z_{\text{phot}} < 0.5$ (see below), using four bands we preserve the same level of completeness and purity as using the five bands catalog.

For these reasons, for the NGVS we built two separate catalogs: the first for the $\sim 20 \text{ deg}^2$ covered by the r' -band and the second for the entire NGVS using only four bandpasses. In this last catalog we corrected for the average shift in λ when applying our thresholds (Licitra et al. 2016b). Hereafter, we define the NGVS catalog obtained on the area covered by the five bandpasses as NGVS5 and the catalog obtained with four bandpasses as NGVS4.

The CFHT-LS W1 published catalog includes 652 cluster candidate detections in an area of $\sim 60 \text{ deg}^2$. The NGVS published catalogs include

279 and 1505 detections, in the $\sim 20 \text{ deg}^2$ with the five band coverage and in the rest of the survey, respectively.

We select cluster subsamples from these catalogs for our weak lensing analysis. Knowing that the peak in the lensing efficiency is found at $z_{\text{phot}} \sim 0.4$ for source galaxies at $z_{\text{phot}} \sim 1$ (Hamana et al. 2004) and that shear measurements from ground based telescopes are reliable for clusters with redshifts $0.2 < z_{\text{phot}} < 0.5$ (Kasliwal et al. 2008), we select detections only in this redshift range. We also discard clusters with richness $\lambda < 10$ and $\lambda > 70$. In fact, as shown in Licitra et al. (2016a) at richness $\lambda < 10$, our purity decreases for a given significance threshold. For our significance threshold of $\sigma_{\text{det}} > 4$, $\lambda < 10$ implies a contamination of false detections larger than $\sim 20\%$. For $\lambda > 70$, we have very few detections and there are not enough clusters to obtain an average profile from a statistically significant sample.

Our final selection for the weak lensing analysis includes 1325 clusters. Their richness and redshift distributions are shown in Figure 1. Hereafter, we will define the catalogs to which we applied the thresholds in significance, richness and redshift for the weak lensing analysis as *selected* catalogs. The published Licitra et al. (2016a,b) catalogs, to which we applied the thresholds in significance and richness, will be referred to as Licitra’s *published* catalogs. The Licitra et al. (2016a,b) catalogs, without any threshold as *complete* catalogs.

3.2. The X-ray Cluster Catalogs

Gozaliasl et al. (2014) analyzed the *XMM-Newton* observations in the $\sim 3 \text{ deg}^2$ overlapping the CFHT-LS W1 field, as a part of the XMM-LSS survey (Pierre et al. 2007)⁶. They presented a catalog of 129 X-ray groups, in a redshift range $0.04 < z_{\text{phot}} < 1.23$, characterized by a rest frame $0.1 - 2.4 \text{ keV}$ band luminosity range $10^{41} - 10^{44} \text{ ergs s}^{-1}$. They removed the contribution of AGN point sources from their flux estimates and applied a correction of $\sim 10\%$ for the removal of cool core flux based on the high resolution *Chandra* data on COSMOS as shown in Leauthaud et al. (2010). They used a two-color red-sequence finder to identify group members and calculate the

mean group photometric redshift. They inferred cluster’s M_{200} masses using the $L_X - M$ relation of Leauthaud et al. (2010), with a systematic uncertainty of $\sim 20\%$.

Mehrtens et al. (2012) presented the first data release of the XMM Cluster Survey (XCS), a serendipitous search for galaxy clusters in the *XMM-Newton* Science Archive data⁷. The catalog consists of 503 optically confirmed clusters, in a redshift range $0.06 < z_{\text{phot}} < 1.46$. 402 of these clusters have measured X-ray temperatures in the range $0.4 < T_X < 14.7 \text{ keV}$. They derived photometric redshifts with the red-sequence technique, using one color. They used a spherical β -profile model (Cavaliere & Fusco-Fermiano 1976) to fit the surface brightness profile and derive the bolometric (0.05 - 100 keV band) luminosity in units of $10^{44} \text{ erg s}^{-1}$ within the radius R_{200} and R_{500} .

In Section 5.3, we will use these catalogs to compare our lensing masses with X-ray masses and calculate the scaling relations between lensing masses and X-ray temperature and luminosity. We analyze the two catalogs separately because the different treatment of the emission from the central regions of the clusters leads to different mass estimates. In Section 6.2 we will discuss these results.

4. WEAK LENSING ANALYSIS

In this Section, we describe our weak lensing analysis. Our aim is to infer cluster masses by reconstructing the tangential shear radial profile $\gamma_t(R)$, averaging in concentric annuli around the halo center, and fitting it to a known density profile. $\gamma_t(R)$ accounts for the distortion, due to the gravitational potential of the lens, of the shape of the background sources in the tangential direction with respect to the center of the lens and it’s defined as:

$$\gamma_t = -Re [\gamma e^{-2i\phi}] \quad (1)$$

with $\gamma = \epsilon_1 + i\epsilon_2 = |\gamma|e^{2i\phi}$, where ϵ_1 and ϵ_2 are the ellipticity components of the galaxy and ϕ is the position angle of the galaxy respect to the center of the lens (Schneider 2005).

As described in Wright & Brainerd (2000), the tangential shear profile $\gamma_t(R)$ is related to the surface density contrast by:

$$\Delta\Sigma(R) = \langle \gamma_t(R) \rangle \Sigma_c \quad (2)$$

⁶<https://heasarc.gsfc.nasa.gov/W3Browse/all/cfhtlsgxmm.html>

⁷<https://heasarc.gsfc.nasa.gov/W3Browse/all/xcs.html>

Where R is the projected radius with respect to the center of the lens and:

$$\Sigma_c = \frac{c^2}{4\pi G} \frac{D_s}{D_l D_{ls}} \quad (3)$$

is the critical surface density. Here c is the speed of light and D_s , D_l , D_{ls} are the angular diameter distances from the observer to the source, from the observer to the lens, and from the lens to the source, respectively.

To infer cluster masses, we fit the measured $\Delta\Sigma(R)$ profile, obtained as described in Section 4.1, to the theoretical models introduced in Section 4.2.

4.1. Cluster Profile Measurement

To measure cluster masses, we need to fit the cluster radial profiles. This is possible individually only for the most massive clusters in our sample ($M_{200} > 4 \times 10^{14} M_\odot$ for a signal-to-noise ratio $S/N > 3$; they represent the $\sim 2\%$ of the sample), while the noise dominates for the others. In order to increase the signal-to-noise ratio and measure average radial profiles for all the other detections, we stack galaxy clusters in six richness bins, from $\lambda = 10$ to $\lambda = 70$, in steps of 10 in richness.

We select the background galaxy sample using the following criteria:

$$i' < 24.7 \text{ mag} \quad (4a)$$

$$0.2 < z_{\text{phot}} < 1.3 \quad (4b)$$

to obtain reliable shape measurement and photometric redshifts (Kettula et al. 2015; Hildebrandt et al. 2012; Raichoor et al. 2014). As in Kettula et al. (2015), for each cluster we select only background galaxy with redshift:

$$z_{\text{phot},s} > z_{\text{phot},l} + 0.15 \quad (5)$$

where $z_{\text{phot},s}$ is the source redshift and $z_{\text{phot},l}$ is the lens redshift.

Following Ford et al. (2015), we then sort the background galaxies in 10 logarithmic radial bins from 0.09 Mpc from the center of the lens to 5 Mpc . In fact, at radii closer than 0.09 Mpc , galaxy counts are dominated by cluster galaxies,

and at larger radii the mass estimate can be underestimated as much as $\sim 20\%$ because of the contribution of large scale structure (Becker & Kravtsov 2011; Oguri & Hamana 2011).

In each radial bin we perform a weighted average of the lensing signal as follows:

$$\Delta\Sigma(R) = \frac{\sum_{i=0}^l \sum_{j=0}^s w_{ij} \Sigma_{c,ij} \gamma_{t,ij}}{\sum_{i=0}^l \sum_{j=0}^s w_{ij}} \quad (6)$$

where we sum over every *lens-source* pair (i.e. i - j indices up to the l number of lenses and s number of sources). The weights $w_{ij} = \Sigma_{c,ij}^{-2} w_{\text{lens}}$ (Mandelbaum et al. 2005) quantify the quality of the shape measurements through the *lensfit* weights w_{lens} (defined in Section 2.1) and down-weight source galaxies that are close in redshift to the lens through $\Sigma_{c,ij}^{-2}$, which is evaluated for every *lens-source* pair using z_{phot} to calculate the angular diameter distances that appear in Equation 3.

We need then to correct the measured signal, applying the calibration corrections introduced in Section 2.1. As shown in Heymans et al. (2012), the ellipticity estimated by *lensfit* can be related to the true ellipticity (i.e. the sum of the shear and of the galaxy intrinsic ellipticity) as $\epsilon_{\text{lens}} = (1 + m)[\gamma + \epsilon_{\text{int}}] + c$, where m and c are the multiplicative and additive biases. While the latter can be simply added on single ellipticity measurements, the first needs to be applied as a weighted ensemble average correction:

$$1 + K(R) \equiv \frac{\sum_{i=0}^l \sum_{j=0}^s w_{ij} [1 + m_{ij}]}{\sum_{i=0}^l \sum_{j=0}^s w_{ij}} \quad (7)$$

This is done to avoid possible instabilities in case the term $(1 + m)$ tends to zero. In this way we also remove any correlation between the calibration correction and the intrinsic ellipticity (Miller et al. 2013). The calibrated signal is written as:

$$\Delta\Sigma_{\text{cal}}(R) = \frac{\Delta\Sigma(R)}{1 + K(R)} \quad (8)$$

To estimate the errors on $\Delta\Sigma(R)$, we create a set of 100 bootstrap realizations for each richness bin, selecting the same number of clusters for each

stack but taking them with replacements. We apply Equation 6 to obtain $\Delta\Sigma(R)$ for each bootstrap sample.

Following Ford et al. (2015), we then calculate the covariance matrix:

$$C(R_i, R_j) = \left[\frac{N}{N-1} \right]^2 \frac{1}{N} \sum_{k=1}^N [\Delta\Sigma_k(R_i) - \overline{\Delta\Sigma}(R_i)] \times [\Delta\Sigma_k(R_j) - \overline{\Delta\Sigma}(R_j)] \quad (9)$$

where R_i and R_j are the radial bins, N is the number of bootstrap samples and $\overline{\Delta\Sigma}(R_i)$ is the average over all bootstrap realizations.

For each radial bin, we weight the shear using the *lensfit* weights as shown in Equation 6, so these error bars also include the error on the shape measurements of the source galaxies. We calculate the covariance matrix to take into account the correlation between radial bins and the contribution to the stacked signal of clusters with different masses inside the same richness bin.

4.2. Cluster Profile Model

To fit the tangential shear profiles we use an analytic model for the cluster profile:

$$\Delta\Sigma(R) = p_{cc}[\Delta\Sigma_{\text{NFW}}(R) + \Delta\Sigma_{\text{nw}}(R)] + (1 - p_{cc})\Delta\Sigma_{\text{sm}}(R) + \Delta\Sigma_{\text{2halo}}(R) \quad (10)$$

$\Delta\Sigma_{\text{NFW}}$ is the surface density contrast calculated from an NFW density profile, assumed as the halo profile. $\Delta\Sigma_{\text{nw}}$, $\Delta\Sigma_{\text{sm}}$ and $\Delta\Sigma_{\text{2halo}}$ are correction terms that take into account, respectively, non-weak shear, cluster miscentering and the contribution to the signal from large scale structure. p_{cc} is a free parameter related to the miscentering term and represents the percentage of correctly centered clusters in each stack. Each term and the free parameters of the model will be described in detail in the following Sections.

In addition to this basic model, hereafter Model 1, we also consider two model extensions discussed in Section 4.3.

All the averages in the equations below are performed using the same weighting as in equation 6.

4.2.1. $\Delta\Sigma_{\text{NFW}}$ Profile

For the cluster halo profile, we assume an NFW profile. Numerical simulations have shown that dark matter halos density profiles, resulting from the dissipationless collapse of density fluctuations, can be well described by this profile:

$$\rho_{\text{NFW}}(r) = \frac{\delta_c \rho_c}{\left(\frac{r}{r_s}\right)\left(1 + \frac{r}{r_s}\right)^2} \quad (11)$$

$$\rho_c = \frac{3H(z)^2}{8\pi G} \quad (11a)$$

$$r_s = \frac{r_{200}}{c} \quad (11b)$$

$$\delta_c = \frac{200}{3} \frac{c^3}{\ln 1 + c - \frac{c}{1+c}} \quad (11c)$$

where ρ_c is the critical density of the universe; c is the concentration parameter; δ_c is a dimensionless parameter that depends only on the concentration; r_s is a scale radius that depends on r_{200} ; r_{200} is the radius at which the density is 200 times the critical density of the Universe and can be considered as an approximation of the virial radius of the halo. The mass M_{200} is the mass of a sphere of radius r_{200} and average density of $200\rho_c$:

$$M_{200} = M(r_{200}) = \frac{4\pi}{3} r_{200}^3 \times 200\rho_c \quad (12)$$

Simulations have also shown that there is a relation between M_{200} and c (e.g. Navarro, Frenk & White 1996; Bullock et al. 2001). In order to take this into account, we use the Dutton & Macció (2014) mass-concentration relation:

$$\log c_{200} = a + b \log (M_{200}/[10^{12} h^{-1} M_{\odot}]) \quad (13)$$

with $a = 0.520 + (0.905 - 0.520) \exp(-0.617z^{1.21})$ and $b = -0.101 + 0.026z$. This reduces the dimensionality of the model to one parameter, r_{200} , from which we can calculate the halo mass using Equation 12.

Integrating the tridimensional NFW density profile along the line of sight, we can calculate the NFW surface density:

$$\Sigma_{\text{NFW}}(R) = 2 \int_0^{\infty} \rho_{\text{NFW}}(R, z) dz \quad (14)$$

Integrating again, we get $\bar{\Sigma}_{\text{NFW}}(R)$, the average surface density inside a radius R :

$$\bar{\Sigma}_{\text{NFW}}(< R) = \frac{2}{R^2} \int_0^R R' \Sigma_{\text{NFW}}(R') dR' \quad (15)$$

Finally, we can calculate the first term in Equation 10:

$$\Delta \Sigma_{\text{NFW}} = \bar{\Sigma}_{\text{NFW}}(< R) - \Sigma_{\text{NFW}}(R) \quad (16)$$

4.2.2. Miscentering Term

Since the NFW density profile is spherically symmetric, an error in the determination of the halo center would lead to systematically underestimate the lens mass. In fact, the random stacking offset smooths the differential surface mass density profile (George et al. 2012).

Following Licitra et al. (2016a), we match our RedGOLD detections to X-ray detections in the same areas (Gozaliasl et al. 2014) to measure our average offset between RedGOLD and X-ray cluster centers, which we consider as the true centers. We perform the match between the RedGOLD and the Gozaliasl et al. (2014) catalogs by imposing a maximum separation between centers of 1 Mpc and a maximum difference in redshift of $\Delta z = 0.1$.

We find that the distribution of the offsets between the X-ray and the RedGOLD centers in two dimensions can be modeled as a Rayleigh distribution with a mode of 13 $arcsec$ (Figure 2, on the left; see also Johnston et al. 2007; George et al. 2012; Ford et al. 2015). In Figure 2, on the right, we also show the offset distribution in kpc . This distribution is consistent with the center offset distribution predicted from cosmological simulations for X-ray detected clusters, including AGN feedback (Cui et al. 2016).

We assume that this distribution represents the general offset distribution for our entire RedGOLD sample $P(R_{\text{off}})$, and model it following Johnston et al. (2007):

$$P(R_{\text{off}}) = \frac{R_{\text{off}}}{\sigma_{\text{off}}^2} \exp \left[-\frac{1}{2} \left(\frac{R_{\text{off}}}{\sigma_{\text{off}}} \right)^2 \right] \quad (17)$$

where R_{off} is the offset between the true and the estimated center, projected on the lens plane, and

σ_{off} is the mode, or scale length, of the distribution. The surface density measured at the coordinates (R, θ) , with θ the azimuthal angle, relative to the offset position, R_{off} , is:

$$\Sigma_{\text{NFW}}(R, \theta | R_{\text{off}}) = \Sigma_{\text{NFW}} \left(\sqrt{R^2 + R_{\text{off}}^2 - 2RR_{\text{off}} \cos \theta} \right) \quad (18)$$

and the azimuthal averaged surface density around R_{off} is given by:

$$\Sigma_{\text{NFW}}(R | R_{\text{off}}) = \frac{1}{2\pi} \int_0^{2\pi} \Sigma_{\text{NFW}}(R, \theta | R_{\text{off}}) d\theta \quad (19)$$

To model the effect of miscentering, we smooth the $\Sigma_{\text{NFW}}(R | R_{\text{off}})$ profile convolving it with $P(R_{\text{off}})$:

$$\Sigma_{\text{sm}}(R) = \int_0^{\infty} \Sigma_{\text{NFW}}(R | R_{\text{off}}) P(R_{\text{off}}) dR_{\text{off}} \quad (20)$$

and obtain the stacked surface density profile $\Sigma_{\text{sm}}(R)$ around the offset positions of our ensemble of clusters with offset distribution $P(R_{\text{off}})$ (Yang et al. 2006; Johnston et al. 2007; George et al. 2012).

Finally we can write the miscentering term as:

$$\Delta \Sigma_{\text{sm}}(R) = \bar{\Sigma}_{\text{sm}}(< R) - \Sigma_{\text{sm}}(R) \quad (21)$$

with $\bar{\Sigma}_{\text{sm}}(< R)$ being, as before, the average surface density within the radius R .

The miscentering term adds two free parameters to our model, σ_{off} and p_{cc} , which is the percentage of correctly centered clusters in the stack, already introduced in Equation 10.

4.2.3. Non-weak Shear Term

The non-weak shear correction arises from the fact that what we actually measure is the reduced shear:

$$g_t = \frac{\gamma_t}{1 - k} \quad (22)$$

where $k \equiv \Sigma_{\text{NFW}}/\Sigma_c$ is the convergence. Usually in the weak lensing regime $g_t \approx \gamma_t$, if $\gamma_t \ll 1$ and $k \ll 1$, but for relatively massive halos this assumption may no longer hold at the innermost radial bins in which we want to measure the cluster profile.

As described in Johnston et al. (2007), we introduce the non-weak shear correction term, calculated in Mandelbaum et al. (2006). In the non-weak regime, the tangential ellipticity component, ϵ_t is proportional to g_t , instead of γ_t . We can expand ϵ_t in power series as:

$$\begin{aligned} \epsilon_t &= \sum_{n=0}^{\infty} A g_t^{2n+1} \\ &= A \left(\frac{\gamma_t}{1-k} \right)^{2n+1} = A \left(\frac{\Delta \Sigma \Sigma_c^{-1}}{1 - \Sigma \Sigma_c^{-1}} \right)^{2n+1} \end{aligned} \quad (23)$$

As shown in detail in appendix A of Mandelbaum et al. (2006), we can calculate the correction term from the expansion in power series to second order of ϵ_t , in powers of Σ_c . We obtain the following term, that we add in Equation 10:

$$\Delta \Sigma_{\text{nw}}(R) = \Delta \Sigma_{\text{NFW}}(R) \Sigma_{\text{NFW}}(R) \frac{\langle \Sigma_c^{-3} \rangle}{\langle \Sigma_c^{-2} \rangle} \quad (24)$$

4.2.4. Two-halo Term

On large scales, the lensing signal is dominated by nearby mass concentrations, halos, and filaments. Seljak (2000) developed an analytic halo model, in which all the matter in the Universe is hosted in virialized halos, described by a universal density profile. They computed analytically the power spectrum of dark matter and galaxies, and their cross-correlation based on the Press & Schechter (1974) model. They found that, ignoring the contribution from satellite galaxies, a cluster can be modeled by two contributions, the one-halo term and the two-halo term. The first represents the correlation between the central galaxy and the host dark matter halo and corresponds to $\Delta \Sigma_{\text{NFW}}(R)$. The second accounts for the correlation between the cluster central galaxy and the host dark matter halo of another cluster.

On large scales, the two-halo power spectrum is proportional to the halo bias and the linear power spectrum, $P_{\text{2halo}} \propto b(M_{200,z}) P_{\text{lin}}(k)$. In order to calculate the surface density associated to the two-halo term, we integrate the galaxy-dark matter linear cross-correlation function $\xi_{\text{lin}}(r)$, obtained by the Fourier transform of the linear power spectrum.

Following Johnston et al. (2007) and Ford et al.

(2015), we can write the two-halo term as:

$$\begin{aligned} \Delta \Sigma_{\text{2halo}}(R, b) &= \\ &= b(M_{200}, z) \Omega_m \sigma_8^2 D(z)^2 \Delta \Sigma_1(R) \end{aligned} \quad (25)$$

where $b(M_{200}, z)$ is the bias factor, Ω_m is the matter density parameter, σ_8^2 is the amplitude of the power spectrum on scales of $8 h^{-1} Mpc$, $D(z)$ is the growth factor and

$$\Delta \Sigma_1(R) = \bar{\Sigma}_1(< R) - \Sigma_1(R) \quad (26)$$

where

$$\begin{aligned} \Sigma_1(R, z) &= \\ &= (1+z)^3 \rho_{c,0} \int_{-\infty}^{\infty} \xi_{\text{lin}} \left((1+z) \sqrt{R^2 + y^2} \right) dy \end{aligned} \quad (27)$$

The factor $(1+z)$ arises from the conversion from physical units to comoving units.

For the bias factor, we use the analytic formula calculated by Seljak & Warren (2004), and for $P_{\text{lin}}(k)$, we use tabulated values from CAMB (Lewis, Challinor & Lasenby 2000).

4.3. Model Extensions

To take into account possible profile fitting biases, we introduce two modifications of the basic Model 1.

Previous work (Becker et al. 2007; Rozo et al. 2009) have shown that, when fitting the model profile to the halo profile derived from the observations in richness bins, the intrinsic scatter between the dark matter halo mass and the richness biases mass measurements. Following their modeling, we assume that the mass M_{200} has a log-normal distribution at fixed richness, with the variance in $\ln M_{200}$, $\sigma_{\ln M_{200}|\lambda}$, and, in our first modification (hereafter Model 2), we add $\sigma_{\ln M_{200}|\lambda}$ as a new parameter to Model 1.

In addition, as shown by Gavazzi et al. (2007), the two contributions to the shear signal from the luminous and dark matter can be distinguished by fitting a two-component mass model, which take into account the contribution from the stellar mass of the halo central galaxy M_{BCG} . In the second modification (hereafter Model 3), we add this contribution to the total halo mass in Model 1. In order to model the BCG signal, we follow Johnston et al. (2007) and add a point mass term to

Equation 10:

$$\frac{M_{\text{BCG}}}{\pi R^2} \quad (28)$$

and add $\log(M_{\text{BCG}})$ as an additional parameter to Model 1:

$$\begin{aligned} \Delta\Sigma(R) = & \frac{M_{\text{BCG}}}{\pi R^2} + \\ & p_{\text{cc}}[\Delta\Sigma_{\text{NFW}}(R) + \Delta\Sigma_{\text{nw}}(R)] + \\ & (1 - p_{\text{cc}})\Delta\Sigma_{\text{sm}}(R) + \Delta\Sigma_{\text{2halo}}(R) \quad (29) \end{aligned}$$

5. RESULTS

5.1. Cluster Mass Estimation

5.1.1. Fit the Profile Model to the Shear Profile

We fit the shear profiles obtained as described in Section 4.1 with the density profile models of Section 4.2, for Model 1, 2 and 3.

We perform the fit using Markov Chains Monte Carlo (MCMC; Metropolis et al. 1953). This method is particularly useful when the fitting model has a large number of parameters, the posterior distribution of the parameters is unknown, or the calculation is computationally expensive. MCMC allow to efficiently sample the model likelihood by constructing a Markov chain that has the target posterior probability distribution as its stationary distribution. Each step of the chain is drawn from a model distribution and is accepted, or not, based on the criteria defined by the sampler algorithm.

To run our MCMC, we use *emcee*⁸ (Foreman-Mackey et al. 2013), a Python implementation of the parallel Stretch Move by Goodman & Weare (2010). In order to choose the starting values of the chain we first perform a minimization with the Python version of the Nelder-Mead algorithm, also known as downhill simplex (Nelder & Mead 1965). We choose to use uninformative priors (i.e. a uniform distribution within a given range) for all parameters. Our initial priors, for the three different models, are shown in Table 1. All parameters are constrained to be positive and inside a range chosen according to their physical meaning. To choose the range for the intrinsic scatter, we refer to the values calculated by Licitra et al. (2016a). They

found $\sigma_{\ln M|\lambda} = 0.39 \pm 0.07$ using the X-ray catalog of Gozaliasl et al. (2014) and $\sigma_{\ln M|\lambda} = 0.30 \pm 0.13$ from Mehrtens et al. (2012).

MCMC produce a representative sampling of the likelihood distribution, from which we obtain the estimation of the error bars on the fitting parameters and of the confidence regions for each couple of parameters. We calculate the model likelihood using the bootstrap covariance matrix of Equation 9:

$$\begin{aligned} \ln\mathcal{L} = & -\frac{1}{2} (\Delta\Sigma_{\text{data}} - \Delta\Sigma_{\text{model}})^T C^{-1} \\ & (\Delta\Sigma_{\text{data}} - \Delta\Sigma_{\text{model}}) \quad (30) \end{aligned}$$

We use an ensemble of 100 walkers, a chain length of 1000 steps and a burn-in of 100 steps leading to a total of 90000 points in the parameters space. In order to test the result of our chain, we check the acceptance fraction and the autocorrelation time to be sure of efficiently sample the posterior distribution and having enough independent samples.

5.1.2. Fit Parameters

We perform the fit of the models to the observed profiles on each of the three samples, CFHT-LS W1, NGVS5 and NGVS4. We then combine the CFHTLS and NGVS5, and all the three sample together.

For Model 1, we measure the radius r_{200} and the miscentering parameters, p_{cc} and σ_{off} . We calculate the mass M_{200} from Equation 12. For Model 2, instead of measuring the mean radius r_{200} , we directly calculate $\log M_{200}$. In order to do so, for each bin, we use the mass-richness relation calculated from Model 1 to infer the mean mass of the stacked clusters, as a first approximation. We then randomly scatter the mass using a gaussian distribution with mean $\langle \ln M_{200} \rangle$ and width $\sigma_{\ln M_{200}|\lambda}$, to take into account the intrinsic scatter effect, as described in Section 4.3. For Model 3, we add to Model 1 the point mass term with the new parameter M_{BCG} (see Equation 29).

The profiles obtained using Model 1 and the complete sample (CFHT-LS W1 + NGVS5 + NGVS4) are shown in green in Figure 3. The error bars on the shear profiles are the square root of the diagonal elements of the covariance matrix.

The profiles measured using the CFHT-LS W1 + NGVS5 sample (shown in Figure 4), and the

⁸<https://github.com/dfm/emcee>

complete sample, are consistent within 1σ and the error bars are smaller in the last case. We can conclude that the richness shifts applied to NGVS4 seem not to bias our results, when this sample is added to the other two, covered by five bands. Increasing the sample size, we notice a progressive improvement in the profiles which are recovered with a lower noise level.

Since the miscentering correction is the one that most affects the mass estimation, in Figure 3 we also show the profiles that we would obtain with and without the miscentering term to show how an incorrect modeling of this effect leads to biased mass values (i.e. mass underestimation between 10–40%, Ford et al. 2015). The red lines represent the profiles we would obtain in the case in which all the clusters in the stack were perfectly centered ($p_{cc} = 1$) and the blue lines show the opposite case ($p_{cc} = 0$).

We show the results of our fits in Table 2, 3, 4, for Model 1, 2, 3, respectively. The values of the miscentering parameters, in each richness bin, are consistent within 1σ , for the three models. Since the center of the most massive clusters should be easier to identify, we would expect σ_{off} to decrease and p_{cc} to increase, for increasing masses. However, we do not observe this trend. In fact, the number of stacked clusters decreases for higher richness values, leading to more noisy smoothed profiles.

This is confirmed from the lensing signal-to-noise ratio maps shown in Figure 5. These maps were calculated using aperture mass statistics (Schneider 1996; Schirmer et al. 2006; Du & Fan 2014). For each richness bin, we create a grid with a side of $1 Mpc$ and binning of $0.001 deg$, centered on the stacked clusters. In each cell, we evaluate the amount of tangential shear, filtered by a function that maximizes the signal-to-noise ratio of an NFW profile, inside a circular aperture, following Schirmer et al. (2006).

For stacked clusters, a $S/N \sim 10$ is considered sufficient to recover the fitting parameters (Oguri & Takada 2011). All bins, except the last two, have $S/N > 10$, explaining the more regular behavior and the smaller error bars of the respective shear profiles.

In Figure 6, we show an example of error bars and the confidence regions of the param-

eters, obtained using the python package *corner* by Foreman-Mackey et al. (2016). This example corresponds to the third richness bin, fitted with Model 1. On the diagonal, we show the one-dimensional histograms of the parameter values, representing the marginalized posterior probability distributions. Under the diagonal, we show the two-dimensional histograms for each couple of parameters and the confidence levels corresponding to 0.5σ , 1σ , 1.5σ and 2σ .

5.2. Mass-Richness Relation

Using the mass measured for each richness bin, we perform a fit to a power law to infer the mass richness relation for all three models, using the python orthogonal distance regression routine (ODR; Boggs & Rogers 1990) to take into account the errors in both $\log \lambda$ and $\log M_{200}$:

$$\log M_{200} = \log M_0 + \alpha \log \lambda / \lambda_0 \quad (31)$$

with a pivot richness $\lambda_0 = 40$.

We use different richness bins to test the stability of our results. At first we use all richness bins. Then, we consider only the bins with the best statistics. As we discussed, from the shear profiles and the signal-to-noise ratio maps we notice that the two highest richness bins are more noisy when compared to the others, because they include less detections. We also know, from Licitra et al. (2016a), that at a given significance threshold, a lower richness implies a more contaminated sample. For this reason, we repeat the fit discarding the lowest and the two highest richness bins, restraining our sample to an optimized richness range $20 < \lambda \leq 50$. With $\lambda > 20$ and $z < 0.5$, we expect our sample to be $\sim 90\%$ pure and $\sim 100\%$ complete, significantly reducing contamination from false detections (see Figure 7 and 8 from Licitra et al. 2016a). This sample (hereafter *best richness bin* sample) includes 346 clusters.

In Figure 7, on the left, we plot the results obtained fitting all the bins and, on the right, fitting only the *best richness bin* sample. The three models are shown in black (Model 1), blue (Model 2) and red (Model 3). For each richness bin, the masses estimated are compatible within 1σ , for the three models. We notice that the uncertainties in the fit of Model 2 are much larger. This is due to the fact that we add more uncertainty through the

intrinsic scatter parameter. Our results are shown in Table 5. The slope and the normalization values are all consistent within 1σ when discarding the first and the higher richness bins.

The advantage of using the ODR is clear when we use all data points (plot on the left), since applying an ordinary least square method would have resulted in a steep fit dominated by the highest richness bins, which present the lowest errors. We also note that, in this case, the fit is mainly driven by the last three points that have much smaller error bars both in $\log M_{200}$ and $\log \lambda$, and have more weight in the fit. In contrast with the other two models, when using Model 2, for which the error bars in $\log M_{200}$ are an order of magnitude larger than in the other two models, the difference between the parameters obtained fitting all bins and only three bins is minimal. However, when considering all bins, the slopes obtained when fitting Model 1 and 3 are steeper and have four times larger errors.

To take into account the intrinsic scatter between richness and mass also in Model 1 and 3 and compare results with those obtained when using Model 2, we apply an a posteriori correction as in Ford et al. (2015). Using the mass-richness relation inferred from Model 1 and 3, we calculate the mass of all the clusters in the sample then we scatter those masses assuming a log-normal distribution centered on $\log M_{200}$ and with a width $\sigma_{\ln M|\lambda} = 0.39$, based on the scatter measured by Licitra et al. (2016a). We repeat this procedure creating 1000 bootstrap realizations, choosing masses randomly with replacements from the entire sample. We calculate the new mean mass values in each richness bin and average them over all bootstrap realizations. We then repeat the fit to infer the new mass-richness relation. This procedure is illustrated in Figure 8, where we show the results from the fit to Model 3 (in black), the scattered masses (in light red), and the new mean masses and mass-richness relation (in red). Due to the shape of the halo mass function, the net effect of the intrinsic scatter correction is to lead to a slightly higher normalization value of the mass-richness relation. The difference in normalization for Model 1 and 3, and their scattered versions is less than 1%.

In Figure 9 we show the BCG masses inferred from the fit to Model 3 compared to the stellar

mass of the central galaxies of each cluster, and their mean values in each richness bin. We obtain the BCG stellar masses using our photometric and photometric redshift catalogs from Raichoor et al. (2014), and Bruzual & Charlot (2003) stellar population models with *LePhare*, in fixed redshift mode at the galaxy photometric redshift. We find that the BCG stellar masses obtained with our fit are in good agreement with those from *LePhare*, while they are about one order of magnitude smaller than the BCG masses that we would expect, using the halo mass - BCG mass relation of Johnston et al. (2007). This discrepancy could be due to the fact that in Johnston et al. (2007) the halo concentration is a free parameter, and they obtained on average higher concentration values than ours, calculated from Dutton & Macció (2014) mass-concentration relation. In fact, because of the degeneracy between the two mass parameters, a higher concentration would lead to a lower halo mass value and therefore to a higher BCG mass to compensate for the excess of signal.

Hereafter, we quote as our final mass-richness relation the one calculated from Model 3, with the *best richness bin* sample, and after the intrinsic scatter correction: $\log M_0 = 14.48 \pm 0.04$ and $\alpha = 1.14 \pm 0.23$. In fact, the a posteriori intrinsic scatter correction is more reliable than the results from Model 2, in which $\sigma_{\ln M|\lambda}$ is not well constrained by the data. Model 3, with the inclusion of the BCG mass, is also more complete than Model 1.

5.3. Comparison with X-ray Mass Proxies

To compare our mass estimates with X-ray mass proxies, we follow the same matching procedure as in Licitra et al. (2016a). We use the Gozaliasl et al. (2014) and Mehrrens et al. (2012) X-ray catalogs, and perform the match between their and our detections imposing a maximum separation of 1 *Mpc* and a maximum difference in redshift of 0.1. We include detections from both the *published* and the *complete* catalogs to broaden our sample, and have more statistics to perform the scaling relation fits. Results obtained with the *complete* catalogs might be affected by contamination biases, since for those, we estimated the purity to decrease to $\sim 60\%$ (Figure 8-9 of Licitra et al. 2016a).

Within all three fields, we recover 36(27) ob-

jects from the match of the *complete(published)* catalog with Gozaliasl et al. (2014) (in this case all objects are from the CFHT-LS W1 field), and 21(17) from objects from the match of the *complete(published)* catalog with Mehrtens et al. (2012). As shown in Licitra et al. (2016a), RedGOLD recovers 38 clusters, up to $z \sim 1$, in the 3 deg^2 of the CFHT-LS W1 field, covered by Gozaliasl et al. (2014) catalog. The clusters detected by RedGOLD that don't have an X-ray counterpart seem to be, from visual inspection, small galaxy groups. It is possible that these systems have an X-ray emission below the X-ray detection limit, or that they are not relaxed systems and don't have any X-ray emission at all.

As explained in Section 3.2, Gozaliasl et al. (2014) M_{200} masses were estimated using the $M_X - L$ relation of Leauthaud et al. (2010). We estimate Mehrtens et al. (2012) M_{200} masses from the r_{200} values given in their catalog, using Equation 12. Our masses M_{200}^{lens} are calculated using our final mass-richness relation.

In Figure 10, we compare the normalized difference between X-ray and lensing masses $(M_{200}^X - M_{200}^{lens})/M_{200}^X$ as a function of M_{200}^X , obtained using Model 3, with those obtained with the other two models. M_{200}^X is from Gozaliasl et al. (2014) and from Mehrtens et al. (2012) in the top and bottom panels, respectively.

For all models, the mean differences obtained using M_{200}^X from Gozaliasl et al. (2014) ($\sim 0.5 - 0.7$ dex) are lower than those obtained using Mehrtens et al. (2012) ($\sim 1 - 1.7$ dex). As explained in Section 3.2, Gozaliasl et al. (2014) masses were calculated from the X-ray luminosity, after the excision of the AGN contribution and the correction for cool core flux removal. We find that this leads to mass estimates that are more in agreement with masses derived with weak lensing than those calculated without core excision.

Using Gozaliasl et al. (2014) catalog and the lensing masses estimated from the mass-richness relation derived from our best model, Model 3, applied on the *complete* catalogs, we find a mean residual of 0.66 dex, considering the complete mass range. If we consider two different mass ranges, we find a mean residual of 0.77 dex for $M_{200}^X < 10^{14} M_\odot$, and a mean residual of 0.41 dex for $M_{200}^X \geq 10^{14} M_\odot$.

Hereafter, we will use only the Gozaliasl et al. (2014) sample, given the higher number of matches, and because core-excised X-ray temperatures better correlate with cluster masses (Pratt et al. 2009). For our sample, this is also shown in Table 5, where the mean ratios between X-ray and lensing masses are biased 20 – 40% higher for Mehrtens et al. (2012), for the best bins, while are ~ 1 when using Gozaliasl et al. (2014). This means that non core-excised temperatures lead to masses that are on average higher than those derived with weak lensing measurements.

To obtain scaling relations, we exclude the two clusters with mass $M_{200}^X < 2 \times 10^{13} M_\odot$ from the matched sample with Gozaliasl et al. (2014), because both our and the X-ray catalog are incomplete at these low masses. We also do not consider the two highest mass matches ($M_{200}^X > 2 \times 10^{14} M_\odot$), because our catalog is incomplete in this mass range, given our low area coverage. All four excluded clusters were matches with the Licitra's *published* catalog.

In Figure 11, we plot the $M_{200}^X - M_{200}^{lens}$ relation, and in Figure 12, the $L_X - M_{200}^{lens}$ and the $T_X - M_{200}^{lens}$ relations. In those plots, the black dots represent matches with the RedGOLD cluster detections in Licitra's *published* catalogs, while the black squares represent all those with the *complete* catalogs (see Section 3.1).

In Figure 11, we show the relation between X-ray and lensing masses:

$$\log(M_{200}^{lens}) = a + b \log(M_{200}^X) \quad (32a)$$

The black dotted line is the diagonal, the solid lines are the fit to the *published* catalogs, and the dashed lines are the fit to the *complete* catalogs. The red lines were obtained with the slope as a free parameter of the fit, and the green lines with the slope fixed at unity. For the *published* catalogs, our threshold in richness and σ_{det} is meant to select clusters with $M_{200} > 10^{14} M_\odot$ with a completeness $\sim 80\%$. Part of these detections have X-ray masses lower than our selection threshold of $M_{200} > 10^{14} M_\odot$, in fact their X-ray masses are in the range $2 \times 10^{13} M_\odot < M_{200}^X < 10^{14} M_\odot$. We expect to have a contamination of clusters with these lower masses, and our purity of $\sim 80\%$ is calculated for real clusters with $M_{200}^X > 10^{13} M_\odot$.

However our completeness decreases ($<80\%$) in this mass range ($M_{200}^X < 10^{14} M_\odot$), as shown in Licitra et al. (2016a).

When fixing the slope at the unity, we obtain $a = 0.18 \pm 0.03$ ($a = 0.22 \pm 0.04$), and a scatter of $\sigma_M = 0.22$ ($\sigma_M = 0.18$), for the *complete(published)* catalogs. In this case, the difference in a for the two samples is negligible, $\sim 0.04 \pm 0.05$ dex. The small shift in normalization (~ 0.2 dex) compared to the diagonal is expected, since lensing mass estimates are generally higher than X-ray masses (Rasia et al. 2012; Zhang et al. 2008; Simet et al. 2015). When leaving the slope as a free parameter, we find $a = -1.6 \pm 3.3$ and $b = 1.1 \pm 0.2$, with a scatter of $\sigma_M = 0.22$ ($a = 5.7 \pm 3.5$ and $b = 0.61 \pm 0.25$, with a scatter of $\sigma_M = 0.16$) for the *complete(published)* catalogs. The incompleteness when using the *published* catalogs appears to bias our fit slope, which becomes much shallower than the diagonal.

In Figure 12, we show the mass-luminosity and mass-temperature relations. We apply a logarithmic linear fit, in the form:

$$\log\left(\frac{M_{200}E(z)}{M_0}\right) = a + b \log\left(\frac{L_X}{L_0 E(z)}\right) \quad (33a)$$

$$\log\left(\frac{M_{200}E(z)}{M_0}\right) = a + b \log\left(\frac{T_X}{T_0}\right) \quad (33b)$$

where $E(z) = H(z)/H_0$, $M_0 = 8 \times 10^{13} h^{-1} M_\odot$ for the $M_{200} - L_X$, $M_0 = 6 \times 10^{13} h^{-1} M_\odot$ for the $M_{200} - T_X$, $L_0 = 5.6 \times 10^{42} h^{-2} \text{erg/s}$, and $T_0 = 1.5 \text{ keV}$.

For the mass-luminosity relation, we find $a = 0.11 \pm 0.04$ and $b = 0.66 \pm 0.13$, with a scatter $\sigma_{\log M_{200}|L_X} = 0.22$ ($a = 0.17 \pm 0.04$ and $b = 0.45 \pm 0.14$, with a scatter $\sigma_{\log M_{200}|L_X} = 0.16$) for the *complete(published)* catalogs. For the mass-temperature relation, we find $a = 0.23 \pm 0.04$ and $b = 1.57 \pm 0.31$, with a scatter $\sigma_{\log M_{200}|T_X} = 0.22$ ($a = 0.29 \pm 0.04$ and $b = 1.09 \pm 0.32$, with a scatter $\sigma_{\log M_{200}|T_X} = 0.16$), for the *complete(published)* catalogs. The relations obtained with the *published* catalogs show again shallower slopes.

We summarize our results in Table 6.

6. DISCUSSION

6.1. Comparison to Previously Derived Mass-Richness Relations

In this Section, we discuss our results in the context of similar current studies.

As stated before and shown in Licitra et al. (2016a,b), our richness estimator λ is defined in a similar way as the richness from redMaPPer (Rykoff et al. 2014). The redMaPPer richness is defined as $\lambda_{\text{RM}} = \sum p_{\text{mem}} \theta_L \theta_R$, where p_{mem} is the probability that each galaxy in the vicinity of the cluster is a red-sequence member and θ_L, θ_R are weights that depend on luminosity and radius. In this calculation, only galaxies brighter than $0.2L_*$ and within a scale radius R_λ are considered. The radius is richness dependent and it scales as $R_\lambda = 1.0(\lambda/100)^{0.2} h^{-1} \text{Mpc}$.

The RedGOLD richness is a simplified version of λ_{RM} . We constrained the radial distribution of the red-sequence galaxies with an NFW profile and applied the same luminosity cut and radius scaling as in Rykoff et al. (2014) but did not apply a luminosity filter. Unlike the redMaPPer definition, our richness is not a sum of probabilities. Those choices were made to minimize the scatter in the mass-richness relation. For redshifts $z < 0.3$, the difference $\frac{\lambda_{\text{RM}} - \lambda}{\lambda}$ is only of 5 – 15%, while it increases to 40 – 60% at $0.4 < z < 0.5$, where the redMaPPer richness is systematically higher (Licitra et al. 2016a). This difference might be due to the different depths of the CFHTLenS and SDSS surveys. This means that we can compare our results with others obtained using the redMaPPer cluster sample.

Simet et al. (2016) performed a stacking analysis of the redMaPPer cluster sample, using shear measurements from the SDSS. Their sample is much larger than ours, consisting of 5,570 clusters, with a redshift range $0.1 < z < 0.3$, lower than the one used for this work, and a richness range $20 \leq \lambda_{\text{RM}} \leq 140$. With these data, they were able to characterize the different systematic errors arising in their analysis with great accuracy. For the mass-richness relation, they obtained the normalization $\log(M_0 [h^{-1} M_\odot]) = 14.34 \pm 0.04$ (the error includes both statistical and systematic error) and the slope $\alpha = 1.33_{-0.1}^{+0.9}$.

To compare our results to theirs, we use our

masses in units of $h^{-1}M_{\odot}$ and we repeat our fits. Using Model 3, we obtain $\log M_0 = 14.32 \pm 0.03$ and $\alpha = 1.14 \pm 0.22$ (the errors are only statistical). Our normalization and slope are consistent with Simet et al.’s within 1σ . Comparing the masses at the pivot richness, $\lambda_0 = 40$, we obtain $2.13 \times 10^{14}h^{-1}M_{\odot} \pm 0.03$ compared to Simet et al.’s $2.21 \times 10^{14}h^{-1}M_{\odot} \pm 0.15$.

In another recent work, Farahi et al. (2016) inferred the mass-richness relation using the same sample of SDSS redMaPPer clusters ($0.1 < z < 0.3$ and $\lambda_{\text{RM}} > 20$), performing a stacking analysis and estimating the velocity dispersion of the dark matter halos from satellite-central galaxy pairs measurements. For the mass-richness relation, they found a normalization of 14.19 ± 0.1 and a slope of 1.31 ± 0.19 (the error includes both statistical and systematic error), using a pivot $\lambda_0 = 30$. Repeating the fit using their pivot richness, we obtain $\log M_0 = 14.19 \pm 0.03$ and $\alpha = 1.14 \pm 0.22$, consistent within less than 1σ with their results. At the pivot richness $\lambda_0 = 30$ our mass is $1.53 \times 10^{14}M_{\odot} \pm 0.03$, consistent with their value of $1.56 \times 10^{14}M_{\odot} \pm 0.35$.

Melchior et al. (2016) calibrated the mass-richness relation and its evolution with redshift up to $z < 0.8$, using 8000 RedMaPPer clusters in the Dark Energy Survey Science Verification (DES; Dark Energy Survey Collaboration 2016) with $5 \leq \lambda_{\text{RM}} \leq 180$. They found a normalization $M_0 = 2.35 \pm 0.34 \times 10^{14}M_{\odot}$ and a slope 1.12 ± 0.26 , using the pivot richness $\lambda_0 = 30$ and a mean redshift $z = 0.5$. Their errors include both statistical and systematic errors. Once again these results are consistent with ours within less than 1σ , even if this sample has a larger average redshift, where we expect our richness definitions to be less similar. We can not compare our results with the scaling relations obtained in Johnston et al. (2007), Covone et al. (2014), Ford et al. (2015) and van Uitert et al. (2015) because their definition of richness is different.

We conclude that our fit of the mass-richness relation is in agreement with all the other works cited above. These results confirm the efficiency of the RedGOLD richness estimator, and quantify the relation between the RedGOLD richness measurements and the total cluster masses obtained with weak lensing. Even without using a probability distribution, our richness is as efficient as the

more sophisticated redMaPPer richness definition.

6.2. Weak Lensing vs X-ray Masses

In Figure 12, we compare our lensing mass versus X-ray mass proxies relations, with other works in literature.

In the $L_X - M_{200}^{\text{lens}}$ plot, we compare our results with those from Kettula et al. (2015) and Leauthaud et al. (2010). We remind the reader that the fit to the *published* catalogs (solid red line) shows a shallower slope because of our selection in mass, which, while optimizes purity, leads to a bias in slope due to the lack of clusters detected at masses $M_{200} < 10^{14}M_{\odot}$ (see discussion in Section 5.3).

Because of the large uncertainties, the fit to both the *complete* and *published* catalogs (dashed red line) are consistent within $< 1\sigma$ and $< 2\sigma$, respectively, in normalization and slope with results from Kettula et al. (2015), even if our normalizations are higher.

With respect to the $E(z)M_{200}$ derived from Leauthaud et al. (2010) (and, as a consequence, from Gozaliasl et al. (2014), since they use Leauthaud et al. (2010) to derive their mass relations), we are consistent within $< 2\sigma$ in normalization and within $< 1\sigma$ in slope for the *complete* catalogs. For the *published* catalogs, we are inconsistent in normalization (the normalization difference is $\sim 3.4\sigma$) and are consistent in slope within $< 1\sigma$.

Both Kettula et al. (2015) and Leauthaud et al. (2010) didn’t apply the miscentering correction but, while the first performed their lensing analysis on single clusters, the latter stacked their low mass clusters in very poorly populated bins. This procedure could have introduced a bias that lead to more smoothed profiles and thus to lower mass estimates and to a lower normalization of the scaling relation.

In the $T_X - M_{200}^{\text{lens}}$ plot, we compare our results with Kettula et al. (2015) and Mantz et al. (2016). Since their masses are derived at the overdensity $\Delta = 500$, we convert their M_{500} values to M_{200} , using $M_{200} = 1.35M_{500}$ from Rines et al. (2016), derived considering that the mass-concentration relation weakly depends on mass (Bullock et al. 2001) and assuming an NFW profile with a fixed concentration $c = 5$. We find that the normalization and slope of our fit to the *complete*(*published*)

catalogs are consistent with the Kettula et al. (2015) results within $< 1\sigma$ ($\lesssim 1.5\sigma$), and with Mantz et al. (2016) results within $< 1\sigma$ ($< 1\sigma$) in normalization and slope.

In Table 7, we show the differences in normalization, Δa , and in slope, Δb , between our results and those used for comparison for the mass-luminosity, and the mass-temperature relations.

Given that our results based on the RedGOLD *complete* catalogs are consistent with other results in the literature, we conclude that the thresholds that we apply in the RedGOLD *published* catalog introduces systematics in the fit of the cluster lower mass end.

Simulations predict that mass measurements from lensing are systematically lower by $\sim 5-10\%$ and those from X-ray proxies by $\sim 25-35\%$ than the cluster true total mass, with $\langle M_X^{sim}/M_L^{sim} \rangle \sim 0.7-0.8$ (Meneghetti et al. 2010; Rasia et al. 2012). When we compare our weak lensing mass measurements to X-ray Gozaliasi et al. (2014) cluster masses (Figure 10 and Table 5) in our three best bins for Model 1 and 3, we obtain $\langle M_X/M_L \rangle \sim 1$, when we do not consider the intrinsic scatter correction, and $\langle M_X/M_L \rangle \sim 0.9$ when we do. The intrinsic scatter correction leads to a small (within 1σ) positive shift in the normalization of the mass-richness relation and to a better agreement with simulations.

For Model 2, we obtain $\langle M_X/M_L \rangle \sim 1$, at odds with simulation predictions. This might be due to the greater uncertainties introduced by the intrinsic scatter as a free parameter in the fit of the shear profiles.

As we mentioned before in Section 5.3, and from Table 5 and Figure 10, the mean residuals and ratio values obtained using Mehrrens et al. (2012) catalog are much higher, with $\langle M_X/M_L \rangle \sim 1.2-1.3$, which means that non core-excised temperature lead to overestimated X-ray masses, as expected (Pratt et al. 2009).

Previously published XMM-Newton X-ray to lensing mass ratios show values of $\langle M_X/M_L \rangle \sim 0.91-0.99$ (Zhang et al. 2008) and $\sim 0.72-0.96$ (Simet et al. (2015), using observations from Piffaretti et al. 2011; Hajian et al. 2013), consistent with our results. Also our uncertainty on $\langle M_X/M_L \rangle$ ($\sigma_{\langle M_X/M_L \rangle} \sim 40-50\%$) is similar to those cited in these works ($\sigma_{\langle M_X/M_L \rangle} \sim 30-50\%$).

There is a known tension between the constraints on the cosmological parameters derived using the number density of S-Z galaxy clusters detected by Planck, and those derived from the CMB temperature power spectrum. Planck cluster masses are derived with hydrostatic mass measurements applied to XMM-Newton X-ray observations. One possible explanation of this discrepancy could then be that these masses are biased low with respect to true masses. Our results are consistent with this explanation.

It is also known that XMM-Newton and Chandra have different instrument calibrations that lead to different temperature estimations, with Chandra X-ray temperatures being higher, and leading to higher cluster mass estimation (Israel et al. 2014; von der Linden et al. 2014; Schellenberger et al. 2015). Applying the correction from Schellenberger et al. (2015), to convert XMM-Newton masses to Chandra masses, we find $\langle M_X/M_L \rangle_{\text{Chandra}} \sim 1$, using the lensing masses from our best model.

7. SUMMARY AND CONCLUSIONS

We measure weak lensing galaxy cluster masses for optically detected cluster candidates stacked by richness. We fit the weak lensing mass versus richness relation and compare our findings to X-ray detected mass proxies in the area.

Our cluster sample was obtained with the RedGOLD (Licitra et al. 2016a) optical cluster finder algorithm. The algorithm is based on a revised red-sequence technique and searches for passive ETG overdensities. RedGOLD is optimized to detect massive clusters ($M_{200} > 10^{14} M_\odot$) with both high completeness and purity. We use the RedGOLD cluster catalogs from Licitra et al. (2016a,b) for the CFHT-LS W1 and NGVS surveys. The catalogs give the detection significance and an optical richness estimate that corresponds to a proxy for the cluster mass.

For our weak lensing analysis, we use a sample of 1325 published clusters, selected with a threshold in significance of $\sigma_{\text{det}} \geq 4$ and in richness $\lambda \geq 10$ at redshift $0.2 \leq z \leq 0.5$, for which our published catalogs are $\sim 100\%$ complete and $\sim 80\%$ pure Licitra et al. (2016a). In order to obtain the mass-richness relation, we concentrate on our best richness bins $20 < \lambda < 50$, which in-

clude a subsample of 346 clusters, which is $\sim 100\%$ complete and $\sim 90\%$ pure (Licitra et al. 2016a). At $\lambda > 50$ we detect very few clusters, and find large lensing mass scatters. To compare to X-ray mass proxies we considered both the *published* and *complete* Licitra et al.’s catalogs, as defined in our data Sections. Our photometric and photometric redshift catalogs were obtained with a modified version of the THELI pipeline (Erben et al. 2005, 2009, 2013; Raichoor et al. 2014), and weak lensing shear measurements with the shear measurement pipeline described in Erben et al. (2013), Heymans et al. (2012), and Miller et al. (2013).

We calculate our cluster mean shear radial profiles by averaging the tangential shear in logarithmic radial bins in stacked cluster detections binned by their richness. We apply lens-source pairs weights that depend on the lensing efficiency and on the quality of background galaxy shape measurements.

We obtain the average cluster masses in each richness bin by fitting the measured shear profiles using three models: (1) a basic halo model (Model 1), with an NFW surface density contrast and correction terms that take into account cluster miscentering, non-weak shear and the second halo term; (2) a model that includes the intrinsic scatter in the mass–richness relation (Model 2); (3) a model that includes the contribution of the BCG stellar mass (Model 3). In Model 1 and 3, we apply an a posteriori correction to take into account the intrinsic scatter in the mass–richness relation.

We find that our *best model* is Model 3 which, with the inclusion of the a posteriori correction for the intrinsic scatter in the mass–richness relation, is more complete in taking into account the systematics, and more reliable in the obtained results. The BCG masses obtained with this model are consistent with the BCG stellar masses obtained from their spectral energy distribution fit.

Our main results are:

- Comparing weak lensing masses to RedGOLD optical richness, we calibrate our optical richness with the lensing masses, fitting the power law $\log M_{200} = \log M_0 + \alpha \log \lambda/\lambda_0$. For our *best model*, we obtain $\log M_0 = 14.48 \pm 0.04$ and $\alpha = 1.14 \pm 0.23$, with a pivot richness $\lambda_0 = 40$. Even if our sample is one order of magnitude smaller

than the SDSS and DES redMaPPer cluster samples used in Simet et al. (2016), Farahi et al. (2016) and Melchior et al. (2016), our results are consistent with theirs within 1σ . This confirms that our cluster selection is not biased towards a different cluster selection when compared to the SDSS and DES redMaPPer cluster samples, as we expect.

- Using our mass–richness relation, we infer scaling relations between lensing masses and X-ray proxies. For the $M_{200}^{lens} - M_{200}^X$ relation, fixing the slope at 1, we obtain $\log M_{200}^{lens} = (0.18 \pm 0.03) \log M_{200}^X$.

For the lensing mass vs X-ray luminosity relation $\log \left(\frac{M_{200}E(z)}{M_0} \right) = a + b \log \left(\frac{L_X}{L_0 E(z)} \right)$, we find $a = (0.11 \pm 0.04)$ and $b = (0.66 \pm 0.13)$, with $M_0 = 8 \times 10^{13} h^{-1} M_\odot$ and $L_0 = 5.6 \times 10^{42} h^{-2} \text{erg/s}$.

For the lensing mass vs X-ray temperature relation $\log \left(\frac{M_{200}E(z)}{M_0} \right) = a + b \log \left(\frac{T_X}{T_0} \right)$, we obtain $a = (0.23 \pm 0.04)$ and $b = (1.57 \pm 0.31)$, with $M_0 = 6 \times 10^{13} h^{-1} M_\odot$ and $T_0 = 1.5 \text{KeV}$.

Our results are consistent with those of Kettila et al. (2015) and Mantz et al. (2016), within $< 1\sigma$. Our normalization is consistent within $< 2\sigma$, and our slope within 1σ , with the results of Leauthaud et al. (2010) (and therefore with Gozaliasl et al. (2014)).

- We find a scatter of 0.22, for all three relations, consistent with redMaPPer scatters, confirming the Licitra et al. (2016a,b) results that the RedGOLD optical richness is an efficient mass proxy. This is very promising since our mass range is lower than that probed by redMaPPer, and the scatter does not increase as expected to these lower mass ranges.

In order to increase the accuracy on the weak lensing mass estimates, it will be important to increase the number density of background sources to achieve a higher signal-to-noise ratio in the shear profile measurements in the future. This will be possible with ground- and space-based large-scale surveys such as the Large Synoptic Sur-

vey Telescope(LSST⁹), *Euclid*¹⁰ and WFIRST¹¹. Also, the next generation radio surveys such as SKA¹² will allow us to extend weak lensing measurements to the radio band, giving access to even larger scales. Cluster samples will then be an order of magnitude bigger than the one used for this work, allowing us to constrain with even higher accuracy cluster masses and their scaling relations (e.g. Sartoris et al. (2016), Ascaso et al. (2016)).

This work is based on observations obtained with MegaPrime/MegaCam, a joint project of CFHT and CEA/IRFU, at the Canada-France-Hawaii Telescope (CFHT) which is operated by the National Research Council (NRC) of Canada, the Institut National des Sciences de l'Univers of the Centre National de la Recherche Scientifique (CNRS) of France, and the University of Hawaii. This research used the facilities of the Canadian Astronomy Data Centre operated by the National Research Council of Canada with the support of the Canadian Space Agency. CFHTLenS data processing was made possible thanks to significant computing support from the NSERC Research Tools and Instruments grant program. R.L., S.M. and A.Ra. acknowledge the support of the French Agence Nationale de la Recherche (ANR) under the reference ANR10-BLANC-0506-01-Projet VIRAGE (PI: S.Mei). S.M. acknowledges financial support from the Institut Universitaire de France (IUF), of which she is senior member. H.H. is supported by the DFG Emmy Noether grant Hi 1495/2-1. We thank the Observatory of Paris and the University of Paris D. Diderot for hosting T.E. under their visitor programs.

Facilities: CFHT.

REFERENCES

- Abell, G. O. 1958, ApJS, 3, 211
- Ahn, C. P., Alexandroff, R., Allende Prieto, C., et al. 2014, ApJS, 211, 17
- Allen, S. W., Evrard A. E. & Mantz, A. B. 2011, ARA&A, 49, 409
- Arnouts, S., Cristiani, S., Moscardini, L., et al. 1999, MNRAS, 310, 540
- Arnouts, S., Moscardini, L., Vanzella, E., et al. 2002, MNRAS, 329, 355
- Ascaso, B., Mei, S., Bartlett, J.G., Benítez, N. 2016, MNRAS, 464, 2270
- Becker, M. R., McKay, T.A., Koester, B., et al. 2007, ApJ, 669, 905
- Becker, M. R. & Kravtsov, A. V. 2011, ApJ, 740, 25
- Benítez N. 2000, ApJ, 536, 571
- Benítez, N., Ford, H., Bouwens, R., et al. 2004, ApJS, 150, 1
- Benítez, N., Dupke, R., Moles, M., et al. 2014, arXiv:1403.5237v1
- Bertin, E. & Arnouts, S. 1996, A&AS, 117, 393
- Boggs, P. T. & Rogers, J. E. 1990, Contemporary Mathematics, 112, 186.
- Boulade, O., Charlot, X., Abbon, P. et al. 2003, Proc. SPIE, 4841, 72
- Bullock, J. S., Kolatt, T. S., Sigad, Y., et al. 2001, MNRAS, 321, 559
- Capak, P., Cowie, L. L., Hu, E. M., et al. 2004, AJ, 127, 180
- Carlstrom, J. E., Ade, P. A. R., Aird, K. A., et al. 2011, PASP, 123, 568
- Cavaliere, A. & Fusco-Fermiano, R. 1976, A&A, 49, 137
- Chiang, Y.-K., Overzier, R., Gebhardt, K. 2013, ApJ, 779, 127
- Coe, D., Benítez, N., Sánchez, S. F., et al. 2006, AJ, 132, 926
- Covone, G., Sereno, M., Kilbinger, M., Cardone, V. F. 2014, ApJL, 784, 2
- Cui, W., Power, C., Biffi, V., et al. 2016, MNRAS, 465, 3
- Dark Energy Survey Collaboration 2016, MNRAS, 460, 1270

⁹<https://www.lsst.org/>

¹⁰<http://euclid-ec.org>

¹¹<http://wfirst.gsfc.nasa.gov>

¹²<http://www.skatelescope.org>

- Davis, M., Faber, S. M., Newman, J. A., et al. 2003, *Proc. SPIE*, 4834, 161
- Du, W. & Fan, Z. 2014, *ApJ*, 785, 57
- Dutton, A. A. & Macció, A. V. 2014, *MNRAS*, 441, 3359
- Erben, T., Schirmer, M., Dietrich, J. P., et al. 2005, *Astron. Nachr.*, 326, 432
- Erben, T., Hildebrandt, H., Lerchster, M., et al. 2009, *A&A*, 493, 1197
- Erben, T., Hildebrandt, H., Miller, L., et al. 2013, *MNRAS*, 433, 2545
- Evrard, A. E., Bialek, J., Busha, M., et al. 2008, *ApJ*, 672, 1
- Farahi, A., Evrard, A. E., Rozo, E., Rykoff, E. S., Wechsler, R. H. 2016, *MNRAS*, 460, 3900
- Ferrarese, L., Cote, P., Cuillandre, J.-C., et al. 2012, *ApJS*, 200, 4
- Finoguenov, A., Borgani, S., Tornatore, L., Böhringer, H. 2003, *A&A*, 398, L35
- Finoguenov, A., Connelly, J. L., Parker, L. C., et al. 2009, *ApJ*, 704, 564
- Ford, J., van Waerbeke, L., Milkeraitis, M., et al. 2015, *MNRAS* 447, 1304
- Foreman-Mackey, D., Hogg, D. W., Lang, D., Goodman, J. 2013, *PASP*, 125, 925
- Foreman-Mackey, D., Voutsden, W., Price-Whelan, A., et al. 2016, *corner.py*, v1.0.2, Zenodo, doi:10.5281/zenodo.45906
- Gavazzi, R., Treu, T., Rhodes, J. D., et al. 2007, *ApJ*, 667, 176
- George, M. R., Leauthaud, A., Bundy, K., et al. 2011, *ApJ*, 742, 125
- George, M. R., Leauthaud, A., Bundy, K., et al. 2012, *ApJ*, 757, 2
- Gillis, B. R., Hudson, M. J., Erben, T., et al. 2013, *MNRAS*, 431, 1439
- Goodman, J. & Weare, J. 2010, *CaMCoS*, 5, 65
- Gozaliasl, G., Finoguenov, A., Khosroshahi, H. G., et al. 2014, *A&A* 566, 140
- Guzzo, L., Scodreggio, M., Garilli, B., et al., 2014, *A&A*, 556, 108
- Gwyn, S. D. J. 2012, *ApJ*, 143, 38
- Hajian, A., Battaglia, N., Spergel, D. N., et al. 2013, *JCAP*, 11, 64
- Hamana, T., Takada, M. & Yoshida, N. 2004, *MNRAS*, 350, 893
- Heymans, C., van Waerbeke, L., Miller, L., et al. 2012, *MNRAS*, 427, 146
- Hildebrandt, H., Erben, T., Kuijken, K., et al. 2012, *MNRAS*, 421, 2355
- Ilbert, O., Arnouts, S., McCracken, H. J., et al. 2006, *A&A*, 457, 841
- Israel, H., Reiprich, T., Erben, T., et al. 2014, *A&A*, 564, A129
- Johnston, D. E., Sheldon, E. S., Wechsler, R. H., et al. 2007, *arXiv:0709.1159*
- Kasliwal, M. M., Massey, R., Ellis, R. S., Miyazaki, S., Rhodes, J. 2008, *ApJ*, 684, 1
- Kettula, K., Giodini, S., van Uitert, E., et al. 2015, *MNRAS*, 451, 1460
- Laureijs, R., Amiaux, J., Auguères, J.-L., et al. 2011, *ESA/SRE*
- Leauthaud, A., Finoguenov, A., Kneib, J.-P., et al. 2010, *ApJ*, 709, 114
- Le Fèvre, O., Vettolani, G., Garilli, B., et al. 2005, *A&A*, 439, 845
- Le Fèvre, O., Cassata, P., Cucciati, O., et al. 2013, *A&A*, 559, A14
- Lewis, A., Challinor, A. & Lasenby, A. 2000, *ApJ*, 538, 473
- Licitra, R., Mei, S., Raichoor, A., et al. 2016, *ApJ*, 829, 44
- Licitra, R., Mei, S., Raichoor, A., Hildebrandt, H. 2016, *MNRAS*, 455, 3020
- Lin, Y.-T., Mohr, J. J., Stanford, S. A. 2004, *ApJ*, 610, 745
- Mandelbaum, R., Hirata, C. M., Seljak, U., et al. 2005, *MNRAS*, 361, 1287

- Mandelbaum, R., Seljak, U., Cool, R. J., et al. 2006, MNRAS, 372, 758
- Mantz, A. B., Allen, S. W., Morris, R. G., et al. 2016, MNRAS, 463, 3582
- Marriage, T. A., Acquaviva, V., Ade, P. A. R., et al. 2011, ApJ, 737, 61
- McGee, S. L., Balogh, M. L., Bower, R. G., Font, A. S., McCarthy, I. G. 2009, MNRAS, 400, 937
- Mead, J. M. G., King, L. J., Sijacki, D., Leonard, A., Puchwein, E., McCarthy, I. G. 2010, MNRAS, 406, 434
- Mehrtens, N., Romer, A. K., Hilton, M., et al. 2012, MNRAS, 423, 1024
- Mei, S., Holden, B. P., Blakeslee, J. P., et al. 2009, ApJ, 690, 42
- Melchior, P., Gruen, D., McClintok, T., et al. 2016, arXiv:1610.06890v1
- Meneghetti, M., Rasia, E., Merten, J., et al. 2010, A&A, 514, A93
- Merloni, A., Predehl, P., Becker, W., et al. 2012, eROSITA science book: mapping the structure of the energetic universe (Standort: AS 24/105). Garching: Max-Planck-Institut für extraterretrische Physik
- Metropolis, N., Rosenbluth, A. W., Rosenbluth, M. N., et al. 1953, JChPh, 21,1087
- Miller L., Heymans, C., Kitching, T. D., et al. 2013, MNRAS, 429, 2858
- Navarro J. F., Frenk C. S., White S. D. M. 1996, ApJ, 462, 563
- Nelder, J. A. & Mead, R. 1965, CompJ, 7, 308
- Newman, J. A., Lee, A. B., Richards, J. W., et al. 2013, ApJS, 208, 5
- Oguri, M. & Hamana, T. 2011, MNRAS, 414, 1851
- Oguri, M. & Takada, M. 2011, Phys. Rev. D, 83, 023008
- Oke, J. B. & Gunn, J. E. 1983, ApJ, 266, 713
- Pierre, M., Chiappetti, L., Pacaud, F., et al. 2007, MNRAS, 382, 279
- Piffaretti, R., Arnaud, M., Pratt, G. W., Pointecouteau, E., Melin, J.-B. 2011, A&A, 534, A109
- Postman, M., Lubin, L. M., Gunn, J. E., et al. 1996, AJ, 111, 615
- Pratt, G. W., Croston, J. H., Arnaud, M., Böhringer, H. 2009, A&A 498, 361
- Press, W. H. & Schechter, P. 1974, ApJ, 187, 425
- Raichoor, A., Mei, S., Erben, T., et al. 2014, ApJ, 797, 102
- Rasia, E., Meneghetti, M., Martino, R., et al. 2012, NJPh, 14
- Rines, K. J., Geller, M. J., Diaferio, A., et al. 2016, ApJ, 819, 63
- Rozo, E., Rykoff, E. S., Evrard, A., et al. 2009, ApJ, 699, 768
- Rozo, E. & Rykoff, E. S. 2014, ApJ, 783, 80
- Rykoff, E. S., Koester, B. P., Rozo, E., et al. 2012, ApJ, 746, 178
- Rykoff, E. S., Rozo, E., Busha, M. T., et al. 2014, ApJ, 785, 104
- Rykoff, E. S., Rozo, E., Hollowood, D., et al. 2016, ApJS, 224, 1
- Sarazin, C.L. 1988, Cambridge Univ. Press
- Sartoris, B., Biviano, A., Fedeli, C., et al. 2016, MNRAS, 459, 1764
- Schechter, P., 1976, ApJ 203, 297
- Schellenberger, G., Reiprich, T. H., Lovisari, L., Nevalainen, J., David, L. 2015, A&A 575, A30
- Schirmer, M., Erben, T., Hetterscheidt, M., Schneider, P. 2006, A&A, 462, 875
- Schneider, P. 1996, MNRAS, 283, 837
- Schneider, P. 2005, Springer Berlin, 33, 269
- Seljak, U. 2000, MNRAS. 318, 203
- Seljak, U. & Warren, M. S. 2004, MNRAS, 355, 129
- Shankar, F., Marulli, F., Bernardi, M., et al. 2013, MNRAS, 428, 109

- Simet, M., Battaglia, N., Mandelbaum, R., Seljak, U. 2015, arXiv:1502.01024v2
- Simet, M., McClintock, T., Mandelbaum, R., et al. 2016, arXiv:1603.06953v1
- Sirianni, M., Jee, M. J., Benítez, N., et al. 2005, PASP, 117, 1049
- Strauss, M. A., Weinberg, D. H., Lupton, R. H., et al. 2002, AJ, 124, 1810
- Sunyaev, R. A. & Zeldovich, Y. B., 1972, CoASP, 4, 173
- van Uitert, E., Gilbank, D. G., Hokstra, H., et al. 2015, A&A, 586, A43
- Voit, G. M. 2005, RvMP, 77, 207
- von der Linden, A., Mantz, A., Allen, S., et al. 2014, MNRAS, 443, 3
- Wright, C. O. & Brainerd, T. G. 2000, ApJ, 534, 34
- Yang, X., Mo, H. J., van den Bosch, F. C., et al. 2006, MNRAS, 373, 1159
- York, D. G., Adelman, J., Anderson, Jr. J. E., et al. 2000, AJ, 120, 1579
- Zhang, Y.-Y., Finoguenov, A., Böhringer, H., et al. 2008, A&A 482, 451
- Zhang, H.-X., Peng, E. W., Côté, P., et al. 2015, ApJ, 802, 30

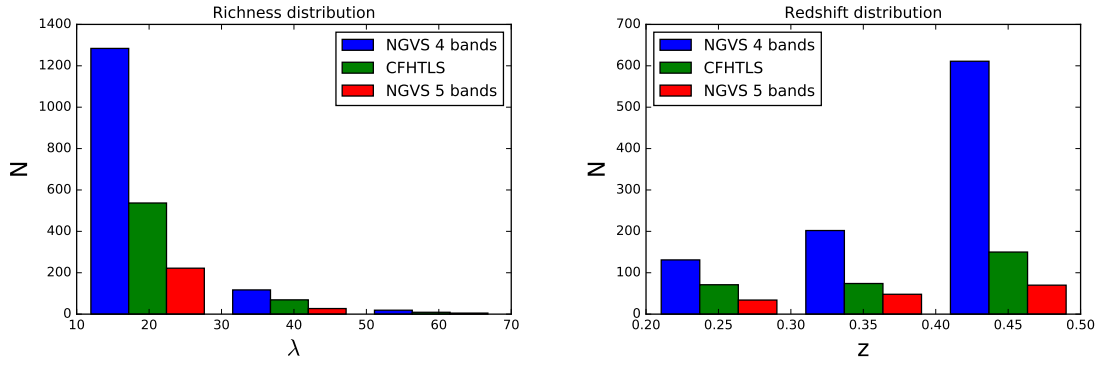


Fig. 1.— The richness and redshift distributions of the RedGOLD CFHT-LS W1, NGVS5 and NGVS4 1325 clusters from published catalogs and selected for our weak lensing analysis (see text for the description of the catalogs). The richness is plotted in bins of $\Delta\lambda = 20$, and the redshift in bins of $\Delta z = 0.1$. In each bin, the bars corresponding to the three different samples are plotted next to each other.

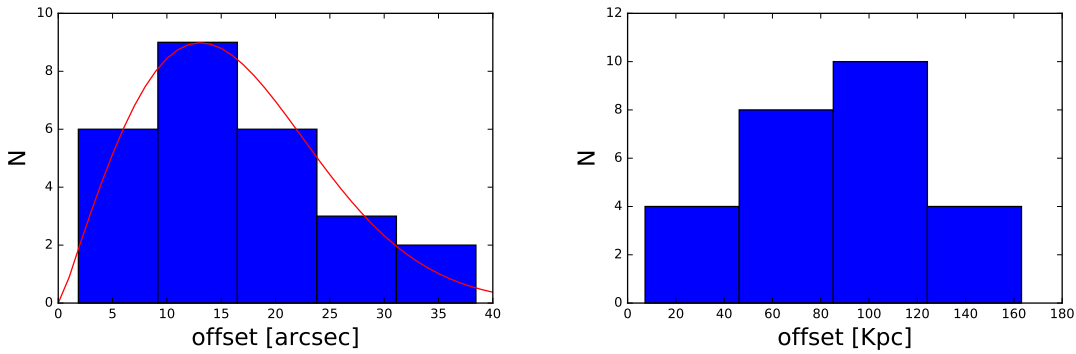


Fig. 2.— On the left, distribution of the offsets, in arcmin, between the RedGOLD and X-ray cluster centers. We show in red the fitted Rayleigh distribution with mode of 13 arcsec. On the right, the offset distribution in kpc.

$\Delta\Sigma$ profiles

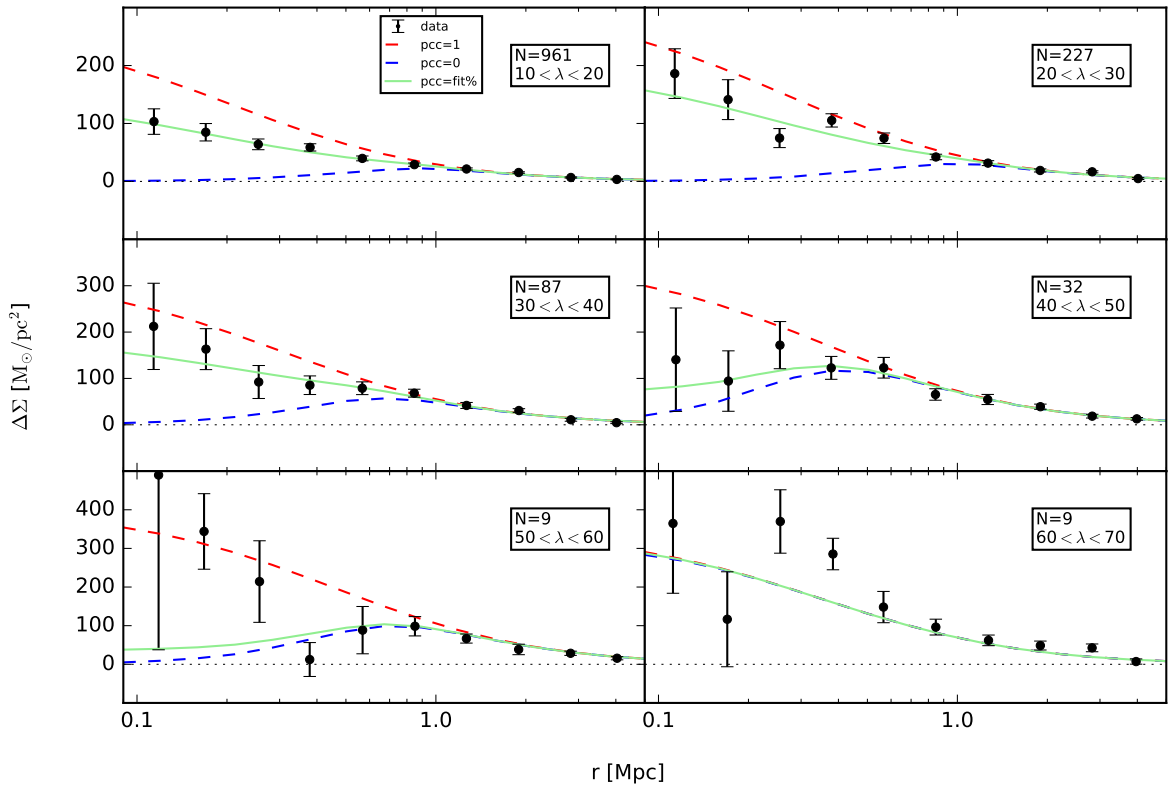


Fig. 3.— Shear profiles measured with our weak lensing analysis selected sample (CFHT-LS W1 + NGVS5+ NGVS4). The fits were obtained using Model 1. We show our shear profile measurement (black), the fit results (green), the ideal profiles that we would obtain in the case in which all the clusters in the stack were perfectly centered (red) and when they would have been all miscentered (blue). The dotted lines show $\Delta\Sigma(R) = 0$. We get similar results using Model 2 and Model 3.

$\Delta\Sigma$ profiles

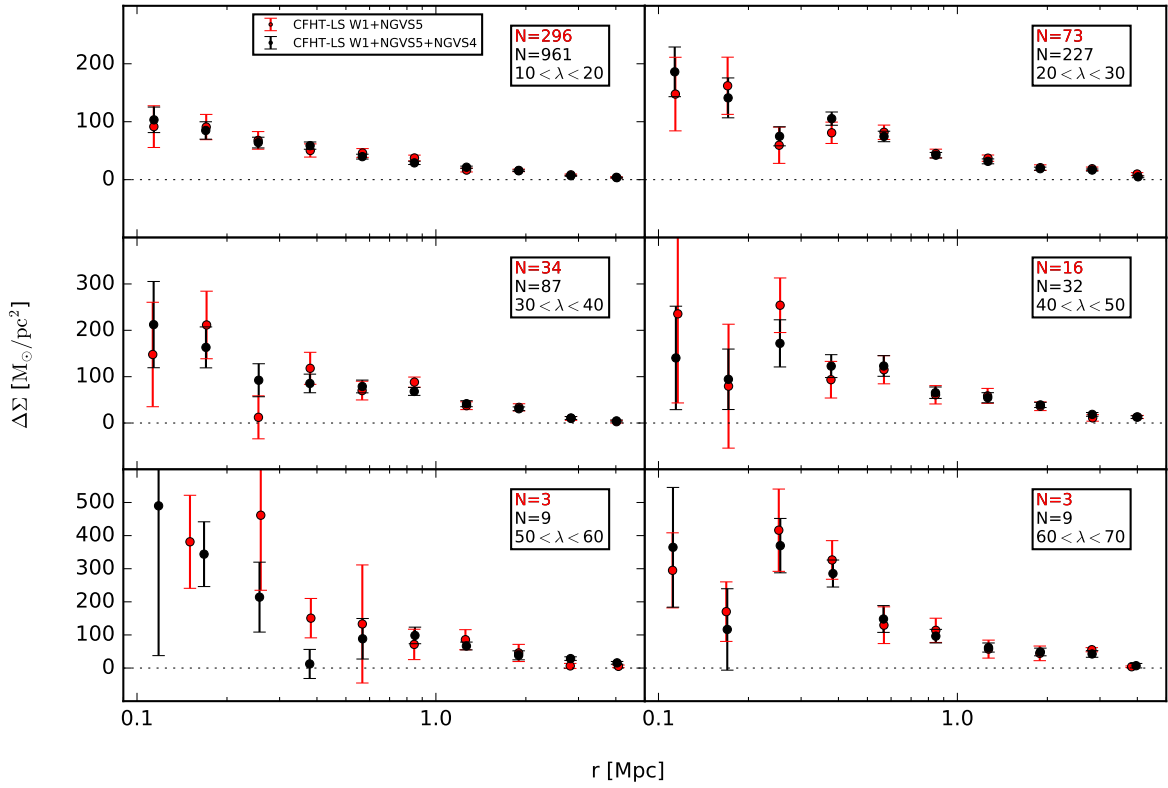


Fig. 4.— Shear profiles measured with the weak lensing selected CFHT-LS W1 + NGVS5, in red, and with the weak lensing selected CFHT-LS W1 + NGVS5 + NGVS4, in black. We notice that the addition of the four bands sample does not significantly change the profiles. The profiles measured using the two different samples are compatible within 1σ and the profiles obtained using CFHT-LS W1 + NGVS5 + NGVS4 have smaller error bars.

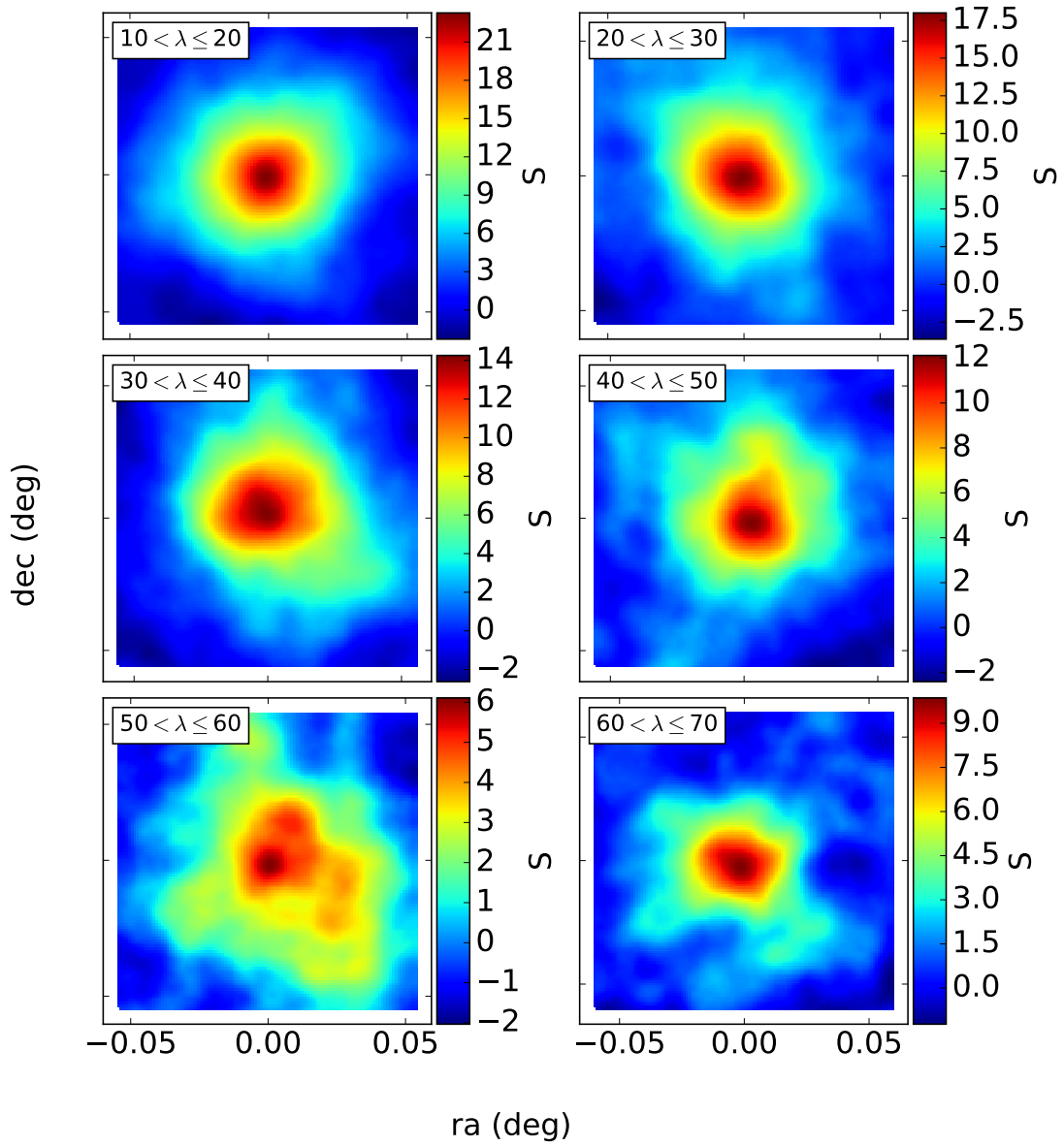


Fig. 5.— *Lensing signal-to-noise ratio maps in each richness bin for our weak lensing selected CFHT-LS W1 + NGVS5 + NGVS4 catalog. We applied aperture mass statistics.*

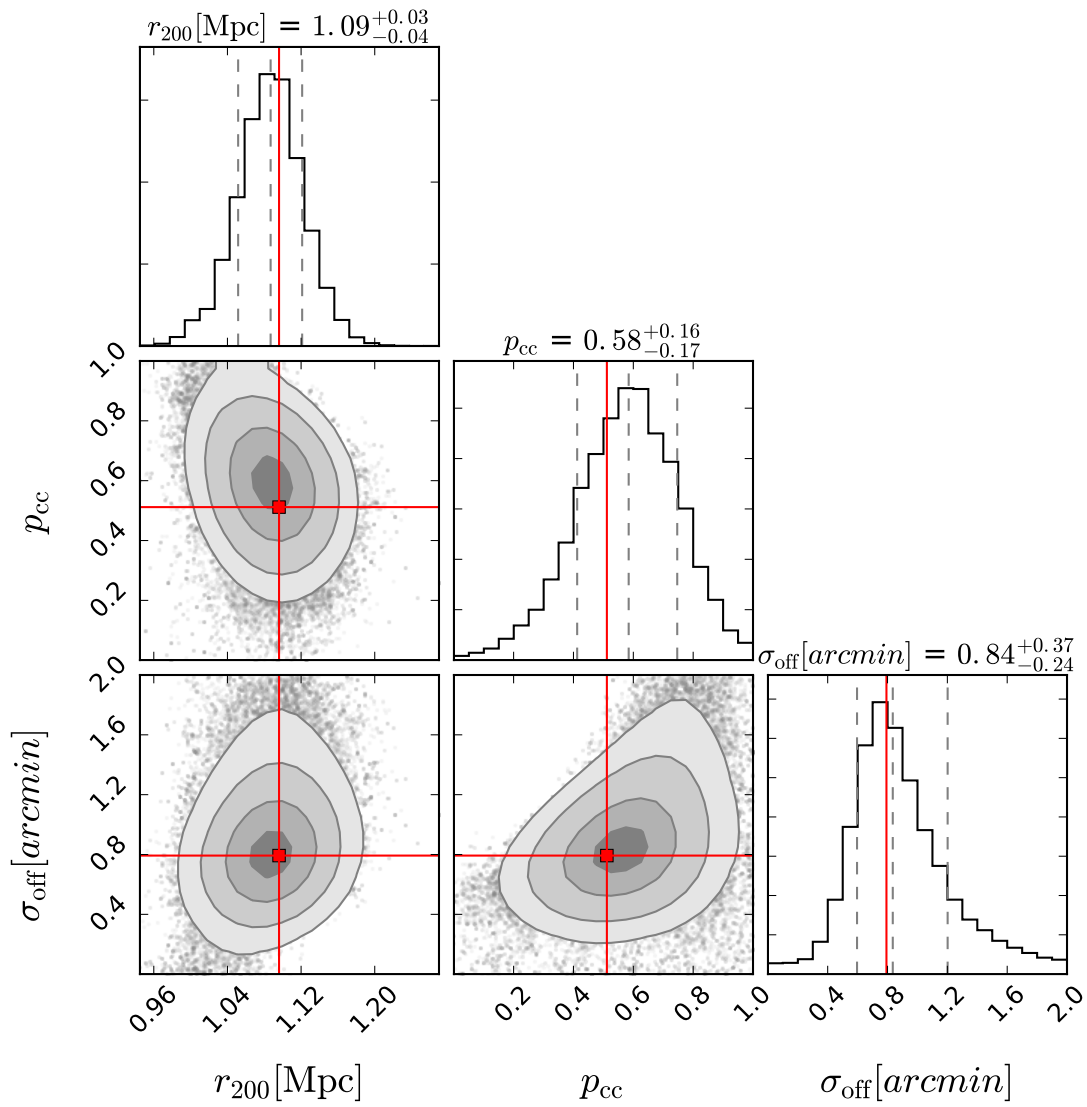


Fig. 6.— Confidence levels on the fit parameters obtained with our MCMC analysis. On the diagonal, we show the 1-D histograms of each parameter. The 2-D histograms are also shown for each couple of parameters with confidence levels corresponding to 0.5σ , 1σ , 1.5σ , 2σ . The parameter values and errors are based on the 16th, 50th and 84th quantiles (shown as dashed lines in the 1-D histograms). The red squares and lines represents the values that correspond to the maximum likelihood.

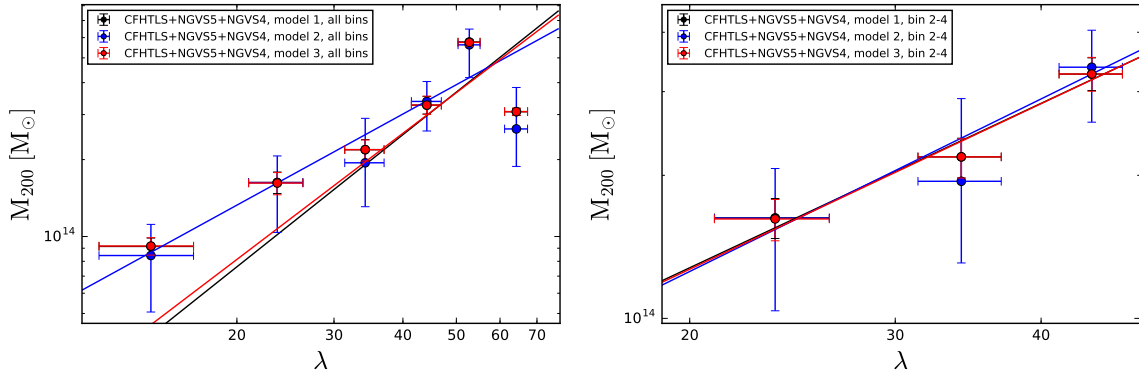


Fig. 7.— *The weak lensing mass-richness relation. On the left we show the results obtained from the fit to all richness bins, and on the right those obtained using our best bin sample. In both plots, the circles show the mean masses obtained using the three different models that we considered (see text for the description of the models). The colors correspond to the models shown in the legend.*

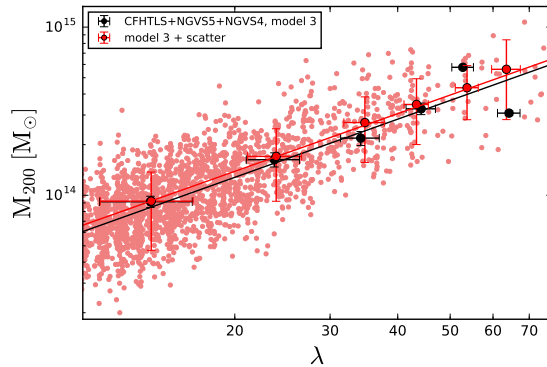


Fig. 8.— *Effect of the a posteriori intrinsic scatter correction. Using the mass-richness relation inferred from Model 3 (in black), we calculated cluster masses for our selected sample. We scattered those masses assuming a log-normal distribution centered on $\log M_{200}$ and with a width $\sigma_{\ln M|\lambda} = 0.39$, based on the value measured by Licitra et al. (2016a) (in light red). We repeated this procedure creating 1000 bootstrap realizations and calculated the new mean mass values in each richness bin, averaging over all realizations. We then repeated the fit to infer the new mass-richness relation (in red), which is shifted towards larger masses.*

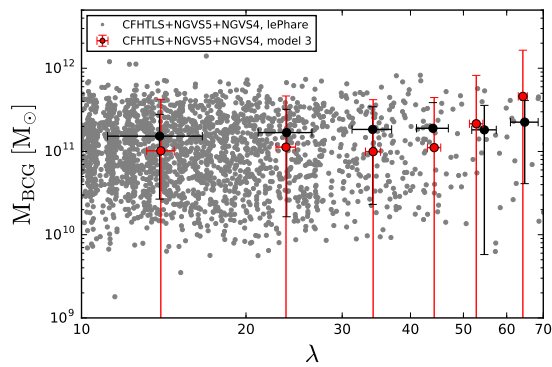


Fig. 9.— *BCG mass versus richness. In red, we show the BCG mean masses obtained as a free parameter from the fit to Model 3. In grey, we show the stellar masses of the central galaxies calculated from their spectral energy distribution, and in black, their mean values in each richness bin. The two BCG mass estimates are in good agreement.*

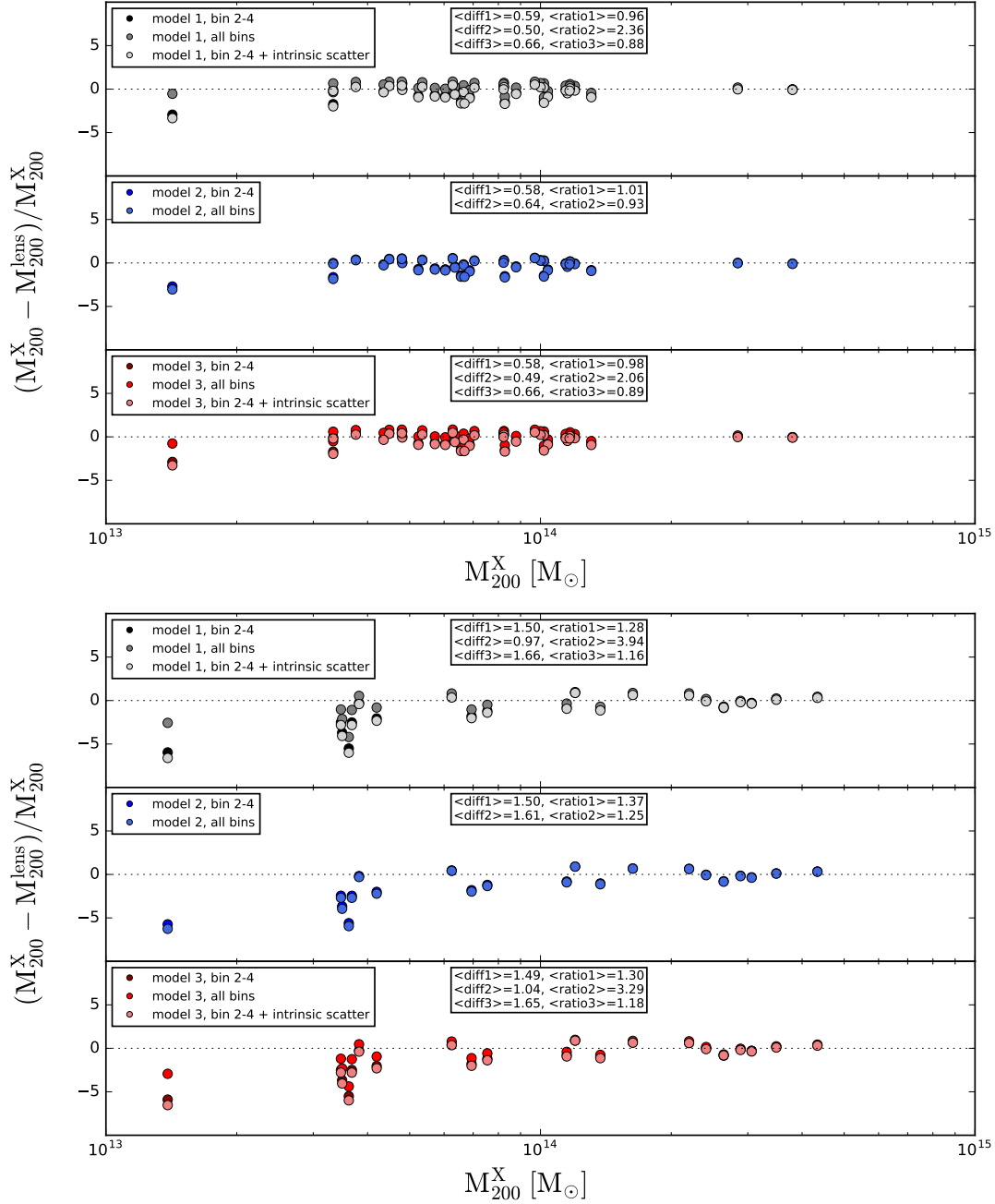


Fig. 10.— Comparison of X -ray masses and lensing masses calculated from the fitted mass-richness relations obtained using all bins, our best bins, and our best bins with the a posteriori correction for the intrinsic scatter in the mass-richness relation, for all three models. For the top plot we used Gozaliasl et al. (2014) catalog and for the bottom plot Mehrstens et al. (2012) catalog. From our best model, using Gozaliasl et al. (2014) catalog, we obtain a mean normalized difference of 0.66 and a mean ratio of 0.89, while using Mehrstens et al. (2012) catalog, we find 1.65 and 1.18, respectively.

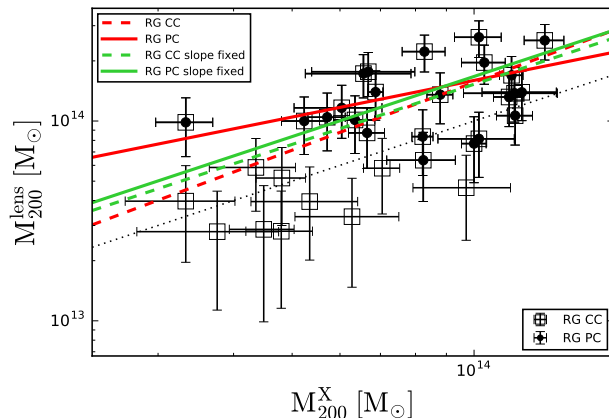


Fig. 11.— We compare our derived weak lensing masses with the X-ray masses from Gozaliasl et al. (2014) catalog. The weak lensing masses have been derived from our fit of the mass-richness relation using Model 3 and our best bins, after the intrinsic scatter correction. The black dots are the RedGOLD detections from the published catalogs (RG PC) and the black squares are the detections from the complete catalogs (RG CC). The red lines show the fits obtained with the slope as a free parameter, and the green lines those obtained with the slope fixed at unity. In both cases, solid lines refer to the published catalogs, and the dashed lines, to the complete catalogs. The black dotted line is the diagonal. See Section 3.1.2 for the catalog definitions.

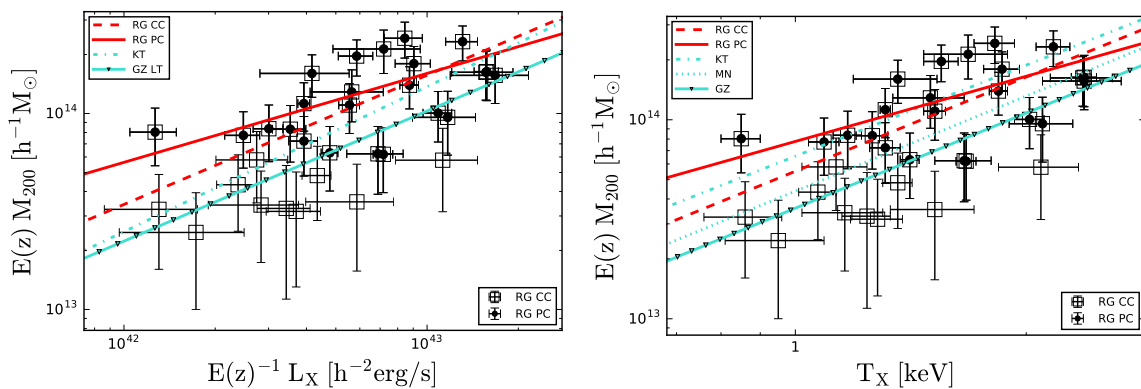


Fig. 12.— We compare our derived weak lensing masses with X-ray mass proxies. On the left we show our mass-luminosity relation, and on the right our mass-temperature relation, compared with the literature. The black dots and the black squares have the same meaning as in Figure 11. The different cyan lines show the relations obtained using the X-ray masses from Gozaliasl et al. (2014) catalog (GZ), calculated with the M-L relation of Leauthaud et al. (2010) (LT), the relations inferred by Kettula et al. (2015) (KT), and by Mantz et al. (2016) (MN) (see the legend for the line styles).

	Model 1	Model 2	Model 3
$r_{200}[\text{Mpc}]$	(0, 2)	—	(0, 2)
$\sigma_{\text{off}}[\text{arcmin}]$	(0, 2)	(0, 2)	(0, 2)
p_{cc}	(0, 1)	(0, 1)	(0, 1)
$\sigma_{\ln M \lambda}$	—	(0.1, 0.7)	—
$\log(M_{200}/M_{\odot})$	—	(11, 17)	—
$\log(M_{\text{BCG}}/M_{\odot})$	—	—	(9, 13)

Table 1: *MCMC uninformative prior values for the different parameters of the three models. The lack of a numerical value indicates that the parameter is not included in the respective model.*

λ range	N	λ	z	r_{200} Mpc	M_{200} $10^{13}M_{\odot}$	σ_{off} arcmin	p_{cc}
$10 < \lambda \leq 20$	961	14 ± 3	0.40	$0.81_{-0.02}^{+0.02}$	9_{-1}^{+1}	$1.1_{-0.3}^{+0.2}$	$0.5_{-0.1}^{+0.1}$
$20 < \lambda \leq 30$	227	24 ± 3	0.39	$0.98_{-0.03}^{+0.03}$	16_{-2}^{+2}	$1.2_{-0.5}^{+0.6}$	$0.7_{-0.1}^{+0.1}$
$30 < \lambda \leq 40$	87	34 ± 3	0.39	$1.09_{-0.03}^{+0.04}$	22_{-2}^{+2}	$0.8_{-0.4}^{+0.2}$	$0.6_{-0.2}^{+0.2}$
$40 < \lambda \leq 50$	32	44 ± 3	0.39	$1.24_{-0.03}^{+0.03}$	33_{-3}^{+2}	$0.4_{-0.1}^{+0.1}$	$0.2_{-0.2}^{+0.1}$
$50 < \lambda \leq 60$	9	53 ± 2	0.40	$1.50_{-0.01}^{+0.01}$	58_{-1}^{+2}	$0.8_{-0.1}^{+0.1}$	$0.1_{-0.1}^{+0.1}$
$60 < \lambda \leq 70$	9	64 ± 3	0.35	$1.23_{-0.01}^{+0.01}$	31_{-1}^{+1}	$0.0_{-0.2}^{+0.0}$	$0.6_{-0.4}^{+0.4}$

Table 2: *Parameters derived from the fit of the Model 1 shear profile to our measurements. λ is the cluster optical richness derived with RedGOLD and the first column gives the richness range; N is the number of stacked clusters in each bin; z is the mean redshift; r_{200} is the mean radius in Mpc; M_{200} is the mean mass in units of $10^{13}M_{\odot}$; σ_{off} is the scale length of the offset distribution in arcmin; p_{cc} is the percentage of correctly centered clusters in the stack.*

λ range	N	λ	z	r_{200} Mpc	M_{200} $10^{13}M_{\odot}$	σ_{off} arcmin	p_{cc}	$\sigma_{\ln M \lambda}$
$10 < \lambda \leq 20$	961	14 ± 3	0.40	$0.79_{-0.08}^{+0.10}$	8_{-3}^{+3}	$1.1_{-0.3}^{+0.2}$	$0.5_{-0.1}^{+0.1}$	$0.4_{-0.2}^{+0.2}$
$20 < \lambda \leq 30$	227	24 ± 3	0.39	$0.98_{-0.09}^{+0.12}$	16_{-4}^{+6}	$1.1_{-0.6}^{+0.5}$	$0.6_{-0.1}^{+0.1}$	$0.4_{-0.2}^{+0.2}$
$30 < \lambda \leq 40$	87	34 ± 3	0.39	$1.04_{-0.17}^{+0.11}$	19_{-10}^{+6}	$0.8_{-0.3}^{+0.2}$	$0.6_{-0.2}^{+0.2}$	$0.4_{-0.2}^{+0.2}$
$40 < \lambda \leq 50$	32	44 ± 3	0.39	$1.25_{-0.08}^{+0.10}$	34_{-7}^{+8}	$0.4_{-0.1}^{+0.1}$	$0.2_{-0.2}^{+0.1}$	$0.4_{-0.2}^{+0.2}$
$50 < \lambda \leq 60$	9	53 ± 2	0.40	$1.48_{-0.08}^{+0.13}$	56_{-9}^{+14}	$0.8_{-0.1}^{+0.6}$	$0.2_{-0.3}^{+0.1}$	$0.4_{-0.2}^{+0.2}$
$60 < \lambda \leq 70$	9	64 ± 3	0.35	$1.17_{-0.18}^{+0.11}$	26_{-12}^{+8}	$0.0_{-0.1}^{+0.0}$	$0.5_{-0.4}^{+0.4}$	$0.4_{-0.2}^{+0.2}$

Table 3: *The same as in Table 2, for the parameters derived from the fit of Model 2, i.e. with the addition of the intrinsic scatter of the mass-richness relation $\sigma_{\ln M|\lambda}$.*

λ range	N	λ	z	r_{200} Mpc	M_{200} $10^{13}M_{\odot}$	σ_{off} arcmin	pcc	M_{BCG} $10^{11}M_{\odot}$
$10 < \lambda \leq 20$	961	14 ± 3	0.40	$0.81^{+0.03}_{-0.03}$	9^{+1}_{-1}	$1.1^{+0.3}_{-0.3}$	$0.5^{+0.1}_{-0.1}$	$1.1^{+3.4}_{-3.2}$
$20 < \lambda \leq 30$	227	24 ± 3	0.39	$0.97^{+0.04}_{-0.03}$	16^{+2}_{-1}	$1.0^{+0.5}_{-0.7}$	$0.6^{+0.1}_{-0.1}$	$1.2^{+3.9}_{-3.7}$
$30 < \lambda \leq 40$	87	34 ± 3	0.39	$1.08^{+0.04}_{-0.04}$	22^{+3}_{-2}	$0.8^{+0.2}_{-0.4}$	$0.6^{+0.2}_{-0.2}$	$1.4^{+4.5}_{-4.1}$
$40 < \lambda \leq 50$	32	44 ± 3	0.39	$1.23^{+0.03}_{-0.04}$	32^{+3}_{-3}	$0.4^{+0.1}_{-0.2}$	$0.2^{+0.1}_{-0.2}$	$0.7^{+2.1}_{-2.3}$
$50 < \lambda \leq 60$	9	53 ± 2	0.40	$1.51^{+0.02}_{-0.02}$	59^{+3}_{-2}	$0.8^{+0.1}_{-0.1}$	$0.1^{+0.1}_{-0.1}$	$1.4^{+4.3}_{-4.2}$
$60 < \lambda \leq 70$	9	64 ± 3	0.35	$1.23^{+0.02}_{-0.01}$	31^{+1}_{-1}	$0.0^{+0.0}_{-0.2}$	$0.6^{+0.4}_{-0.4}$	$3.6^{+14.5}_{-10.0}$

Table 4: *The same as in Table 2, for the parameters derived from the fit of Model 3, i.e. with the addition of the the BCG stellar mass M_{BCG} in units of $10^{11}M_{\odot}$.*

Model	Bins	$\log M_0$	α	$\langle \text{diff} \rangle_1$	$\langle \text{diff} \rangle_2$	$\langle M_X/M_L \rangle_1$	$\langle M_X/M_L \rangle_2$
1	all	14.39 ± 0.12	1.72 ± 0.89	0.50	0.97	2.36	3.94
	2-4	14.45 ± 0.03	1.15 ± 0.21	0.59	1.50	0.96	1.28
	2-4 + ISC	14.48 ± 0.04	1.13 ± 0.22	0.66	1.66	0.88	1.16
2	all	14.48 ± 0.06	1.18 ± 0.33	0.64	1.61	0.93	1.25
	2-4	14.46 ± 0.04	1.21 ± 0.35	0.58	1.50	1.01	1.37
3	all	14.40 ± 0.12	1.64 ± 0.84	0.49	1.04	2.06	3.29
	2-4	14.45 ± 0.03	1.16 ± 0.22	0.58	1.49	0.98	1.30
	2-4 + ISC	14.48 ± 0.04	1.14 ± 0.23	0.66	1.65	0.89	1.18

Table 5: *Results of the fit of the mass-richness relation: $\log M_{200} = \log M_0 + \alpha \log \lambda / \lambda_0$, with a pivot $\lambda_0 = 40$, obtained using the three models in different richness bins. All bins correspond to the richness range $10 \leq \lambda \leq 70$, and bins 2-4 to the range $20 \leq \lambda \leq 50$. For Model 1 and 3 we also show the results after applying the a posteriori intrinsic scatter correction (ISC). The last four columns show the normalized average difference between X-ray and lensing masses $\langle \text{diff} \rangle = (M_{200}^X - M_{200}^{\text{lens}}) / M_{200}^X$, and the average ratio of the two, using the X-ray detections of Gozaliasl et al. (2014) ($\langle M_X/M_L \rangle_1$) and Mehrtens et al. (2012) ($\langle M_X/M_L \rangle_2$).*

Relation	Sample	a	b	scatter
$M_L - M_X$	CC	-1.61 ± 3.25	1.13 ± 0.23	0.22
	PC	5.67 ± 3.48	0.61 ± 0.25	0.16
$M_L - M_X$	CC	0.18 ± 0.03	fixed at 1	0.22
	PC	0.22 ± 0.04	fixed at 1	0.18
$M_L - T_X$	CC	0.23 ± 0.04	1.57 ± 0.31	0.22
	PC	0.29 ± 0.04	1.09 ± 0.32	0.16
$M_L - L_X$	CC	0.11 ± 0.04	0.66 ± 0.13	0.22
	PC	0.17 ± 0.04	0.45 ± 0.13	0.16

Table 6: Results of the fit of the weak lensing mass versus X-ray mass and mass proxy relations: $\log M_L = a + b \log M_X$; $\log (M_{200}E(z)/M_0) = a + b \log (L_X/L_0E(z))$; $\log (M_{200}E(z)/M_0) = a + b \log (T_X/T_0)$. "CC" refers to the complete catalogs and "PC" to the published catalogs (See text for the catalogs definitions and for the values of the pivot mass, luminosity and temperature used in the fit of the scaling relations).

Relation	Comparison	Sample	Δa	Δb	a compatibility	b compatibility
$M_L - T_X$	Kettula et al. (2015)	CC	0.04 ± 0.16	0.05 ± 0.35	1σ	1σ
		PC	0.23 ± 0.16	0.43 ± 0.36	1.5σ	1σ
	Mantz et al. (2016)	CC	0.35 ± 0.27	0.00 ± 0.13	1σ	1σ
		PC	0.14 ± 0.53	0.29 ± 0.27	1σ	1σ
$M_L - L_X$	Kettula et al. (2015)	CC	0.02 ± 0.16	0.08 ± 0.15	1σ	1σ
		PC	0.22 ± 0.16	0.29 ± 0.16	1.5σ	2σ
	Leauthaud et al. (2010)	CC	0.18 ± 0.09	0.00 ± 0.19	2σ	1σ
		PC	0.31 ± 0.09	0.21 ± 0.19	3σ	1σ

Table 7: Comparison of our mass-temperature and mass-luminosity relations with others in literature. "CC" refers to the results obtained using the complete catalogs and "PC" using the published catalogs (See text for the catalogs definitions). Δa is the difference in normalization, and Δb the difference in slope, between our results and those obtained by Kettula et al. (2015), Mantz et al. (2016) and Leauthaud et al. (2010). The last two columns show that our relations are consistent, in normalization and slope, within $\lesssim 2 \sigma$ with the others in literature, when using the complete catalogs.

BIBLIOGRAPHY

- Abell, G. O. 1958, *ApJS*, 3, 211
- Ahn, C. P., Alexandroff, R., Allende Prieto, C., et al. 2014, *ApJS*, 211, 17
- Allen, S. W., Evrard A. E. & Mantz, A. B. 2011, *ARA&A*, 49, 409
- Allen, S. W., Mantz, A. B., Morris, R. G., et al. 2013, [arXiv:1307.8152v1](https://arxiv.org/abs/1307.8152v1)
- Amodeo, S., Mei, S., Standford, S. A., et al. 2017, [arXiv:1704.07891v1](https://arxiv.org/abs/1704.07891v1)
- Angulo, R. E., Springel, V., White, S. D. M., et al. 2012, *MNRAS*, 426, 2046
- Arnaud, M., Pointecouteau, E., Pratt, G., W. 2007, *A&A*, 474, L37
- Arnaud, M., Pratt, G., W., Piffaretti, R., et al. 2010, *A&A*, 517, A92
- Arnouts, S., Cristiani, S., Moscardini, L., et al. 1999, *MNRAS*, 310, 540
- Arnouts, S., Moscardini, L., Vanzella, E., et al. 2002, *MNRAS*, 329, 355
- Ascaso, B., Mei, S., Bartlett, J.G., Benítez, N. 2016, *MNRAS*, 464, 2270
- Bacon, D. J., Refregier, A. R., Ellis, R. S. 2000, *MNRAS*, 318, 652
- Bartelman, M. 1995, [arxiv:9410076](https://arxiv.org/abs/9410076)
- Bartelmann, M. & Schneider, P. 2001, *PhR*, 340, 4-5
- Bartelmann, M. & Maturi, M. 2016, [arxiv:1612.06535v1](https://arxiv.org/abs/1612.06535v1)
- Becker, M. R., McKay, T.A., Koester, B., et al. 2007, *ApJ*, 669, 905
- Becker, M. R. & Kravtsov, A. V. 2011, *ApJ*, 740, 25
- Becker, M. R., (DES Collaboration) et al. 2016, *Phys. Rev.*, D94, 022002

- Benítez N. 2000, ApJ, 536, 571
- Benítez, N., Ford, H., Bouwens, R., et al. 2004, ApJS, 150, 1
- Benson, B. A., de Haan, T., Dudley, J. P., et al. 2011, ApJ, 763, 2
- Bertin, E. & Arnouts, S. 1996, A&AS, 117, 393
- Bertin, E. 2011, ASP Conference Series, 442
- Bhattacharya, S., Heitmann, K., White, M., et al. 2011, ApJ, 732, 122
- Bocquet, S., Saro, A., Mohr, J. J., et al. 2015, ApJ, 799, 2
- Bocquet, S., Saro, A., Dolag, K., Mohr, J. J. 2016, MNRAS, 456, 2361
- Boggs, P. T. & Rogers, J. E. 1990, Contemporary Mathematics, 112, 186
- Bonamente, M., Joy, M. K., LaRoque, S. J., et al. 2006, ApJ, 647, 25
- Bond, J. R., Cole, S., Efstathiou, G., Kaiser, N. 1991, ApJ, 379, 440
- Böhringer, H., Dolag, K., Chon, G. 2011, A&A, 539, A120
- Boulade, O., Charlot, X., Abbon, P. et al. 2003, Proc. SPIE, 4841, 72
- , Brammer, G. B., van Dokkum, P. G., Coppi, P. 2008, ApJ, 686, 1503
- Bullock, J. S., Kolatt, T. S., Sigad, Y., et al. 2001, MNRAS, 321, 559
- Caldwell, C. E., McCarthy, I. G., Baldry, I. K., et al. 2016, MNRAS, 462, 4117
- Capak, P., Cowie, L. L., Hu, E. M., et al. 2004, AJ, 127, 180
- Carlstrom, J. E., Ade, P. A. R., Aird, K. A., et al. 2011, PASP, 123, 568
- Cavaliere, A. & Fusco-Fermiano, R. 1976, A&A, 49, 137
- Coe, D., Benítez, N., Sánchez, S. F., et al. 2006, AJ, 132, 926
- Cohn, J. D., Evrard, A. E., White, M., Croton, D., Ellingson, E. 2007, MNRAS, 382, 1738
- Coles, P. & Lucchin, F. 2002, John Wiley & Sons, Ltd, "Cosmology, The origin and Evolution of Cosmic Structure"
- Corless, V. L. & King, L. J. 2007, MNRAS, 380, 149

- Coupon, J., Arnouts, S., van Waerbeke, L., et al. 2015, MNRAS, 449, 2
- Covone, G., Sereno, M., Kilbinger, M., Cardone, V. F. 2014, ApJL, 784, 2
- Crocce, M., Fosalba, P., Castander, F. J., Gaztañaga, E. 2010, MNRAS, 403, 1353
- Cui, W., Power, C., Biffi, V., et al. 2016, MNRAS, 465, 3
- Dahle, H., Pedersen, K., Lilje, P. B., Maddox, S. J., Kaiser, N. 2003, ApJ, 591, 662
- Dark Energy Survey Collaboration 2016, MNRAS, 460, 1270
- Dark Energy Survey Collaboration 2016, Phys. Rev., D94, 0022001
- Davis, M., Faber, S. M., Newman, J. A., et al. 2003, Proc. SPIE, 4834, 161
- de Haan, T., Benson, B. A., Bleem, L. E., et al. 2016, ApJ, 832, 1
- Donahue, M., Mack, J., Scharf, C., et al. 2001, ApJ Lett. 552, L93
- Donahue, M., Scharf, C., Mack, J., et al. 2001, ApJ 569, 689
- Du, W. & Fan, Z. 2014, ApJ, 785, 57
- Durret, F. Adami, C., Cappi, A., et al. 2011, A&A, 535, A65
- Dutton, A. A. & Macció, A. V. 2014, MNRAS, 441, 3359
- Edge, A., Sutherland, W., Kuijken, K., et al., 2013, The Messenger, 154, 32
- Efron, B. 1979, Ann. Statist. 7, 1
- Eisenstein, D. J. & Hu, W. 1998, ApJ, 469, 605
- Erben, T., Schirmer, M., Dietrich, J. P., et al. 2005, Astron. Nachr., 326, 432
- Erben, T., Hildebrandt, H., Lerchster, M., et al. 2009, A&A, 493, 1197
- Erben, T., Hildebrandt, H., Miller, L., et al. 2013, MNRAS, 433, 2545
- Evrard, A. E., Bialek, J., Busha, M., et al. 2008, ApJ, 672, 1
- Fahlman, G., Kaiser, N., Squires, G., Woods D. 1994, ApJ, 437, 56
- Farahi, A., Evrard, A. E., Rozo, E., Rykoff, E. S., Wechsler, R. H. 2016, MNRAS, 460, 3900

Feldmann, R., Carollo, C. M., Porciani, C., et al. 2006, MNRAS, 372, 2

Fenech Conti, I., Herbonnet, R., Hoekstra, H., et al. 2016, arXiv:1606.05337

Ferrarese, L., Cote, P., Cuillandre, J.-C., et al. 2012, ApJS, 200, 4

Ford, J., van Waerbeke, L., Milkeraitis, M., et al. 2015, MNRAS 447, 1304

Foreman-Mackey, D., Hogg, D. W., Lang, D., Goodman, J. 2013, PASP, 125, 925

Foreman-Mackey, D., Vousden, W., Price-Whelan, A., et al. 2016, corner.py, v1.0.2, Zenodo, doi:10.5281/zenodo.45906

Fosalba, P., Crocce, M., Gaztañaga, E., Castander, F. 2015, MNRAS, 448, 2987

Gavazzi, R., Treu, T., Rhodes, J. D, et al. 2007, ApJ, 667, 176

George, M. R., Leauthaud, A., Bundy, K., et al., 2012, ApJ, 757, 2

Gilbank, D. G., Bower, R. G., Castander, F. J., Ziegler, B. L., 2004, MNRAS, 348, 551

Gilks, W. R., Richardson, S., Spiegelhalter, D. J., "Markov Chain Monte Carlo in Practice", 1996, Chapman & Hall

Gladders, M. D. & Yee, H. K. C. 2000, AJ, 120, 2148

Goodman, J. & Weare, J. 2010, CaMCoS, 5, 65

Gozaliasl, G., Finoguenov, A., Khosroshahi, H. G., et al. 2014, A&A 566, 140

Grove, L. F., Benoist, C., Martel, F. 2009, A&A, 494, 845

Guzzo, L., Scodreggio, M., Garilli, B., et al., 2014, A&A, 556, 108

Gwyn, S. D. J. 2012, ApJ, 143, 38

Hajian, A., Battaglia, N., Spergel, D. N., et al. 2013, JCAP, 11, 64

Hamana, T., Takada, M. & Yoshida, N. 2004, MNRAS, 350, 893

Hamana, T., Sakurai, J., Koike, M., Miller., L. 2015, MNRAS, 67, 3

Hastings ,W. K. 1970, Biometrika, Vol. 57, 1

- Henriques, B. M. B., White, S. D. M., Lemson, G., et al. 2012, MNRAS, 421, 2904
- Henry, J. P., Evrard, A. E., Hoekstra, H., Babul, A., Mahdavi, A. 2009, ApJ, 691, 1307
- Heymans, C., van Waerbeke, L., Miller, L., et al. 2012, MNRAS, 427, 146
- Hildebrandt, H., Erben, T., Kuijken, K., et al. 2012, MNRAS, 421, 2355
- Hildebrandt, H., Viola, M., Heymans, C., et al. 2016, MNRAS, stw2805
- Hoekstra, H. 2001, A&A, 370, 743
- Hoekstra, H. 2003, MNRAS, 339, 1155
- Hoekstra, H., Mellier, Y., van Waerbeke, L., et al. 2005, ApJ, 647, 1
- Hoekstra, H., Mahdavi, A., Babul, A., Bildfell, C. 2012, MNRAS, 427, 2
- Hoekstra, H., Bartelmann, M., Dahle, H. et al. 2013, Space Sci. Rev., 177, 75.
- Hoekstra, H., Herbonnet, R., Muzzin, A., et al. 2015, MNRAS, 449, 685
- Hogg, D. W. 2000, arXiv:astro-ph/9905116v4
- Hu, W. & Sugiyama, N. 1996, ApJ, 471, 542
- Huchara, J. P. & Geller, M. J. 1982, ApJ, 257, 423
- Ilbert, O., Arnouts, S., McCracken, H. J., et al. 2006, A&A, 457, 841
- Israel, H., Erben, T., Reiprich, T. H., et al. 2010, A&A, 520, A58
- Israel, H., Reiprich, T., Erben, T., et al. 2014, A&A, 564, A129
- Jenkins, A., Frenk, C., White, S. D., et al. 2001, MNRAS, 321, 372
- Johnson, A., Blake, C., Amon, A., et al., 2017, MNRAS, 465, 4
- Johnston, D. E., Sheldon, E. S., Wechsler, R. H., et al. 2007, arXiv:0709.1159
- Kasliwal, M. M., Massey, R., Ellis, R. S., Miyazaki, S., Rhodes, J. 2008, ApJ, 684, 1
- Kettula, K., Giodini, S., van Uitert, E., et al. 2015, MNRAS, 451, 1460

Kinney, A. L., Calzetti, D., Bohlin, R. C., et al. 1996, *ApJ*, 467, 38

Kochanek, C. S., White, M., Huchra, J., et al. 2003, *ApJ*, 585, 161

Kratochvil, J. M., Haiman, Z., May, M. 2010, *Phys. Rev. D*, 81, 043519

Lacey, C. & Cole, S. 1993, *MNRAS*, 262, 627

Laureijs, R., Amiaux, J., Auguères, J.-L., et al. 2011, *ESA/SRE*

Leauthaud, A., Finoguenov, A., Kneib, J.-P., et al. 2010, *ApJ*, 709, 114

Le Fèvre, O., Vettolani, G., Garilli, B., et al. 2005, *A&A*, 439, 845

Le Fèvre, O., Cassata, P., Cucciati, O., et al. 2013, *A&A*, 559, A14

Lewis, A., Challinor, A. & Lasenby, A. 2000, *ApJ*, 538, 473

Li, R., Shan, H., Mo, H., et al. 2014, *MNRAS*, 438, 4

Li, R., Shan, H., Kneib, J.-P., et al. 2016, *MNRAS*, 458, 3

Licitra, R., Mei, S., Raichoor, A., et al. 2016, *ApJ*, 829, 44

Licitra, R., Mei, S., Raichoor, A., Hildebrandt, H. 2016, *MNRAS*, 455, 3020

Liu, X., Pan, C., Li, R., et al. 2015, *MNRAS*, 450, 3

Liu, J., Petri, A., Haiman, Z., et al. 2015, *Phys. Rev. D*, 91, 063507

Mahdavi, A., Hoekstra, H., Babul, A. et al. 2012, *ApJ*, 767, 116

Mandelbaum, R., Hirata, C. M., Seljak, U., et al. 2005, *MNRAS*, 361, 1287

Mandelbaum, R., Seljak, U., Cool, R. J., et al. 2006, *MNRAS*, 372, 758

Mandelbaum, R., Seljak, U., Hirata, C. M. 2008, *JCAP*, 08, 006

Mandelbaum, R., Seljak, U., Hirata, C. M., et al. 2008, *MNRAS*, 386, 781

Mantz, A., Allen, S. W., Rapetti, D., Ebeling, H. 2010, *MNRAS* 406, 1759

Mantz, A., von der Linden, A., Allen, S. W., et al. 2015, *MNRAS*, 446, 2205

Mantz, A. B., Allen, S. W., Morris, R. G., et al. 2016, *MNRAS*, 463, 3582

Marriage, T. A., Acquaviva, V., Ade, P. A. R., et al. 2011, *ApJ*, 737, 61

Martinet, N., Bartlett, J., Kiessling, A., Sartoris, B. 2015, *A&A* 581, A101

- Maturi, M., Bartelmann, M., Dolag, K., Moscardini, L. 2005, *A&A*, 442, 851
- Mazure, A., Adami, C., Pierre, M., et al. 2007, *A&A*, 467, 49
- Mehrtens, N., Romer, A. K., Hilton, M., et al. 2012, *MNRAS*, 423, 1024
- Mei, S., Holden, B. P., Blakeslee, J. P., et al. 2009, *ApJ*, 690, 42
- Melin, J.-B., Bartlett, J., 2015, *A&A*, 578, A21
- Melchior, P., Gruen, D., McClintok, T., et al. 2016, arXiv:1610.06890v1
- Meneghetti, M., Rasia, E., Merten, J., et al. 2010, *A&A*, 514, A93
- Meneghetti, M., Natarajan, P., Coe, D., et al. 2016, arXiv:1606.04548v1
- Merloni, A., Predehl, P., Becker, W., et al. 2012, eROSITA science book: mapping the structure of the energetic universe (Standort: AS 24/105). Garching: Max-Planck-Institut für extraterretrische Physik
- Metropolis, N., Rosenbluth, A. W., Rosenbluth, M. N., et al. 1953, *JChPh*, 21,1087
- Milkeraitis, M., van Waerbeke, L., Heymans, C., et al. 2010, *MNRAS*, 406, 673
- Miller L., Heymans, C., Kitching, T. D., et al. 2013, *MNRAS*, 429, 2858
- Moore, B., Ghigna, S., Governato, F. 1998, *ASP Conference Series*, 136
- Munari, E., Biviano, A., Borgani, S., Murante, G., Fabjan, D. 2013, *MNRAS*, 430, 2638
- Navarro J. F., Frenk C. S., White S. D. M. 1996, *ApJ*, 462, 563
- Nelder, J. A. & Mead, R. 1965, *CompJ*, 7, 308
- Newman, J. A., Lee, A. B., Richards, J. W., et al. 2013, *ApJS*, 208, 5
- Newman, J. A., Abate, A., Abdalla, F. B., et al., 2015, *APh*, 63, 81
- Oguri, M., Takada, M., Umetsu, K., Broadhurst, T. 2005, *ApJ*, 632, 2
- Oguri, M. & Hamana, T. 2011, *MNRAS*, 414, 1851
- Oguri, M. & Takada, M. 2011, *Phys. Rev. D*, 83, 023008
- Oguri, M., Bayliss, M. B., Dahle, H., et al. 2012, *MNRAS*, 420, 4

Oke, J. B. & Gunn, J. E. 1983, *ApJ*, 266, 713

Olsen, L. F., Benoist, C., Cappi, A., et al. 2007, *A&A*, 461, 81

Pacaud, F., Clerc, N., Giles, P. A., et al. 2016, *A&A*, 592, A2

Penna-Lima, M., Bartlett, J. G., Rozo, E., et al. 2016, arXiv:1608.05356

Penzias, A. A. & Wilson, R. W. 1965, *ApJ*, 142, 419

Phillips, M. M. 1993, *ApJ*, 413, L105

Pierre, M., Chiappetti, L., Pacaud, F., et al. 2007, *MNRAS*, 382, 279

Piffaretti, R., Arnaud, M., Pratt, G. W., Pointecouteau, E., Melin, J.-B. 2011, *A&A*, 534, A109

Planck Collaboration IX 2016, *A&A*, 594, A9

Planck Collaboration XV 2016, *A&A*, 594, A15

Planck Collaboration XXIV 2016, *A&A*, 594, A24

Planck Collaboration XXVII 2016, *A&A*, 594, A27

POLARBEAR Collaboration 2014, *Phys. Rev. Lett.*, 113, 021301

Postman, M., Lubin, L. M., Gunn, J. E., et al. 1996, *AJ*, 111, 615

Postman, M., Coe, D., Benítez, N., et al. 2012, *ApJS*, 199, 25

Pozzetti, L., Hirata, C. M., Geach, J. E., et al., 2016, *A&A*, 590, A3

Pratt, G. W., Croston, J. H., Arnaud, M., Böhringer, H. 2009, *A&A*, 498, 361

Press, W. H. & Schechter, P. 1974, *ApJ*, 187, 425

Raichoor, A., Mei, S., Erben, T., et al. 2014, *ApJ*, 797, 102

Rasia, E., Tormen, G., Moscardini, L. 2003, *MNRAS*, 351, 237

Rasia, E., Meneghetti, M., Martino, R., et al. 2012, *NJPh*, 14

Reiprich, T. H. & Böhringer, H., 2002, *ApJ*, 567, 716

Rines, K. J., Geller, M. J., Diaferio, A., et al. 2016, *ApJ*, 819, 63

Rozo, E., Rykoff, E. S., Evrard, A., et al. 2009, ApJ, 699, 768

Rozo, E., Wechsler, R. H., Rykoff, E. S., et al. 2009, ApJ, 708, 1

Rozo, E., Wechsler, R. H., Rykoff, E. S., et al. 2010, ApJ, 708, 645

Rozo, E. & Rykoff, E. S. 2014, ApJ, 783, 80

Ryden, B. 2006, "Introduction to Cosmology"

Rykoff, E. S., Koester, B. P., Rozo, E., et al. 2012, ApJ, 746, 178

Rykoff, E. S., Rozo, E., Busha, M. T., et al. 2014, ApJ, 785, 104

Rykoff, E. S., Rozo, E., Hollowood, D., et al. 2016, ApJS, 224, 1

Sarazin, C.L. 1988, Cambridge Univ. Press

Saro, A., Bocquet, S., Rozo, E., et al. 2015, MNRAS, 454, 2305

Sartoris, B., Biviano, A., Fedeli, C., et al. 2016, MNRAS, 459, 1764

Schechter, P., 1976, ApJ 203, 297

Schellenberger, G., Reiprich, T. H., Lovisari, L., Nevalainen, J., David, L. 2015, A&A 575, A30

Schirmer, M., Erben, T., Schneider, P., et al. 2003, A&A, 407, 869

Schirmer, M., Erben, T., Hetterscheidt, M., Schneider, P. 2006, A&A, 462, 875

Schneider, P. 1996, MNRAS, 283, 837

Schneider, P. 2005, Springer Berlin, 33, 269

Seljak, U. 2000, MNRAS. 318, 203

Seljak, U. & Warren, M. S. 2004, MNRAS, 355, 129

Simet, M., Battaglia, N., Mandelbaum, R., Seljak, U. 2015, arXiv:1502.01024v2

Shectman, S. A. 1985, ApJS, 57, 77

Sheldon, E. S. 2014, MNRAS, 444, 1

Sheth, R. K., Tormen, G., 1999, MNRAS, 308, 119

Sifón, C., Cacciato, M., Hoekstra, H., et al. 2015, MNRAS, 454, 4

Simet, M., McClintock, T., Mandelbaum, R., et al. 2016, arXiv:1603.06953v1

Sirianni, M., Jee, M. J., Benítez, N., et al. 2005, PASP, 117, 1049

Smith, R. E., Peacock, J. A., Jenkins, A., et al. 2003, MNRAS, 341, 1311

Strauss, M. A., Weinberg, D. H., Lupton, R. H., et al. 2002, AJ, 124, 1810

Sunyaev, R. A. & Zeldovich, Y. B., 1972, CoASP, 4, 173

Thanjavur, K, Willis, J. & Crampton, D. 2009, ApJ, 706, 571

Tinker, J. L., Kravtsov, A. V., Klypin, A., et al. 2008, ApJ, 688, 709

Tinker, J. L., Sheldon, E. S., Wechsler, R. H., et al. 2012, ApJ, 745, 16

van Engelen, A., Keisler, R., Zahn, O., et al. 2012, ApJ, 756, 2

van Uitert, E., Gilbank, D. G., Hokstra, H., et al. 2015, A&A, 586, A43

van Uitert, E., Cacciato, M., Hoekstra, H, et al. 2016, MNRAS, 459, 3

Vikhlinin, A., Kravtsov, A. V., Burenin, R. A., et al. 2009, ApJ, 692, 1060

Voit, G. M. 2005, RvMP, 77, 207

von der Linden, A., Mantz, A., Allen, S., et al. 2014, MNRAS, 443, 3

Watson, W. A., Iliev, I. T., D’Aloisio, A., et al. 2013, MNRAS, 433, 1230

Weinberg, D. H., Mortonson, M. J., Eisenstein, D. J., et al. 2013, PhR, 530, 2

Wittman, D., Tyson, J. A., Margoniner, V. E., Cohen, J. G., Dell’Antonio, I. P. 2001, ApJ, 557, L89

Wittman, D., Margoniner, V. E., Tyson, et al. 2003, ApJ, 597, 218

Wright, C. O. & Brainerd, T. G. 2000, ApJ, 534, 34

Xue, Y. & Wu, X. 2000, ApJ, 538, 65

Yang, X., Mo, H. J., van den Bosch, F. C., et al. 2006, MNRAS, 373, 1159

Yang, X., Kratochvil, J. M., Wang, S., et al. 2011, Phys. Rev. D 84, 043529

Yee, H. K. C. & Ellingson, E., 2003, ApJ, 585, 215

York, D. G., Adelman, J., Anderson, Jr. J. E., et al. 2000, AJ, 120, 1579

Zhang, Y.-Y., Finoguenov, A., Böhringer, H., et al. 2008, A&A 482, 451

Zhang, H.-X., Peng, E. W., Côté, P., et al. 2015, ApJ, 802, 30

Zuntz, J., Kacprzak, T., Voigt, L., et al. 2013, MNRAS, 434, 2